

NAM

Dynamic Geomechanical Modelling to Assess and Minimize the Risk for Fault Slip during Reservoir Depletion of the Groningen Field

Part 1: 1D Geomechanical Model

Part 2: 3D Geomechanical Model

Baker RDS

Romain Guises, Jean-Michel Embry and Colleen Barton

Date June 2015

Editors Jan van Elk & Dirk Doornhof

General Introduction

In support of Winningsplan 2013, a number of geomechanical studies were carried out. These have been described in the addendum document to Winningsplan 2013 (Ref. 1) and in separate reports (Ref. 2 to 4). Stress data from the Groningen field was analysed to assess the initial and later stress state in the reservoir rock (Ref. 2).

In Part 1 of the current report (1D Geomechanical Model) geomechanical models are presented for a number of offset wells to provide an understanding and constraint of the current stress field. This study complements the study into the tectonic stresses in the Groningen field (Ref. 2) and the modelling study of single faults (Ref. 3).

In Part 2 of the current report (3D Geomechanical Model) a geomechanical model is prepared for the for the entire field. This study is in that respect similar to the Geomechanical Analysis (Ref. 4).

References

1. Technical Addendum to the Winningsplan Groningen 2013; Subsidence, Induced Earthquakes and Seismic Hazard Analysis in the Groningen Field, Nederlandse Aardolie Maatschappij BV (Jan van Elk and Dirk Doornhof, eds), November 2013.
2. Neotectonic Stresses in the Permian Slochteren Formation of the Groningen Field, Rob van Eijs, November 2015.
3. Impact of various modelling options on the onset of fault slip and fault slip response using 2-dimensional Finite-Element modelling, Peter van den Bogert, July 2015
4. Groningen 2015 Geomechanical Analysis, Suvrat P. Lele, Jorge L. Garzon, Sheng-Yuan Hsu, Nora L. DeDontney, Kevin H. Searles and Pablo F. Sanz (ExxonMobil Upstream Research Company, Spring, TX), March 2016.



NAM

Title	Assess and Minimize the Risk for Fault Slip during Reservoir Depletion of the Groningen Field Part 1: 1D Geomechanical Model Part 2: 3D Geomechanical Model		Date	June 2015
			Initiator	NAM
Autor(s)	Romain Guises, Jean-Michel Embry and Colleen Barton	Editors	Jan van Elk and Dirk Doornhof	
Organisation	Baker - RDS	Organisation	NAM	
Place in the Study and Data Acquisition Plan	<p><u>Study Theme:</u> Geomechanical Modelling</p> <p><u>Comment:</u></p> <p>In support of Winningsplan 2013, a number of geomechanical studies were carried out. These have been described in the addendum document to Winningsplan 2013 (Ref. 1) and in separate reports (Ref. 2 to 4). Stress data from the Groningen field was analysed to assess the initial and later stress state in the reservoir rock (Ref. 2).</p> <p>In Part 1 of the current report (1D Geomechanical Model) geomechanical models are presented for a number of offset wells to provide an understanding and constraint of the current stress field. This study complements the study into the tectonic stresses in the Groningen field (Ref. 2) and the modelling study of single faults (Ref. 3).</p> <p>In Part 2 of the current report (3D Geomechanical Model) a geomechanical model is prepared for the for the entire field. This study is in that respect similar to the Geomechanical Analysis (Ref. 4).</p>			
Directly linked research	(1) Seismological Model			
Used data	Stress data from 13 wells in the Goningen field.			
Associated organisation	NAM			
Assurance				



A Baker RDS Project for **NAM**

**Dynamic Geomechanical Modelling to
Assess and Minimize the Risk for Fault Slip
during Reservoir Depletion of the
Groningen Field.**

1D Geomechanical Model – *Final Report*

Project Reference: NAM0001

Revision No. 1

21st January 2014

Document Approval & Distribution

For Baker RDS

Prepared by	Signature	Date
Yan Zheng – Senior Geomechanics Specialist		28/09/13
Romain Guises, Ph.D. – Senior Geomechanics Specialist		28/09/13

Reviewed by

David Wiprut, Ph.D. – Global Geomechanics Advisor.		01/10/13
--	--	----------

Approved for Issue

Jackeline Rodrigues – Geomechanics Team Leader, Europe-Africa.		16/10/13
--	--	----------

Report Distribution

Number of Copies	NAM Assen
1	Schepersmaat 2 P.O. Box 28000 9400 HH ASSEN The Netherlands

Objectives

On behalf of NAM Assen (NAM), GeoMechanics International (GMI), a division of Baker Hughes Reservoir Development Services, proposes to build a three dimensional (3-D) geomechanical model for the Groningen Field, onshore Netherlands for the purpose to conduct geomechanical simulations. The main goal of this study is to understand the stress state prior to production and the stress evolution during the depletion of the Groningen field. The stress evolution will be used to evaluate the risk of (seismic) slip on reservoir faults over the life of the field and propose production strategies and related scenarios so as to minimize any seismic risk.

The proposed geomechanical study will include the following tasks:

1. Building of 1-D geomechanical models from a number of offset wells to provide a preliminary understanding and constraint of the present day stress field. A range of offset wells data (thirteen wells) collected during the different stages of the field developments will be selected based on their relevance and log coverage.
2. Building a 3-D geomechanical model for the entire field. This 3D model is based on the available data including (but not limited to) the 3-D structural and reservoir models of the area (i.e., Petrel and ECLIPSE models), overburden, pore pressure, fracture gradient, depth profile, lithology data, historic geomechanical studies, LOT data, DST data, core testing results and drilling reports which will be supplied by the Client (as available).
3. Perform 3D finite element analyses for a number of pressure scenarios and calculate changes and variations of in situ stress, strains, and displacements over time (i.e., with changing pore pressure) and assess related impact on fault reactivation (i.e., derive shear and normal stress on selected fault planes and how these change with depletion) possibly leading to seismicity.
4. Utilize the results from (3) to suggest a number of field development scenarios in terms of pore pressure and depletion to assess how the risk of seismicity can be minimized. Report of the 3D study will be reported separately.

Executive Summary

The results of the 3D finite element analyses and the impact of stress variation on fault reactivation leading to possibly seismicity can be summarized as follows:

1D Geomechanical Model

A 1D geomechanical model has been developed using data from thirteen offset wells located inside the Groningen field. The resultant in-situ stresses from the geomechanical model indicate that a normal faulting environment is dominating the field in which the vertical stress (S_v) is larger than both horizontal stresses, that is, $S_v > S_{Hmax} > S_{Hmin}$.

The vertical stress has been derived by integration of the bulk density data and its magnitude varies between 2.20SG to 2.40SG at the top of the Slochteren formation due to variation in the thickness of the Zechstein salt.

The pore pressure is hydrostatic down to approximately 1200m TVDSS and the background pore pressure (shale pressure) in the overburden formations has been interpreted to be slightly overpressured to 1.12SG at the top the Rotliegend and from this point the reservoir pressure varies between 330 and 360 bars

The magnitude of the least principal stress (S_{Hmin}) has been determined through analysis of Leak of Test (LOT) values available and conducted at various depths on the offset wells. As results, the minimum horizontal stress magnitude at the top of the reservoir formation ranges between 1.54SG to 1.67SG.

For the determination of the magnitude and orientation of S_{Hmax} , image logs for wells KWR-1A and RDW-1 have been analysed in order to identify any stress induced wellbore failures. Several breakouts were identified in the Slochteren and Carboniferous formations. The S_{Hmax} azimuth has been interpreted to be ~ SSE160°NNW. The magnitude of the maximum horizontal stress (S_{Hmax}) was constrained by performing stress modelling with GMI•SFIB using the breakout widths in intervals where wellbore failure were observed. This permitted confirmation of a normal faulting stress regime in the field and at the top of the Slochteren formation, the maximum horizontal stress magnitude is ~ 1.73 – 1.82SG EMW (500-560 bars).

Based on empirical relations between wireline sonic logs and rock strength, UCS profiles for the reservoir and the overburden shales have been derived. Calibration has only been performed in the reservoir formation where rock mechanical tests were available. The UCS within the Slochteren varies between 15MPa and 26MPa and internal friction coefficient (μ_i) varying between 0.42 and 0.62 (23° and 32°). Log derived UCS and internal friction values reflect a similar distribution of mechanical rock properties as found from the lab tests.

Effective stress ratio (ESR) values of 0.4 and 0.55 were used to calculate S_{hmin} and S_{Hmax} magnitudes respectively. ESR is defined as the ratio of effective horizontal stress to effective vertical stress.

The 1D geomechanical generated, with all parameters described above, has been verified against the wellbore failures identified in the image logs and also against the drilling events such as losses, tight spots, stuck pipes, etc. reported on each of the thirteen offset wells. The verification process indicated good agreement between the predicted wellbore failures using the geomechanical model described and the failures measured by the image logs.

Contents

Document Approval & Distribution.....	ii
Objectives	iii
Executive Summary.....	v
Contents	vii
List of Tables	ix
List of Figures	x
1.0 Introduction	15
1.1. Work Flow Overview	15
1.2. Available Data	16
2.0 1-D Geomechanical Model	18
2.1. Overburden	19
2.2. Pore Pressure	22
2.3. Rock Properties.....	24
2.3.1. Laboratory Rock Tests Interpretation	26
Triaxial Tests.....	26
Uniaxial Compression Tests	28
2.3.2. Log-Based Mechanical Properties	29
Internal Friction and Poisson Ratio.....	32
Young's Modulus	33
2.4. Minimum Horizontal Stress (S_{hmin}) under virgin reservoir conditions.....	36
2.5. Maximum Horizontal Stress (S_{Hmax}) under virgin conditions	39
2.5.1. S_{Hmax} Orientation	40
KWR-1A.....	40
RDW-A.....	41
2.5.2. S_{Hmax} Magnitude.....	42
2.6. Verification of the Geomechanical Model	46
2.6.1. Drilling Experience	46
2.6.2. Model Calibration using GMI•WellCheck™	48
3.0 Model Uncertainties	51
3.1. 1D Geomechanical Model.....	51

4.0	Summary.....	52
5.0	Recommendations	53
6.0	References.....	54
7.0	Nomenclature.....	55
8.0	Appendices	57
	Appendix 1 Pore Pressure.....	58
	Appendix 2 UCS and Rock Properties	59
	Appendix 3 Stress Polygon and Constraining Horizontal Stress Magnitudes	64
	Appendix 4 Results from the CSTR module using GMI•SFIB™	66
	Appendix 5 Model Verification	68
	Appendix 6 Drilling Summaries of the Offset Wells	73
	Appendix 7 Available Data.....	80

List of Tables

Table 1. Summary of available data gathered, reviewed and analysed for the this study	17
Table 2. Description of Formation Names Abbreviation	20
Table 3. t Zand-12 triaxial strength test data (courtesy of NAM)	25
Table 4. Froombosch-8 triaxial strength test data (courtesy of NAM)	25
Table 5. Zuidlaarderveen-6 triaxial strength test data (courtesy of NAM)	26
Table 6. Summary of interpreted triaxial tests for FRB-8, ZND-12 and ZLV-6	28
Table 7. Uiterburen-10 Uniaxial strength data (provided by NAM through electronic communication, e-mail)	29
Table 8. UCS statistic summary for ROSLN and Carboniferous	32
Table 9. Internal Friction and Poisson Ratio values for Halite, ROCLT, ROSLN and DC using equation 9, 10 and 11	33
Table 10. EKL-12 and ZPD-12 laboratory Young's Modulus and Porosity (courtesy of NAM)	34
Table 11. Summary of LOT dataset (courtesy of NAM) – at virgin reservoir conditions	38
Table 12. List of the S_{Hmax} interval results of the GMI•SFIB™ analysis	66

List of Figures

Figure 1. Generic workflow for generating a consistent 3-D dynamic model.....	15
Figure 2. Location of the offset wells in the Groningen field, Netherland (courtesy of NAM)..	18
Figure 3. Composite density built up for the Well ZRP-1: for the very shallow section of the well (from surface to 350mTVDRT), an exponential trend line was used. For the rest of the well section, the density was directly used except for two short intervals at around 350-850mTVDRT and 2000-2200mTVDRT where the pseudo density log (Gardner's relationship) was selected, because the density was considered as being affected by wellbore enlargement.	21
Figure 4. Overburden (Sv) profiles for the thirteen offset wells. The overburden varies from 2.20 – 2.40 SG at 3200m TVDRT. Density was not available for SLO-3 (highlighted curve in black box) hence the overburden for this well has been estimated using the pseudo-density derived from Gardner correlation.....	22
Figure 5. Virgin Pressure data available for 5 offset wells in Groningen. For Groningen the formation water gradient is 1.166 bar/10m and the gas gradient is 0.18 bar/10m (courtesy of NAM "Groningen Fault Stability Assessment. P.A.J. van den Bogert, R.M.H.E. van Eijs, O. Van der Wal"). There is no evidence of different pressure compartments in the reservoir despite the amount of faults present in the field.	23
Figure 6. Pore pressure profiles in blue for Wells BRW-2, EKL-1 and HGZ-1. The vertical stress is plotted in dark red in addition to the MW in green used to drill the wells and the RFT data (red dots) to calibrate the reservoir PP.	23
Figure 7. Pore pressure profiles (blue) for Wells KWR-1A, OVS-1 and POS-1. The vertical stress is plotted in dark red in addition to the MW (green) used to drill the wells and the RFT data (red dots) to calibrate the reservoir PP.	24
Figure 8. Interpretation of triaxial tests collected in the t-Zandt-12 at two intervals: 2817.75m and 2819.53m.....	27
Figure 9. Interpretation of triaxial tests collected in the t-Zandt-12 for the combined interval between 2817.75m and 2819.53m.....	27
Figure 10. Log derived UCS calibration. Calibration of log derived UCS shown in blue plotted against lab UCS data in red dots. The UCS across ROSLN ranges from 15 – 26 MPa..	30
Figure 11. EKL-12 and ZPD-12 Young's Modulus and Porosity Cross-Plot. Exponential correlation for deriving Young's Modulus in the Slochteren Fm. from reservoir porosity extracted from MoRes. The correlation is valid for porosity ranging from 8 – 25 %.	35
Figure 12. Composite diagram of the rock mechanical properties for EKL-12. UCS in blue on the left track, poisson ration and internal friction in black and pink respectively on the	

middle track and the static and dynamic Young's Modulus in red triangles and purple respectively on the right track..... 36

Figure 13. Available LOTs values extracted from NAM database including the two LOT at original reservoir conditions from NAM internal report⁴. The brown line shows the S_{hmin} constrained to the lower limit of the data. The stress variation in Slochteren is between 400 – 550 psi at depth ranging between 2600 and 3000m TVD..... 37

Figure 14. Interpreted minimum horizontal stress based on effective stress ratio (ESR) method. The ESR is shown as K_{hmin} in blue on the left and on the right side the resultant S_{hmin} in dashed green can be seen along with the PP shown as reference, RFT, the LOT data and the vertical stress in dark red. All values are plotted as a function of depth. 39

Figure 15. Breakouts identified through the Slochteren and Carboniferous formations in KWR-1A. The pink squares represent the breakouts identified with their respective widths. ... 40

Figure 16. Statistics of breakout azimuth and breakout width in KWR-1A. All selected breakouts can be observed in one single track on the left (areas highlighted in pink). ... 41

Figure 17. Breakouts identified through the Slochteren and Carboniferous formations in RDW-1. The pink squares represent the breakouts identified with their respective widths. 41

Figure 18. Statistics of breakout azimuth and breakout width in RDW-1 42

Figure 19. Example of S_{Hmax} modelling performed on wellbore breakouts recorded in the well KWR-1A at 3468m MDRT. The S_{Hmax} has been constrained for UCS range between 15 – 20 MPa which are the P10 and P50 of the rock strength across Slochteren. The figure displays a stress polygon that is consistent with the presence of failure at 3402m TVDSS within the Slochteren Fm. in well KWR-1A. The red contour lines indicate the values of uniaxial compressive rock strength (UCS) in MPa. The green lines indicate the lower bound and upper bound values of S_{min} and S_{Hmax} . The red rectangle delineates the possible rock strength range at the vicinity of 3402m TVDSS. The green right brace indicates the S_{Hmax} range (1.67-1.85 SG) for the given S_{hmin} and rock strength ranges. Pressures and stresses are shown in units of SG. NF: normal faulting environment; SS: strike-slip faulting environment; RF: reverse faulting environment. ; μ_i : coefficient of internal friction (IntFric); μ_f : coefficient of sliding friction (SlidFric); ν : Poisson's ratio (PoisRat); α : Biot's elastic coefficient; wBO: breakout width; Diff. Mud Pressure: refers to the overbalanced used to drill the well (MW-Pp)..... 43

Figure 20. UCS Histogram for the Slochteren formation in KWR-1A. The Breakouts were identified across the shale which is weaker than the sand. P10 and P50 UCS values across the shale intervals have been for stress modelling. 44

Figure 21. Graphical summary of the GMI•SFIB™ module CSTR (Constrain Stress) for the most relevant breakouts identified in wells KWR-1A and RDW-1. The red horizontal lines represent the possible range of S_{Hmax} considering the uncertainties in the UCS for the

three depths where wellbore failures were analysed. The effective stress ratio selected to fit the breakouts and drilling experiences is 0.55 (vertical red line), thus this value has been used to obtain the local S_{Hmax} magnitude in the Groningen Field. Here is also displayed the estimated ESR for S_{Hmin} (green line) which is 0.40. 44

Figure 22. Summary of the principal stress magnitudes and the pore pressure as function of depth (example from well POS-1). S_v in dark red, S_{Hmin} in dashed green, S_{Hmax} in dashed red and pore pressure in blue. Here is also displayed the MW used to drill this well (bright green) and the formation pressure measurements. 46

Figure 23. Summary of the time depth drilling events related to geomechanical issues encountered while drilling the Well KWR-1A. The most relevant event was when the pipe got stuck and the well had to be sidetracked. 47

Figure 24. Calibration of the geomechanical model against drilling experience from the well KWR-1A. The two tracks on the left show the geomechanical model (principal stresses and rock properties) as a function of depth. The two next tracks represent the well trajectory and the caliper response for this well. The right hand side track displays the breakout width predicted by the geomechanical model for each depth. As can be observed from the two tracks on the right, good verification is found between the predicted failure (red intervals) and those measured with the single caliper. 49

Figure 25. Comparison of predicted breakouts and the measured ones from images in well KWR-1A across the Slochteren Fm. As can be seen on the right hand side of the figure, an excellent verification is found between the breakout widths predicted in red and the breakout widths measured from the image logs. These results provide confidence and verify well the geomechanical model used in the prediction. 49

Figure 26. Calibration of the geomechanical model against drilling experience from the well RDW-1. Good verification between the predicted failure (red intervals) and the tight spots reported in across the reservoir section. 50

Figure 27. Comparison of predicted breakouts and the measured ones from images in well RDW-1A. As can be seen on the right track, the amount of breakouts predicted is higher than that measured. However, the widths of the breakouts are similar to those measured and the failures verify well with the tight spot events reported between 3150m – 3180m even though no breakouts were seen in the image logs. 50

Figure 28. Pore pressure profiles for Wells RDW-1, SLO-3 and UHM-1 58

Figure 29. . Pore pressure profiles for Wells ZND-1, ZPD-1, ZRP-1 and ZWD-1 58

Figure 30. Interpretation of triaxial tests collected in the FRB-8 at 2757.03m and 2761.05m. 59

Figure 31. Interpretation of triaxial tests collected in the FRB-8 at combined intervals between 2757.03m and 2761.05m 59

Figure 32. Interpretation of triaxial tests collected in the ZLV-6 at 3796.1m and 3796.9m..... 60

Figure 33. Interpretation of triaxial tests collected in the ZLV-6 at combined intervals between 3796.1m and 3796.9m.	60
Figure 34. Composite rock mechanical properties for BRW-2 and HGZ-1.	61
Figure 35. Composite rock mechanical properties for KWR-1A and OVS-1.	61
Figure 36. Composite rock mechanical properties for POS-1 and RDW-1.	62
Figure 37. Composite rock mechanical properties for SLO-3 and UHM-1A.	62
Figure 38. Composite rock mechanical properties for ZND-1 and ZPD-1.	63
Figure 39. Composite rock mechanical properties for ZRP-1 and ZWD-1.	63
Figure 40. This figure shows the combining information about the Earth with observations of wellbore failure (right plot) to constrain stress magnitude. Example not from this study.	65
Figure 41. Example of S_{Hmax} modelling performed on wellbore breakouts recorded in the well RDW-1 at 3276m MDRT.	66
Figure 42. Example of S_{Hmax} modelling performed on wellbore breakouts recorded in the well RDW-1 at 3381m MDRT.	67
Figure 43. Calibration of the geomechanical model against drilling experience from the well BRW-2.	68
Figure 44. Calibration of the geomechanical model against drilling experience from the well EKL-1.	68
Figure 45. Calibration of the geomechanical model against drilling experience from the well HGZ-1.	69
Figure 46. Calibration of the geomechanical model against drilling experience from the well OVS-1.	69
Figure 47. Calibration of the geomechanical model against drilling experience from the well POS-1.	70
Figure 48. Calibration of the geomechanical model against drilling experience from the well UHM-1A.	70
Figure 49. Calibration of the geomechanical model against drilling experience from the well ZPD-1.	71
Figure 50. Calibration of the geomechanical model against drilling experience from the well ZRP-1.	71
Figure 51. Calibration of the geomechanical model against drilling experience from the well ZRP-1.	72
Figure 52. Calibration of the geomechanical model against drilling experience from the well ZND-1.	72

Figure 53. Drilling summary for the well RDW-1	73
Figure 54. Drilling summary for the well POS-1	74
Figure 55. Drilling summary for the well ZRP-1	74
Figure 56. Drilling summary for the well BRW-2	75
Figure 57. Drilling summary for the well HGZ-1	75
Figure 58. Drilling summary for the well OVS-1	76
Figure 59. Drilling summary for the well SLO-3.....	76
Figure 60. Drilling summary for the well UHM-1A	77
Figure 61. Drilling summary for the well ZND-1	77
Figure 62. Drilling summary for the well ZPD-1.....	78
Figure 63. Drilling summary for the well ZWD-1.....	78
Figure 64. Drilling summary for the well EKL-1	79
Figure 65. Available data for well POS-1	80
Figure 66. Available data for well ZRP-1	80
Figure 67. Available data for well BRW-2.....	81
Figure 68. Available data for well EKL-1	81
Figure 69. Available data for well HGZ-1	82
Figure 70. Available data for well OVS-1	82
Figure 71. Available data for well SLO-3.....	83
Figure 72. Available data for well UHM-1A	83
Figure 73. Available data for well ZND-1.....	84
Figure 74. Available data for well ZPD-1	84
Figure 75. Available data for well ZWD-1	85

1.0 Introduction

1.1. Work Flow Overview

The workflow for this project can be divided into four (4) main tasks (see Figure 1):

1. Building a calibrated 1-D geomechanical model from thirteen offset wells to provide a preliminary understanding and constraint of the present day stress field.
2. Building a calibrated 3-D geomechanical model for the entire Groningen field (with particular detail in the area of seismicity); this 3-D model is based on the available data including (but not limited to) the 3-D structural and reservoir models of the area (i.e., Petrel and ECLIPSE models), lithology data, historic geomechanical studies, LOT data, drill stem data (DST), core testing results and drilling reports, all of which have been supplied by NAM and when available.
3. Perform 3-D finite element analyses and calculate changes and variations of in-situ stress, strains, and displacements over time (i.e. with changing pore pressure) and assess related impact on fault reactivation (i.e. derive shear and normal stress on selected fault planes and how these change with depletion) possibly leading to seismicity.
4. Using the results from (3) to suggest a number of field development scenarios in terms of pore pressure and depletion to assess how the risk of seismicity can be minimized.

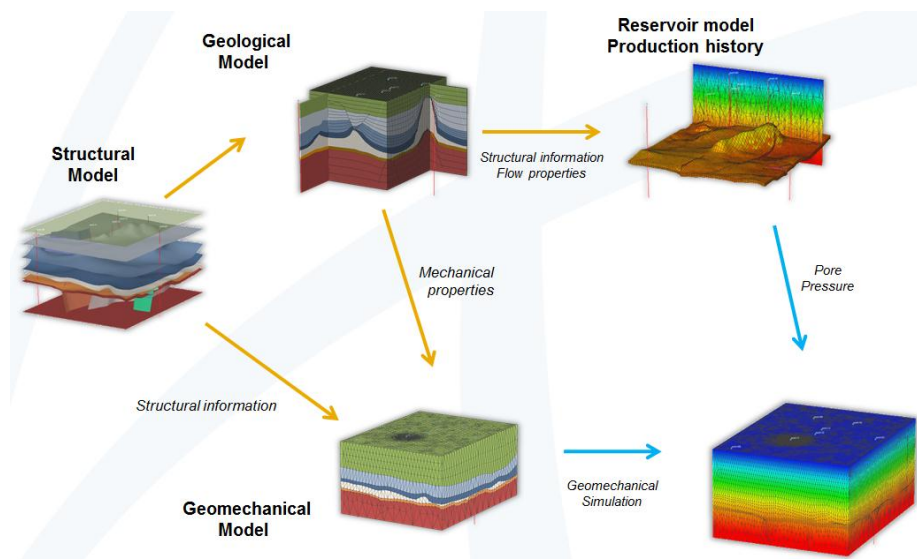


Figure 1. Generic workflow for generating a consistent 3-D dynamic model

1.2. Available Data

The accuracy of every 3-D geomechanical model lies in the availability and detailed generation of 1-D geomechanical models constructed from best quality available offset well data. Wells typically hold a multitude of partly high-resolution data sets including wire-line logs, well tests and in many cases rock strength measurements obtained from core plugs, which are then combined with the drilling experience for calibration, to build 1D geomechanical models.

The main components of a 1-D geomechanical model are the three in situ principal stresses which are typically the vertical stress (S_v), the maximum horizontal stress (S_{Hmax}) and the minimum horizontal stress (S_{Hmin}) along with their orientations. Furthermore, the pore pressure and the rock mechanical properties (such as compressive strength, internal friction, Poisson's ratio and Young's modulus) are also part of the geomechanical model. Single point data such as these are used to calibrate the continuous log-derived rock properties along the entire well trajectory as a function of depth (both MD and TVD). The essential applications of the 1-D geomechanical model are wellbore stability analyses to determine fracture gradients or the planning of mud programs to avoid wellbore collapse or, as in this case, to provide the geomechanical framework for a 3-D model.

The available data for this project are summarized as below:

- Thirteen offset wells (Table 1) selected in agreement with NAM with full sets of processed and interpreted logs (electric, acoustic and wireline logs).
- Image log data from two wells, KWR-1A and RDW-1, located outside the Groningen area but next to the limits of the field. The analyses of the wellbore failures identified from the images provided the orientation of the stresses in the area.
- Additionally, formation pressure measurements, LOT data and rock mechanical properties such as UCS, TWC, Young's Modulus and Poisson's ratio were also provided and used to constrain the geomechanical model.
- Various documents such as daily drilling reports (DDR), final well reports (FWR) and previous analytical reports were collected and reviewed.
- Interpreted horizons and polylines defining the geometry of the faults used as input for the structural modelling.

Table 1. Summary of available data gathered, reviewed and analysed for the this study

Well name	Log Data/ TD	Image Files	LOTS/ Minifrac	Daily Drilling Reports/ Final Well Report	Formation Tops	Pore Pressure (MDT/RFT)	Mud Weights	Rock Tests
BRW-2	Wireline logs, TD: 3270m MDRT	N/A	N/A	Available	Available	Available	Available	N/A
EKL-1	Wireline logs, TD: 2885m MDRT	N/A	N/A	Available	Available	N/A	Available	N/A
HGZ-1	Wireline logs reservoir. TD: 3791m MDRT	N/A	Available	Available	Available	Available	Available	N/A
KWR-1A	Wireline logs, TD: 3490m MDRT	Available	Available	Available	Available	Available	Available	N/A
OVS-1	Wireline logs, TD: 3013m MDRT	N/A	N/A	Available	Available	Available	Available	N/A
POS-1	Wireline logs, TD: 3004m MDRT	N/A	N/A	Available	Available	Available	Available	N/A
RWD-1	Wireline logs, TD: 3400m MDRT	Available	Available	Available	Available	Available	Available	N/A
SLO-3	Wireline logs (no density), TD: 2873m MDRT	N/A	N/A	Available	Available	N/A	Available	N/A
UHM-1A	Wireline logs (RHOB res), TD: 3183m MDRT	N/A	N/A	Available	Available	N/A	Available	N/A
ZND-1	Wireline logs, TD: 3017m MDRT	N/A	N/A	Available	Available	Available	Available	N/A
ZPD-1	Wireline logs, TD: 3065m MDRT	N/A	N/A	Available	Available	Available	Available	N/A
ZRP-1	Wireline logs, TD: 3112m MDRT	N/A	N/A	Available	Available	Available	Available	N/A
ZWD-1	Wireline logs, TD: 3277m MDRT	N/A	N/A	Available	Available	Available	Available	N/A

2.0 1-D Geomechanical Model

The input data for the three dimensional geomechanical model of the Groningen field is based on the individual 1-D geomechanical models from the following thirteen offset wells:

- Borgsweer (BRW-2), Eemskanaal (EKL-1)
- Hoogezand (HGZ-1), Kielwindeweer (KWR-1A)
- Overschild (OVS-1), Ten Post (POS-1)
- Rodewolt (RDW-1), Slochteren (SLO-3)
- Uithuizermeeden (UHM-1A), T Zand (ZND-1)
- Zuiderpolder (ZPD-1), Zeerijp (ZRP-1)
- Zuidwending (ZWD-1)

Figure 2 shows the locations of the wells within the field.

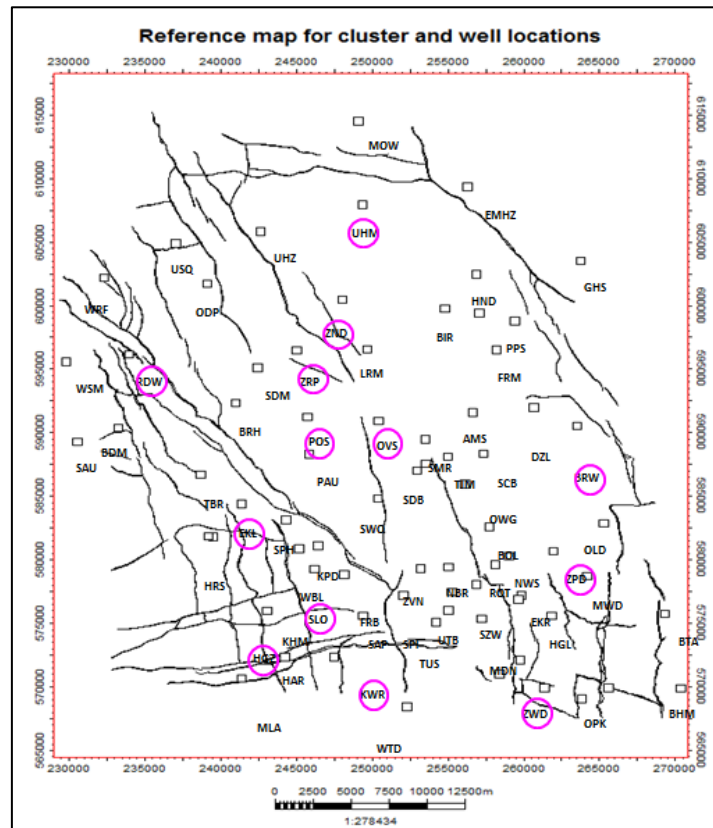


Figure 2. Location of the offset wells in the Groningen field, Netherland (courtesy of NAM)

A geomechanical model is composed of the magnitudes and the orientation of the three principal stresses (S_{Hmax} , S_{hmin} and S_v), the pore pressure, and rock properties such as the uniaxial compressive strength (UCS), internal friction coefficient (μ_i), Poisson's ratio (ν) and Young's Modulus (E).

2.1. Overburden

Gravitational loading at any point in the earth is caused by the weight of the rock column overlaying that point. The overburden stress (S_v) at depth, z , is calculated by integrating the weight above the point (z) using the following equation:

$$S_v = \int_0^z (\rho(z) * g) dz \quad (1)$$

Where,

S_v : vertical / overburden stress

$\rho(z)$: formation bulk density

g : gravitational acceleration

z : depth (true vertical depth)

In the study area, the magnitude of the total overburden gradient was obtained by integrating the available density logs with depth along the well paths of the thirteen key wells shown in Table 1. Since the formation bulk density log is not available to the surface, an exponential curve was used to fit the measured data and to calculate the formation density using the Gardner formula¹. In some sections, where the density data is unreasonably low or high (due to poor quality density log from an enlarged hole), the density log is interpolated by a best-fit line or by using pseudo density from the acoustic log using the Gardner's relationship.

Figure 3 shows the overburden compositor curve (blue) built from an exponential trend line, the pseudo density from the Gardner relationship and the bulk density for the offset well ZRP-1A.

All formation names are abbreviation of formation and member names extracted from the composite logs. Table 2 shows a description of the formation names abbreviation:

Table 2. Description of Formation Names Abbreviation

Group	Member	Names Abbreviation
U North Sea	NU	NU
M North Sea	NMRF	NM
L North Sea	NLFFB	NL
	NLFFS	
	NLFFY	
	NLFFT	
	NLFFC	
Chalk	CKGR	CK
	CKTXP	
	CKTXM	
Rijnland	KNGL	KN
	KNNC	
	KNNSF	
Upper Triassic	RNMUU	RN
	RNMUA	
	RNMUE	
	RNMUL	
	RNROU	
	RNRO2	
	RNROM	
	RNRO1	
	RNSOC	
	RNSOB	
Lower Triassic	RBMVC	RB
	RBMVL	
	RBSHR	
	RBSHM	
	RBSHL	
Zeichstein	ZEZ2A	ZE
	ZEZ2C	
	ZEZ1W	
	ZEZ1C	
	ZEZ1K	
Rotliegend (Ten Boer)	ROCLT	ROCTL
Rotliegend (Slochteren)	ROSL	ROSLN
Carboniferous	DC	DC

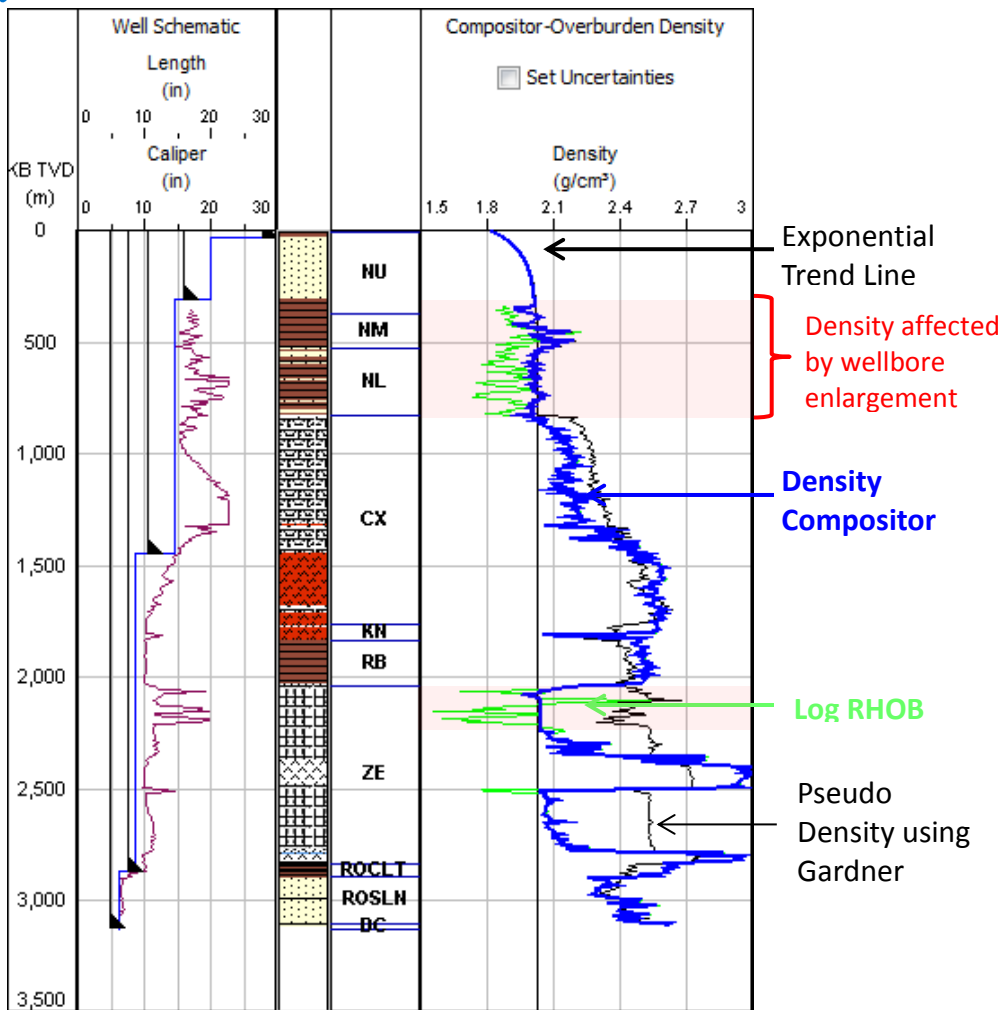


Figure 3. Composite density built up for the Well ZRP-1: for the very shallow section of the well (from surface to 350mTVDRT), an exponential trend line was used. For the rest of the well section, the density was directly used except for two short intervals at around 350-850mTVDRT and 2000-2200mTVDRT where the pseudo density log (Gardner's relationship) was selected, because the density was considered as being affected by wellbore enlargement.

Figure 4 shows a compilation of the overburden gradient curves (in equivalent mud weights) for the thirteen offset wells. The resulting overburden gradients present similar behaviour and therefore provide a good representation of the overburden for the entire field.

The vertical gradient varies between 2.20 and 2.40 SG at 3200m TVDRT due to variation in the thickness of the Zechstein salt layer and variation in the density data around the Loppersum area indicating lower overburden gradient at the centre of the Groningen field. From Figure 4 it can be seen that S_v is larger than 2.15 SG for depths deeper than 2000m TVD.

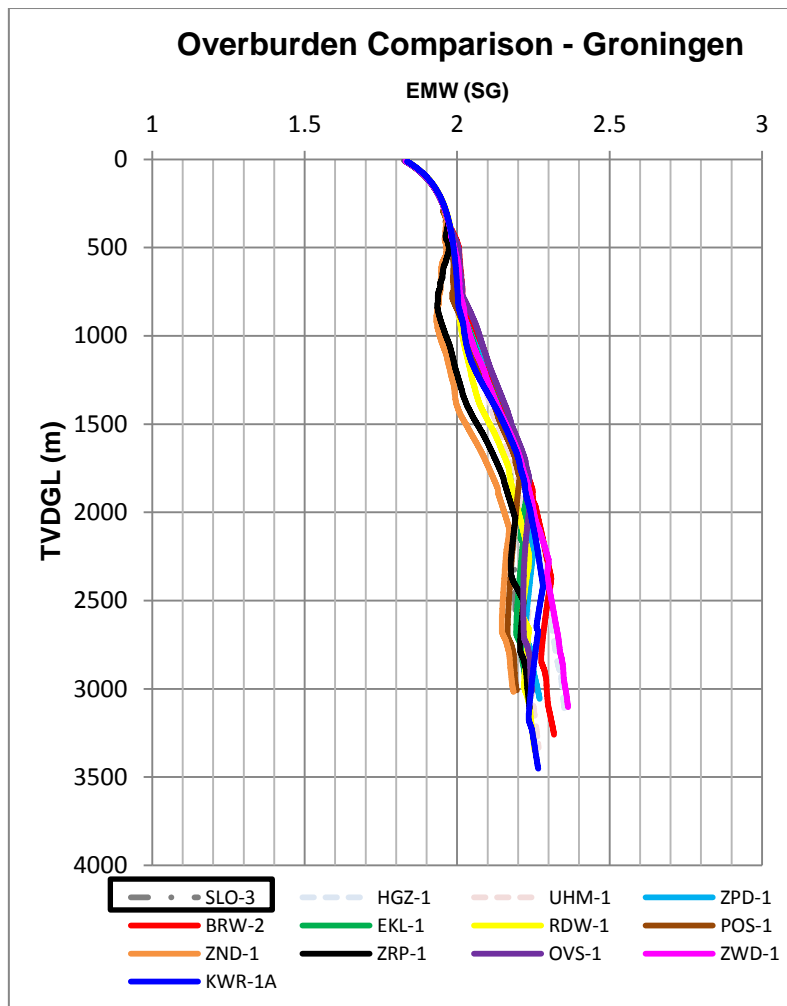


Figure 4. Overburden (Sv) profiles for the thirteen offset wells. The overburden varies from 2.20 – 2.40 SG at 3200m TVDRT. Density was not available for SLO-3 (highlighted curve in black box) hence the overburden for this well has been estimated using the pseudo-density derived from Gardner correlation.

2.2. Pore Pressure

Pore pressure plays a fundamental role in geomechanics (i.e., when managing wellbore stability during drilling and production or when drilling through depleted formations such as the Slochteren). Direct measurements of formation pressure were available in the reservoir formations for most of the wells used in the present study. In the overburden sections, mud weights and drilling experience have been used to estimate the pore pressure. We inferred a hydrostatic pore pressure regime down to approximately 1200m TVDSS, which is in line with the mud weight used to drill the shallow hole sections and the reported drilling events. The shale pore pressure (P_p) in the overlying formations has been interpreted to be slightly overpressured to 1.12 SG at the top of the Rotliegend following information provided by NAM during our bi-weekly progress meeting. This information indicates that the water gradient in the Slochteren formations is higher than the fresh water gradient and based on formation

pressure measurements the virgin reservoir pore pressure ranges between 330 and 360 bar. Figure 5 illustrates the pressure data available for Groningen at virgin conditions.

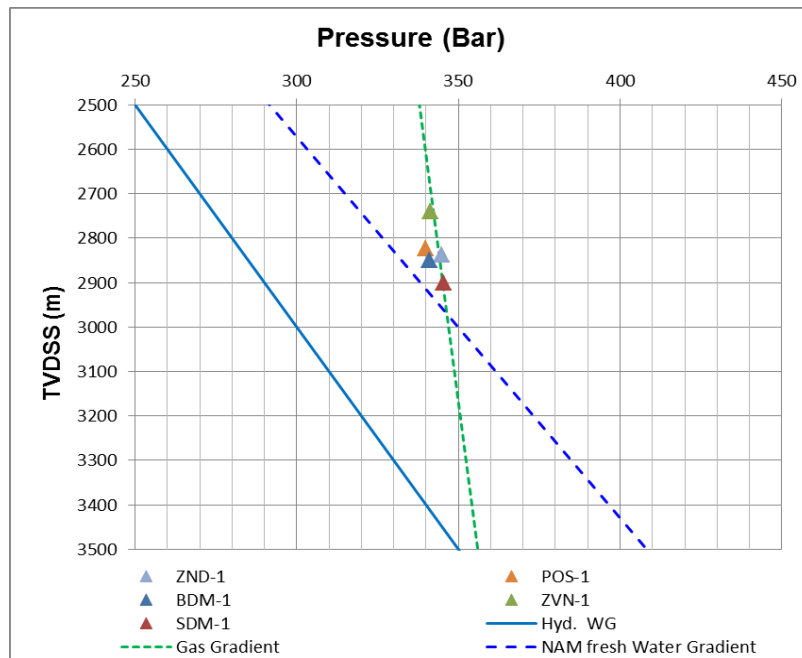


Figure 5. Virgin Pressure data available for 5 offset wells in Groningen. For Groningen the formation water gradient is 1.166 bar/10m and the gas gradient is 0.18 bar/10m (courtesy of NAM “Groningen Fault Stability Assessment. P.A.J. van den Bogert, R.M.H.E. van Eijs, O. Van der Wal”). There is no evidence of different pressure compartments in the reservoir despite the amount of faults present in the field.

Figure 6 and Figure 7 show the interpreted pore pressure and the overburden profiles derived for six of the selected offset wells. For additional wells see **Appendix 1 Pore Pressure**.

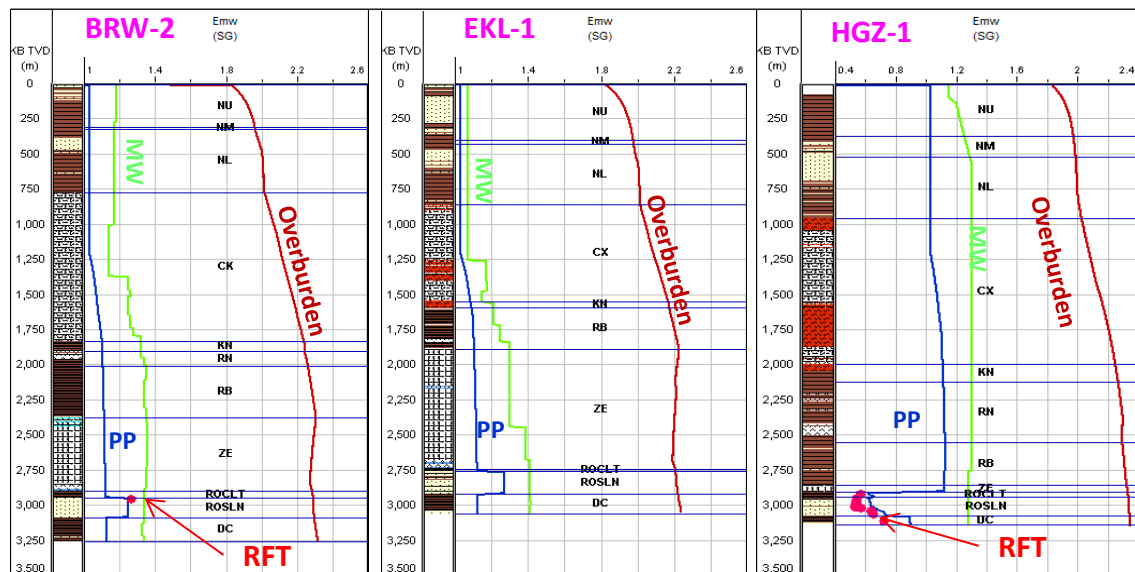


Figure 6. Pore pressure profiles in blue for Wells BRW-2, EKL-1 and HGZ-1. The vertical stress is plotted in dark red in addition to the MW in green used to drill the wells and the RFT data (red dots) to calibrate the reservoir PP.

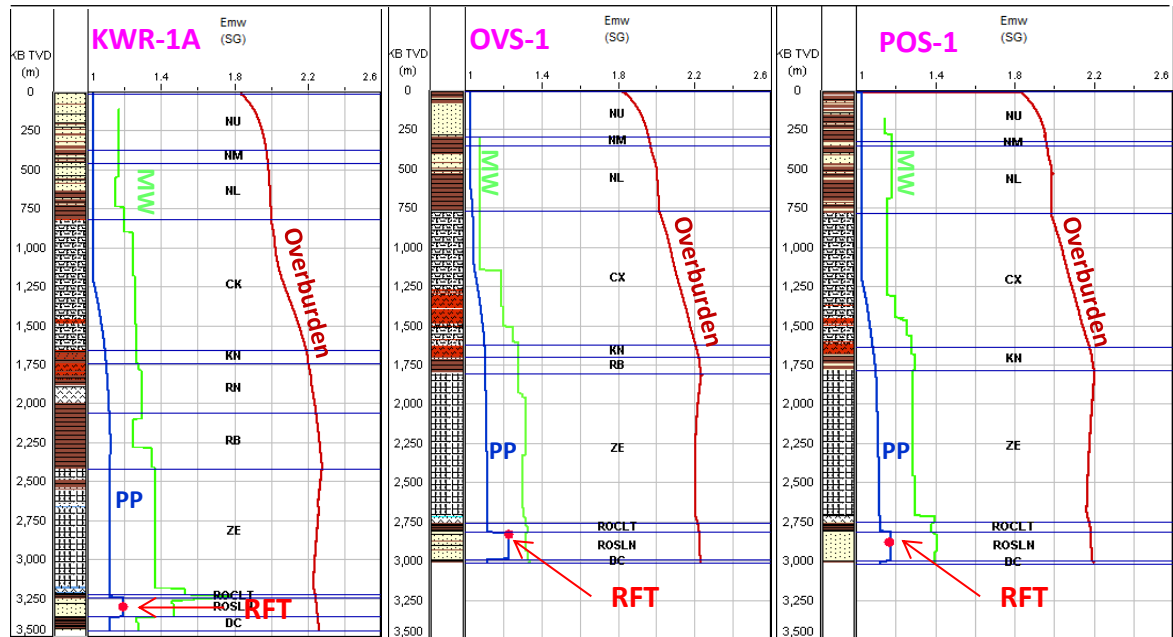


Figure 7. Pore pressure profiles (blue) for Wells KWR-1A, OVS-1 and POS-1. The vertical stress is plotted in dark red in addition to the MW (green) used to drill the wells and the RFT data (red dots) to calibrate the reservoir PP.

The interpreted pore pressure profiles shown in blue in Figure 6 and Figure 7 indicate virgin pressures ranging between 1.18SG to 1.25SG at the top of the reservoir and there are wells such as HGZ-1 and ZWD-1 that have been depleted down to 0.6SG and 1.03SG respectively as per formation pressure measurements.

2.3. Rock Properties

The mechanical response of rocks to changes in stresses is controlled, amongst other factors, by its mechanical properties. Understanding rock mechanical properties such as compressive strength, friction coefficient, Young's modulus, Poisson's ratio, etc. is an integral part of the geomechanical model. Therefore, an adequate laboratory testing program on core retrieved from the reservoir (or formation of interest) is valuable in providing accurate constraints for the required parameters.

For this study, two reports summarising rock mechanics testing, conducted by NAM, on core samples from wells Froombosch-8, t-Zandt-12 and Zuidlaarderveen-6, were available². The tests included uniaxial, single-stage triaxial compression tests and thick wall cylinder tests. All the laboratory rock tests were performed on samples of sandstone selected from cored sections from the Rotliegend reservoir formations. The results of these uniaxial and triaxial tests were then used to calibrate the log-based rock properties. Table 3, Table 4 and Table 5 refer to the triaxial strength data for the wells t-Zandt-12, Froombosch-8 and Zuidlaarderveen extracted from NAM's internal report².

Table 3. t Zand-12 triaxial strength test data (courtesy of NAM)

Table E2: Triaxial strength test data: 't Zand-12 st

Depth (m)	Sample no.	σ_r (bar)	Yield		Failure		E (kbar)	ν (-)
			$\sigma_a + \sigma_r$ (bar)	$\sigma_a - \sigma_r$ (bar)	$\sigma_a + \sigma_r$ (bar)	$\sigma_a - \sigma_r$ (bar)		
2816.47	-	0	-	-	30	30	4.2	-
2816.63	8	76	457	307	553	403	44	-
2818.18	1	26	222	170	247	195	10	-
2818.65	2	5	91	81	111	101	18	-
2818.85	3	50	322	222	407	307	44	-
2819.10	4	75	359	209	457	307	49	-
2819.33	5	101	503	301	595	393	40	-
2819.40	9	250	868	368	1052	552	51	0.10
2819.50	6	125	542	292	675	425	43	-
2820.33	7	150	581	281	724	424	33	-

Note: - Interval characterised by TWC strength of 255 bar and BHN of 5 kg/mm² [22].

Table 4. Froombosch-8 triaxial strength test data (courtesy of NAM)

Table E1: Triaxial strength test data: Froombosch-8

Depth (m)	Sample no.	BHN (kg/mm ²)	Yield-old			Yield-new		Failure		E (kbar)
			σ_r (bar)	$\sigma_a + \sigma_r$ (bar)	$\sigma_a - \sigma_r$ (bar)	$\sigma_a + \sigma_r$ (bar)	$\sigma_a - \sigma_r$ (bar)	$\sigma_a + \sigma_r$ (bar)	$\sigma_a - \sigma_r$ (bar)	
2756.84	18	1-5	450	1405	505	1250	350	1506	606	73
2756.89	19	1-2	350	1180	480	1050	350	1250	550	49
2757.06	21	2-5	150	730	430	650	350	795	495	48
2757.10	22	4-5	50	397	297	370	270	422	322	36
2757.14	23	5	450	1420	520	1300	400	1570	670	71
2757.17	24	4-5	0	66	66	66	66	76	76	18
2757.35	26*	4-7	400	-	-	540	260	455	345	-
2760.95	3	2	400	1480	680	1300	500	1801	1001	128
2761.01	4	2	200	875	475	800	400	1007	607	83
2761.06	5	0-2	100	485	285	450	250	512	312	36
2761.11	6	0-1	0	-	-	-	-	14	14	-
2761.16	7**	0-1	300	1085	485	1040	440	1111	511	35

* Triaxial extension from $\sigma_r = \sigma_a = 400$ bar.
 ** Sample collapse during hydrostatic loading.

Table 5. Zuidlaarderveen-6 triaxial strength test data (courtesy of NAM)

Table E3: Triaxial strength test data: Zuidlaarderveen-6									
Depth (m)	Sample no.	ϕ (%)	σ_r (bar)	Yield		Failure		E (kbar)	ν (-)
				$\sigma_a + \sigma_r$ (bar)	$\sigma_a - \sigma_r$ (bar)	$\sigma_a + \sigma_r$ (bar)	$\sigma_a - \sigma_r$ (bar)		
3795.96	2*	15.7	890					97	0.15
3795.99	3	15.7	251	1187	685	1335	833	69	0.15
3796.02	4	15.7	0	97	97	108	108	37	0.33
3796.09	6	15.7	5	165	155	194	184	53	0.18
3796.23	8	19.1	151	703	401	861	559	50	0.06
3796.26	9**	19.1	25	217	167	292	242	39/70	0.05/0.15
3796.38	10	19.1	351	1231	529	1516	814	54	0.05
3796.88	12	21.0	50	358	258	446	346	25	0.08
3796.94	14**	21.0	201	860	458	1007	605	65/141	0.05/0.14
3796.98	15	21.0	4	73	65	92	84	9	-
3797.03	17	21.5	99	554	356	620	422	34	0.08
3797.22	18	21.5	0	43	43	57	57	19	0.20

* Hydrostatic test up to 890 bar; E = slope * (1-2 ν).
 ** Second value of E and ν stems from unloading/reloading cycle.

Note: - Interval characterised by TWC strength between 320 and 480 bar and BHN around 8 kg/mm², see Appendix B.

Strength data at both yield and failure conditions were recorded for all three tested wells, (Table 3, Table 4, Table 5), and those taken at failure highlighted in red squares have been the ones used to interpret the unconfined compressive strength (UCS), the cohesion and the rock internal friction coefficients.

2.3.1. Laboratory Rock Tests Interpretation

Triaxial Tests

Rock properties from triaxial and multistage compression tests can be obtained by conducting a series of axial compression tests on cylindrical samples under different confining pressures in a way that each sample is loaded axially until complete failure occurs while maintaining a lateral confinement by a fluid. Triaxial tests use individual plugs and reach the failure limit for each confining pressure whereas multistage tests do not reach the failure stage, permitting the use of a single plug for all the confining pressures. The results of these tests can be plotted in terms of two dimensional mean stress space (Mohr-Coulomb diagram); normal stress σ_n or $(\sigma_1 + \sigma_3)/2$ and shear stress τ or $(\sigma_1 - \sigma_3)/2$. The value of unconfined compressive strength (UCS), internal friction coefficient (μ_i) and cohesion (S) are the three most widely used failure parameters to fully characterize the strength properties of rocks. These parameters can be approximately obtained by drawing a tangent to Mohr's circles plotted in normal and shear space (black line in Figure 8Error! Reference source not found.). The

slope and intercept of this line are termed as internal friction coefficient (μ_i) and cohesion (S), respectively. The Mohr Coulomb failure envelope is described by:

$$\tau = S + \tan(\phi) \sigma_n \tag{2}$$

Figure 8 and Figure 9 show the interpreted Mohr-Coulomb circles (τ - σ_n plane) in the Slochteren formation. for the well t-Zandt-12 covering two intervals plotted separately (2818.75m and 2819.53m) and together (2817.75-2819.53m). Table 6 summarises the interpreted triaxial test results for all three wells ZND-12 (Groningen), FRB-8 (Groningen) and ZLV-6 (Annerveen) (refers to **Appendix 2 UCS and Rock Properties** for more interpreted Mohr Circles results). The analysed triaxial tests show that the UCS within the Slochteren varies between 15MPa and 26 MPa with internal friction coefficient (μ_i) varying between 0.42 and 0.62 (23° and 32°). These results of UCS and μ_i have been used to constrain the magnitude of the maximum horizontal stress (S_{Hmax}) at a later stage.

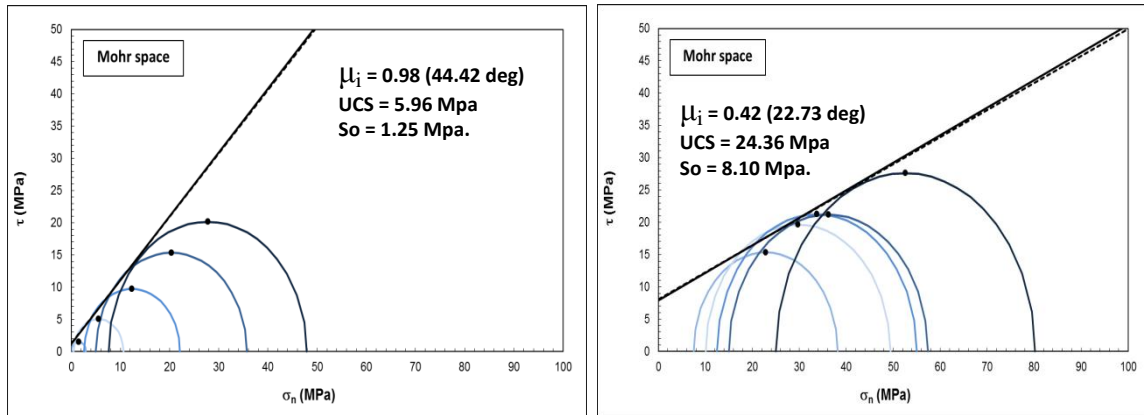


Figure 8. Interpretation of triaxial tests collected in the t-Zandt-12 at two intervals: 2817.75m and 2819.53m.

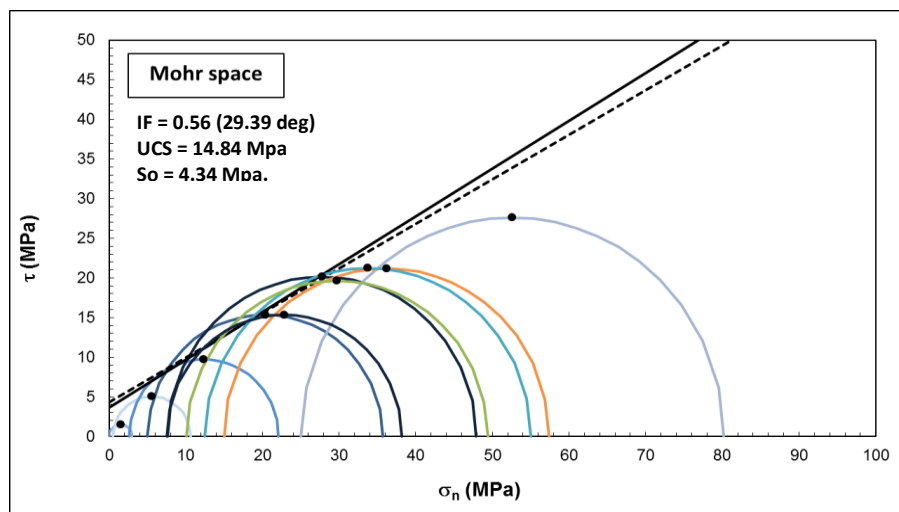


Figure 9. Interpretation of triaxial tests collected in the t-Zandt-12 for the combined interval between 2817.75m and 2819.53m.

Table 6. Summary of interpreted triaxial tests for FRB-8, ZND-12 and ZLV-6

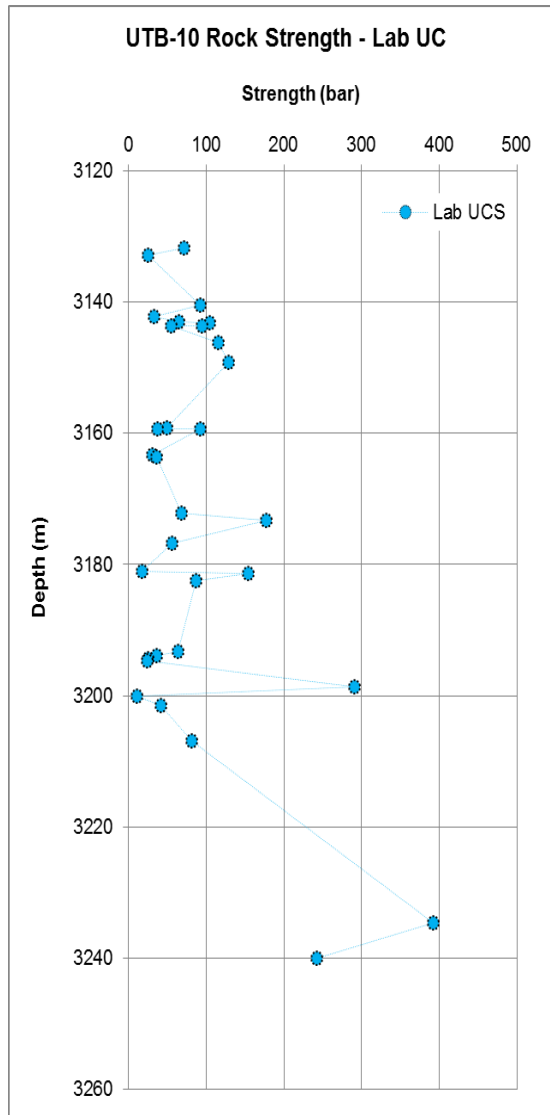
Well	Depth MD (m)	UCS (Mpa)	Internal Friction (deg)	Cohesion (MPa)	Comments	Tested depth
FRB-8	2756.84 - 2757.35	21.4	19.33	7.59	Interval 1	Reservoir
	2760.95 - 2761.16	5.44	31.38	1.53	Interval 2	Reservoir
	2756.81 - 2761.16	16.95	23.73	5.53	Complete Interval	Reservoir
ZND-12	2816.47 - 2818.85	5.96	44.42	1.25	Interval 1	Reservoir
	2819.10 - 2820.33	24.36	22.73	8.1	Interval 2	Reservoir
	2816.47 - 2820.33	14.84	29.39	4.34	Complete Interval	Reservoir
ZDV-6	3795.96 - 3796.26	14.94	35.24	3.87	Interval 1	Reservoir
	3796.38 - 3797.22	14.41	30.61	4.11	Interval 2	Reservoir
	3795.96 - 3797.22	15.3	32.05	4.24	Complete Interval	Reservoir

Uniaxial Compression Tests

Unconfined compressive strength (UCS) is determined by axially loading a plug sample at constant rate until failure occurs with no applied confining pressure. When instrumented with strain gauges, uniaxial tests allow the determination of Young's modulus and Poisson's ratio during the elastic part of the test; the peak strength value is the UCS. In this case, UCS data were also provided for the well Uiterburen-10 (provided by NAM through electronic communication, e-mail) and Table 7 illustrates this data recorded for 31 depths; the average rock strength across the sand was estimated to be around 9 – 10 MPa. These uniaxial data combined with the triaxial ones form the basis for the development of the Groningen strength model.

Table 7. Uiterburen-10 Uniaxial strength data (provided by NAM through electronic communication, e-mail).

UTB-10	
Original Core Depth (AHDD)	UCS
<i>m</i>	<i>bar</i>
3131.80	71
3132.86	25
3140.47	92
3142.25	33
3142.99	65
3143.24	104
3143.56	94
3143.56	55
3146.25	116
3149.20	129
3159.11	49
3159.37	37
3159.37	92
3163.21	30
3163.53	36
3172.14	68
3173.29	177
3176.82	56
3181.08	17
3181.36	154
3182.49	87
3193.17	64
3193.94	36
3194.37	25
3194.62	24
3198.60	291
3200.04	11
3201.54	42
3206.94	81
3234.52	392
3239.97	242



2.3.2. Log-Based Mechanical Properties

The most common method for the continuous estimation of static log-based mechanical properties of a formation is the application of published empirical relationships between static (laboratory measurements) and dynamic (derived from wireline logs) properties. Wireline log data from the thirteen offset wells have been used to determine the unconfined rock strength (UCS) using distinct empirical relations developed for each lithology. Shale, Dolomite/Limestone, Halite/Anhydrite and sandstone were identified using the gamma ray log response, since shale formations experience high gamma ray counts compared to those of sandstone or limestone formations.

In the current study and for the reservoir sandstones laboratory determined UCS data were available but very limited and these have been used to calibrate the log derived UCS

correlations through the Slochteren formation. Figure 10 illustrates the lab UCS values from well ZND-12 (Table 6) plotted on top of the log derived UCS for well ZND-1. The figure indicates the two uniaxial tests from ZND-12 (red squares) and that the average rock strength for the Slochteren formation is around 15 – 26 MPa in the Loppersum area as indicated by the triaxial tests (Figure 9) and therefore the log derived UCS in blue has been calibrated to fall within this range of rock strength. Illustration of the lab UCS data from FRB-8, UTB-10 and ZLV-6 against their log derived UCS curves have not been provided as these wells are outside Groningen and hence have not been included in this study; however, as can be seen from Table 6 and Table 7 the range of UCS values tested from these wells falls within the range of UCS values tested in well ZND-12.

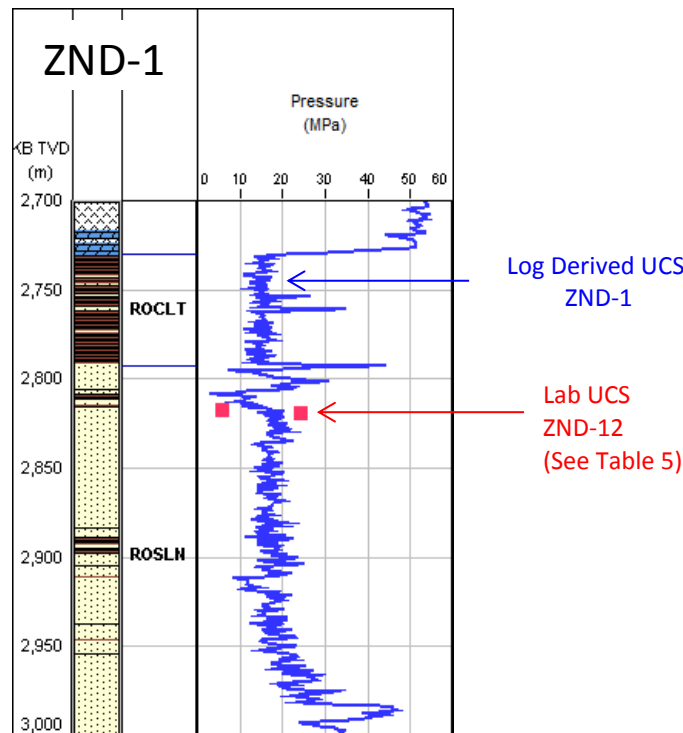


Figure 10. Log derived UCS calibration. Calibration of log derived UCS shown in blue plotted against lab UCS data in red dots. The UCS across ROSLN ranges from 15 – 26 MPa.

Finally, for those formations where no laboratory rock tests exist, the strength model has been calibrated against reported drilling experiences such as tight spots, reaming, back reaming, pack off, stuck pipe etc. Below are the log derived relationships used for determining the rock properties in all formations. The correlations used were selected according to the lithology of the formations and the best derived strength profiles or magnitudes to replicate the wellbore failure (breakouts) and drilling experiences reported.

1. Shale (NU/NM/NL) calculated using modified Horsroutd relation (2001)³.

$$UCS = [0.25 - 1.2](2.12e^9 DTCO^{-2.93}) \quad (3)$$

Where: UCS (psi) Unconfined Compressive Strength
 DTCO (μs/ft) Slowness of compressional wave

2. Sandstone (NU/NM/NL) calculated using modified Horsrud relation (2001).

$$UCS = [0.8 - 1.2](2.12e^9 DTCO^{-2.93}) \quad (4)$$

Where: UCS (psi) Unconfined Compressive Strength
 DTCO (μs/ft) Slowness of compressional wave

3. Shale (CK/KN/RN/RB) calculated using modified Horsrud relation (2001).

$$UCS = [0.3 - 0.37](2.12e^9 DTCO^{-2.93}) \quad (5)$$

Where: UCS (psi) Unconfined Compressive Strength
 DTCO (μs/ft) Slowness of compressional wave.

4. Shale (ROCLT/DC) calculated using modified Horsrud (2001).

$$UCS = [0.37 - 0.4](2.12e^9 DTCO^{-2.93}) \quad (5)$$

Where: UCS (psi) Unconfined Compressive Strength
 DTCO (μs/ft) Slowness of compressional wave.

5. Sandstone (ROSLN) calculated using modified McNally relation (2001)⁴.

$$\left(UCS = [0.3 - 0.4](185165 \exp(-0.037 DTCO)) \right) \quad (7)$$

Where: UCS (psi) Unconfined Compressive Strength
 DTCO (μs/ft) Slowness of compressional wave.

6. Limestone/Marl/Dolomite/Halite/Salt/Anhydrite and Chalk calculated using Militzer (1973)⁵.

$$\left(UCS = [0.8] \left(\frac{7682}{DTCO} \right)^{1.82} \right) \quad (8)$$

Where: UCS (psi) Unconfined Compressive Strength
 DTCO (μs/ft) Slowness of compressional wave.

As can be noted, unlike resistivity and density logs, acoustic logs have been used for derivation of UCS as they appear to be less influenced by hole enlargements. Table 8 illustrates the statistic summary of the UCS for both the ROSLN and the Carboniferous.

Table 8. UCS statistic summary for ROSLN and Carboniferous

Well	UCS ROSLN - Sand				UCS Carboniferous - Shale			
	Pmin	P10	P50	P90	Pmin	P10	P50	P90
BRW-2	15.89	20.68	25.12	29.13	11.16	12.78	19.87	23.53
EKL-1	8.89	14.58	19.57	28.45	No coverage			
HGZ-1	13.35	17.62	23.04	27.47	11.18	18.42	23.82	27.91
KWR-1A	18.89	24.64	31.1	37.57	3.94	14.28	20.85	25.28
OVS-1	8.9	14.78	19.25	30.06	12.7	14.96	15.97	18.45
POS-1	9.47	12.5	16.63	30.82	14.33	14.85	16.5	17.17
RDW-1	11.2	17.11	22.17	29.16	13.99	16.35	18.85	21.8
SLO-3	9.13	11.24	17.08	30.33	6.44	12.24	16.43	18.99
UHM-1A	12.02	17.84	23.6	31.69	No coverage			
ZND-1	2.63	14.23	18.85	30.26	No coverage			
ZPD-1	10.46	19.16	24.28	29.47	4.89	10.76	18.07	21.91
ZRP-1	12.65	16.86	24.89	32.65	16.69	17.97	19.86	21.28
ZWD-1	18.94	24.47	30.42	38.05	9.7	14.13	21.63	25.62

Internal Friction and Poisson Ratio

The Lal V_p^6 equation has been used to derive the internal friction coefficients for all lithologies except for shales, halite and shallow sandstones where constant values have been used (see Table 9). For the reservoir sandstones the internal friction values used are ranging within those values of internal friction estimated from the triaxial test data and shown in Table 6.

$$\mu_i = \tan \left(\text{asin} \left((V_p - 1) / (V_p + 1) \right) \right) \tag{9}$$

Where: μ_i Internal Friction Coefficient
 V_p (km/sec) Compressive Velocity

A theoretical based on an isotropic, homogeneous, linearly elastic medium correlation have been used for the determination of the Dynamic Poisson Ratio for all lithologies except for the reservoir formation where a values of 0.18 has been used throughout the field (this values has been established in agreement with NAM).

$$v = (V_p^2 - 2V_s^2) / (2(V_p^2 - V_s^2)) \tag{10}$$

$$V_s = 0.862V_p - 1.172 \tag{11}$$

Where: V_s (km/sec) Shear Velocity
 V_p (km/sec) Compressional Velocity

Table 9. Internal Friction and Poisson Ratio values for Halite, ROCLT, ROSLN and DC using equation 9, 10 and 11.

Well	Internal Friction			Poisson Ratio			
	Halite	ROSLN	ROCLT/DC	Halite	ROCLT	ROSLN	DC
BRW-2	0.82	0.56	0.56	0.25	0.26	0.18	0.23
EKL-1	0.82	0.5	0.5	0.25	0.27	0.18	N/A
HGZ-1	0.82	0.45	0.5	0.25	0.22	0.18	0.21
KWR-1A	0.82	0.45	0.5	0.25	0.21	0.18	0.23
OVS-1	0.82	0.63	0.56	0.25	0.28	0.18	0.26
POS-1	0.82	0.53	0.56	0.25	0.27	0.18	0.26
RDW-1	0.82	0.53	0.56	0.25	0.24	0.18	0.23
SLO-3	0.82	0.53	0.5	0.25	0.29	0.18	0.26
UHM-1A	0.82	0.53	0.55	0.25	0.25	0.18	N/A
ZND-1	0.82	0.6	0.5	0.25	0.27	0.18	N/A
ZPD-1	0.82	0.53	0.55	0.25	0.27	0.18	0.25
ZRP-1	0.82	0.55	0.55	0.25	0.26	0.18	0.26
ZWD-1	0.82	0.53	0.6	0.25	0.24	0.18	0.23

Young's Modulus

The Young's Modulus is an important parameter for the 3-D dynamic modelling. This has been estimated using the following equation for all lithologies except for the Slochteren reservoir.

$$E_{dyn} = \frac{\rho v_s^2 (3v_p^2 - v_s^2)}{(v_p^2 - v_s^2)} \quad (11)$$

Where: V_s (km/sec) Shear Velocity
 V_p (km/sec) Compressional Velocity
 ρ (g/cm³) Bulk density

Across the reservoir formation, the Young's modulus has been estimated using the relationship derived from laboratory tests of young's modulus and porosity carried out in the wells Eemskanaal-12 and Zuiderpolder-12. The power relationship shown in Figure 11 has been used to derive the Young's modulus magnitude from the Groningen porosity exported from MoRes. Table 10 shows the laboratory results of Young's Modulus and Porosity used to generate the cross-plot, this data have been extracted from NAM internal report "Groningen Fault Stability Assessment".

Table 10. EKL-12 and ZPD-12 laboratory Young's Modulus and Porosity (courtesy of NAM⁷)

Well	TVD (m)	E (Mpa)	Porosity (%)
EKL-12	2740	14704	0.4
	2744.7	12728	6.8
	2751.8	4441	18.7
	2760	6388	19.5
	2761.5	4652	18.9
	2770.4	2660	25.8
	2798.9	5457	20.9
	2800.3	4238	21.1
	2812.8	16039	16.3
	2813.7	6785	19.8
	2715.3	10472	18
	2815.9	10202	18.5
	2815.9	9529	19
	2835.4	26581	7.8
	2840.6	16378	15.2
	2850.4	20616	12.9
	2859	12635	12.2
	2868.4	19253	8.4
	2872.6	25823	7.4
	2876.6	34813	7.4
2900.9	24171	11.2	
ZPD-12	2756	6856	19.6
	2756	6737	19.7
	2837.4	19642	12.1
	2837.4	15977	12.7

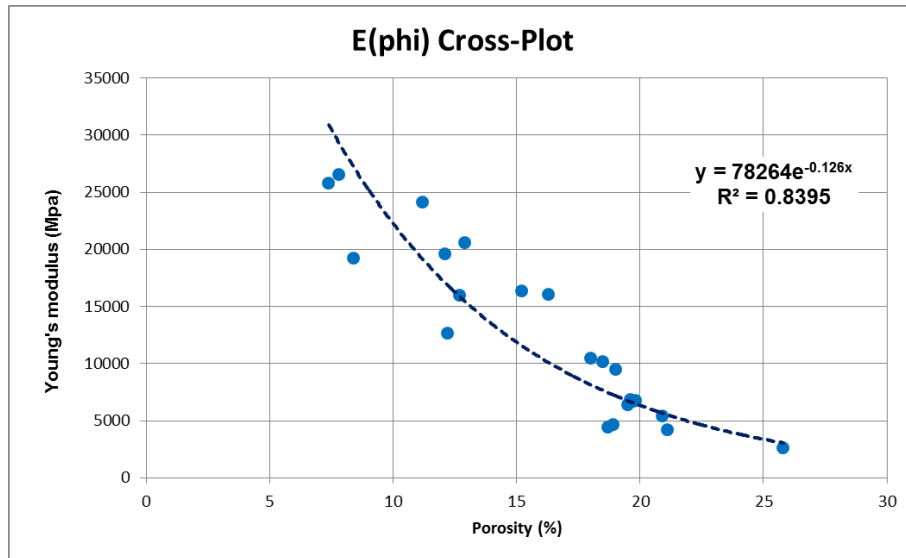


Figure 11. EKL-12 and ZPD-12 Young's Modulus and Porosity Cross-Plot. Exponential correlation for deriving Young's Modulus in the Slochteren Fm. from reservoir porosity extracted from MoRes. The correlation is valid for porosity ranging from 8 – 25 %.

Figure 12 shows the composite diagram of the rock mechanical properties and the calibration of the static Young's Modulus and Poisson Ratio with the laboratory test results for the well EKL-12. The UCS is shown in blue on the left track, Poisson's Ratio and Internal Friction in black and pink on the centre track and the static/dynamic Young's Modulus in red triangles/purple respectively on the right track.

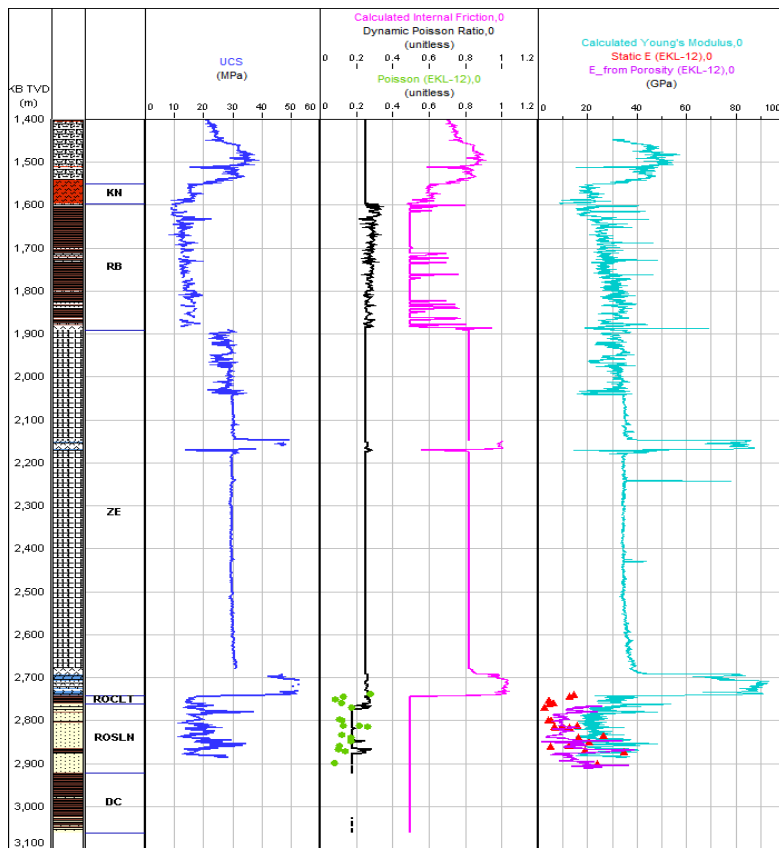


Figure 12. Composite diagram of the rock mechanical properties for EKL-12. UCS in blue on the left track, poisson ration and internal friction in black and pink respectively on the middle track and the static and dynamic Young’s Modulus in red triangles and purple respectively on the right track.

More composite diagrams of rock mechanical properties can be found in **Appendix 2 UCS and Rock Properties**.

2.4. Minimum Horizontal Stress (S_{hmin}) under virgin reservoir conditions

There are several ways of estimating the magnitude of the least principal horizontal stress or minimum horizontal total stress (S_{hmin}): log-based methods, direct measurements (such as leak-off tests, extended leak-off tests, minifrac, wireline, frac jobs, etc.). When properly conducted, leak-off tests and minifrac tests measure the fluid pressure required to create and propagate hydraulically induced fractures, as well as the pressure under which these newly created fractures close (fracture closure pressure = FCP). The FCP is interpreted after monitoring the pressure diffusion as a function of time during the well shut-in period, which is typically 20 minutes. The FCP counteracts the stress in the rock perpendicular to the fracture plane; therefore, this pressure can be considered equal or a lower bound of the magnitude of S_{hmin} . The instantaneous shut-in pressure (ISIP) is by definition the pressure in hydraulic fracturing immediately after shut-in. This pressure may vary from several psi to several

hundreds of psi above the closure pressure depending on the treatment and the rock. The ISIP is generally greater than the closure stress and can be considered an upper bound of S_{hmin} magnitude. Additionally, formation breakdown and fracture initiation may be strongly influenced by the stress concentration around the well, particularly in deviated wells.

The minimum horizontal stress profile is then first defined by utilising any known measurement data that are available; specifically LOT type data. For this study we use LOT (leak-off test), FIT (formation integrity test) and MiniFrac data. LOTs and MiniFrac tests give usually a good indication of the fracture gradient (S_{hmin}), whereas FITs do not as they are not taken to leak-off pressure. FIT can only be used as a guide.

Several leak-off tests (LOT) and formation integrity tests (FIT) were conducted around the Groningen field. However, no pressure-volume plots were available for interpretation of the fracture closure pressure. Additionally, three minifrac tests at depleted conditions were also conducted in the Ten Boer shale within the following offset wells ZND-12B, BRW-5 and ZLV-6 but they did not provide any information of the FCP at virgin conditions. In this sense, the recorded good quality (rank A & B) LOT data provided by NAM have been used to constrain the minimum horizontal stress by using the low range of values available from the selected LOT dataset (see Figure 13). This dataset includes two additional LOTs extracted from NAM's⁸ internal report "Groningen Fault Stability Assessment, section 2.2.2 Horizontal stress". The data plotted in Figure 13 can also be seen in Table 11.

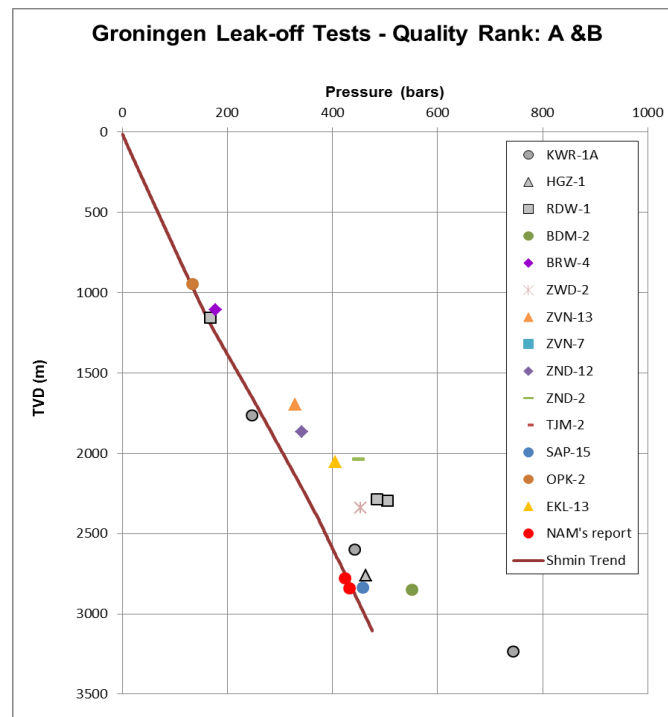


Figure 13. Available LOTs values extracted from NAM database including the two LOT at original reservoir conditions from NAM internal report⁴. The brown line shows the S_{hmin} constrained to the lower limit of the data. The stress variation in Slochteren is between 400 – 550 psi at depth ranging between 2600 and 3000m TVD.

As observed, Figure 13 illustrates the LOT values used to constrain the magnitude of S_{hmin} in the Groningen field; the data indicate stress variation across the Slochteren formation ranging between 400 psi to 550 psi at depth ranging between 2600 and 3000 m TVD. In this sense and for this study, the magnitude of S_{hmin} has been constrained to the lower limit of this cloud of data shown by the brown line which also fits though the two LOT pressure points (red dots) extracted from NAM's internal report.

Table 11. Summary of LOT dataset (courtesy of NAM) – at virgin reservoir conditions

Field	Well	TVD (m)	LOT (bar/10m)	LOT (bar)	Formation
Outside Groningen	KWR-1A	1763	1.4	246.8	RN
		2600	1.7	442.0	ZE
		3234	2.3	743.8	ROCLT
	HGZ-1	2760	1.68	463.7	RB
	RDW-1	1156	1.45	167.6	CK
		2294	2.2	504.7	ZE
2285.0		2.12	484.2	Zechstein Salt (inf) Fm.	
Groningen	BDM-2	2848.5	1.94	551.5	Ten Boer Mb
	BRW-4	1109.0	1.60	177.1	Chalk Gp.
	EKL-13	2056.0	1.97	405.7	Z4 Salt Mb.
	OPK-2	947.3	1.41	133.9	North Sea Spgp
	SAP-15	720.0	1.47	105.8	Lower North Sea Gp
		2838.0	1.62	458.6	Ten Boer Mb
	TJM-2	5004.8	1.82	913.3	Carboniferous Spgp
	ZND-2	2037.0	2.21	449.7	Main Claystone Mb
	ZND-12	1865.0	1.83	342.1	Main Claystone Mb
	ZND-8	1491	1.700	253.5	
	ZVN-7	274.4	1.70	46.6	North Sea Spgp
	ZVN-13	1698.0	1.94	328.9	Z3 Salt Mb
	ZWD-2	2340.0	1.94	453.5	RN/RB
ZWD-1	2018.0	1.67	337.0	RN	
NAM's Report		2778.0		424.0	
		2840.0		433.0	

The discrete data shown in Figure 13 only define a limited number of S_{hmin} points for a particular number of wells conducted normally at each casing shoe. A continuous trend line of S_{hmin} magnitude is defined throughout the entire well using the effective stress ratio (ESR) method:

- The least principal stress generally depends on the pore pressure value. In order to calculate the stresses for different pore pressure conditions and to generate a stress profile as a function of depth, we used the effective stress ratio (ESR or K), which is

defined as the ratio of effective horizontal stress to effective vertical stress. In this case, for the minimum horizontal stress K_{hmin} is defined as:

$$K_{min} = (S_{hmin} - P_p) / (S_v - P_p) \quad (8)$$

The assumption made is that the K_{hmin} value does not change as a function of depth over the interval considered in this study.

The pore pressure was evaluated before each test was conducted, allowing the determination of the effective stress ratio. The minimum horizontal stress magnitude shows a reasonable consistency with the calibration points using K_{hmin} values of 0.40. For this effective stress ratio, the S_{hmin} curve passes on the lower range of LOT dataset from NAM. Figure 14 shows the ESR defining S_{hmin} (K_{min}) as a function of depth on the left track and the pore pressure profile in blue, the least principal stress (S_{hmin}) in dashed green and the overburden in dark red on the right track for the well POS-1. In summary, the minimum horizontal gradient in the field varies between 1.54 SG and 1.67 SG (420-520 bars) at the top of the reservoir.

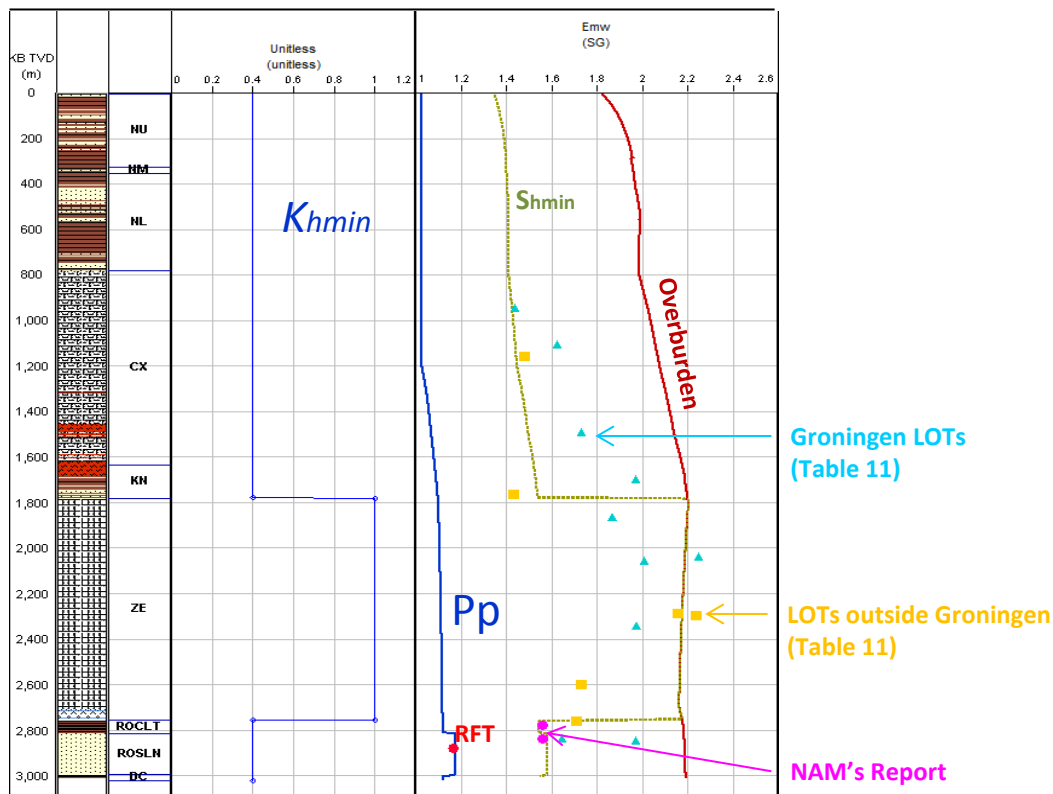


Figure 14. Interpreted minimum horizontal stress based on effective stress ratio (ESR) method. The ESR is shown as K_{hmin} in blue on the left and on the right side the resultant S_{hmin} in dashed green can be seen along with the PP shown as reference, RFT, the LOT data and the vertical stress in dark red. All values are plotted as a function of depth.

2.5. Maximum Horizontal Stress (S_{Hmax}) under virgin conditions

The last remaining components required to fully define the geomechanical model are the magnitude of S_{Hmax} and its orientation. They are determined by analysis of stress-induced

wellbore failures such as Breakouts (BO) and Drilling Induced Tensile Fractures (DITF) from image logs.

Wellbore images from two wells, KWR-1A and RDW-1, have allowed identification of wellbore breakouts occurred along the Slochteren sandstones and the Carboniferous Shale (Figure 15 & Figure 17). Finally, these wellbore failures (average breakout width and azimuth) and the derived rock mechanical properties (UCS and IF) have been used to constrain the magnitude of S_{Hmax} using GMI•SFIB™ module CSTR (Constrain Stress).

2.5.1. S_{Hmax} Orientation

The analysed image logs from both KWR-1A and RDW-1 indicate that the orientation of S_{Hmax} is very similar throughout Groningen following an average azimuth between $156^\circ - 160^\circ \pm 10deg$.

KWR-1A

From averaging the azimuths of the identified breakouts in the image data (pink square in Figure 15), the global S_{Hmax} Azimuth around the KWR-1/1A has been estimated to be around SSE156°NNW $\pm 6.75deg$. In addition, the breakout widths have also been averaged to be around $51.4^\circ \pm 23.04deg$ as seen in Figure 16.

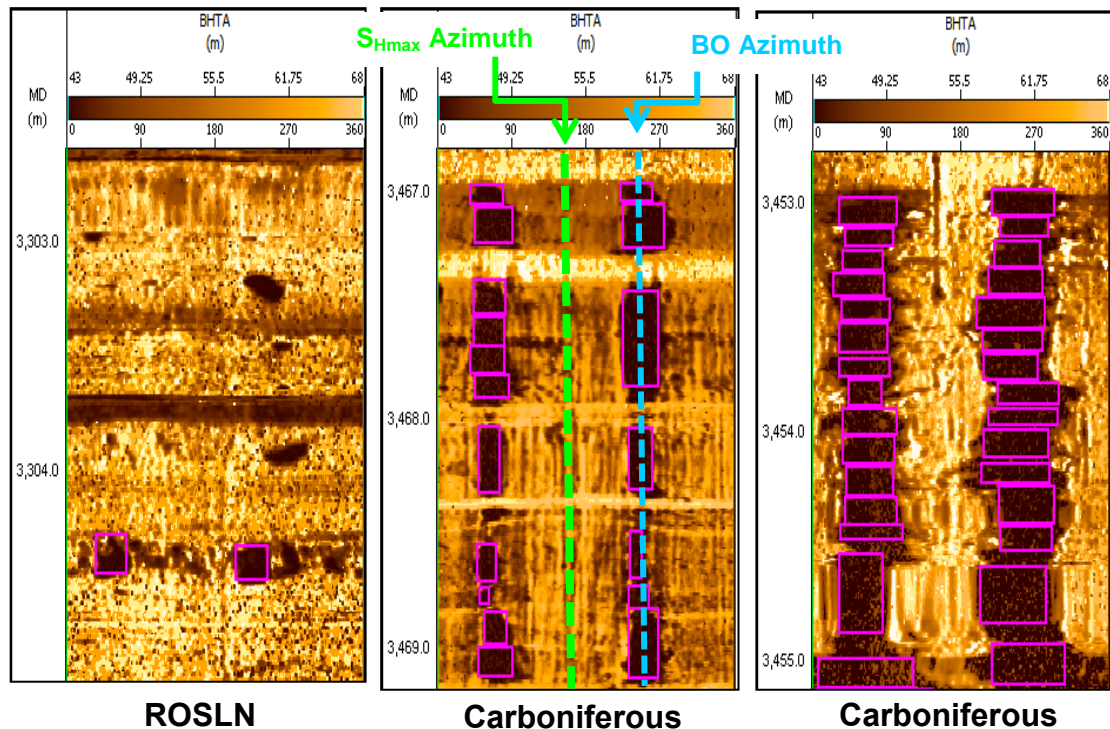


Figure 15. Breakouts identified through the Slochteren and Carboniferous formations in KWR-1A. The pink squares represent the breakouts identified with their respective widths.

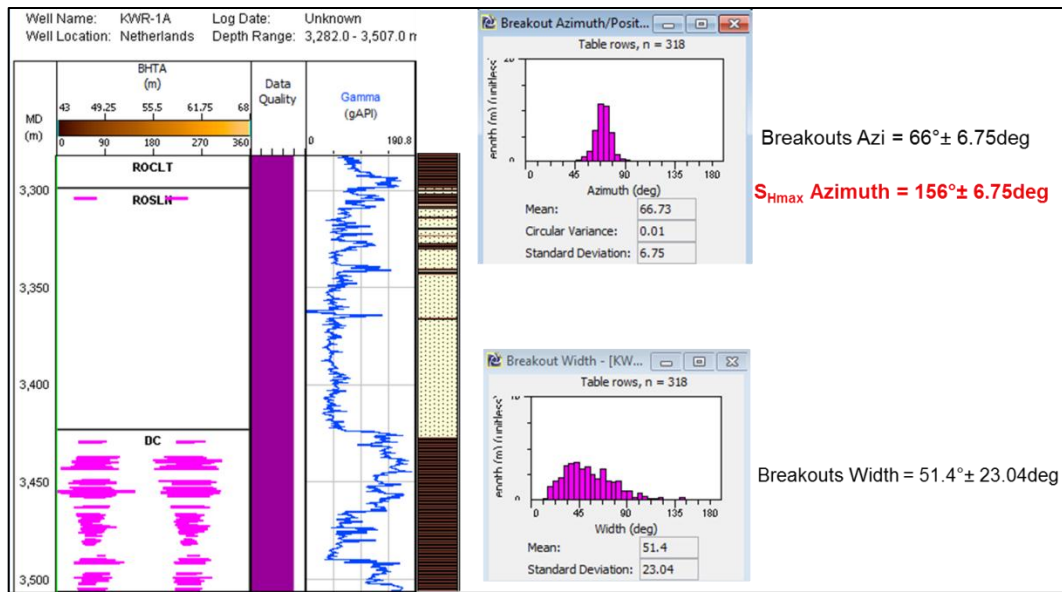


Figure 16. Statistics of breakout azimuth and breakout width in KWR-1A. All selected breakouts can be observed in one single track on the left (areas highlighted in pink).

RDW-A

Analysis has also been carried out on the image logs from RDW-1. Figure 17 illustrates the breakouts identified in both the Slochteren and Carboniferous formations. The average azimuth of the breakouts indicates a global S_{Hmax} azimuth of around $160^\circ \pm 10\text{deg}$ with breakout width average of $47.5^\circ \pm 12\text{deg}$ (Figure 18).

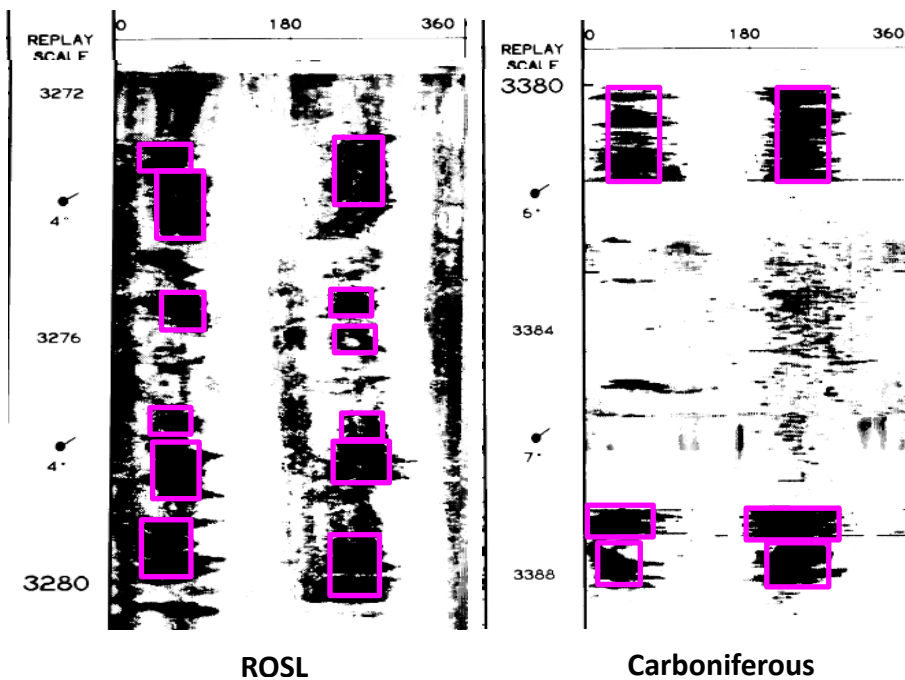


Figure 17. Breakouts identified through the Slochteren and Carboniferous formations in RDW-1. The pink squares represent the breakouts identified with their respective widths.

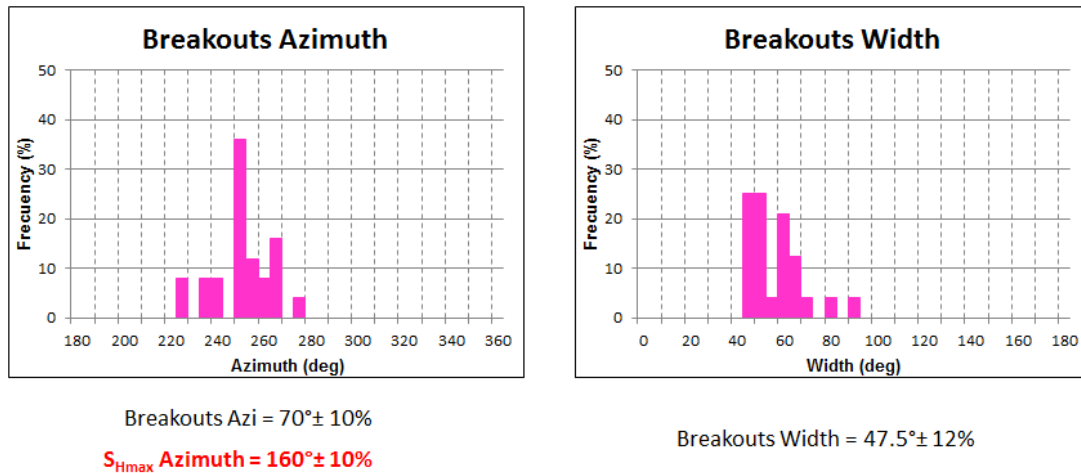


Figure 18. Statistics of breakout azimuth and breakout width in RDW-1

2.5.2. S_{Hmax} Magnitude

The process of constraining the magnitude of S_{Hmax} is carried out using GMI•SFIB™ module CSTR (Constrain Stress) along with the results from the preceding sections. This graphical methodology is well established and has been described in a number of publications (e.g. Zoback, 2007^{9 10 11}) and is also further explained in **Appendix 3 Stress Polygon and Constraining Horizontal Stress Magnitudes**. The three depths chosen to constrain the magnitude of the maximum horizontal stress are located where unambiguous wellbore breakouts (width and orientation) have been identified in the wells KWR-1A and RDW-1. At these depths (3276m, 3381m and 3468 m MD), derived values of vertical stress (S_v) and horizontal stresses (S_{Hmin}, S_{Hmax}) are inputs in the plot. The following Figure 19 illustrates an example of S_{Hmax} constrained in KWR-1A at 3468m MDRT/3402.15m TVSS in the Carboniferous formation.

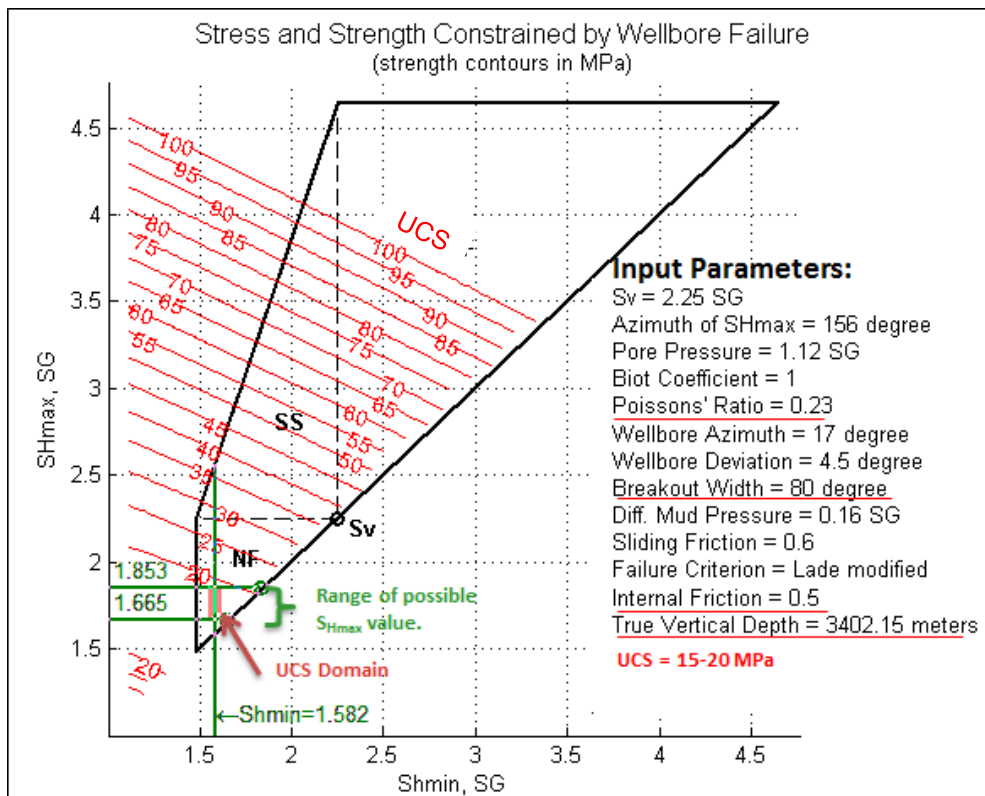


Figure 19. Example of S_{Hmax} modelling performed on wellbore breakouts recorded in the well KWR-1A at 3468m MDRT. The S_{Hmax} has been constrained for UCS range between 15 – 20 MPa which are the P10 and P50 of the rock strength across Slochteren. The figure displays a stress polygon that is consistent with the presence of failure at 3402m TVDSS within the Slochteren Fm. in well KWR-1A. The red contour lines indicate the values of uniaxial compressive rock strength (UCS) in MPa. The green lines indicate the lower bound and upper bound values of S_{min} and S_{Hmax} . The red rectangle delineates the possible rock strength range at the vicinity of 3402m TVDSS. The green right brace indicates the S_{Hmax} range (1.67-1.85 SG) for the given S_{min} and rock strength ranges. Pressures and stresses are shown in units of SG. NF: normal faulting environment; SS: strike-slip faulting environment; RF: reverse faulting environment. ; μ_i : coefficient of internal friction (IntFric); μ_f : coefficient of sliding friction (SlidFric); ν : Poisson's ratio (PoisRat); α : Biot's elastic coefficient; wBO: breakout width; Diff. Mud Pressure: refers to the overbalanced used to drill the well (MW-Pp).

The stress polygon modelled in Figure 19 indicates that the magnitude of the maximum horizontal stress should be constrained between 1.66SG EMW and 1.85SG EMW in order to theoretically recreate the breakouts observed in the well KWR-1A at 3468m MDRT. The range of possible S_{Hmax} magnitude is related to the UCS uncertainties $15MPa \leq UCS \leq 20MPa$. This range represents the P10 and P50 of rock strength across the shale intervals within the Slochteren formation in the well KWR-1A (see Figure 20).

This analysis was performed for each of the three depths (KWR-1A=3402.15m, RDW-1=3240m & 3351m TVDSS) where breakouts were clearly identified. **Appendix 4 Results from the CSTR module using GMI•SFIB™** gathers the analyses performed using GMI•SFIB™ module CSTR. Figure 21 illustrates a graphical summary of the resulting S_{Hmax} range in terms of effective stress ratio for the three selected depths. The width of the red

horizontal lines represents the range of possible S_{Hmax} ESR predicted from the analysed wellbore failures.

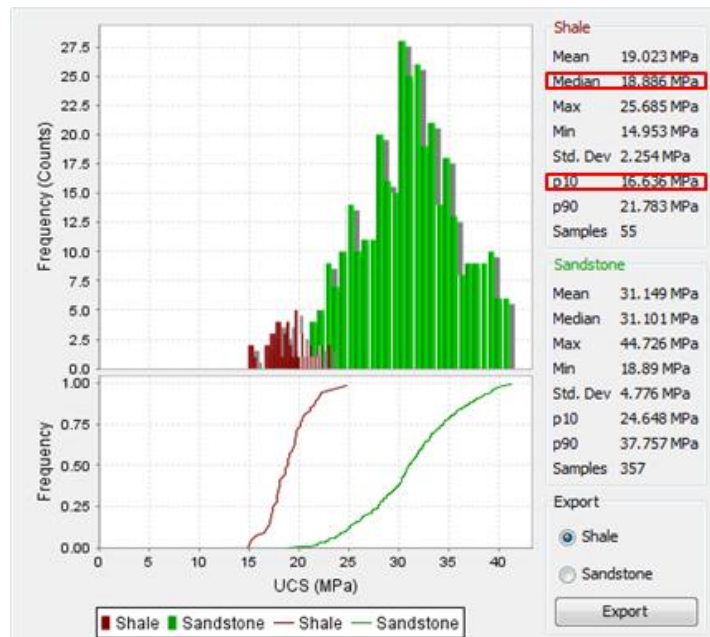


Figure 20. UCS Histogram for the Slochteren formation in KWR-1A. The Breakouts were identified across the shale which is weaker than the sand. P10 and P50 UCS values across the shale intervals have been for stress modelling.

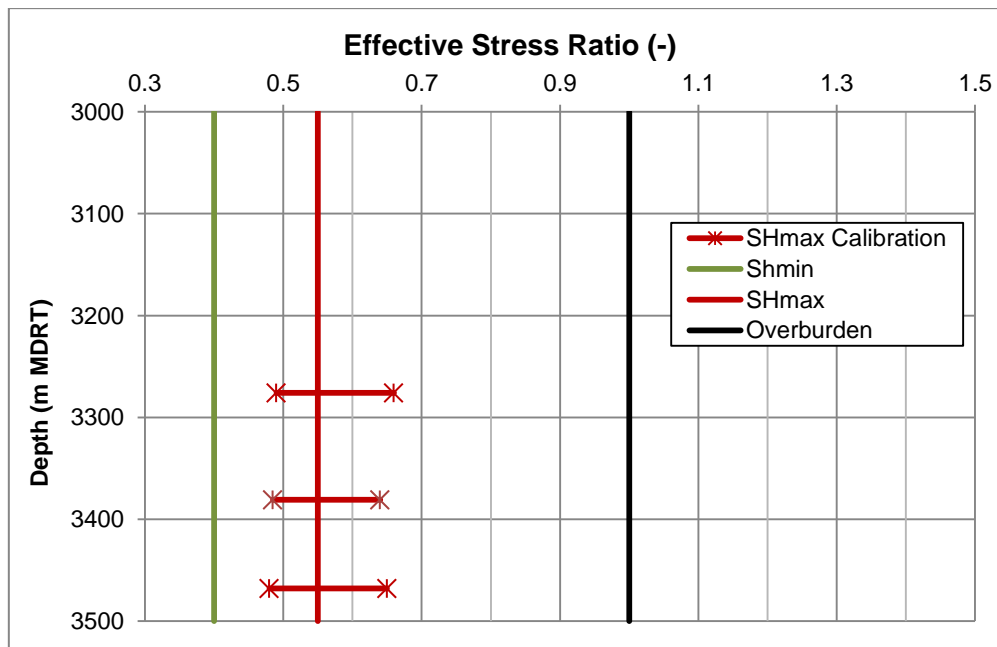


Figure 21. Graphical summary of the GMI-SFIB™ module CSTR (Constrain Stress) for the most relevant breakouts identified in wells KWR-1A and RDW-1. The red horizontal lines represent the possible range of S_{Hmax} considering the uncertainties in the UCS for the three depths were wellbore failures were analysed. The effective stress ratio selected to fit the breakouts and drilling experiences is 0.55 (vertical red line), thus is value has been used to obtained the local S_{Hmax} magnitude in the Groningen Field. Here is also displayed the estimated ESR for S_{hmin} (green line) which is 0.40.

As with the determination of the minimum horizontal stress, the principle for evaluating the S_{Hmax} magnitude consists of using effective stress ratios. For the maximum horizontal stress we have:

$$K_{Hmax} = (S_{Hmax} - P_p) / (S_v - P_p) = 0.55 \quad (9)$$

Where K_{Hmax} is the effective stress ratio used to calculate the maximum horizontal stress magnitude (S_{Hmax}).

The average S_{Hmax} values at the depths where CSTR have been run are used for deriving the K_{Hmax} value shown above and then assumed that this value remains constant across the entire depth profile in order to generate a corresponding S_{Hmax} profile. The stress modelling results, shown in Figure 19, also indicate that an effective stress ratio of 0.55 would be appropriate for establishing the S_{Hmax} profile. The predicted S_{Hmax} gradient in Groningen varies between 1.73 – 1.82 SG (500 – 560 bars) at the top of the Slochteren formation.

A range of S_{Hmax} magnitudes was determined in order to account for the uncertainties linked to the S_{hmin} magnitude and the possible UCS variation (Figure 21). A variety of such analyses consistently point that a normal faulting stress regime ($S_v > S_{Hmax} > S_{hmin}$) is applicable in the field at reservoir depths. Through this analysis we derived a normal faulting stress state model (Figure 22), which is consistent with the local drilling experience and the regional experience. Figure 22 shows the stress state for well POS-1 in EMW on the left track and in absolute pressure on the right track. The pore pressure is shown in blue, the S_{hmin} and S_{Hmax} in dashed green and dashed red respectively, the overburden in dark red and the mud weight used to drill the well in green.

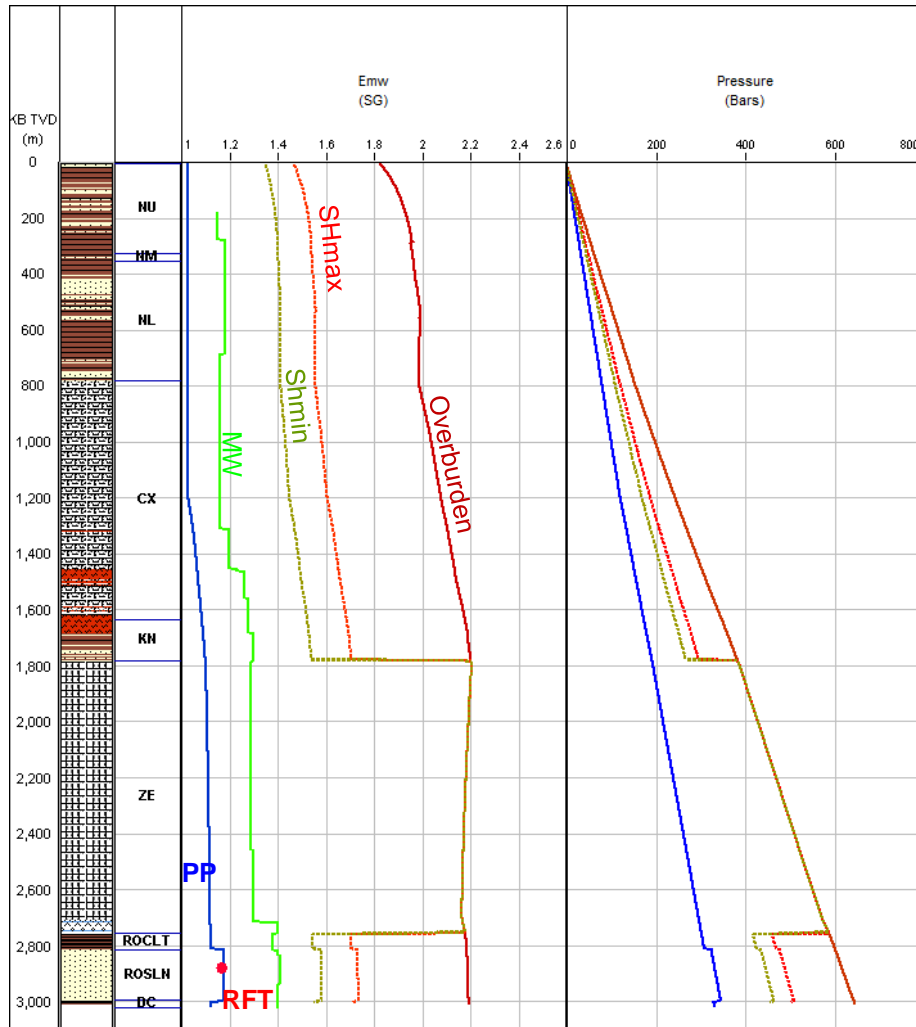


Figure 22. Summary of the principal stress magnitudes and the pore pressure as function of depth (example from well POS-1). S_v in dark red, S_{hmin} in dashed green, S_{Hmax} in dashed red and pore pressure in blue. Here is also displayed the MW used to drill this well (bright green) and the formation pressure measurements.

2.6. Verification of the Geomechanical Model

Review of drilling experience of existing wells is a way to calibrate the wellbore failures predicted by the geomechanical model with the events experienced while drilling the wells. If the geomechanical model can recreate the drilling experience to a reasonable level of accuracy, then it is considered robust enough for further predictive use such as 3D geomechanical modelling or wellbore stability.

2.6.1. Drilling Experience

The analysis of the drilling experience focuses on events that may be related to mechanical instability of the well and subsurface pressure, hence, can be used to calibrate/verify the geomechanical model. Examples of such events are losses or gains of drilling mud where the former helps constrain S_{hmin} and the latter the pore pressure. Stuck pipe or tight hole

conditions, excessive cuttings/cavings and eventually hole reaming, may indicate excessive amounts of cavings as a result of compressive failure (i.e. breakouts or washouts) at the wellbore wall.

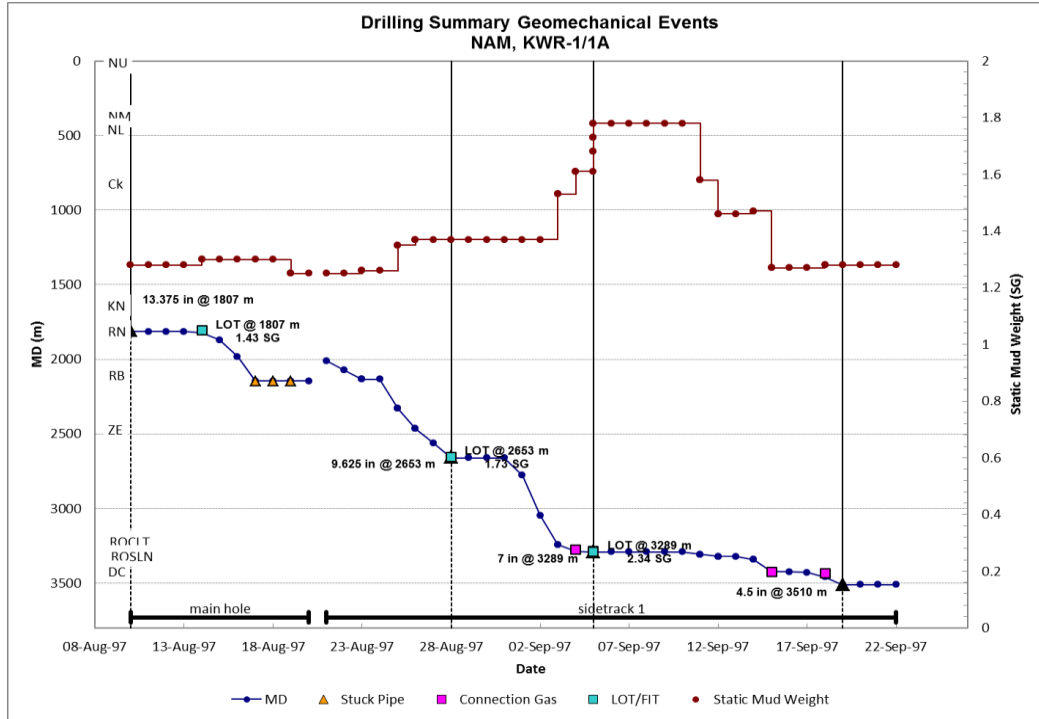


Figure 23. Summary of the time depth drilling events related to geomechanical issues encountered while drilling the Well KWR-1A. The most relevant event was when the pipe got stuck and the well had to be sidetracked.

Analysis of the drilling data indicates that a few issues occurred while drilling the well KWR-A (Figure 23). While drilling around 2100m, the pipe got stuck and the well had to be sidetracked. Connection gas was encountered at around 3280m and the mud weight was increased in order to reduce and control the amount of gas getting into the well. At the end, the well was successfully drilled until TD without much major problems.

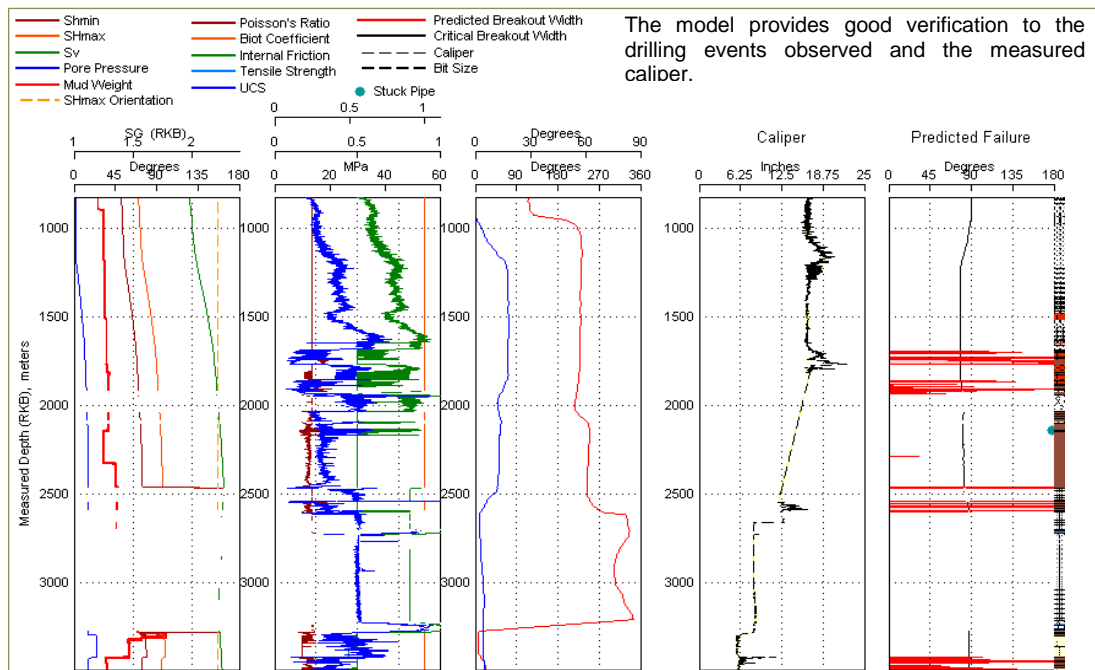
Similar analyses of the daily drilling reports were performed for all the thirteen offset wells. No major wellbore stability incidents were reported except for a few tight spots, reaming and connecting gas. All verification analyses can be found in **Appendix 5 Model Verification**

2.6.2. Model Calibration using GMI•WellCheck™

The methodology used to verify the model is by predicting compressive failure at the wellbore wall (i.e. borehole breakouts) in wells previously drilled, where we consider the stresses, pore pressure, rock strength, individual well paths and the mud weights used for drilling. GMI•WellCheck™ is our standard tool for this purpose. Generally, the model can be verified against failure occurrence as observed in image or (oriented multi-arm) caliper logs, or by comparison of the predictions with the drilling experience (e.g., excessive predicted failure should correlate with difficulties experienced during drilling); this would verify the validity of the geomechanical model.

The geomechanical model was verified for the entire range of depths covered by wireline log data for each of the thirteen offset wells considered for the geomechanical study. **Error! Reference source not found.** Figure 24 display output plots of the verification as a function of breakout width and depth and Figure 25 shows the comparison between these predicted breakout widths by the geomechanical model and those measured from the images for the well KWR-1A. The results show very good agreement between the predicted wellbore failures using the geomechanical model in place and the failures observed and identified in the image logs. Similar verification results are shown in Figure 26 and Figure 27 for the well RDW-1. In this case, the model is predicting more wellbore failures than those measured by the image logs; nonetheless the overall prediction verifies well the drilling events such as tight spots reported all along the interval were failures have been predicted. More analyses can be found in **Appendix 5 Model Verification.**

In summary, the drilling experience of the thirteen wells located throughout Groningen verify well with the predictions based on our geomechanical model. Because of the overall reasonable data quality, the geomechanical model appears well constrained for the reservoir and Carboniferous formations. The overlying formations have been fairly verified against single caliper measurements and a few drilling incidents from few wells. Nonetheless, this requires further calibration in order to increase the robustness of the stress model for the overburden formations.



The model provides good verification to the drilling events observed and the measured caliper.

Figure 24. Calibration of the geomechanical model against drilling experience from the well KWR-1A. The two tracks on the left show the geomechanical model (principal stresses and rock properties) as a function of depth. The two next tracks represent the well trajectory and the caliper response for this well. The right hand side track displays the breakout width predicted by the geomechanical model for each depth. As can be observed from the two tracks on the right, good verification is found between the predicted failure (red intervals) and those measured with the single caliper.

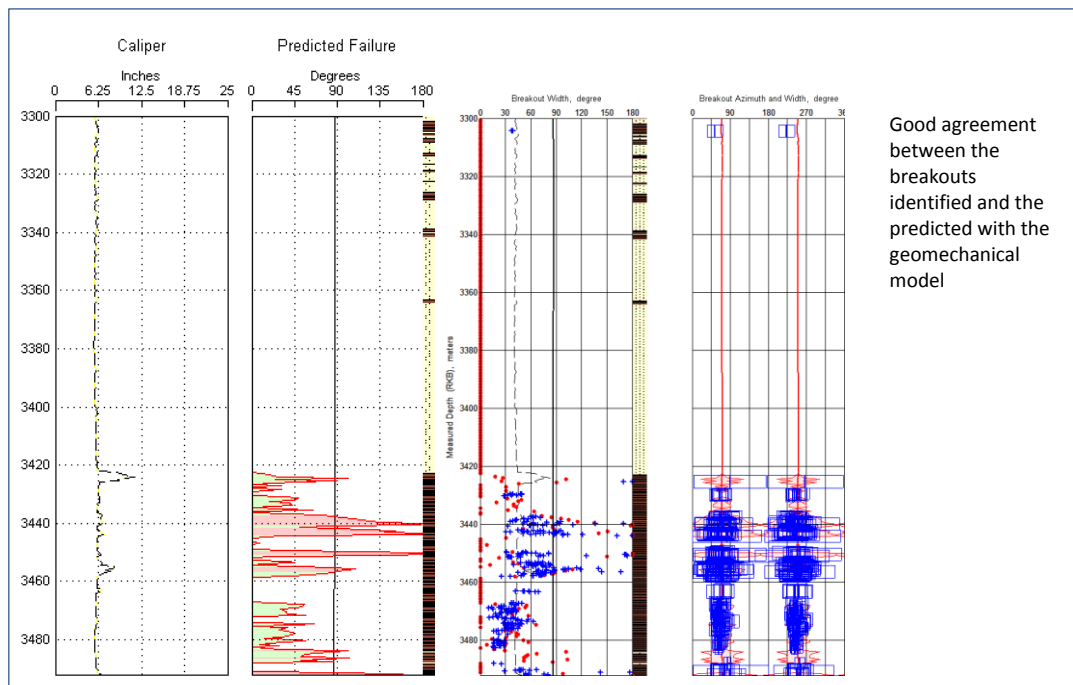
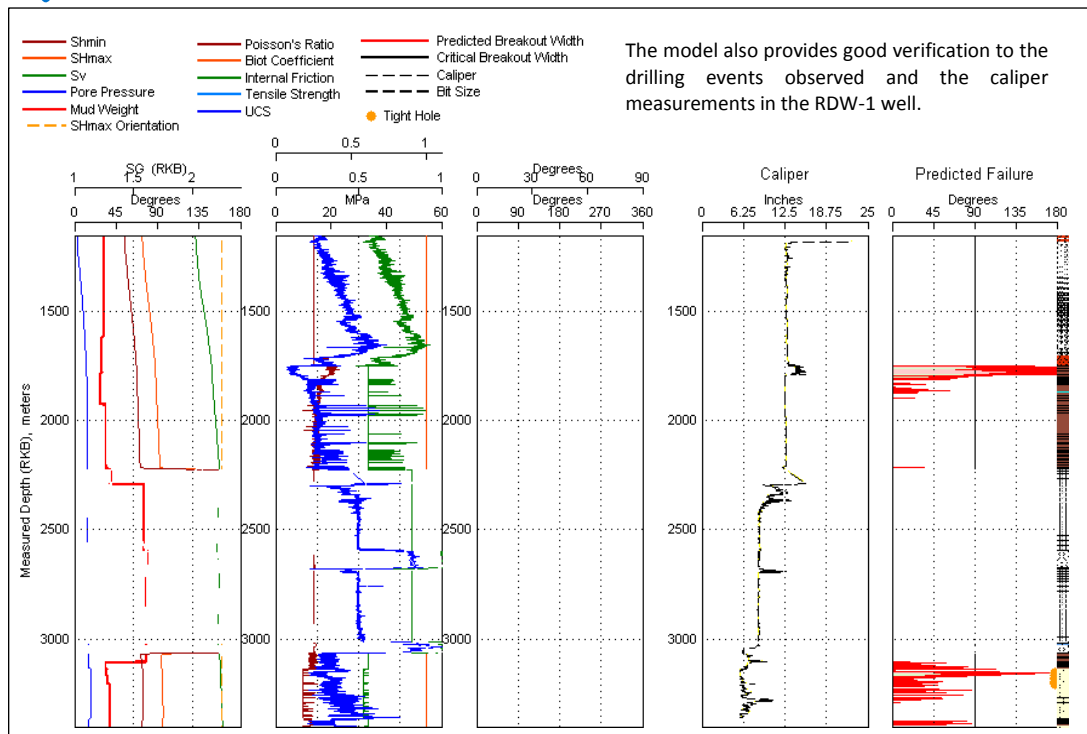
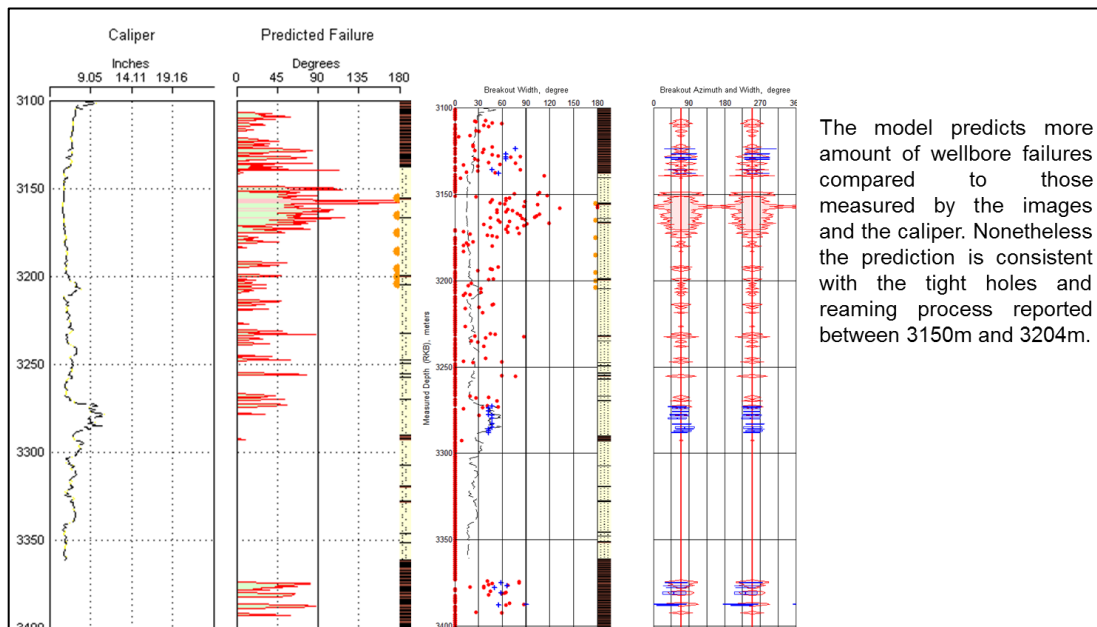


Figure 25. Comparison of predicted breakouts and the measured ones from images in well KWR-1A across the Slochteren Fm. As can be seen on the right hand side of the figure, an excellent verification is found between the breakout widths predicted in red and the breakout widths measured from the image logs. These results provide confidence and verify well the geomechanical model used in the prediction.



The model also provides good verification to the drilling events observed and the caliper measurements in the RDW-1 well.

Figure 26. Calibration of the geomechanical model against drilling experience from the well RDW-1. Good verification between the predicted failure (red intervals) and the tight spots reported in across the reservoir section.



The model predicts more amount of wellbore failures compared to those measured by the images and the caliper. Nonetheless the prediction is consistent with the tight holes and reaming process reported between 3150m and 3204m.

Figure 27. Comparison of predicted breakouts and the measured ones from images in well RDW-1A. As can be seen on the right track, the amount of breakouts predicted is higher than that measured. However, the widths of the breakouts are similar to those measured and the failures verify well with the tight spot events reported between 3150m – 3180m even though no breakouts were seen in the image logs.

3.0 Model Uncertainties

3.1. 1D Geomechanical Model

- No XLOT or mini frac data at virgin conditions were available for determination of the fracture closure pressure (FCP) in order to provide an accurate estimation the least principal stress (S_{hmin}). In this sense, the magnitude of S_{hmin} has been constrained to the lower limit of the LOT dataset and hence its estimation is conservative. An estimated error bar of $\pm 15\%$ should be addressed to the resulting S_{hmin} to assess the uncertainties surrounding the model. The provided error bar has been estimated from the scattered LOT points used in this study (Figure 13).
- The variation of rock strength (UCS) across the Slochteren formation is large (15-26 MPa) which would increase the uncertainties in the estimation of the magnitude of S_{Hmax} . There is also poor knowledge of the rock properties in the overburden formations.
- The range of possible S_{Hmax} magnitude is related to the UCS uncertainties as a large variation in the rock strength has a direct impact on the estimation of S_{Hmax} .

4.0 Summary

- The in situ stress regime in the field is a normal faulting environment, where the vertical stress, S_v , is larger than both horizontal stress magnitudes ($S_v \geq S_{Hmax} \geq S_{Hmin}$).
- The vertical stress (S_v), derived by integrating bulk density log data is equivalent to ~ 2.2 - 2.4SG EMW at the top of the Slochtere formation. S_v is larger than 2.15 SG for depths deeper than 2000m TVD.
- The pore pressure is hydrostatic down to approximately 1200m TVDSS and the Shale pore pressure in the overburden formations has been interpreted to be slightly overpressured to 1.12SG at the top the Rotliegend and from this point the reservoir pressure varies between 330 and 360 bars.
- The magnitude of the least principal stress (S_{Hmin}) is determined through LOT values conducted at various intervals of the selected offset wells. The minimum horizontal stress gradient at the top of the reservoir formation is equal to ~ 1.54 – 1.67SG EMW (420-520 bars).
- Image logs have been analysed in order to identify the stress induced wellbore failures, useful for the determination of the S_{Hmax} azimuth. Several breakouts were identified in the Slochteren and Carboniferous formations. The S_{Hmax} azimuth has been interpreted to be ~ SSE160°NNW.
- Based on empirical relations between wireline sonic logs and rock strength, UCS profiles for the reservoir and the overburden shales have been derived. Calibration has only been performed in the reservoir formation where rock mechanical tests were available. The UCS within the Slochteren varies between 15MPa and 26MPa and internal friction coefficient (μ_i) varying between 0.42 and 0.62 (23° and 32°). Log derived UCS and internal friction values reflect a similar distribution of mechanical rock properties as found from the lab tests.
- The magnitude of the maximum horizontal stress (S_{Hmax}) was constrained by performing stress modelling with GMI-SFIB in intervals where wellbore failure were observed. This permitted confirmation of a normal faulting stress regime in the field and at the top of the Slochtere formation, the maximum horizontal stress magnitude is ~ 1.73 – 1.82SG EMW (500-560 bars).
- Effective stress ratio (ESR) values of 0.4 and 0.55 were used to calculate S_{Hmin} and S_{Hmax} magnitudes respectively.
- The minimum horizontal gradient in the field varies between 1.54 SG and 1.67 SG (420-520 bars) at the top of the reservoir.
- The predicted S_{Hmax} gradient in Groningen varies between 1.73 – 1.82 SG (500 – 560 bars) at the top of the Slochteren formation.

5.0 Recommendations

- To improve the stress model, especially the magnitude of the far field S_{hmin} , it is recommended to perform XLOT's or minifrac and record pressure-volume-time data in small time steps and capture the fracture closure pressure. This will reduce the uncertainties surrounding the estimated S_{hmin} .
- Capture additional image logs or multi arm caliper (4 arm/6 arm) to evaluate hole shape and verify the stress orientation used and to constrain S_{Hmax} magnitude around the Groningen Area.
- Carried out rock testing to calibrate the static and elastic properties of the rocks such as Young's Modulus and internal friction coefficient in both overburden and reservoir formations.

6.0 References

¹ Gardner, G.H.F.; Gardner L.W. & Gregory A.R. (1974). Formation velocity and density -- the diagnostic basics for stratigraphic traps.

² Veeken, G.M.M., Hertogh, G.M.M., Hydendaal, H.G.C. & Van der Meulen, J.T. Groningen Sand Failure Study Status Report Part 2: Rock Stress and Rock Strength in Groningen/Annerven Fields. Group Research Report, September 1990. RKGR.89201.

³ Horsrud, P. Estimating mechanical properties of shale from empirical correlations. SPE Drilling & Completion, pp. 68-73, 2001.

⁴ McNally, G.H., Estimation of Coal measures rock strength using sonic and neutron logs. Geoexploration, 24: pp. 381-395. 1987.

⁵ Militzer, H. & Stoll, R., Einige Beitrageder geophysics zur primadatenerfassung im Bergbau, Neue Bergbautechnik. 3: pp. 21-25. 1973.

⁶ Lal, M., "Shale Stability: drilling fluid interaction and shale strength. SPE Latin American and Caribbean Conference. 1991.

⁷ Van de Bogert, P.A.J., Van, E. & Van der Wal, O. "Groningen Fault Stability Assessment". SR.13. Appendix 4. Elastic reservoir properties. p.53.

⁸ Van de Bogert, P.A.J., Van, E. & Van der Wal, O. "Groningen Fault Stability Assessment". SR.13. Section 2.2.2 Horizontal stress. p.7.

⁹ Zoback, M.D., Reservoir Geomechanics. Cambridge University Press. 2007.

¹⁰ Zoback, M.D., Moos, D., Mastin, L. & Anderson, R.N., Wellbore breakouts and in situ stress. J. Geophys. Res. 90: pp. 5523-5530. 1985.

¹¹ Moos, D. & Zoback, M.D., Utilization of observations of wellbore failure to constrain the orientation and magnitude of crustal stresses: Applicatoin to continental deep sea drilling project and ocean drilling program boreholes. J. Geophys., 95: pp. 9305-9325. 1990.

7.0 Nomenclature

Abbreviation	Meaning
DDR	Daily Drilling Report
FWR	Final Well Report
LOT	Leak Of Test
MDRT	Measured Depth from Rig Table
MDT	Modular formation Dynamic Tester
RFT	Formation Test
S_{Hmax}	Maximum Horizontal Stress
S_{Hmin}	Minimum Horizontal Stress
TVDRT	True Vertical Depth from Rig Table
TVDSS	True Vertical Depth from Sea Surface
UCS	Unconfined Compressive Stress
ESR	Effective Stress Ratio
BO	Breakout
IF	Internal Friction

8.0 Appendices

Appendix 1 Pore Pressure

This appendix shows the additional interpreted pore pressure profiles for the remaining offset wells.

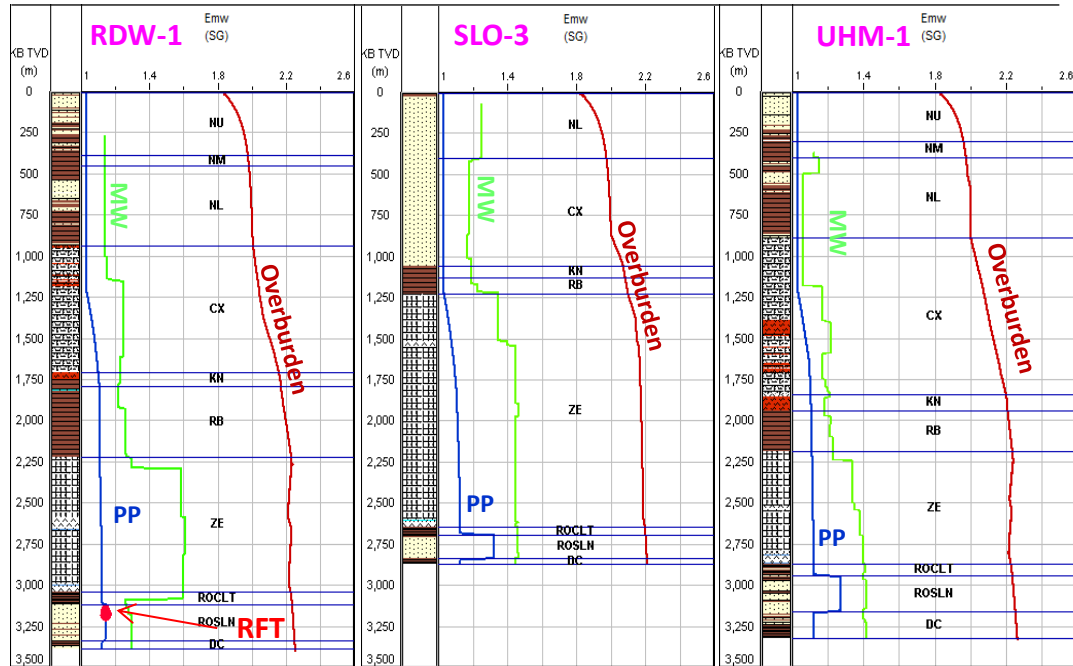


Figure 28. Pore pressure profiles for Wells RDW-1, SLO-3 and UHM-1

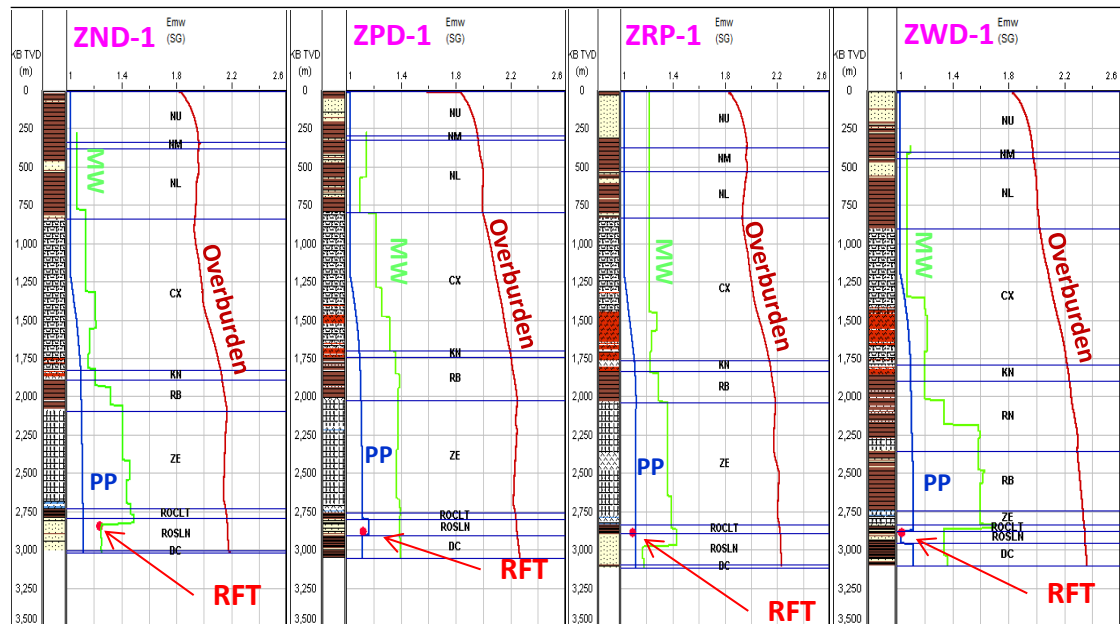


Figure 29. . Pore pressure profiles for Wells ZND-1, ZPD-1, ZRP-1 and ZWD-1

Appendix 2 UCS and Rock Properties

As described above, log based UCS and rock properties interpretations were calibrated according to the triaxial and uniaxial tests performed by NAM. The following figures show the interpreted triaxial tests and the resulted rock mechanical properties profiles for all offset wells.

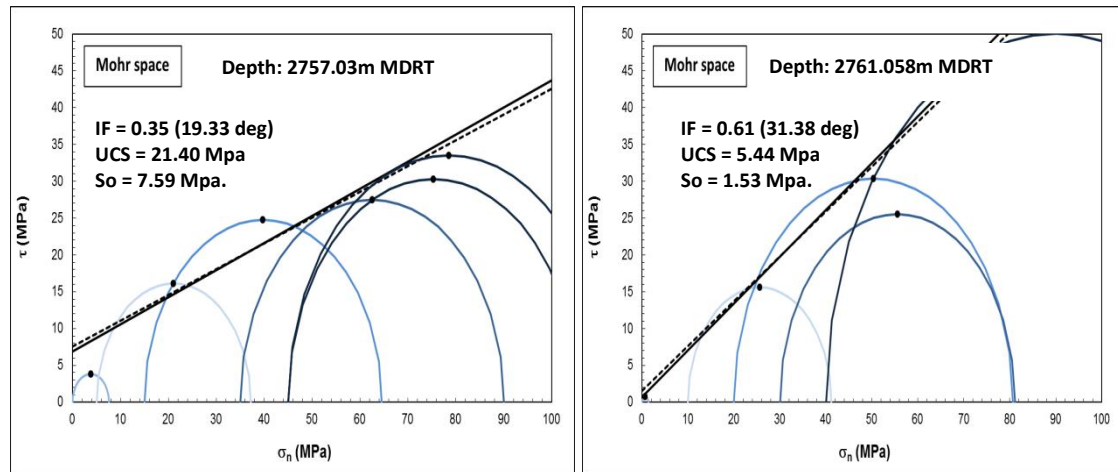


Figure 30. Interpretation of triaxial tests collected in the FRB-8 at 2757.03m and 2761.05m.

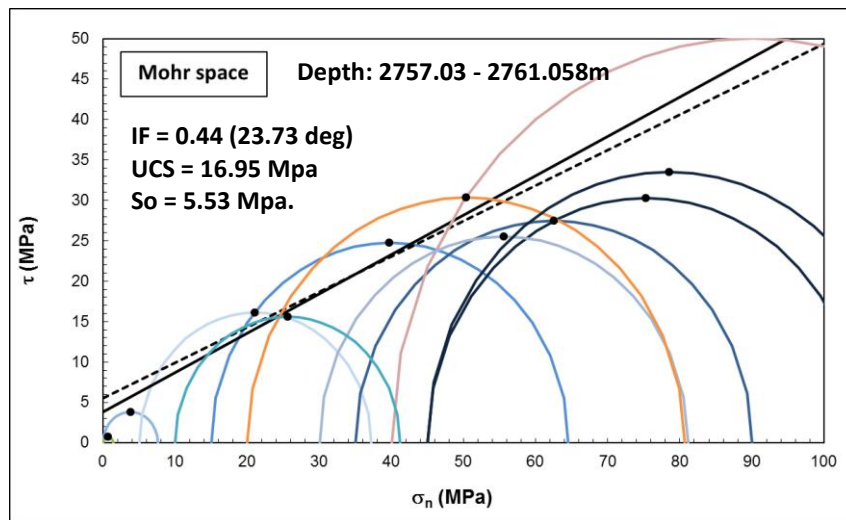


Figure 31. Interpretation of triaxial tests collected in the FRB-8 at combined intervals between 2757.03m and 2761.05m

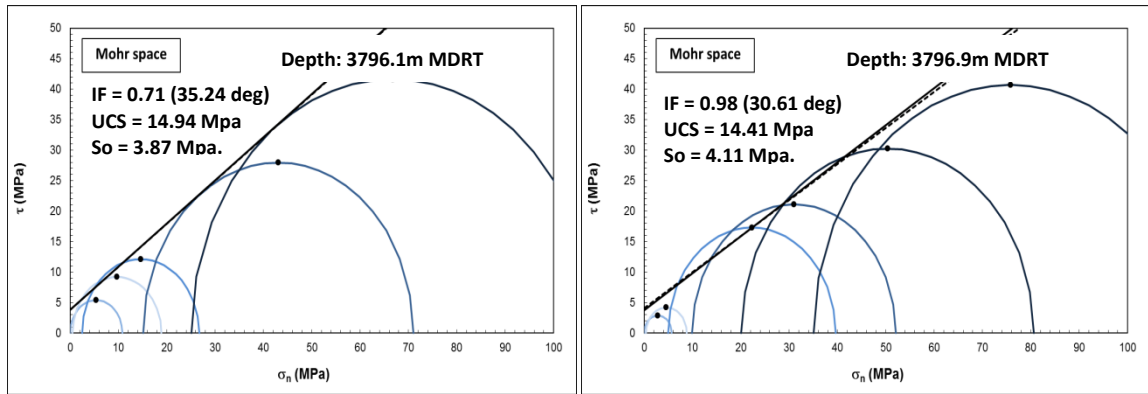


Figure 32. Interpretation of triaxial tests collected in the ZLV-6 at 3796.1m and 3796.9m

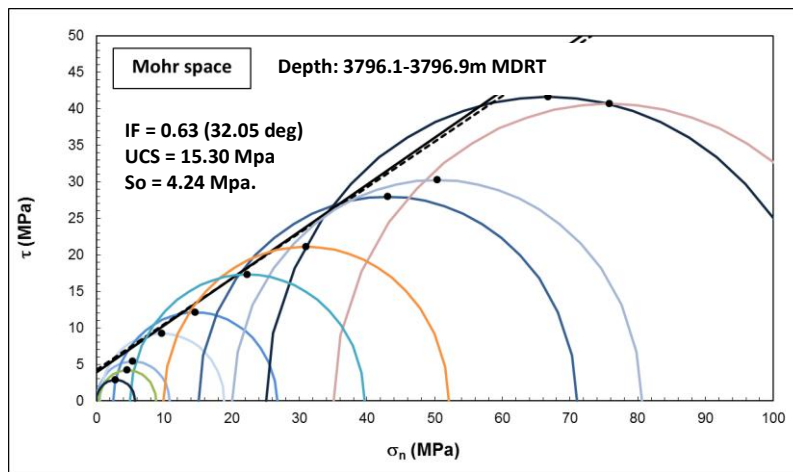


Figure 33. Interpretation of triaxial tests collected in the ZLV-6 at combined intervals between 3796.1m and 3796.9m.

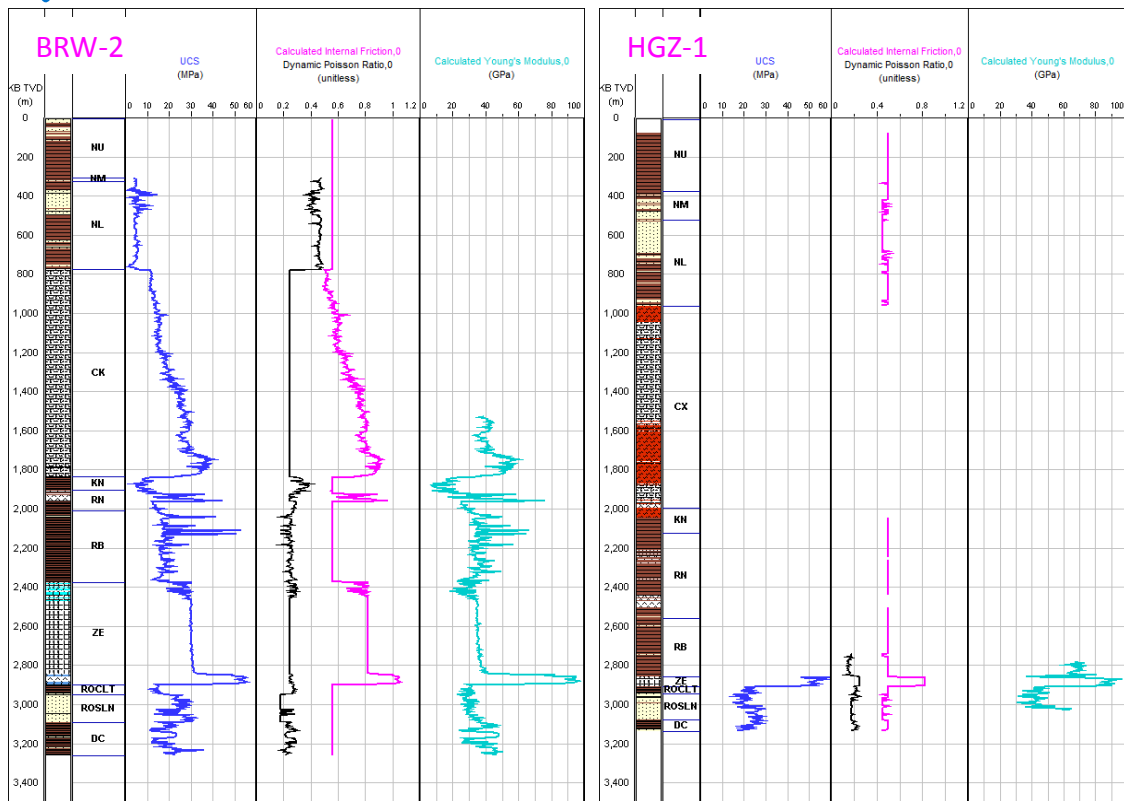


Figure 34. Composite rock mechanical properties for BRW-2 and HGZ-1.

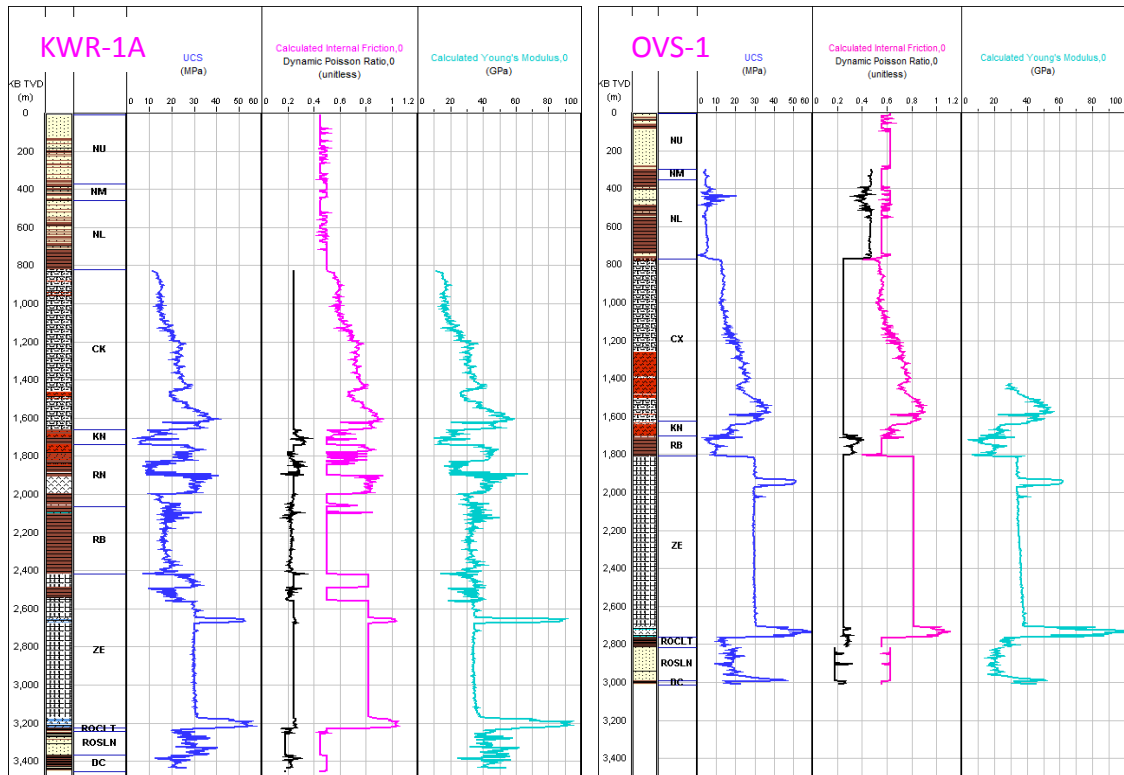


Figure 35. Composite rock mechanical properties for KWR-1A and OVS-1.

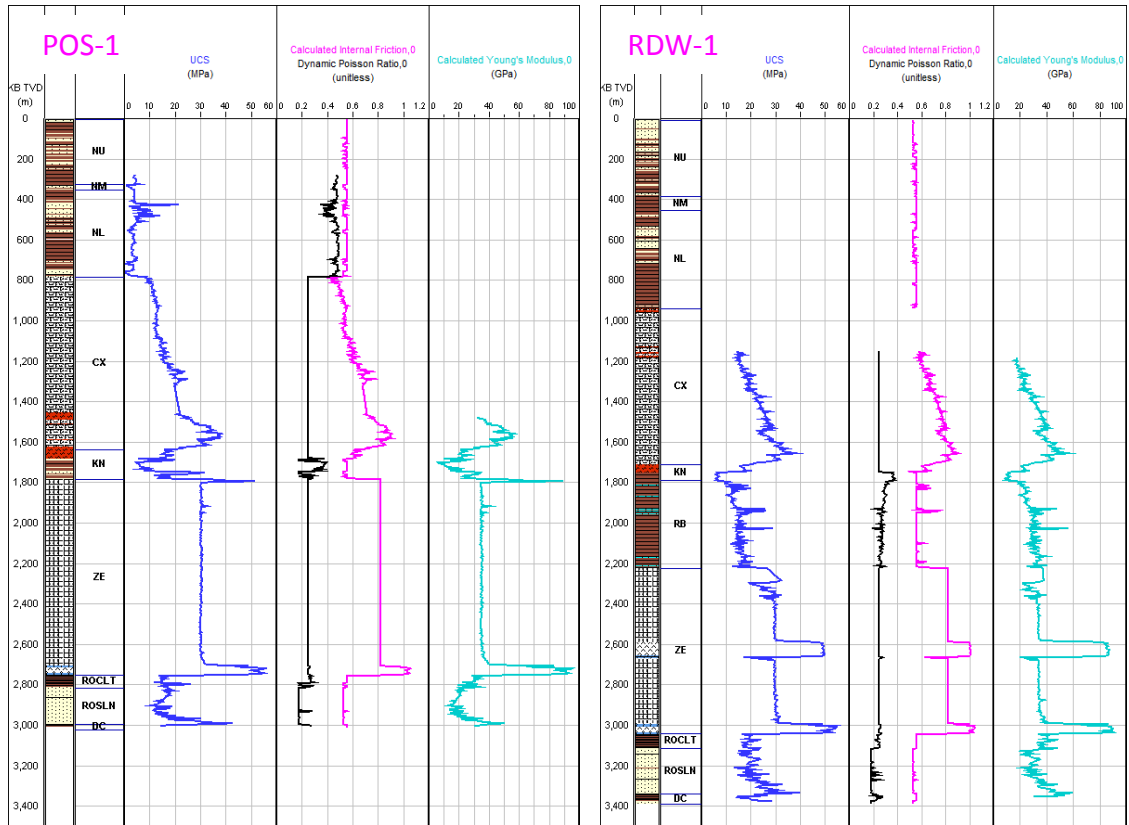


Figure 36. Composite rock mechanical properties for POS-1 and RDW-1.

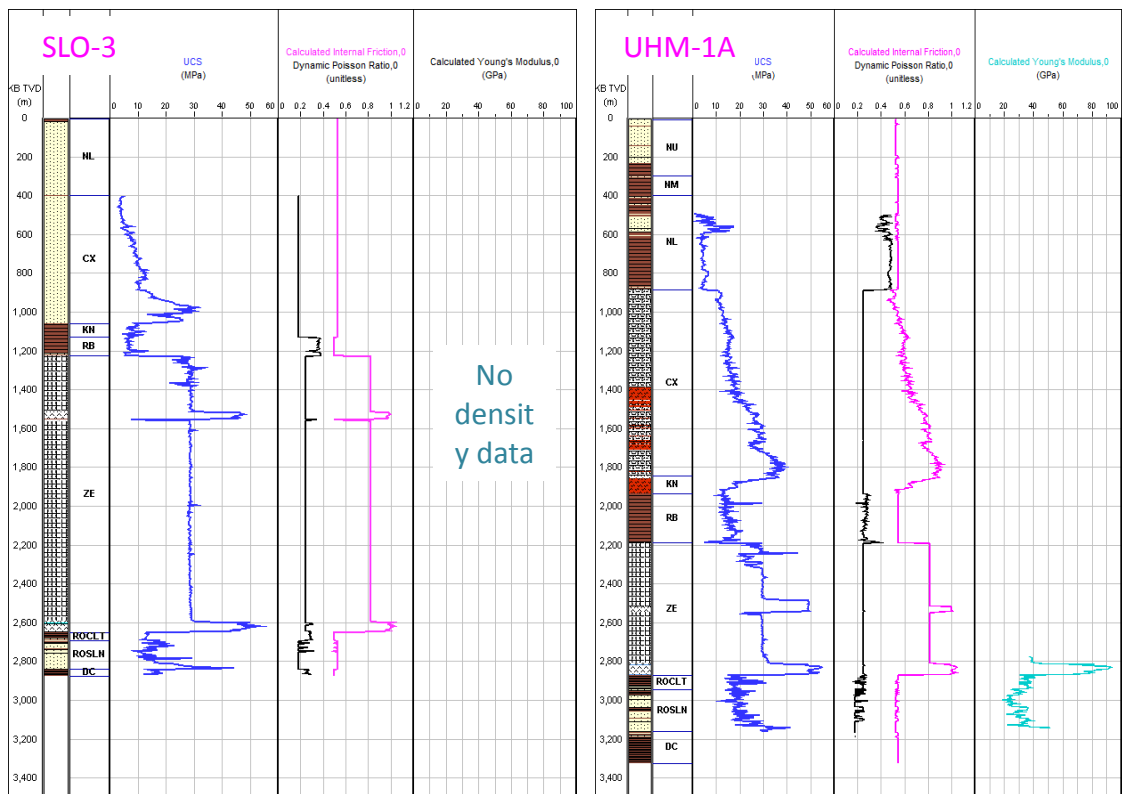


Figure 37. Composite rock mechanical properties for SLO-3 and UHM-1A.

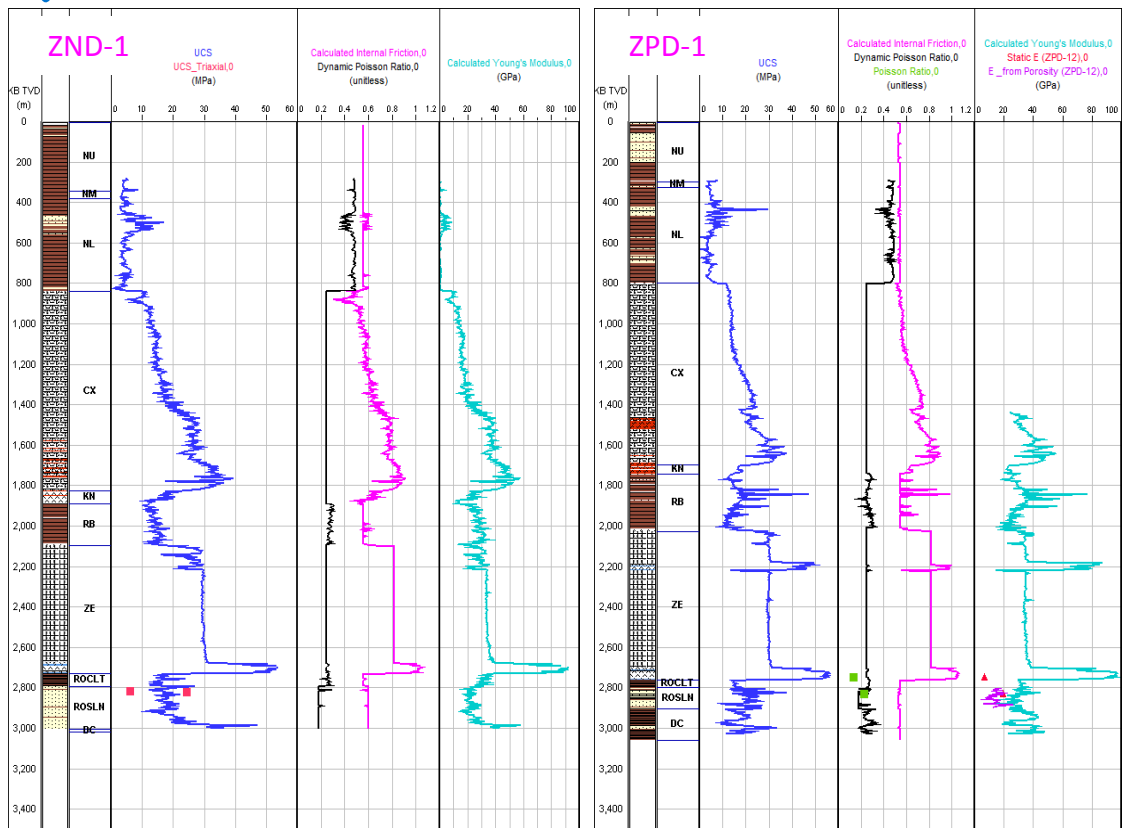


Figure 38. Composite rock mechanical properties for ZND-1 and ZPD-1.

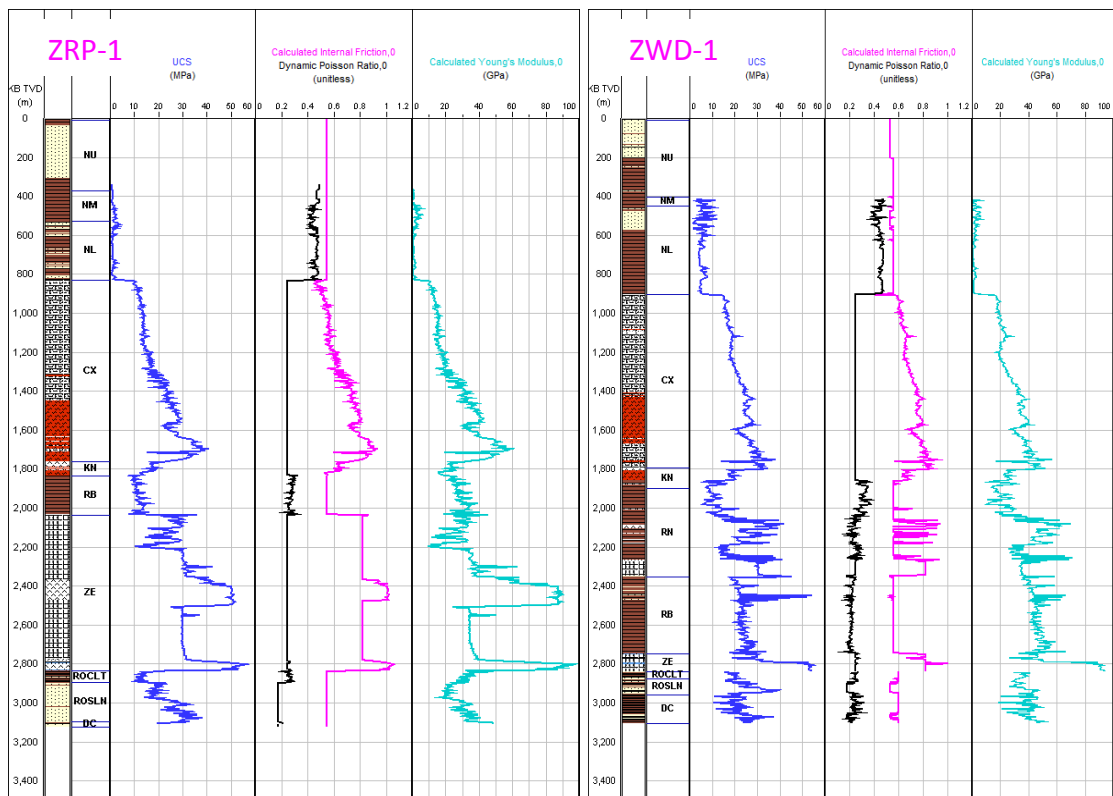


Figure 39. Composite rock mechanical properties for ZRP-1 and ZWD-1.

Appendix 3 Stress Polygon and Constraining Horizontal Stress Magnitudes

The stress polygon, which is used in Figure 21, is a way to display physically possible stress states. The outer bounds of the stress polygon (to the left and to the top) are defined by maximum stress states, which are possible according to the theory of frictional faulting equilibrium. This theory assumes that the state of stress in the crust is controlled by critically oriented faults that allow a build-up of stress only to a certain level. If the stress reaches this level (outer bounds of the stress polygon) the most critically oriented fault in the area slips, and thus decreases the stress.

Figure 40 shows an example of output diagrams from the CSTR module of GMI•SFIB displaying the stress polygon consistent with the occurrence of breakouts. This module is normally used to constrain the magnitudes of the horizontal stresses, from the occurrence of borehole breakouts and/or drilling-induced tensile fracture. The output plot shows the relationship between S_{Hmax} and S_{Hmin} for any given value of S_v to graphically illustrate all possible stress states (i.e., normal fault regime, reverse fault regime, or strike-slip regime) in the form of a polygon as constrained by Coulomb frictional faulting theory (Moos and Zoback, 1990). The perimeter of the stress polygon indicates the limiting values of S_{Hmin} and S_{Hmax} for which the state of stress is in equilibrium with the frictional strength of pre-existing faults, a condition often observed in the earth (e.g., Zoback and Healy, 1992). For any point around the perimeter of the polygon, construction of a Mohr diagram would show that the Mohr circle would be exactly touching the Coulomb frictional failure line for an optimally oriented fault in the current stress field. A coefficient of sliding friction of 0.6-0.8 can be used. The only allowable stress states are those that are either along the perimeter of the polygon or within its interior. This ensures that the in situ stresses never exceed a ratio of shear to effective normal stress that would initiate slip on well-oriented, pre-existing faults.

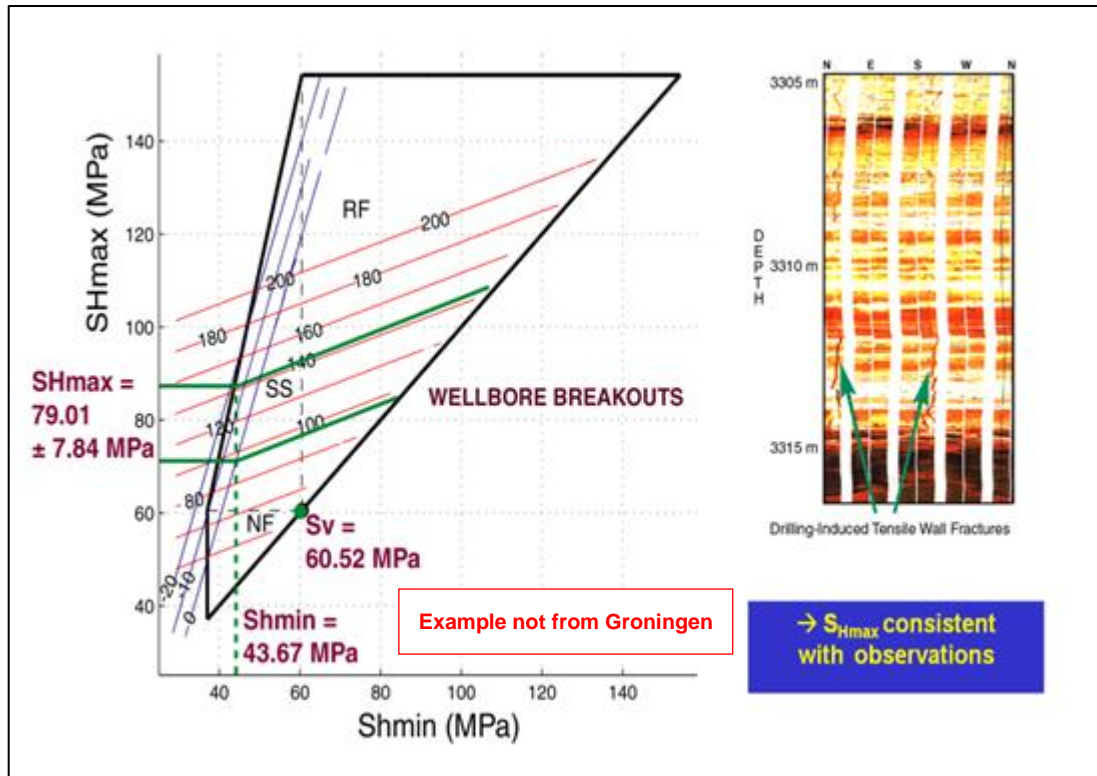


Figure 40. This figure shows the combining information about the Earth with observations of wellbore failure (right plot) to constrain stress magnitude. Example not from this study.

Appendix 4 Results from the CSTR module using GMI•SFIB™

Table 12 summarises the results of the analysis performed with GMI•SFIB™ from the breakouts' information collected on the image data analysis.

Table 12. List of the S_{Hmax} interval results of the GMI•SFIB™ analysis

Depth (mMDRT)	BO Azi (deg)	S_{Hmax} Azi (deg)	BO Width (deg)	S_{Hmax} interval (SG)	S_{Hmin} (SG)	S_V (SG)	PP (SG)	UCS (MPa)	μ (-)	ν (-)	MW (SG)
KWR-1A											
3468	66	156	80	1.66 - 1.85	1.58	2.25	1.12	15-20	0.5	0.23	1.28
RDW-1											
3276	70	160	55	1.69 - 1.87	1.58	2.25	1.14	15-20	0.53	0.18	1.3
3381	70	160	55	1.67 - 1.85	1.58	2.25	1.12	13-18	0.56	0.28	1.28

The following figures summarise the analyses corresponding the two remaining chosen depths from RDW-1 where breakouts have been identified.

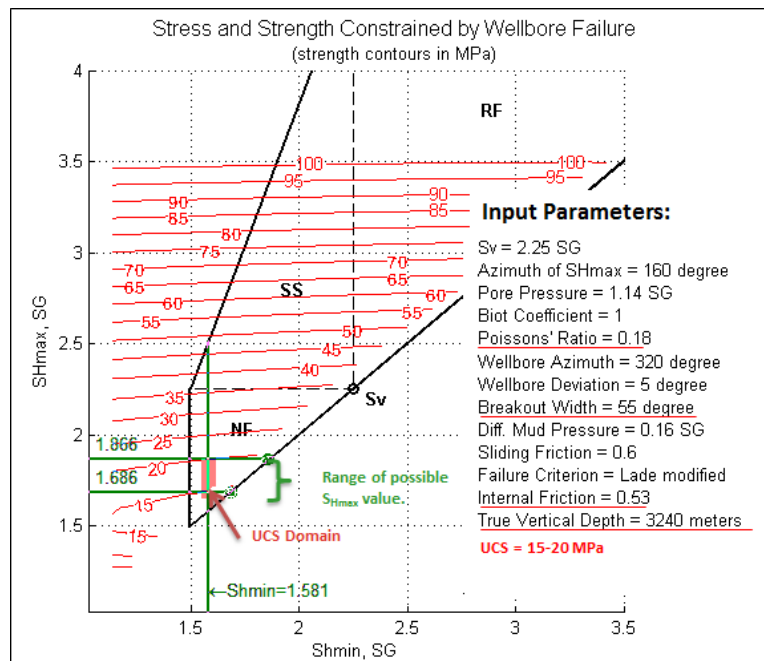


Figure 41. Example of S_{Hmax} modelling performed on wellbore breakouts recorded in the well RDW-1 at 3276m MDRT

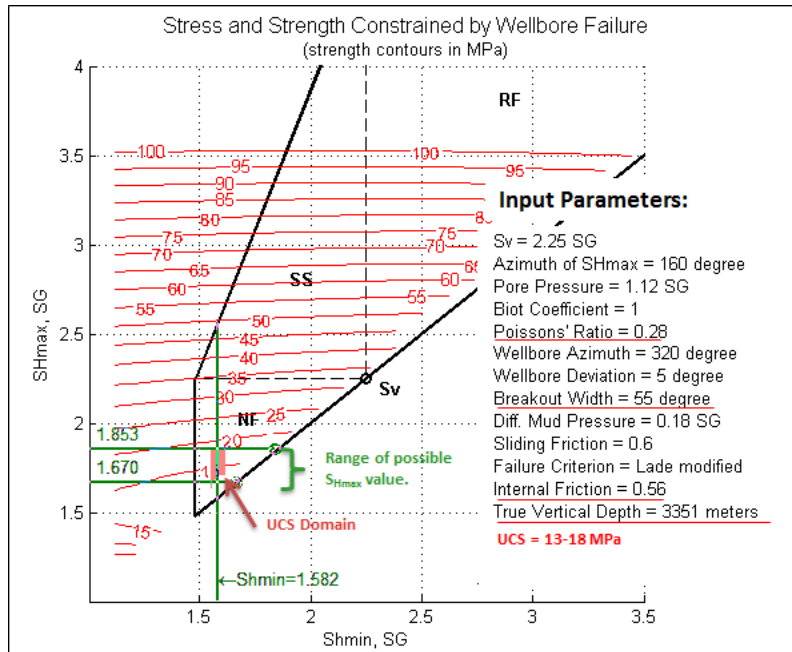


Figure 42. Example of S_{Hmax} modelling performed on wellbore breakouts recorded in the well RDW-1 at 3381m MDRT

Appendix 5 Model Verification

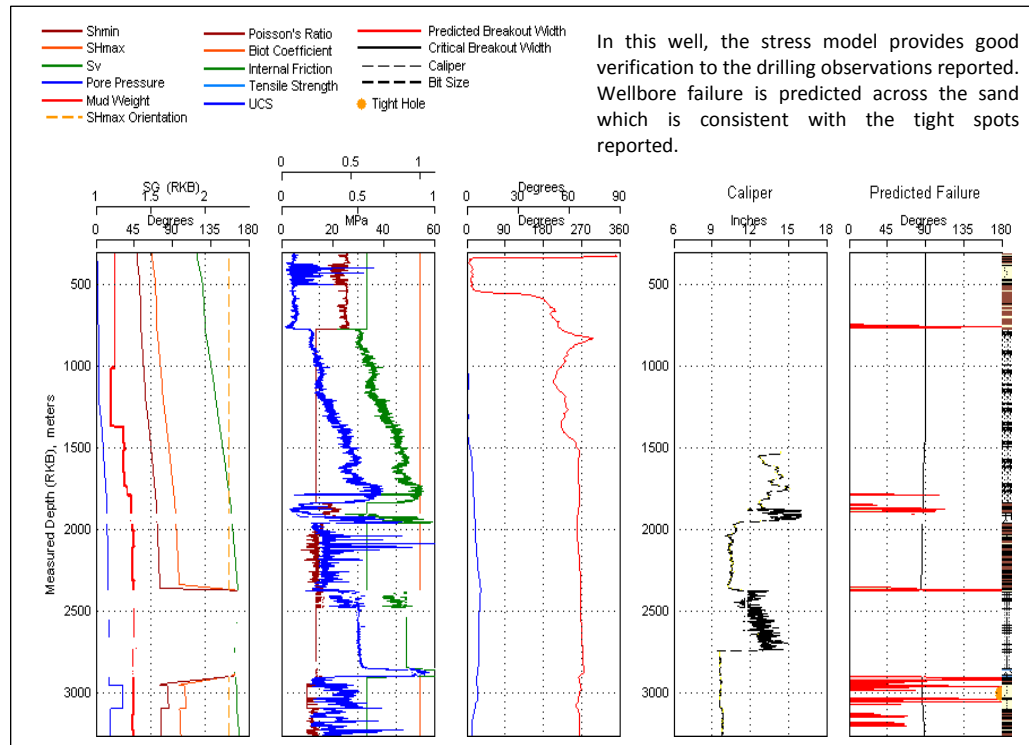


Figure 43. Calibration of the geomechanical model against drilling experience from the well BRW-2

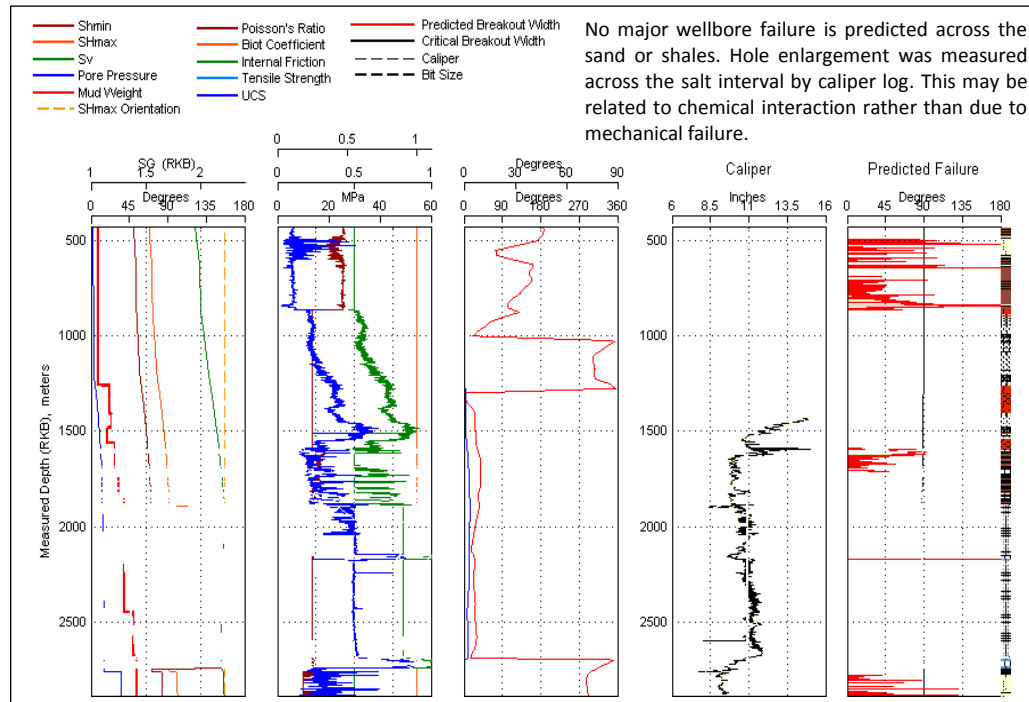


Figure 44. Calibration of the geomechanical model against drilling experience from the well EKL-1

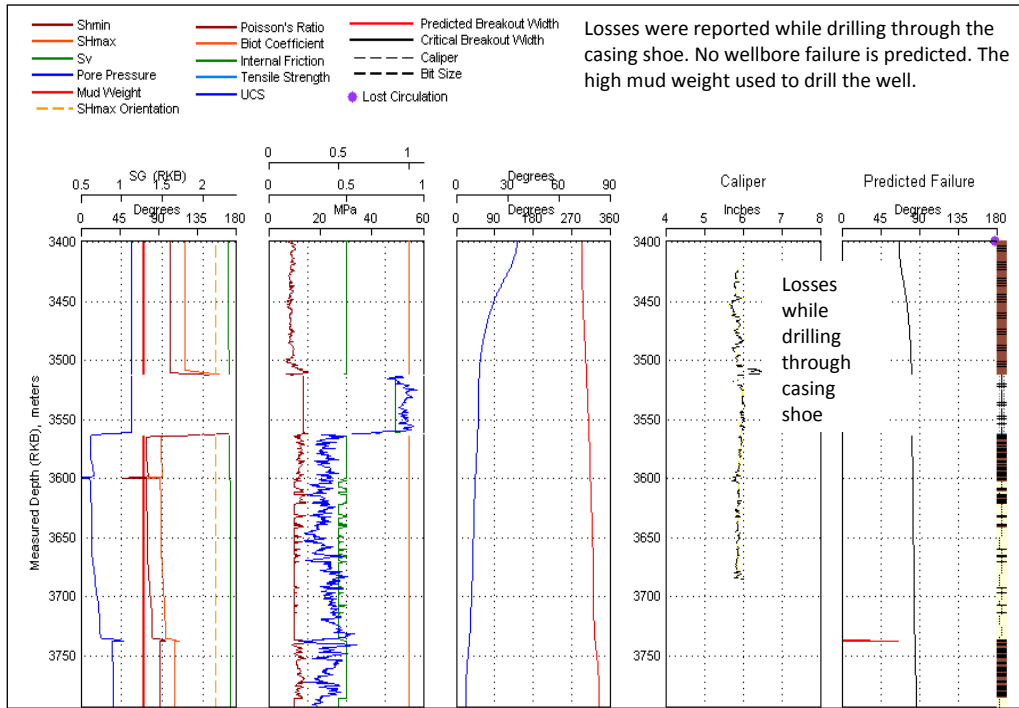


Figure 45. Calibration of the geomechanical model against drilling experience from the well HGZ-1

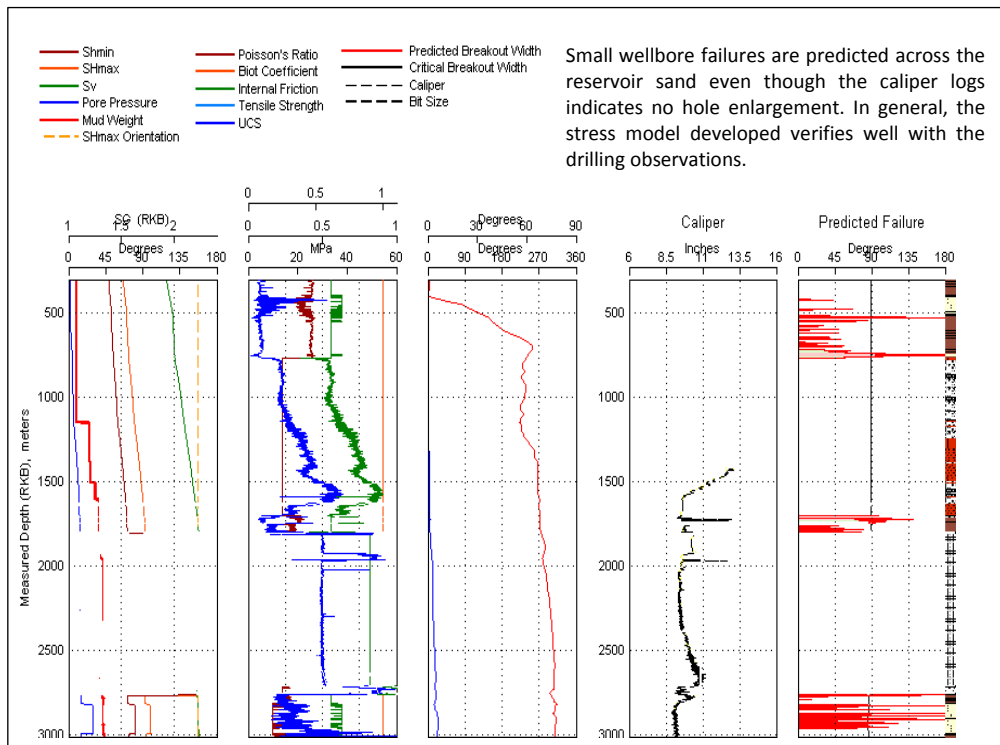


Figure 46. Calibration of the geomechanical model against drilling experience from the well OVS-1

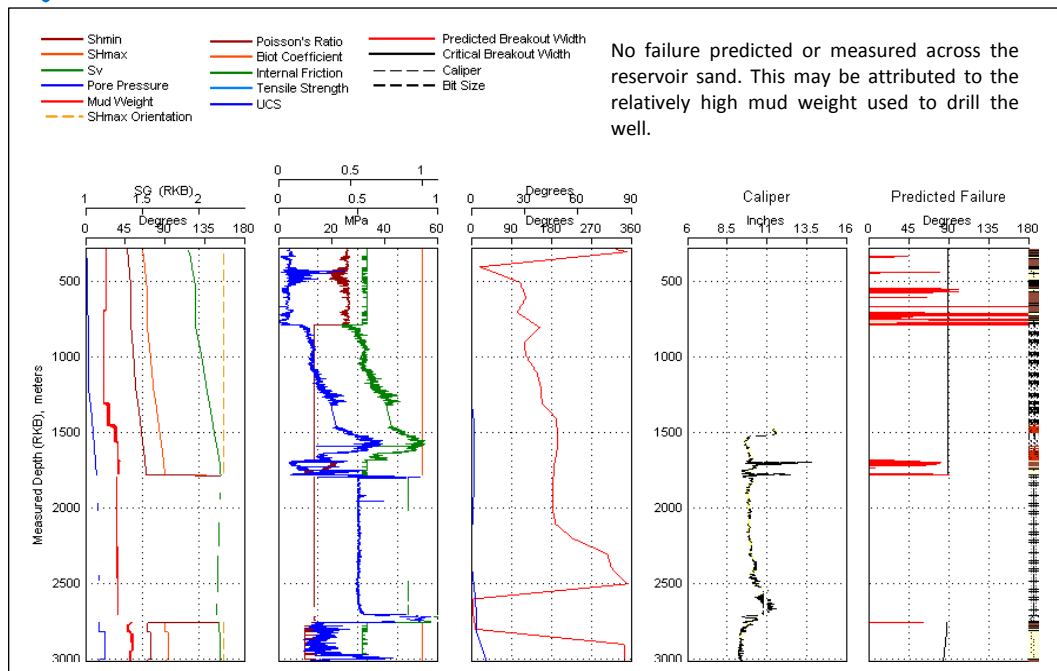


Figure 47. Calibration of the geomechanical model against drilling experience from the well POS-1

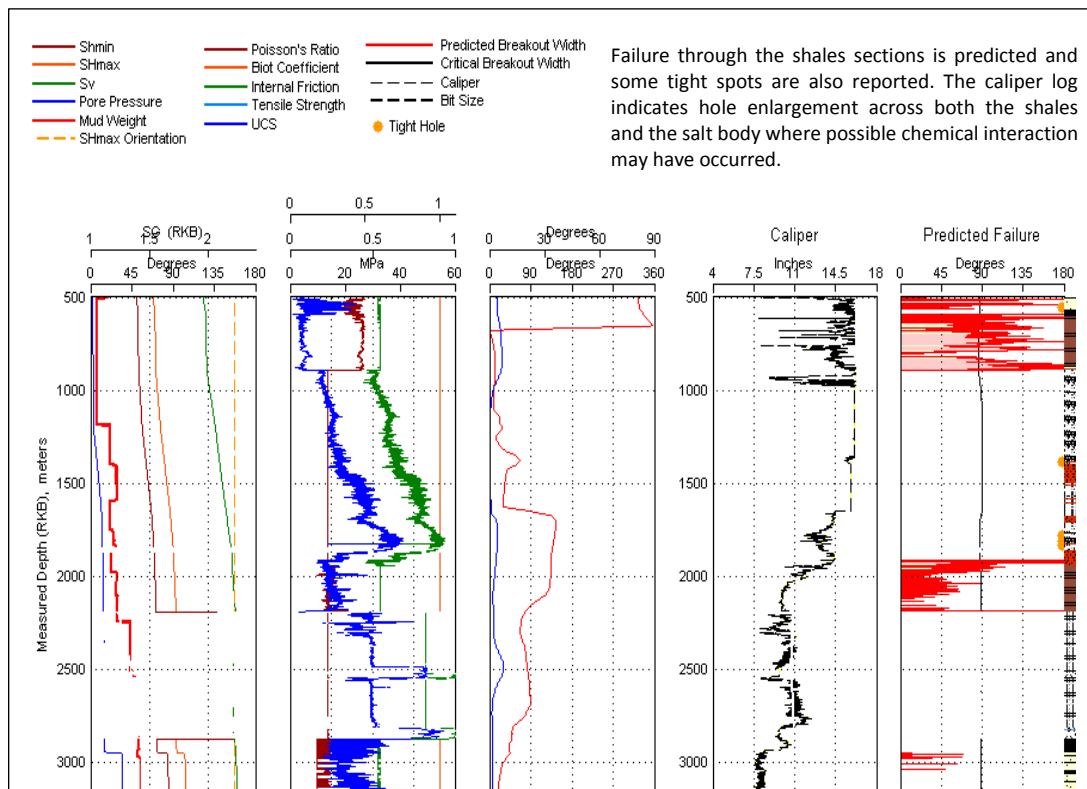


Figure 48. Calibration of the geomechanical model against drilling experience from the well UHM-1A

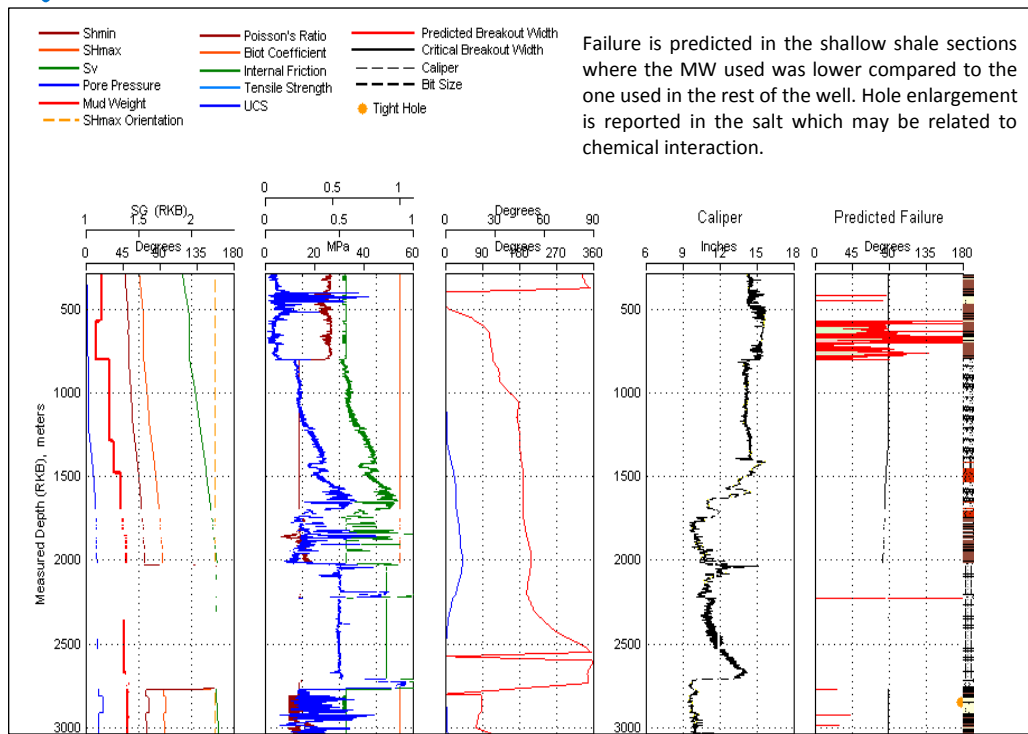


Figure 49. Calibration of the geomechanical model against drilling experience from the well ZPD-1

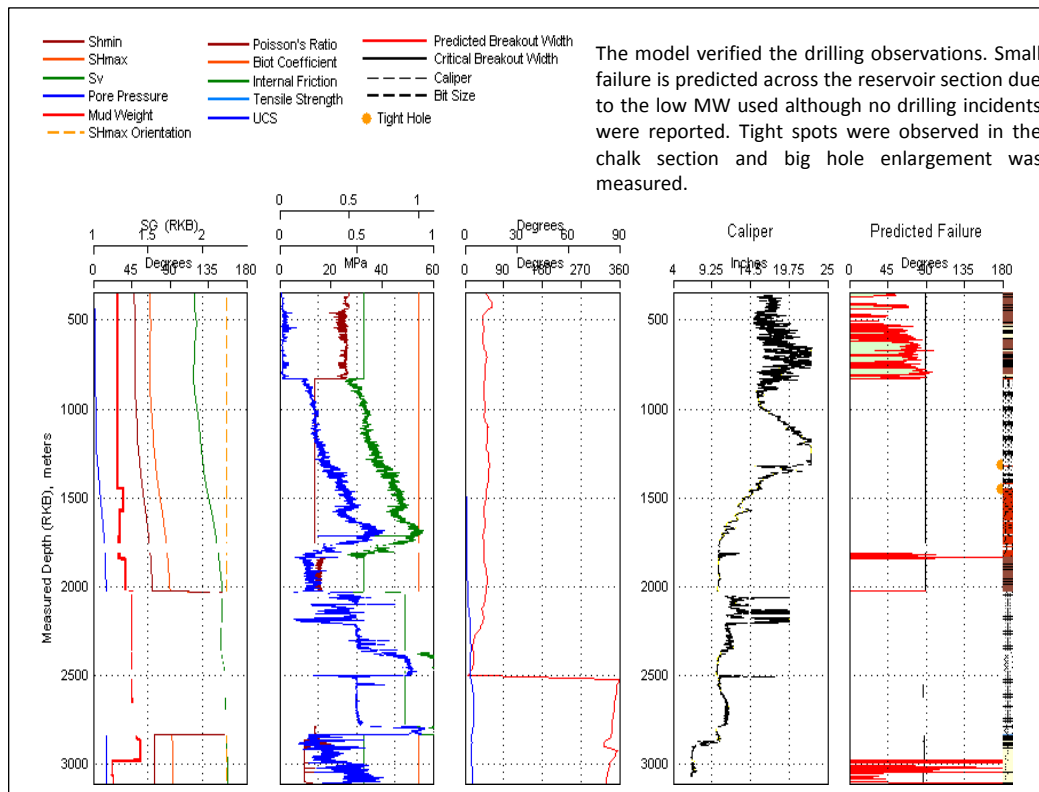


Figure 50. Calibration of the geomechanical model against drilling experience from the well ZRP-1

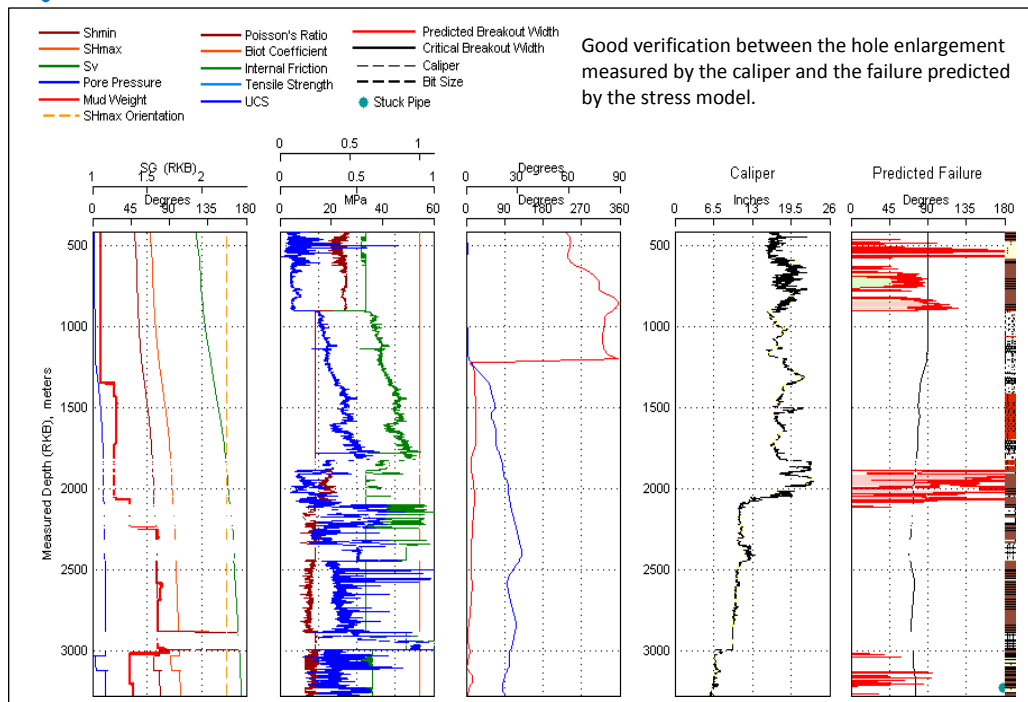


Figure 51. Calibration of the geomechanical model against drilling experience from the well ZRP-1

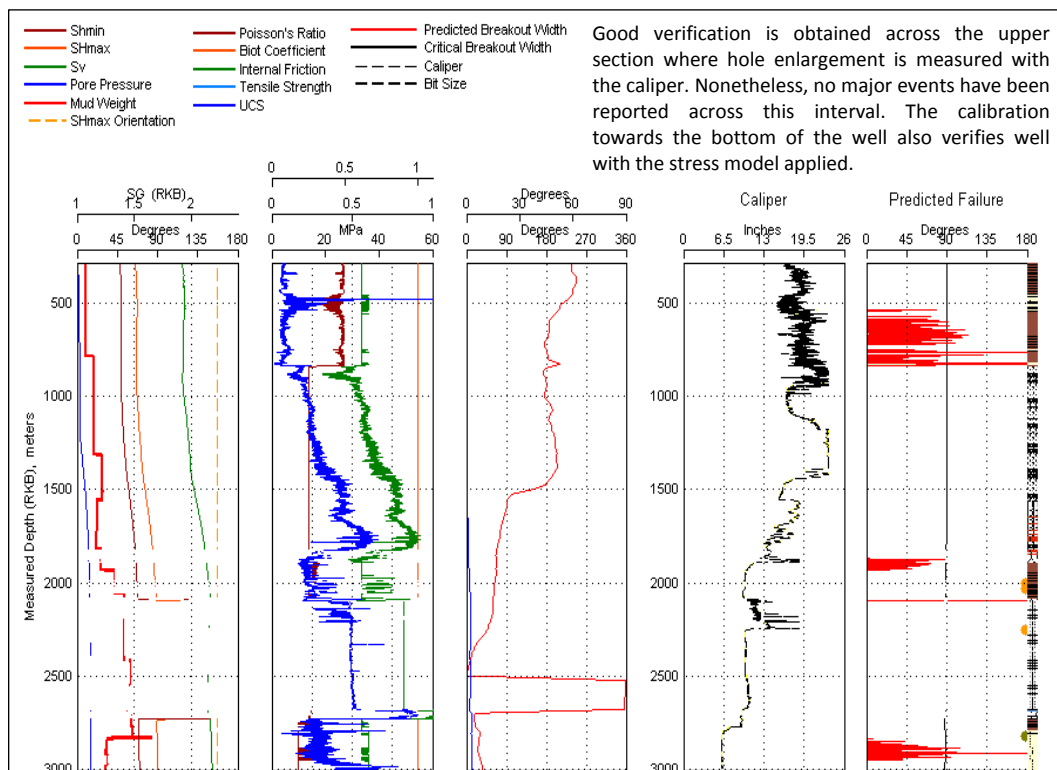


Figure 52. Calibration of the geomechanical model against drilling experience from the well ZND-1

Appendix 6 Drilling Summaries of the Offset Wells

As mentioned previously, Drilling experiences from offset wells provide key information for calibrating the geomechanical model. Reviewing daily drilling reports allows us to understand the drilling practices and their impact on wellbore instability.

In the analysis of drilling experience, information regarding actual mud weight used during drilling and associated drilling problems such as stuck pipe, tight hole, sloughing, pack-off, hole fill and mud losses, etc. is collected. These problems are summarized on plots of days versus depth. The summary helps in diagnosing the nature and causes of drilling problems.

The summaries of drilling experience from the remaining twelve offset wells are presented in this appendix:

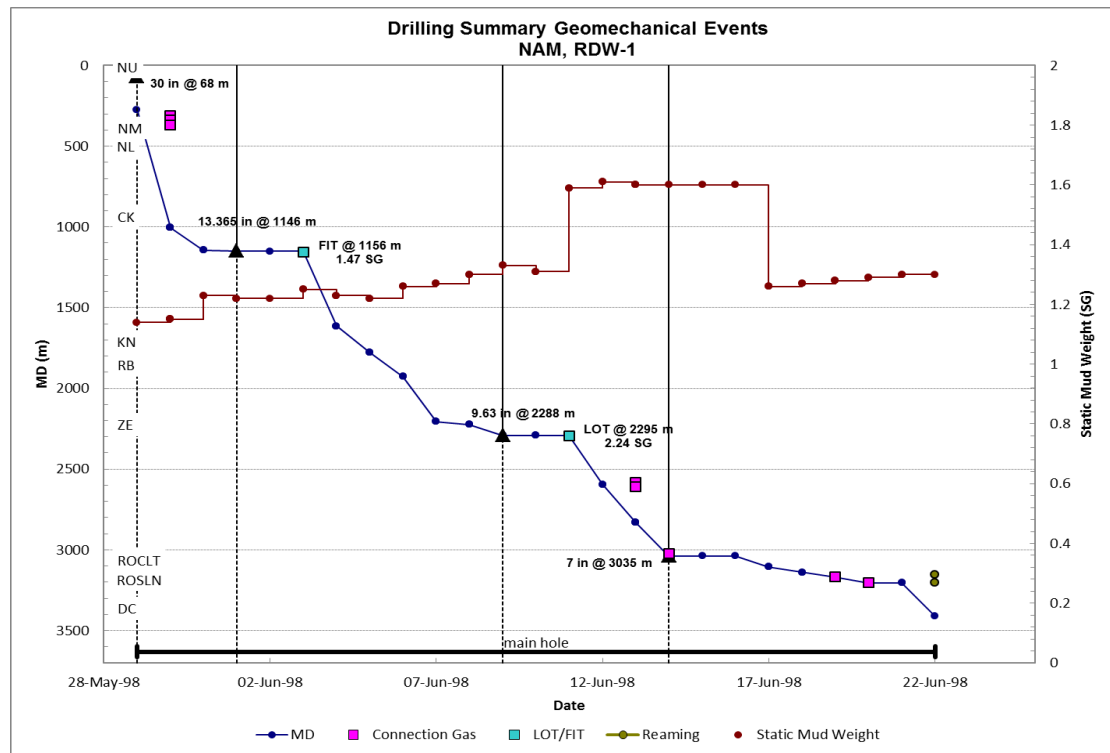


Figure 53. Drilling summary for the well RDW-1

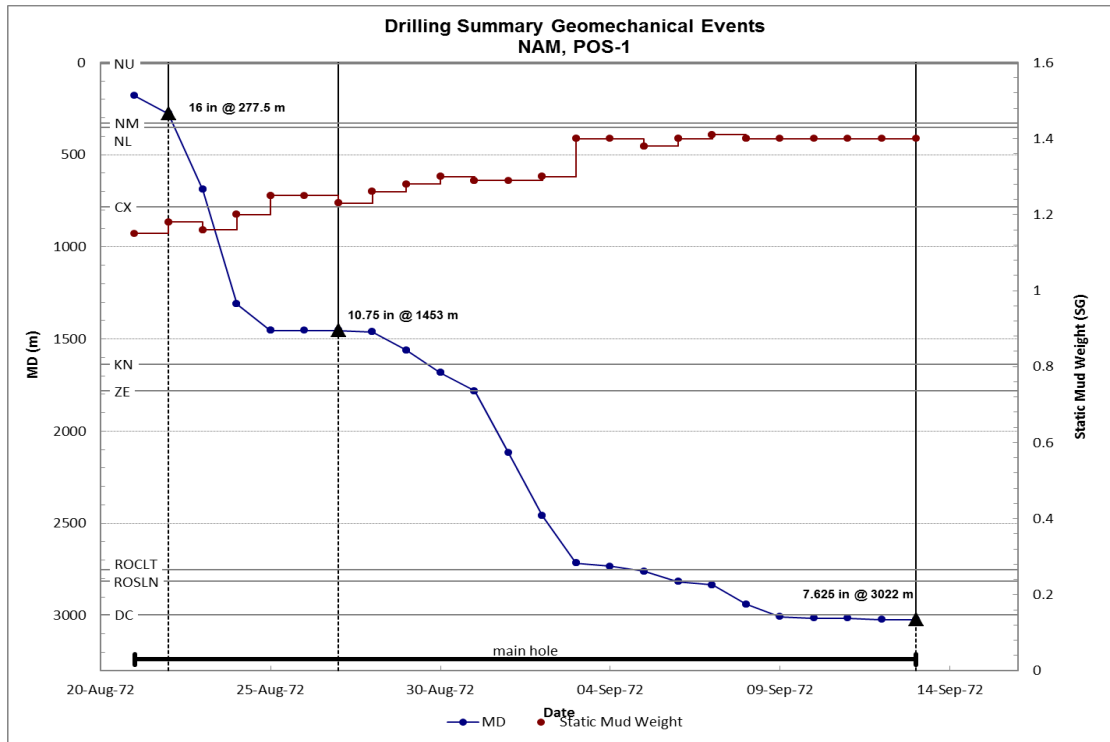


Figure 54. Drilling summary for the well POS-1

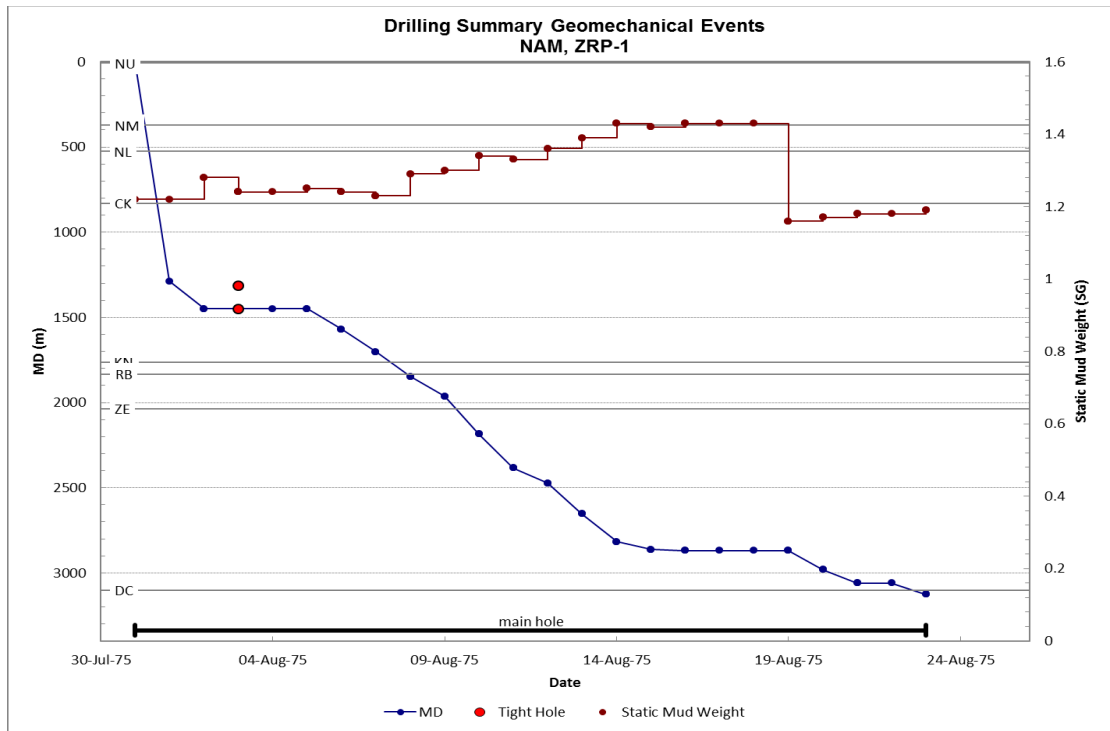


Figure 55. Drilling summary for the well ZRP-1

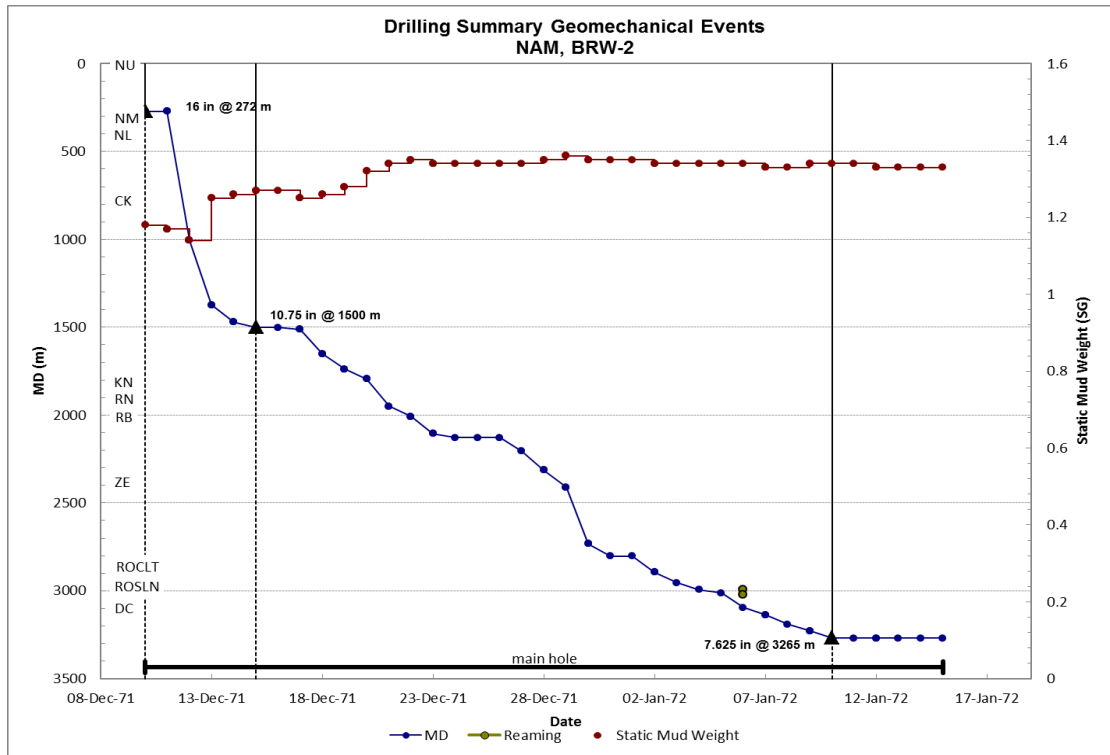


Figure 56. Drilling summary for the well BRW-2

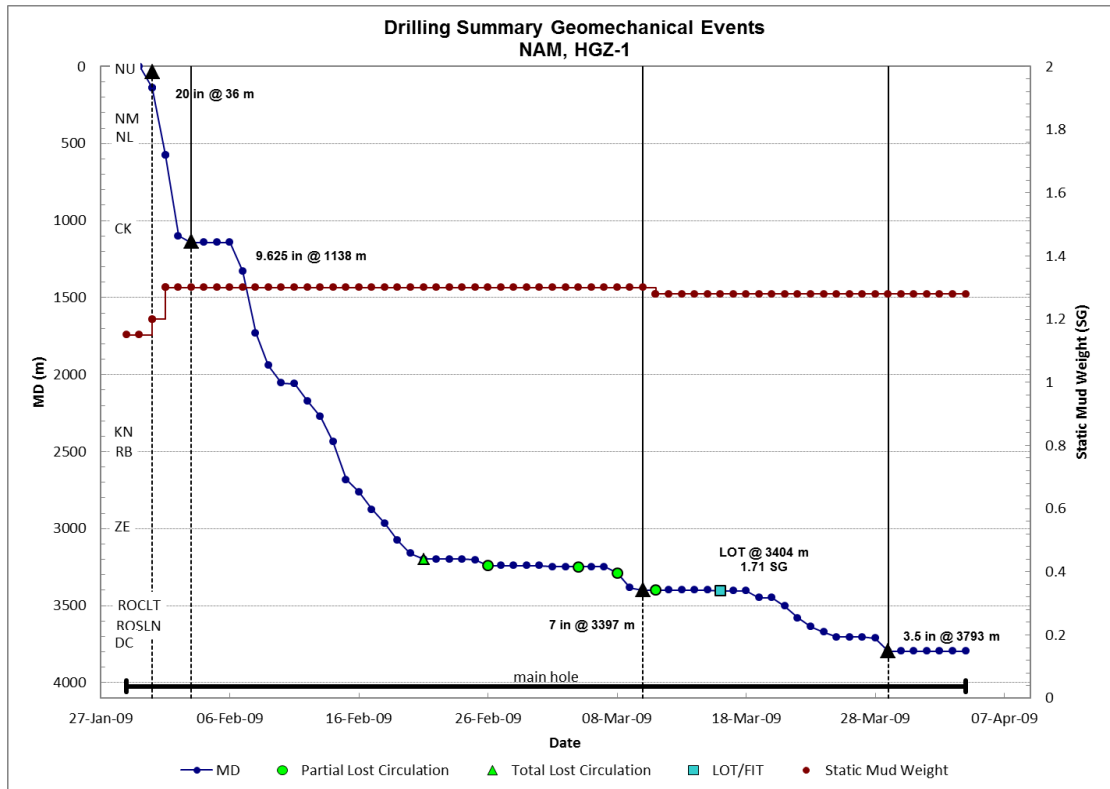


Figure 57. Drilling summary for the well HGZ-1

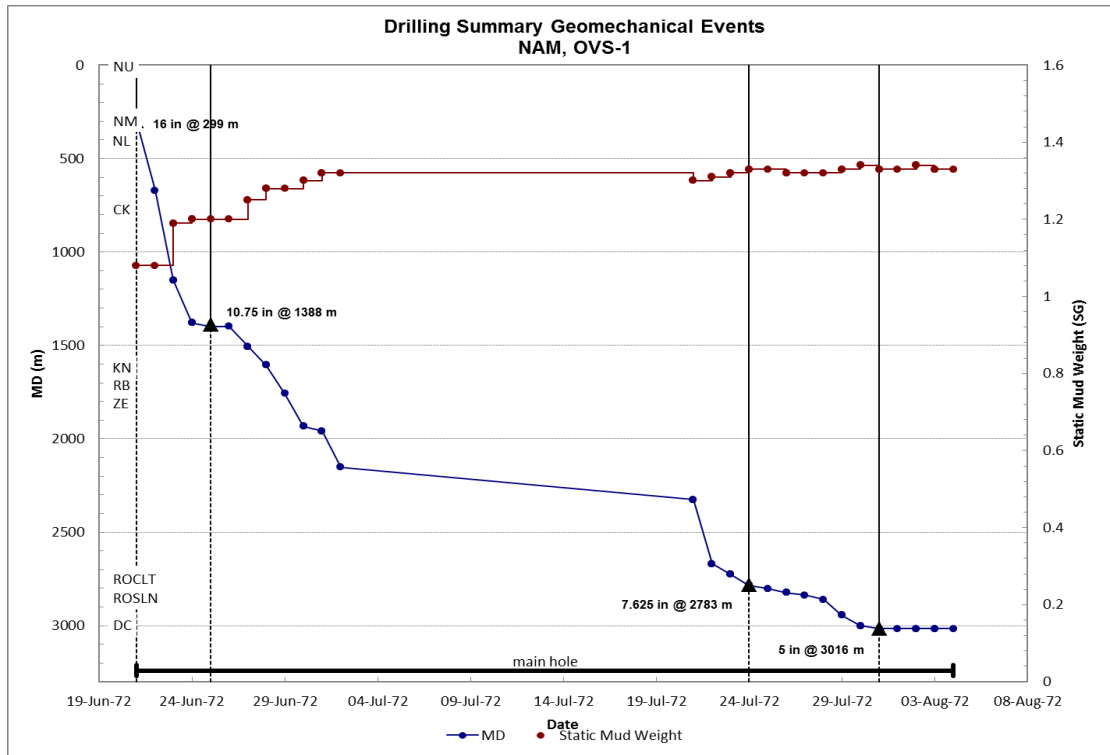


Figure 58. Drilling summary for the well OVS-1

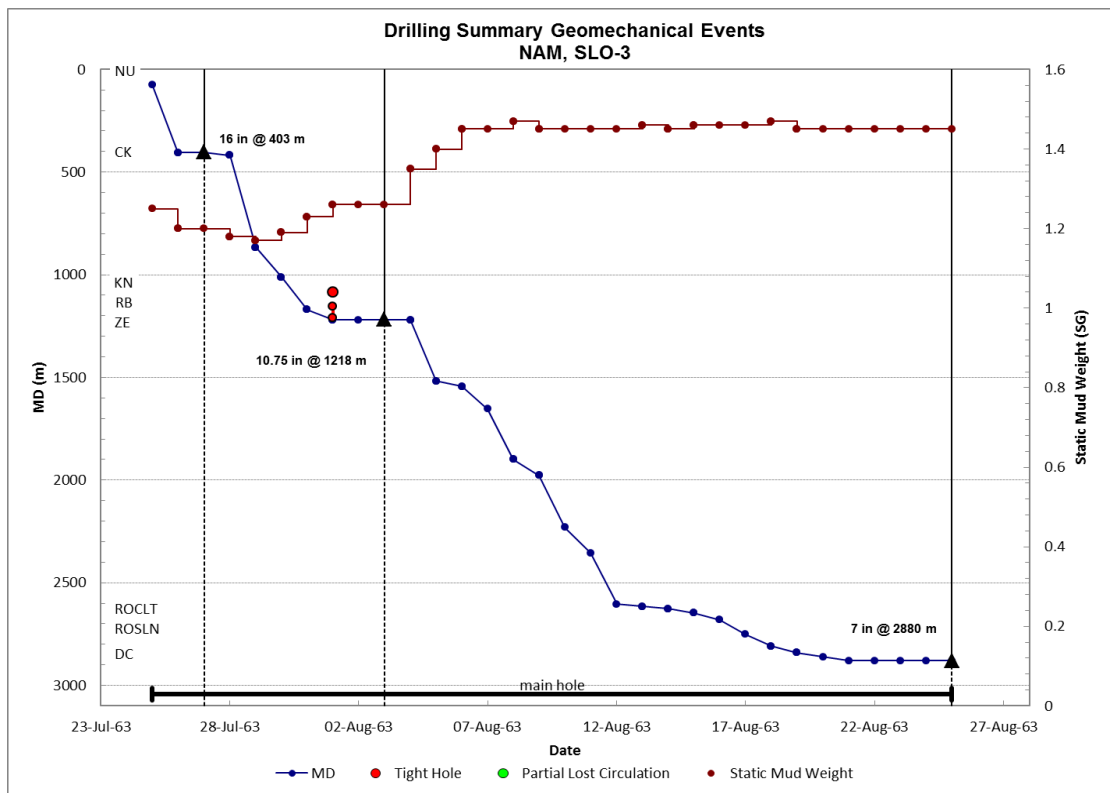


Figure 59. Drilling summary for the well SLO-3

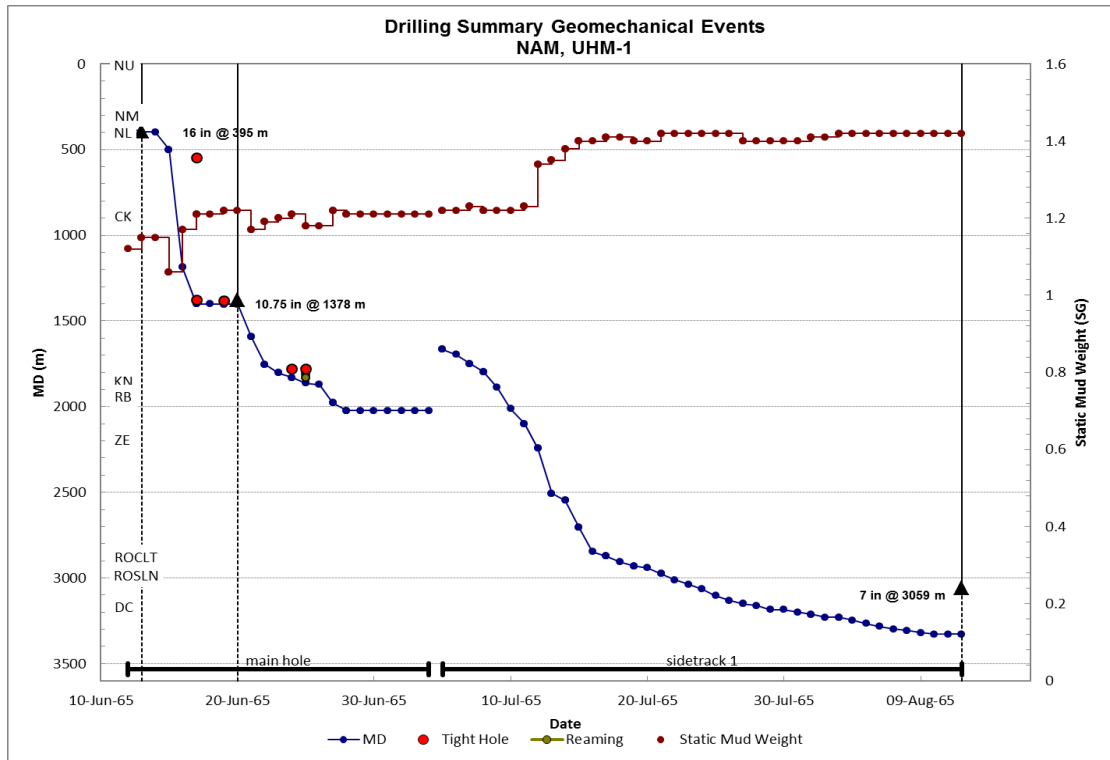


Figure 60. Drilling summary for the well UHM-1A

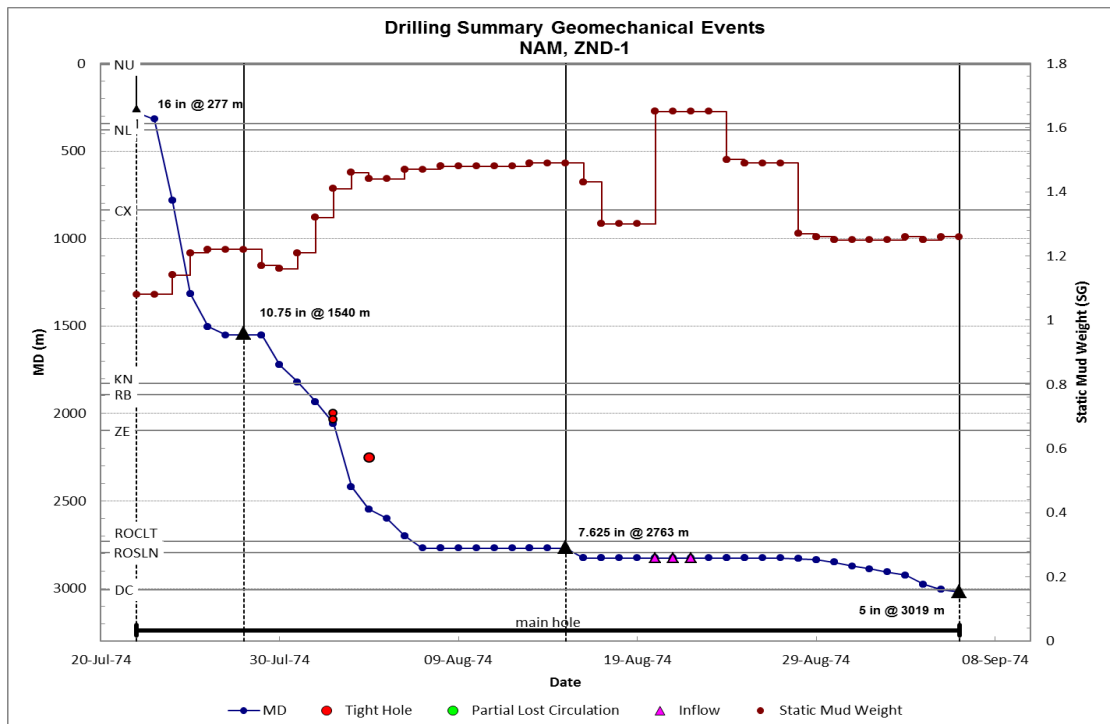


Figure 61. Drilling summary for the well ZND-1

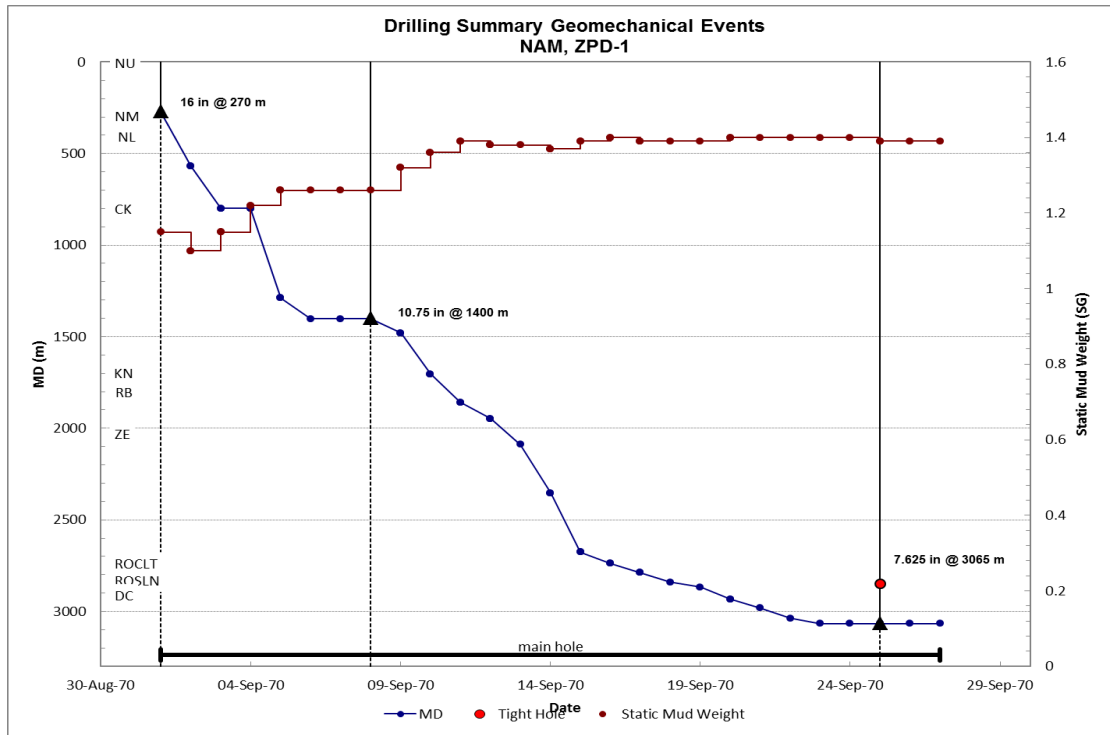


Figure 62. Drilling summary for the well ZPD-1

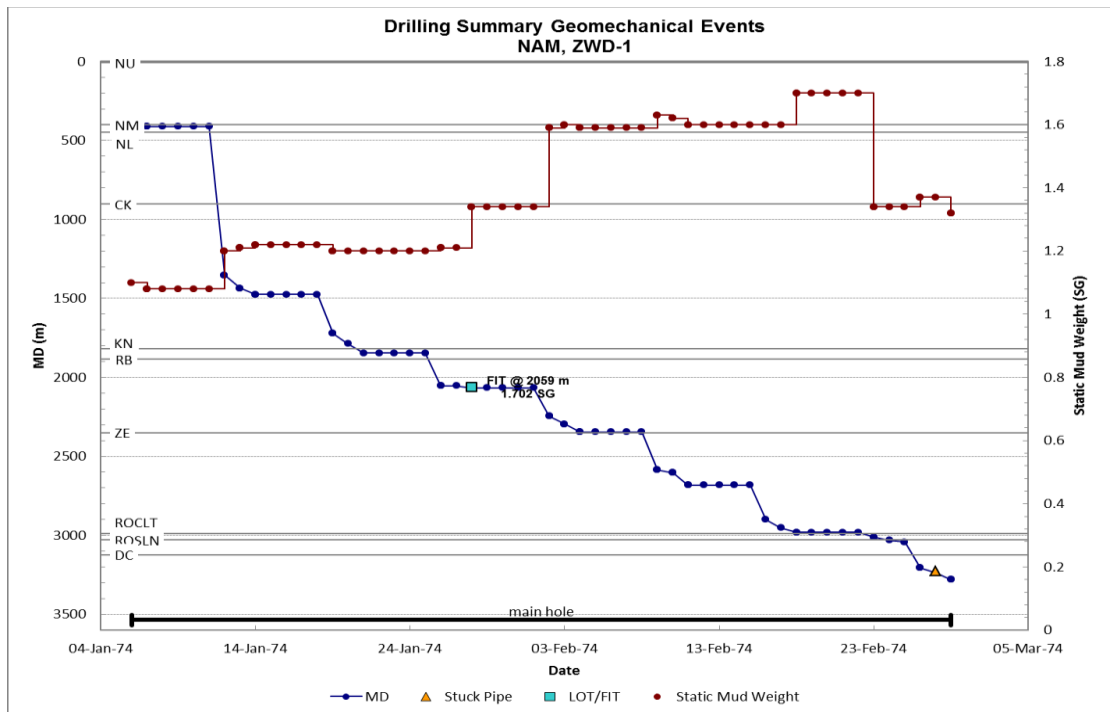


Figure 63. Drilling summary for the well ZWD-1

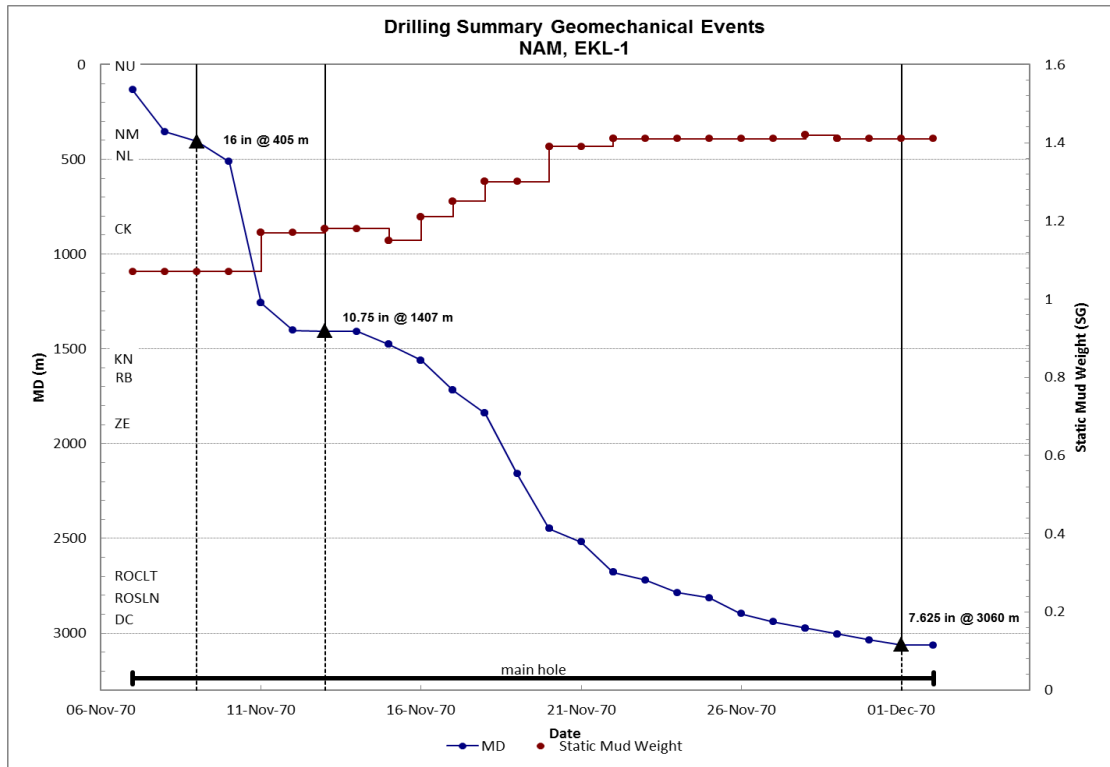


Figure 64. Drilling summary for the well EKL-1

Appendix 7 Available Data

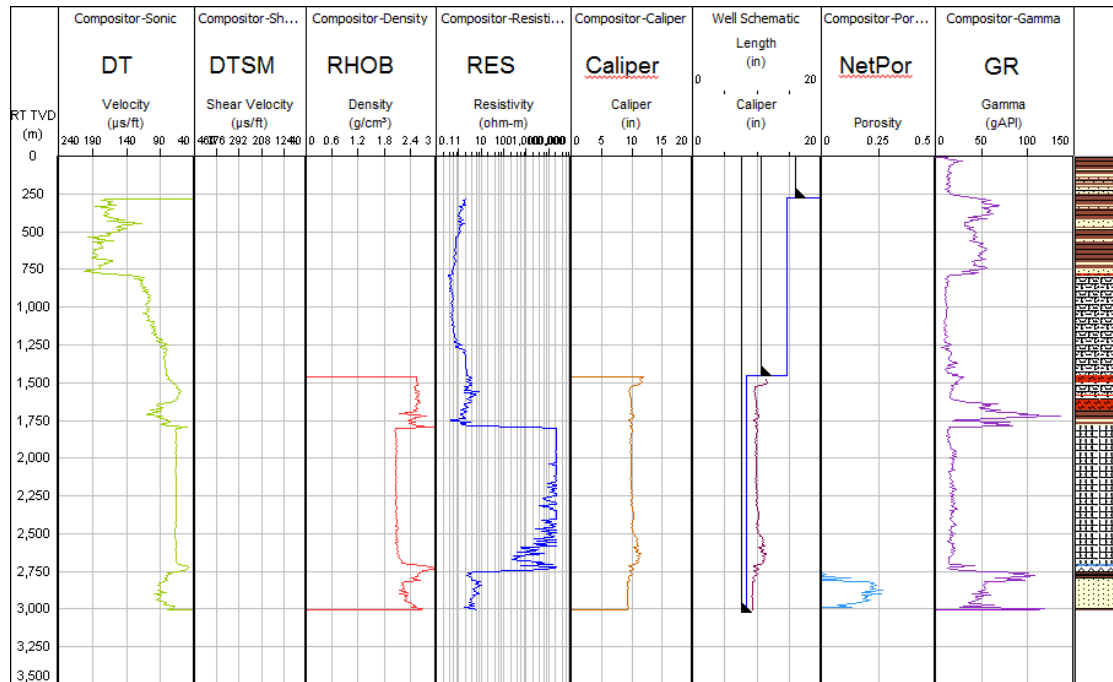


Figure 65. Available data for well POS-1

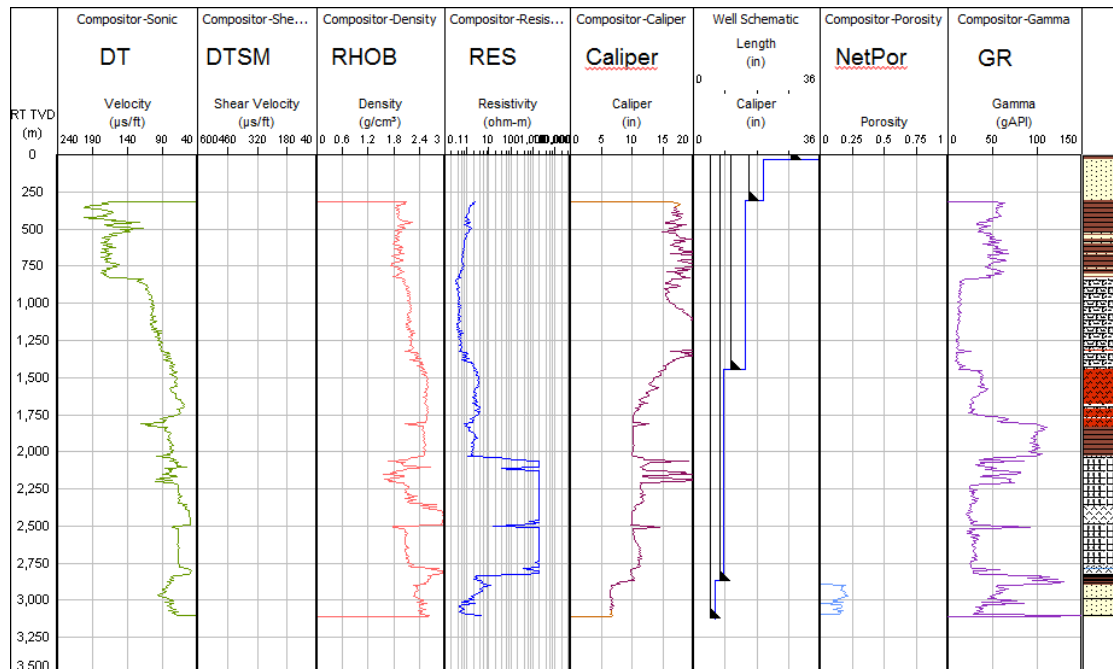


Figure 66. Available data for well ZRP-1

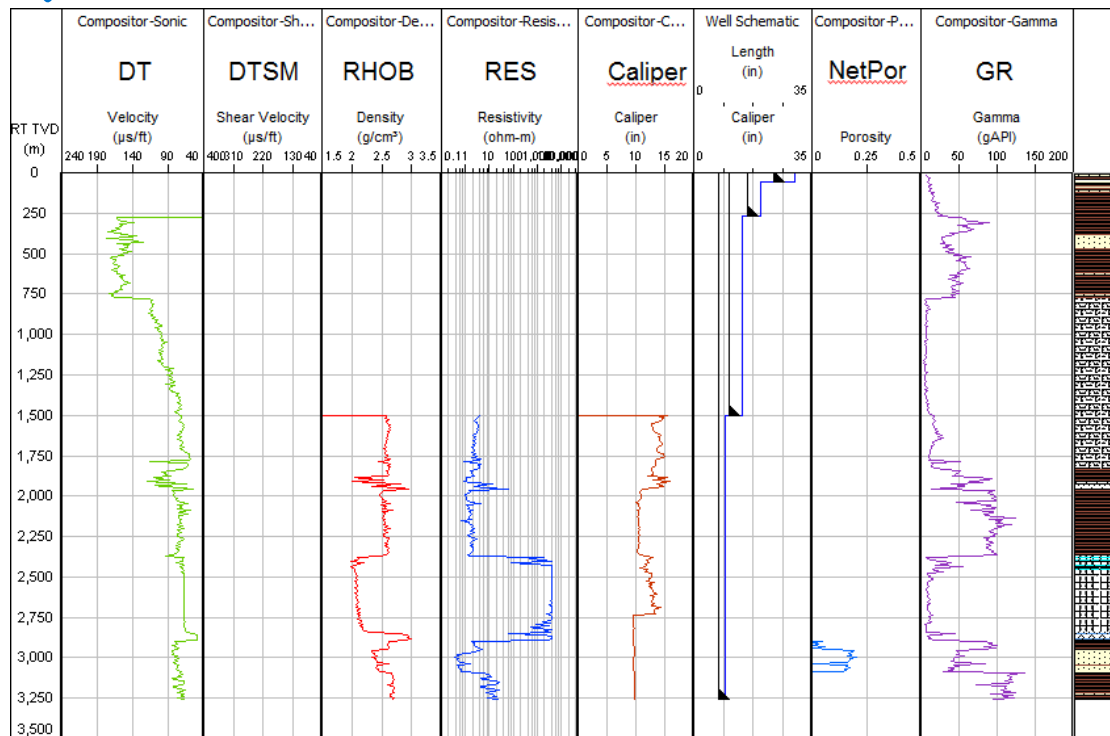


Figure 67. Available data for well BRW-2

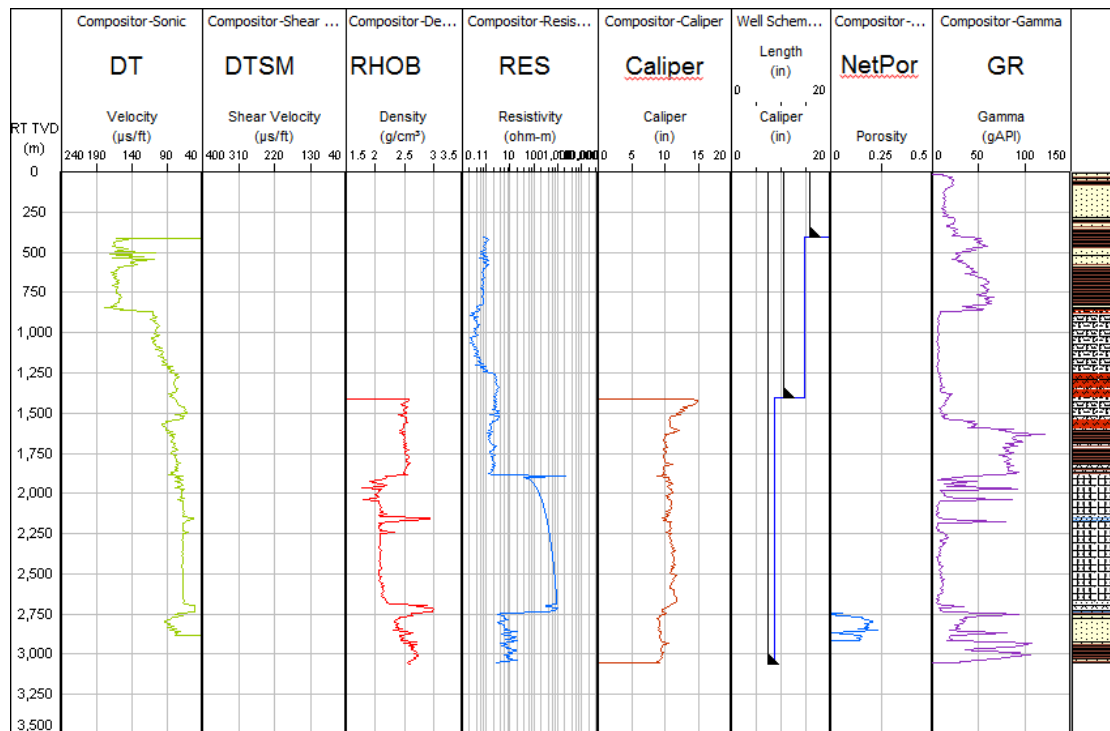


Figure 68. Available data for well EKL-1

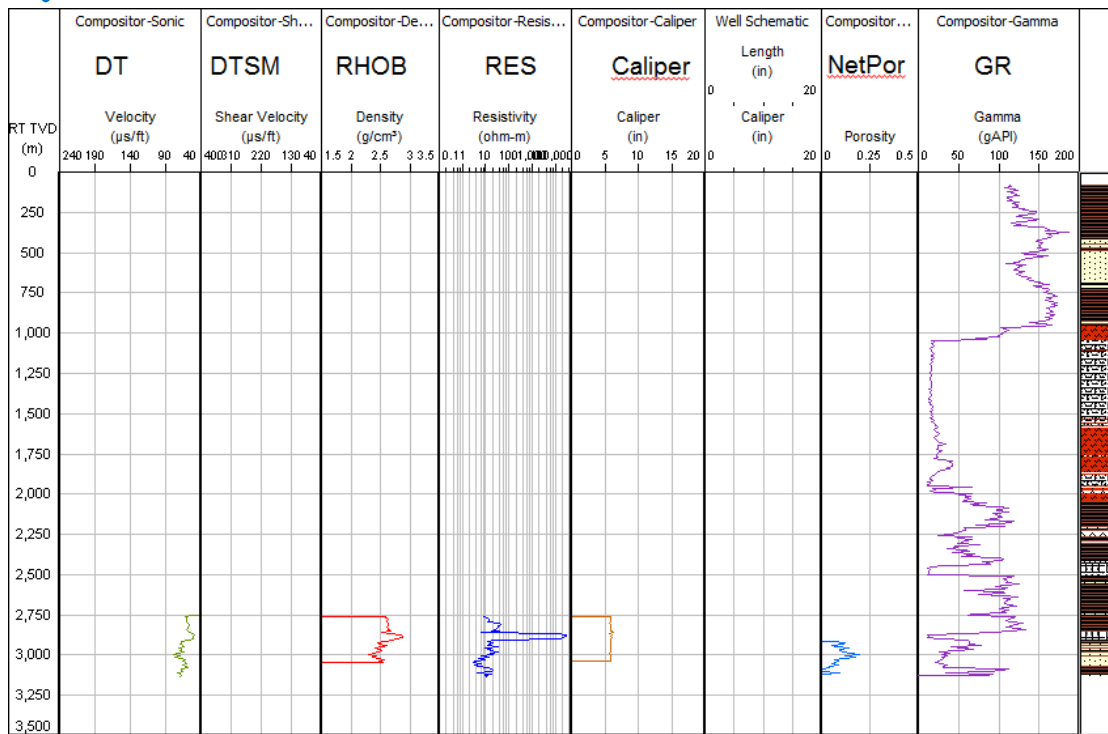


Figure 69. Available data for well HGZ-1

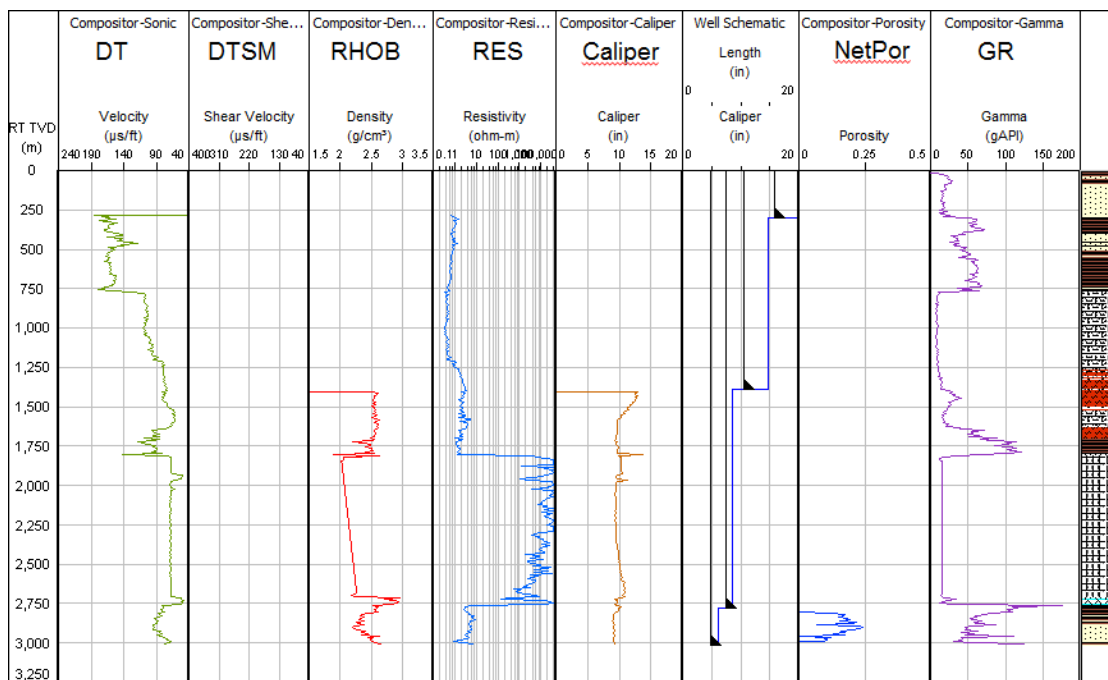


Figure 70. Available data for well OVS-1

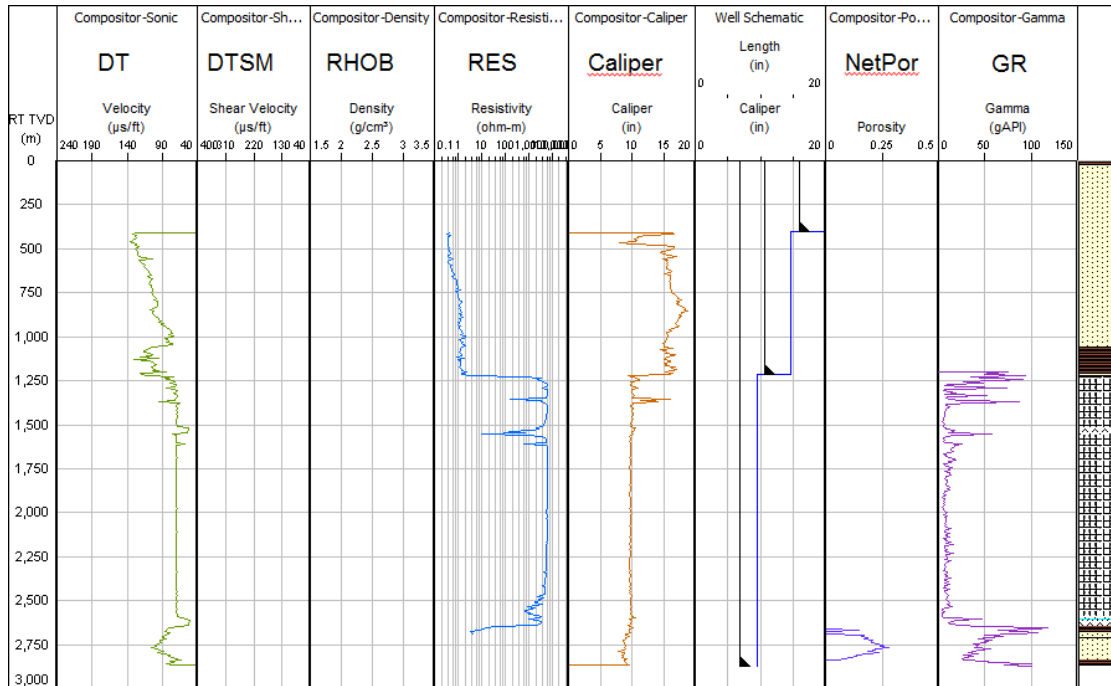


Figure 71. Available data for well SLO-3

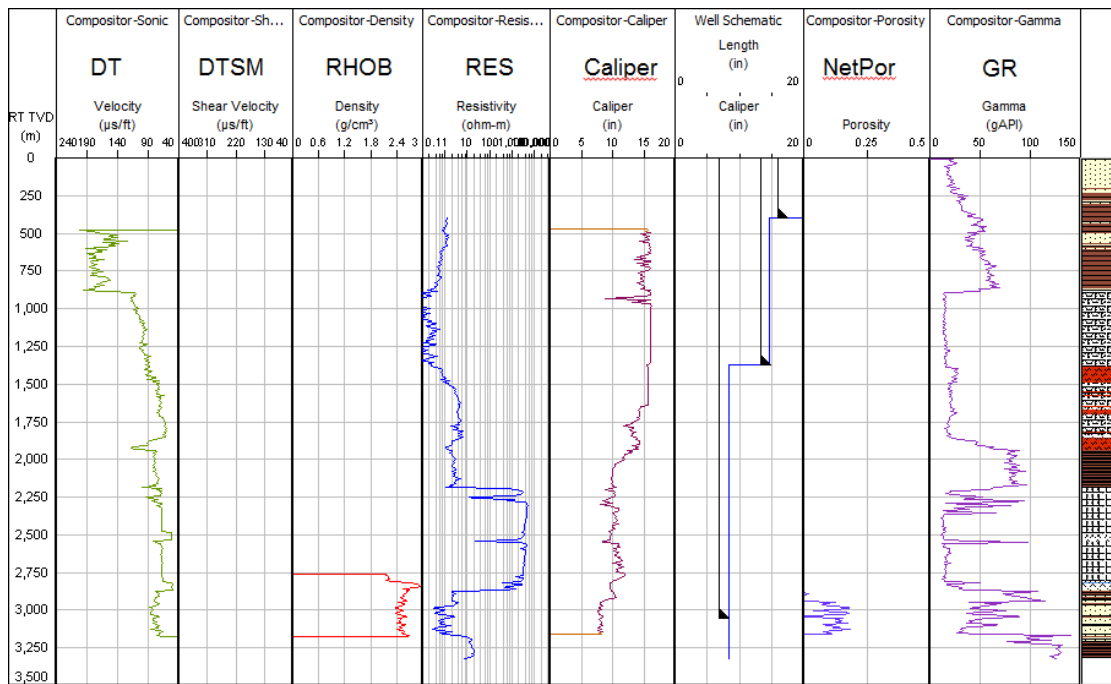


Figure 72. Available data for well UHM-1A

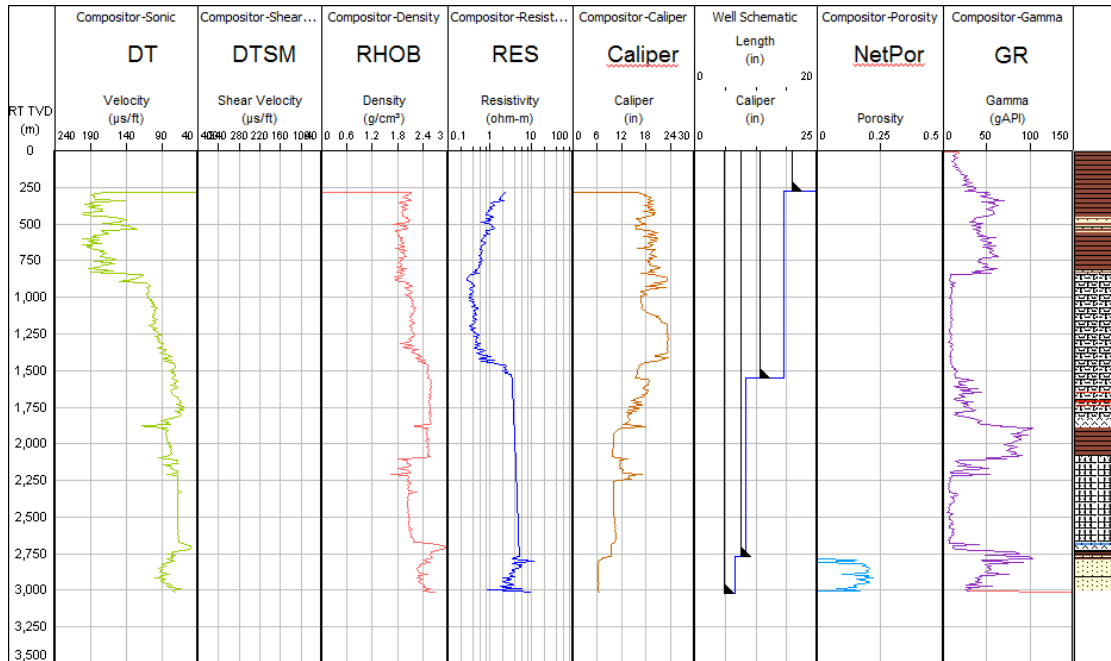


Figure 73. Available data for well ZND-1

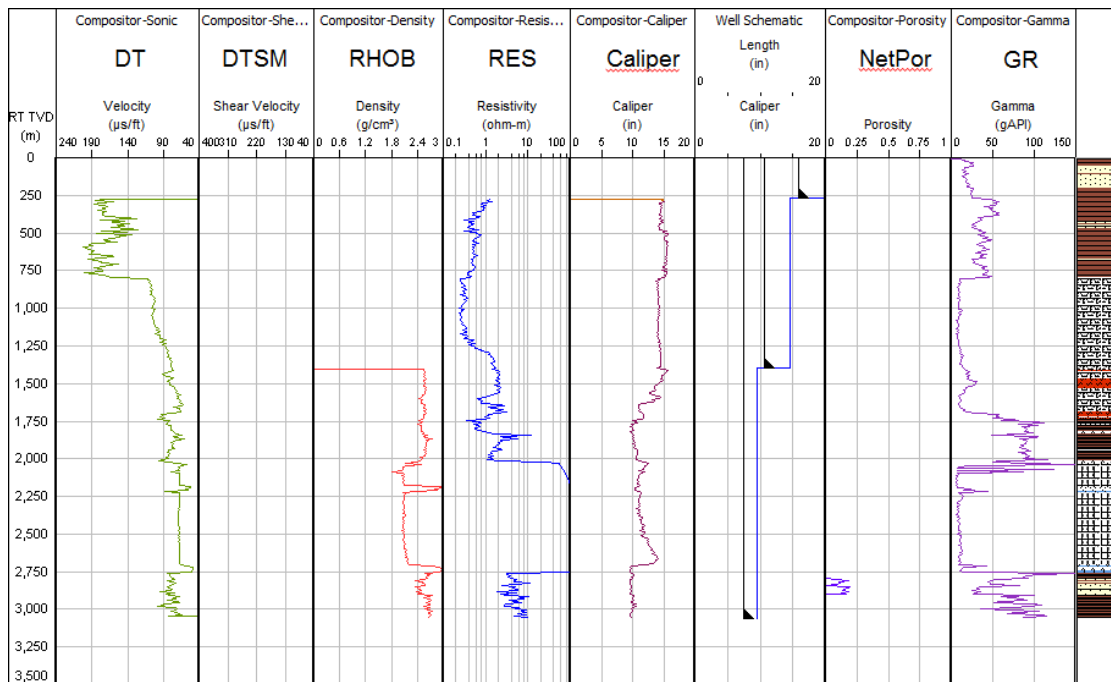


Figure 74. Available data for well ZPD-1

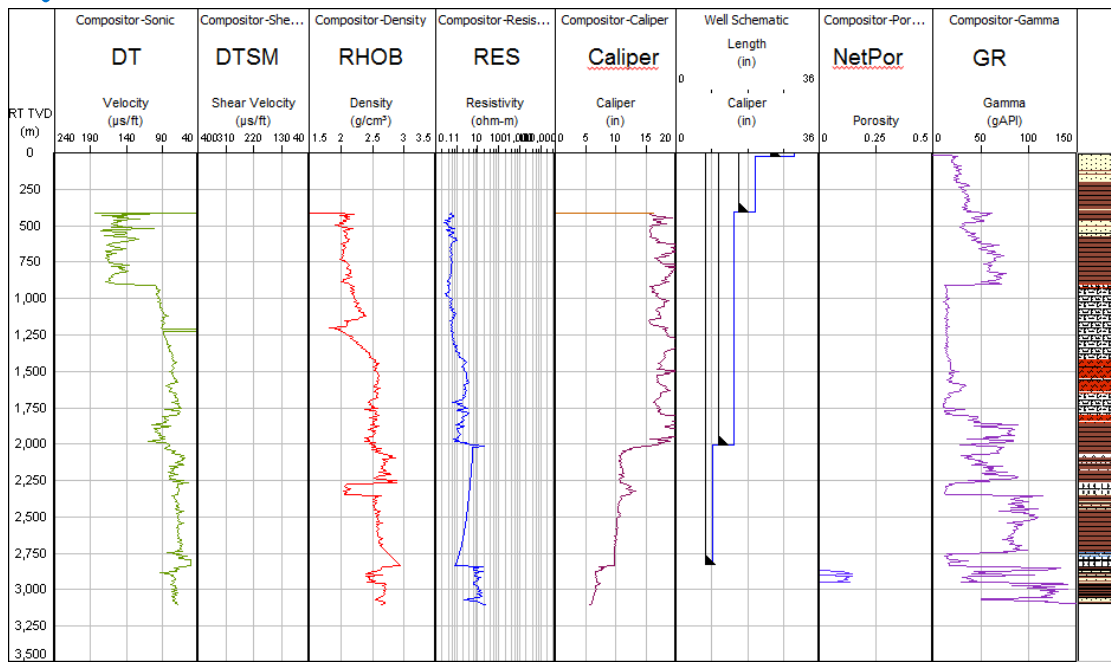


Figure 75. Available data for well ZWD-1



A Baker RDS Project for **NAM**

**Dynamic Geomechanical Modelling to
Assess and Minimize the Risk for Fault Slip
during Reservoir Depletion of the
Groningen Field – 3-D Geomechanical
Model**

NAM0001

Revision No. 2

June 2015

Document Approval & Distribution

For Baker RDS

Prepared by	Signature	Date
Romain Guises, Ph.D. – Senior Geomechanics Specialist		03/06/15
Jean-Michel Embry, M.Sc. – Senior Geomechanics Specialist		

Reviewed by

Colleen Barton, Ph.D. – Senior Technical Advisor		03/06/15
--	--	----------

Approved for Issue

Jackeline Rodrigues, M.Sc. – Geomechanics Team Leader, Europe-Africa.		05/06/15
--	--	----------

Report Distribution

Number of Copies	NAM Assen
1	Schepersmaat 2 P.O. Box 28000 9400 HH ASSEN The Netherlands

Disclaimer

No person other than the Client may directly or indirectly rely upon the contents of this report. This report reflects Baker RDS's informed professional judgments based on accepted standards of professional investigation, the data and information provided by the Client, the limited scope of engagement, and the time permitted to conduct the evaluation. However, this report does not in any way constitute or make a guarantee or prediction of results, and no warranty is implied or expressed that actual outcome will conform to the outcomes presented herein. Baker RDS does not warrant that the judgments or conclusions presented herein are error-free. Baker RDS has not independently verified any information provided by or at the direction of the Client. Baker RDS is acting in an advisory capacity only and disclaims all liability for actions or losses derived from any actual or purported reliance on this report (or any other statements or opinions of Baker RDS) by the Client or by any other person or entity. The opinions expressed herein are subject to and fully qualified by the generally accepted uncertainties associated with the interpretation of geoscience and engineering data and do not reflect the totality of circumstances, scenarios and information that could potentially affect decisions made by the report's recipients and/or actual results. Baker RDS disclaims any obligation to update this report or provide any follow-up support except as expressly provided in a written contract.

Objectives

On behalf of NAM Assen (NAM), Baker Hughes Reservoir Development Services, a division of Baker Hughes, proposes to build a three dimensional (3-D) geomechanical model with the purpose of conducting geomechanical simulations for the Groningen Field, onshore Netherlands. The main goal of this study is to understand the stress state prior to production and the stress evolution during the depletion of the Groningen Field. The stress evolution will be used to evaluate the production strategies and related pressure scenarios with respect to the potential seismic risk of slip on reservoir faults over the life of the field.

In order to fulfil the objective of this study, the following tasks have been completed:

1. Building a 1-D calibrated geomechanical models from a number of offset wells to provide a preliminary understanding and constraint of the present day stress field. A range of offset wells data (thirteen wells) collected during the different stages of field development will be selected based on their relevance and log coverage. The methodologies used for the 1-D modeling are fully described was presented in a separate report (**dynamic Geomechanical Modelling to Assess and Minimize the Risk for Fault Slip during Reservoir Depletion of the Groningen Field – 1D Geomechanical Model**).
2. Building a 3-D geomechanical model for the entire field. The 3-D model is based on the available data including (but not limited to) the 3-D structural and reservoir models of the area (i.e., MoRes and Petrel models), 1-D well specific geomechanical data such as overburden, pore pressure, fracture gradient, lithology data and also historic geomechanical studies, well test data (i.e. LOT, DST), core testing results and drilling reports which will be supplied by the Client (as available).
3. Perform 3-D finite element simulations for five (5) number of pressure scenarios and calculate changes and variations of in situ stress, strains, and displacements over time (i.e., with changing reservoir pressure) and assess related impact on fault reactivation (i.e., derive shear and normal stress on selected fault planes and how these change with depletion).
4. Utilize the results from (3) to simulate a number of field development scenarios in terms of pore pressure and depletion to assess how the risk of seismicity can be minimized.

Executive Summary

This report presents the results of a 3-D dynamic geomechanical modelling study. The study was carried out to fulfil the objectives as specified above. The results of the 3-D finite element analyses and the impact of stress variation on fault reactivation leading to possible seismicity can be summarized as follows:

- A 3-D Geomechanical model of Groningen was built based on thirteen (13) 1-D Geomechanical Models and a structure model composed by nine (9) horizons and twenty-one (21) faults.
- The 3-D geomechanical model is validated by comparing the field subsidence with the response obtained from the numerical analysis using history matched production models
- The analysis indicates that the field production increases the likelihood of seismicity. The number of faults reaching a critical stress state is expected to increase with depletion regardless of the considered depletion scenarios.

3-D geomechanical model

- Finite Element simulations of the response to depletion of the Groningen Field were performed by coupling five different reservoir models (2 history matched, and 3 forecast scenarios) with a finite element solver. The computed 3-D stress and strain fields were calibrated by comparing the vertical displacement calculated from the finite element analysis with the surface measurements of subsidence. The two history matched models (RM1 and RM2) showed reasonable agreement throughout the field (98.5% of the points have less than 10 cm of difference).
- The influence of salt creep during depletion was assessed prior to performing the fault slip analysis. It was shown that these effects were small in comparison to the poro-elastic effects characterising the depleted formations (3MPa vs. 20 MPa).
- The reservoir stress paths, indicative of the sensitivity of the horizontal stresses to variation in pore pressure, were determined based on the first 45 years of production. Although the stress path parameters could not be calibrated using field measurements, it is observed that $A_{SHmin} = A_{SHmax} \sim 0.6$ throughout the field based on the Poisson's ratio distribution.

Fault slip analysis

- The calibrated 3-D stress and strain field was used to assess the stability of the faults during the production of the field. The comparison between two different cases of fault failure properties indicate that the analysis show a better consistency with the recorded

seismic events when using a cohesion of 7 MPa and a sliding friction angle of 13° (sliding friction coefficient = 0.23).

- The first two reservoir models indicated that several faults (essentially those oriented NNE-SSW) became critically stressed during productions, indicating that the risk of fault slip increased. The Loppersum area, where the most intense seismicity has been recorded, concentrated a large number of critically stressed faults.
- The three other reservoir models (RM3, RM4 and RM5) allowed an evaluation of the tau ratio on each faults until 2080. The results indicated that few additional faults would move towards an unstable state for any of the three forecast models. This does not preclude the possible occurrence of seismic tremors in areas where faults are already critically stressed for a number of years in the future.
- Based on the geomechanical simulations and the fault slip analysis performed for this study, there is a likelihood to reactivate slip along existing fault planes. Each of the three (3) projections of the Groningen Field reservoir model indicates that some faults could further destabilize between 2016 and 2050.
- The present model does not consider a sensitivity analysis of the input parameters (rock mechanical properties, stress field, pore pressure). In addition, the stress reorganisation subsequent to a fault slip event (decrease in tangential stress) is not considered in this study. Therefore, the finite element simulations permit the determination of the stress applied on a fault before any slip occurs.

Contents

Document Approval & Distribution	iii
Disclaimer.....	v
Objectives.....	vi
Executive Summary	vii
Contents.....	9
List of Tables.....	11
List of Figures.....	12
1 Introduction	17
a. Work Flow Overview	17
1.1 Available Data.....	18
2 3-D Geomechanical Model	21
2.1 Representative volume of the field	22
2.2 Structural Model.....	23
2.3 Construction of the 3-D Finite Element mesh.....	26
2.3.1 Generation of the mesh based on the structural model	26
2.3.2 Material properties.....	28
Carboniferous layer	29
Salt creep behaviour in the Zechstein Layers	29
2.4 Property Modelling and Mapping.....	29
2.4.1 Rock properties	29
Young's modulus.....	32
Poisson's Ratio.....	33
Viscous properties of the Zechstein salt:	34
2.4.2 Pore Pressure.....	35
Overburden Pore pressure.....	35
Reservoir model	35
3 3-D Dynamic Geomechanical Modelling.....	39
3.1 Set up of the dynamic model	39
3.1.1 Initial in-situ stress state from the offset well analysis.....	39
3.1.2 Finite Element Simulations – Simulation Steps.....	41

Reservoir model 1 (RM1)	42
Reservoir model 3 (RM3) – Production forecast	44
3.2 3-D dynamic simulation results	45
3.2.1 Calibration of the geomechanical response based on the strain response	45
Influence of Salt Creep during production	48
3.2.2 Results of the stress response of the Groningen Field	52
3.3 Evolution of the principal stress magnitudes with depletion (stress paths)	55
4 Fault stability analysis	59
4.1 Principles	59
4.1.1 Tau ratio	61
4.1.2 Mohr representation of fault stability	61
4.2 Results	62
4.2.1 Comparison between the fault properties cases	64
4.2.2 Analysis (Case 2: $C_o = 7 \text{ MPa}$, $\mu_s = 13^\circ$ ($\mu=0.23$))	65
Reservoir model 1	66
Reservoir model 2	66
Forecast reservoir model 3	67
Reservoir model 4	68
Reservoir model 5	69
4.2.3 Analysis (Case 1: $C_o = 0 \text{ MPa}$, $\mu_s = 31^\circ$ ($\mu=0.6$))	69
4.2.4 Discussion	74
5 Model Uncertainties	78
5.1 1D Geomechanical Model	78
5.2 3-D Geomechanical Model	78
6 Summary & Conclusions	79
7 References	81
8 Nomenclature	82
Appendix 1 displacement element in the Carboniferous layers below the reservoir	83
Appendix 2 Assessment of the Effect of Salt Creep on the 3-D geomechanical model	85
Appendix 3 Upscaling data	87

List of Tables

Table 1. Summary of available data gathered, reviewed and analysed for the this study	20
Table 2. Selected faults and horizons for the 3-D structural model.....	25
Table 3. Number of elements per layer utilised to mesh the Groningen Field.....	28

List of Figures

Figure 1. Generic workflow for generating a consistent 3-D dynamic model (not from this study)	18
Figure 2. Location of the 13 offset wells (identified with a pink circle) in the Groningen Field, Netherland (courtesy of NAM)	21
Figure 3. View of the extension of the model to avoid computation boundary effects	22
Figure 4. (Top) Available horizons and faults used for the 3-D dynamic geomechanical modelling. (Bottom) Selected faults used for the 3-D dynamic modelling at the top Ten Boer formation.	24
Figure 5. Original 2D points set (Orange dots) of the Slochteren horizon and resulting coarsened tri-meshed horizon (red triangulated surface)	25
Figure 6. Detail of a cross section of the interpreted geological structure. The original horizons, obtained from 2D grids – Purple and orange coloured lines - were coarsened and adapted in order to reduce the size of the computational domain. The interpreted horizons – Blue and red coloured lines – were modified such that offsets and throws are observed along the M6 fault instead of strongly steepening the formation. Fine scale structural features located away from the geomechanical area were smoothed to diminish the size of the model.....	26
Figure 7. View of a watertight structural model (Slochteren horizon is grey, intersecting faults in blue).	27
Figure 8. Top) Overview of the 3-D meshed structure used for the finite element modelling. Bottom) Overview from the Ten Boer layer used for the finite element modelling before (left) and after (right) discretization and lateral extension.....	28
Figure 9. New FE-Mesh using poro-elastic elements (in blue) in the Ten Boer formation, the Slochteren formation and the shallow layers and visco-elastic elements (in grey) in the salt layer and the base carboniferous layer.	29
Figure 10. Comparison between the original properties (composite density log) and the resulting upscaled density log for the well BRW-2	31
Figure 11. Distribution of the density populated onto the mesh for the Slochteren Formation. The density mapping was performed by interpolation of well log data using an inverse distance weighting algorithm.	32
Figure 12. Porosity-Young’s modulus relationship based on data from the NAM internal report “Groningen Fault Stability Analysis” (Van Den Bogert et al., 2013)	33
Figure 13. Distribution of the Young’s Modulus on the finite element mesh for the Ten Boer formation (left) and the Slochteren formation (right). The Young’s modulus in the Slochteren reservoir is significantly lower ($E_{\text{slochteren}} \sim 10$ GPa) compared with the overlying non reservoir units ($E_{\text{slochteren}} \sim 40 - 90$ GPa). While the Young’s modulus was obtained from porosity values mapped in the	

reservoir grid, the Young's modulus was obtained from interpolated log data on the side of the structure.	33
Figure 14. Distribution of the Poisson's ratio at the top of the Ten Boer formation (left) and the Slochteren formation (right). The colour bar varies between 0.20 (red) to 0.30 (blue).	34
Figure 15. Comparison between the original properties (pore pressure in the figure) in the left and the results of the upscaling in the right for the well BRW-2. The higher pore pressure trend below 3000 meters TVDSS corresponds to the reservoir section.	36
Figure 16. Schematic of method used to map the reservoir pressure into the FE-Mesh	36
Figure 17. Example of the reservoir pore pressure history and forecast at the top of the Ten Boer reservoir for the years 1964, 2026 and 2080 after upscaling (snapshots from RM3). The blue-green patches visible correspond to shaley rock types with low permeability that are not undergoing any depletion.	37
Figure 18. Example of the reservoir pore pressure history and forecast at the top of the Slochteren reservoir for the years 1964, 2026 and 2080 after upscaling (snapshots from RM3). The red areas on the side of the reservoir are indicating cells with no pore pressures. For the simulations, the pore pressure allocated to these cells is obtained from interpolated pressures from the 1D model interpretation.	38
Figure 19. Decrease of the Von Mises stress during the relaxation of the salt through pressure solution creep. At the end of the salt creep modelling, which correspond to the date prior to the beginning of the field production, the salt exhibits very small differential stress (less than 10 kPa to compare with an overburden pressure close to 60 MPa in the Slochteren. Subsequently the stress state in the Zechstein formation, immediately above the reservoir unit is nearly isotropic. Note that the salt creep is largely influenced by the complex structure of the salt body.	40
Figure 20. Display of Von Mises stresses in the Zechstein salt layer after the 2nd tier set up of the initial in situ stress state. Most of the salt has less than 1 MPa differential stress (dark grey colour), which is in agreement with sub-grain size piezometer measurements on natural salt samples (Diggs & Urai, 1997).	41
Figure 21. Evolution of the pore pressure for the reservoir model RM1	43
Figure 22. Evolution of the pore pressure for the reservoir model RM3	44
Figure 23. Comparison between the initial principal stress magnitudes obtained from the 1D model (dotted lines) and the stress field exported along the trajectory based on the Finite Element calculations (solid lines). The data are based on the BRW-2 well location.	46
Figure 24. Difference between the subsidence measured in the Groningen Field location vs. the calculated subsidence based on the 2012 reservoir model RM1. The mismatch reaches a value of about 20 cm in the North West part of the field which is essentially due to the original reservoir model used to estimate the geomechanical response.	47

Figure 25. Difference between the subsidence measured in the Groningen Field location vs. the calculated subsidence based on the 2012 reservoir model RM2 in 2012. 98.5% of the modelled subsidence points have less than 10 cm difference with the measured data. 47

Figure 26. Contour map of the surface subsidence estimate in 2012 using the finite element analysis based on: (left) the reservoir model RM1 and (right) RM2. The scale reported on the contour lines is in meters, therefore the maximum amount of subsidence obtained by both reservoir models is between 35 and 40 cm..... 48

Figure 27. a) Localisation of the cross-section where the salt creep effects are investigated. b) Cross section view of the viscous layer (yellow) and the poro-elastic formations (red). The stress response during the visco-elastic response occurring subsequent to the first 48 years of reservoir production is investigated at two locations; Element 6930, located in the depleted reservoir along large offset faults so that the element is adjacent to the salt. Element 189,596 is located in the Slochteren reservoir, at some distance to faults. Figures c) and d) show the stress response of the three principal stress components during the viscous response. 49

Figure 28. left) pore pressure distribution in the Slochteren reservoir in 2012 based on the RM1 model. Middle) difference between the stress response (S_{hmin}) in 2012 with and without salt relaxation. Right) vertical displacement comparison. The faults incorporated in the model are marked in black colour. 50

Figure 29. Comparison of the stress response between the model without salt creep during production (case 1) and one with salt creep during production (case 2)..... 51

Figure 30. Position of the cross-section plan used for the two following figures on the Groningen Field 52

Figure 31. Cross Evolution of the minimum principal stress from 2014 to 2080 for the Reservoir Model 3 (RM3) 53

Figure 32. Cross Evolution of the medium principal stress from 2012 to 2080 for the Reservoir Model 3 (RM3) 54

Figure 33. Top view from the Slochteren of the S_{hmin} stress path parameter in the Groningen Field (Reservoir model scenarios 3). The stress path parameter shows little variation across the field, with a typical value close to 0.6. 56

Figure 34. Top view from the Slochteren of the S_{hmin} stress path parameter in the Groningen Field (Reservoir model scenarios 3). The stress path parameter shows little variation across the field, with a typical value close to 0.6, very similar to the minimum horizontal stress..... 56

Figure 35. Export of the Stress Path Parameters of both S_{hmin} (yellow) and S_{Hmax} (red) for the timesteps 2014 and 2080 (Reservoir Model 3) in well ELK-1 (left) and ZRP-1 (right) 57

Figure 36. Export of the stress differences between the 2014 and the initial time-steps (black) and between the 2080 and the initial time-steps (grey) for the vertical stress and the minimum horizontal stress..... 58

Figure 37. a) Figure showing the stress conditions on a patch of a fault in a normal 2-D coordinate system. b) Mohr diagram corresponding to the fault presented in a). (The grey zone shows the range of fault orientation that would be critically stressed under the presented state of stresses) 59

Figure 38. In situ stress measurements in relatively deep wells in crystalline rock (Zoback and Townend (2001)) 60

Figure 39. Tau ratio describes the fault slip potential by taking the ratio between the observed or calculated shear stress τ and the critical shear stress τ_{max} 61

Figure 40. Mohr representation of the normal and tangential stress applied on a fault patch caused by the variations in reservoir pressures (not from the analysis) 62

Figure 41. a) Tau ratio on the M_2 fault in 1964. b) Tau ratio in 2012 following 48 years of production without consideration of the viscous relaxation. c) Tau ratio in 2012 after 48 years of production and associated creep effects. d) The plots illustrate the variation of the shear to normal stress on the node 244 (indicated by a red star in a) b) and c)). The red symbol is utilized for the case inclusive of the salt creep effects during the production. The analysis shows that under the expected sliding friction and cohesion, the M_2 fault initially stable, moves towards an unstable state with increasing depletion. The critical state for this node is reached during the first 48 years of production using the reservoir model RM2..... 63

Figure 42. Comparison between the stability of the fault M2 - node 244 – (Figure 42) for the case 1 and case 2 during the production history of the reservoir. The fault properties assumed for case 2 (sliding friction=0.23; cohesion=7 MPa) to assess the fault stability suggests that the faults become critically stressed during the production (sometimes between 1990 and 1995), which is not the case when assuming the case 1 properties. 64

Figure 43. Location of the principal faults considered for the fault slip analysis. The colours indicates the stability conditions of the faults at the least stable point of the fault (critically stressed (red), in near critical condition (orange) or stable (green) in 1964 considering the fault stability parameters of case 2) 65

Figure 44. Comparison between the fault stability prior to field production and as of 2013. 66

Figure 45. Representative time-steps presenting the reactivation risk of the different modelled faults in the Groningen Field (from 1964 to 2013). Most of the faults striking east west have lower risk of reaching an unstable state compared to faults striking NNE-SSW. 66

Figure 46. Time evolution of the fault stability assessment (forecast model RM3). The black arrows indicates locations where a fault passes into a less stable state 67

Figure 47. Time evolution of the fault stability assessment (forecast model RM4). The black arrows indicates locations where a fault passes into a less stable state 68

Figure 48. Time evolution of the fault stability assessment (forecast model RM5). The black arrows indicates locations where a fault passes into a less stable state 69

Figure 49. Representative time-steps presenting the reactivation risk of the different modelled faults in the Groningen Field (from 1964 to 2013) using case 1’s parameters. The black arrow indicates location where a fault passes into a less stable state..... 70

Figure 50. Time evolution of the fault stability assessment (forecast model RM3) using case 1’s parameters. The black arrows indicate locations where a fault passes into a less stable state. .. 71

Figure 51. Time evolution of the fault stability assessment (forecast model RM4) using case 1’s parameters. The black arrows indicate locations where a fault passes into a less stable state. .. 72

Figure 52. Time evolution of the fault stability assessment (forecast model RM5) using case 1’s parameters. The black arrows indicate locations where a fault passes into a less stable state. .. 73

Figure 53. Superposition of the faults included in the model, ranged by critical state using the case 2 failure properties, with the map of the recorded seismic events (1991 – 2010 period) sorted by magnitude. Initial (1964) fault stability state (top) vs. 2012 fault stability assessment (bottom).... 75

Figure 54. Evolution of the tau ratio on each fault during the production of the Groningen Field. The analysis was performed using the fault characteristics from case 2 ($\mu=0.23$ and cohesion = 7 MPa). The results show that most faults are initially in a stable configuration (tau ratio <1) but become critically stressed after years of production. Critically stressed faults starts to appear around 1985, and their numbers increase with time. In 2012, about half of the faults are unstable. 76

Figure 55. Evolution of the normal stress and the shear stress on the node 244 of the fault M_2 (location visible on the Figure 42) (left). Evolution of the shear to normal stress at this location of the M_2 fault. 76

Figure 56. Cross section of the pore pressure in a modelled FE-Mesh using porous elements 83

Figure 57. Cross section of the pore pressure in the modelled FE-Mesh using non-porous elements in the Zechstein and the carboniferous layers 84

Figure 58. Overview of the principal stresses for the two models (with salt creep and without salt creep). 85

Figure 59. Overview of subsidence for the two models (with salt creep and without salt creep). 86

Figure 60. Mapping log data into a 3-D grid without upscaling 87

Figure 61. Mapping log data into a 3-D grid with upscale processing 88

1 Introduction

An understanding of the virgin in situ stress state was obtained in an earlier phase of the project. Thirteen separate offset wells, located in various locations across the Groningen Field, were analysed and a set of well centric (1 dimensional) models were obtained. Based on this detailed knowledge of the stress field, pore pressure and rock mechanical properties, a three dimensional model will be constructed in order to assess and understand the origin of the seismicity recorded in the Loppersum area. To evaluate the evolution of the stress state and the associated seismic risks throughout the life of the Groningen Field, the geomechanical response was determined by performing numerical simulations (Finite Element analysis) coupled with different histories of reservoir pressures.

a. Work Flow Overview

The workflow for this project can be divided into four (4) main tasks (see **Figure 1**):

1. Building a calibrated 1-D geomechanical model from thirteen offset wells to provide a preliminary understanding and constraint of the present day stress field.
2. Building a 3-D geomechanical model for the entire field. The 3-D model is based on the available data including (but not limited to) the 3-D structural and reservoir models of the area (i.e., MoRes and Petrel models), 1-D well specific geomechanical data such as overburden, pore pressure, fracture gradient, lithology data and also historic geomechanical studies, well test data (i.e. LOT, DST), core testing results and drilling reports which will be supplied by the Client (as available).
3. Perform 3-D finite element simulations and calculate changes and variations of in-situ stresses, strains, and displacements over time (i.e. with changing pore pressure).
4. Assess the impact of the stress field response on the fault stability (i.e. derive shear and normal stress on selected fault planes and how these change with depletion).

The dynamic response of the field is estimated using a one way coupled type of model, meaning that the pore pressure available from the reservoir model at different time-steps is used to estimate the geomechanical response, i.e. stress and strain field. However, the variation of volume of the reservoir caused by the poro-elastic response of the field is not sent back to the reservoir model with an updated permeability tensor.

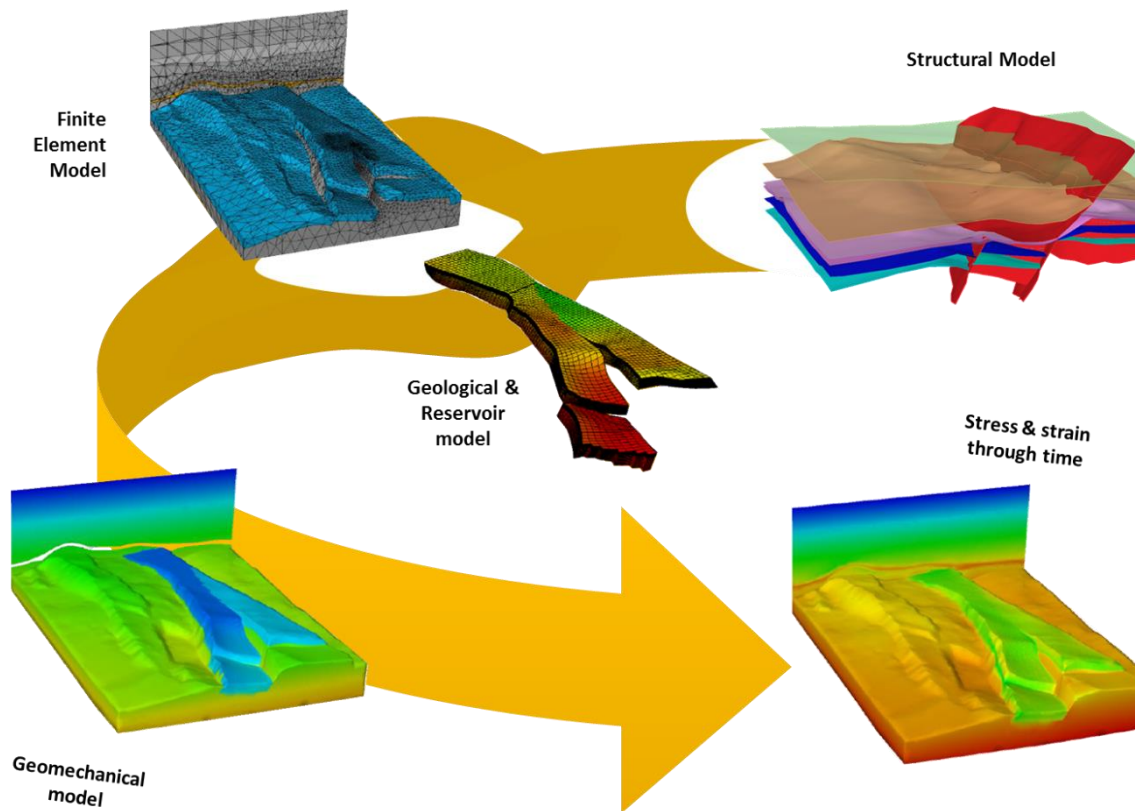


Figure 1. Generic workflow for generating a consistent 3-D dynamic model (not from this study)

1.1 Available Data

The accuracy of every 3-D geomechanical model lies in the availability and detailed generation of 1-D geomechanical models constructed from best quality available offset well data. Wells typically hold a multitude of partly high-resolution data sets including wire-line logs, well tests and in many cases rock strength measurements obtained from core plugs, which are then combined with the drilling experience for calibration, to build 1-D geomechanical models.

The main results of a 1-D well centric geomechanical model are the three in situ principal stresses which are typically the vertical stress (S_v), the maximum horizontal stress (S_{Hmax}) and the minimum horizontal stress (S_{Hmin}) along with their orientations. Furthermore, the pore pressure and the rock mechanical properties (such as compressive strength (UCS), internal friction (μ), Poisson's ratio (ν) and Young's modulus (E)) are also part of the geomechanical model. Single point data such as these are used to calibrate the continuous log-derived rock properties along the entire well trajectory as a function of depth (both MD and TVD).

Applications of 1-D geomechanical models are very diverse and include wellbore stability analysis; the determination of fracture gradients; planning of drilling mud programmes to avoid wellbore collapse and also providing the geomechanical framework for 3-D models. These models are constructed using the key assumption that the vertical stress is also a principle component of the stress tensor. Under certain

circumstances, such as depleted reservoirs or in the proximity of salt formations, this assumption is no longer valid and a field scale (three dimensional) assessment of the stress state has to be performed.

The available data for this project are summarized as below:

- Thirteen offset wells (**Table 1**) selected in agreement with NAM with full sets of processed and interpreted logs (electric, acoustic and wireline logs). The input well data were limited and did not permit a full validation of the pre-production in-situ stress field. These uncertainties are not considered for the time dependent modelling of the field response.
- Image log data from two wells, KWR-1A and RDW-1, located outside the Groningen area but next to the limits of the field. The analyses of the wellbore failures identified from the images provided the orientation of the stresses in the area.
- Additionally, formation pressure measurements, LOT data and rock mechanical properties such as UCS, TWC, Young's Modulus and Poisson's ratio were also provided and used to constrain the geomechanical model.
- Various documents such as daily drilling reports (DDR), final well reports (FWR) and previous analytical reports were collected and reviewed.
- Interpreted horizons and polylines defining the geometry of the faults used as input for the structural modelling.
- Five (5) reservoir models; two that are history matched and 3 forecast scenarios.

Table 1. Summary of available data gathered, reviewed and analysed for the this study

Well name	Log Data/ TD	Image Files	LOTs/ Minifrac	Daily Drilling Reports/ Final Well Report	Formation Tops	Pore Pressure (MDT/RFT)	Mud Weights	Rock Tests
BRW-2	Wireline logs, TD: 3270m MDRT	N/A	N/A	Available	Available	Available	Available	N/A
EKL-1	Wireline logs, TD: 2885m MDRT	N/A	N/A	Available	Available	N/A	Available	N/A
HGZ-1	Wireline logs reservoir. TD:	N/A	Available	Available	Available	Available	Available	N/A
KWR-1A	Wireline logs, TD: 3490m MDRT	Available	Available	Available	Available	Available	Available	N/A
OVS-1	Wireline logs, TD: 3013m MDRT	N/A	N/A	Available	Available	Available	Available	N/A
POS-1	Wireline logs, TD: 3004m MDRT	N/A	N/A	Available	Available	Available	Available	N/A
RWD-1	Wireline logs, TD: 3400m MDRT	Available	Available	Available	Available	Available	Available	N/A
SLO-3	Wireline logs (no density), TD:	N/A	N/A	Available	Available	N/A	Available	N/A
UHM-1A	Wireline logs (RHOB res), TD: 3183m MDRT	N/A	N/A	Available	Available	N/A	Available	N/A
ZND-1	Wireline logs, TD: 3017m MDRT	N/A	N/A	Available	Available	Available	Available	N/A
ZPD-1	Wireline logs, TD: 3065m MDRT	N/A	N/A	Available	Available	Available	Available	N/A
ZRP-1	Wireline logs, TD: 3112m MDRT	N/A	N/A	Available	Available	Available	Available	N/A
ZWD-1	Wireline logs, TD: 3277m MDRT	N/A	N/A	Available	Available	Available	Available	N/A

2 3-D Geomechanical Model

The input data for the three dimensional geomechanical model of the Groningen Field is based on the 1-D geomechanical models obtained from the following thirteen offset wells:

- | | |
|------------------------|--------------------------|
| Borgsweer (BRW-2) | Slochteren (SLO-3) |
| Eemskanaal (EKL-1) | Uithuizermeeden (UHM-1A) |
| Hoogezand (HGZ-1) | T Zand (ZND-1) |
| Kielwindeweer (KWR-1A) | Zuiderpolder (ZPD-1) |
| Overschild (OVS-1) | Zeerijp (ZRP-1) |
| Ten Post (POS-1) | Zuidwending (ZWD-1) |
| Rodewolt (RDW-1) | |

Figure 2 shows the locations of the wells within the field.

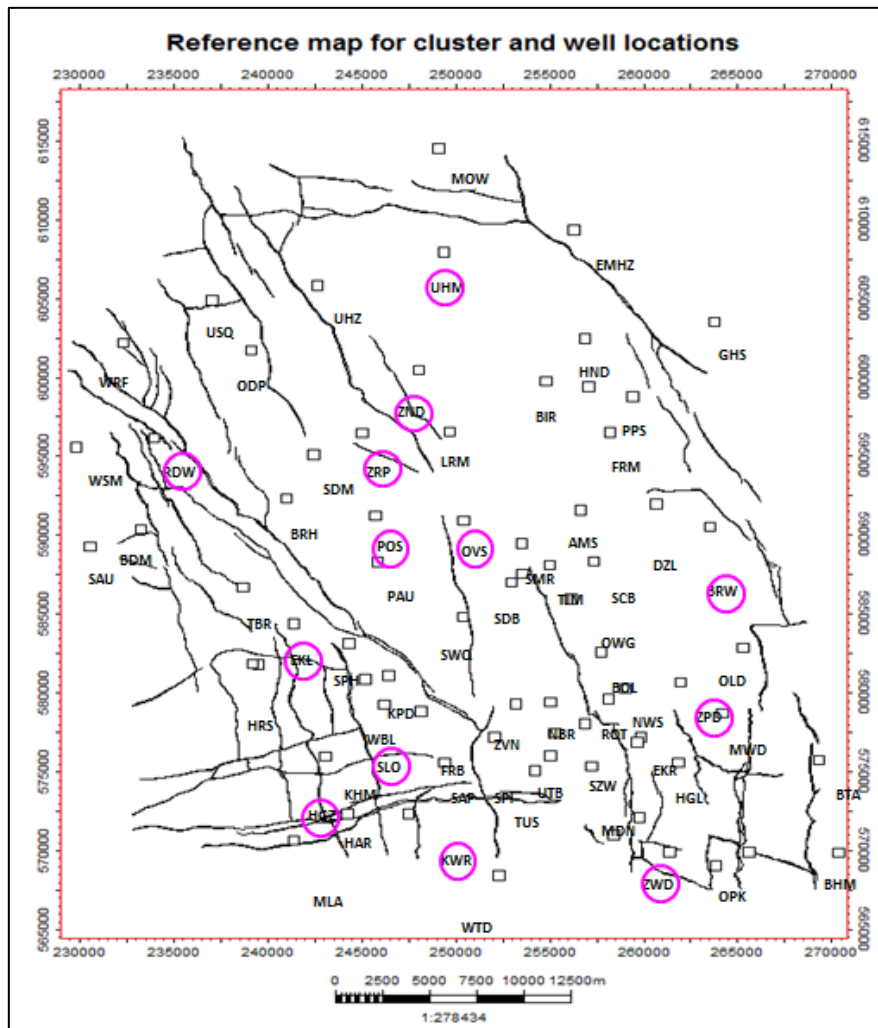


Figure 2. Location of the 13 offset wells (identified with a pink circle) in the Groningen Field, Netherland (courtesy of NAM)

2.1 Representative volume of the field

For modelling the time-dependent (dynamic) response caused by the depletion of the reservoir units, it is necessary to define a representative volume within which the main structural features are properly incorporated. To remove substantial numerical issues related to the finite size of the model during the finite element simulations, it is necessary to expand the boundaries of the simulated area away from the area of attention. Therefore the boundaries of the structural model were extended by a factor four in all horizontal directions from the original size increasing the original area from around 57km by 67km to around 210km by 220km (see **Figure 3**).

For the same reasons, the vertical extension of the simulation volume reaches a depth of ~9,000m, nearly 5,000 m below the reservoir units.

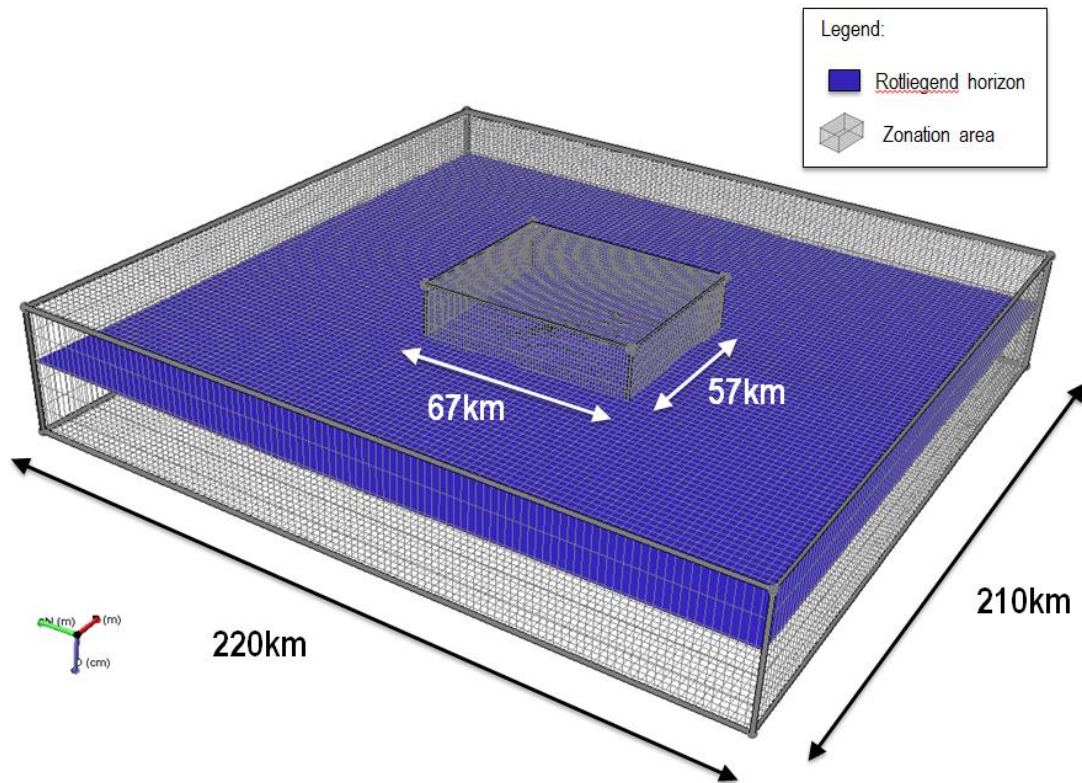


Figure 3. View of the extension of the model to avoid computation boundary effects

2.2 Structural Model

The structural modelling consists of building the geological structure of the field in a three dimensional volume, by importing, editing and interpreting relevant horizons and faults into the model.

The input for the structural model consists of a set of horizons (2-D Point sets) and polylines to define the fault geometry. Polyline sets can be converted into a fault surfaces (tri-mesh¹) using the JewelSuite software. A large number of faults and horizons were interpreted by NAM. The horizons accounted for the structural model were selected based on their geomechanical relevance (top/base Salt; Top/base reservoir) in accordance with NAM's requirements. The selection of horizons was also built in such a way that the structural grid is formed of optimally shaped finite element to limit computational errors. The selection of the faults was based on the location of the recorded seismic events. A total of nine horizons and twenty-one faults (from a total of 707 faults interpreted from seismic) were selected and integrated into the model (see **Figure 4** and **Table 2**). Since the 3-D structure does not include all the known geological features, this model should not be used for any decisions on field wide seismicity.

The size of the structural model was extended outside the limit of the horizons by around 70 km towards each direction in order to reduce the influence of the boundary effects on the finite element modelling. This is discussed in more detail below (see paragraph **2.1 Representative volume of the field** on page **22**).

¹ A tri-mesh is a triangulated surface that describes the geometry of a horizon or a fault.

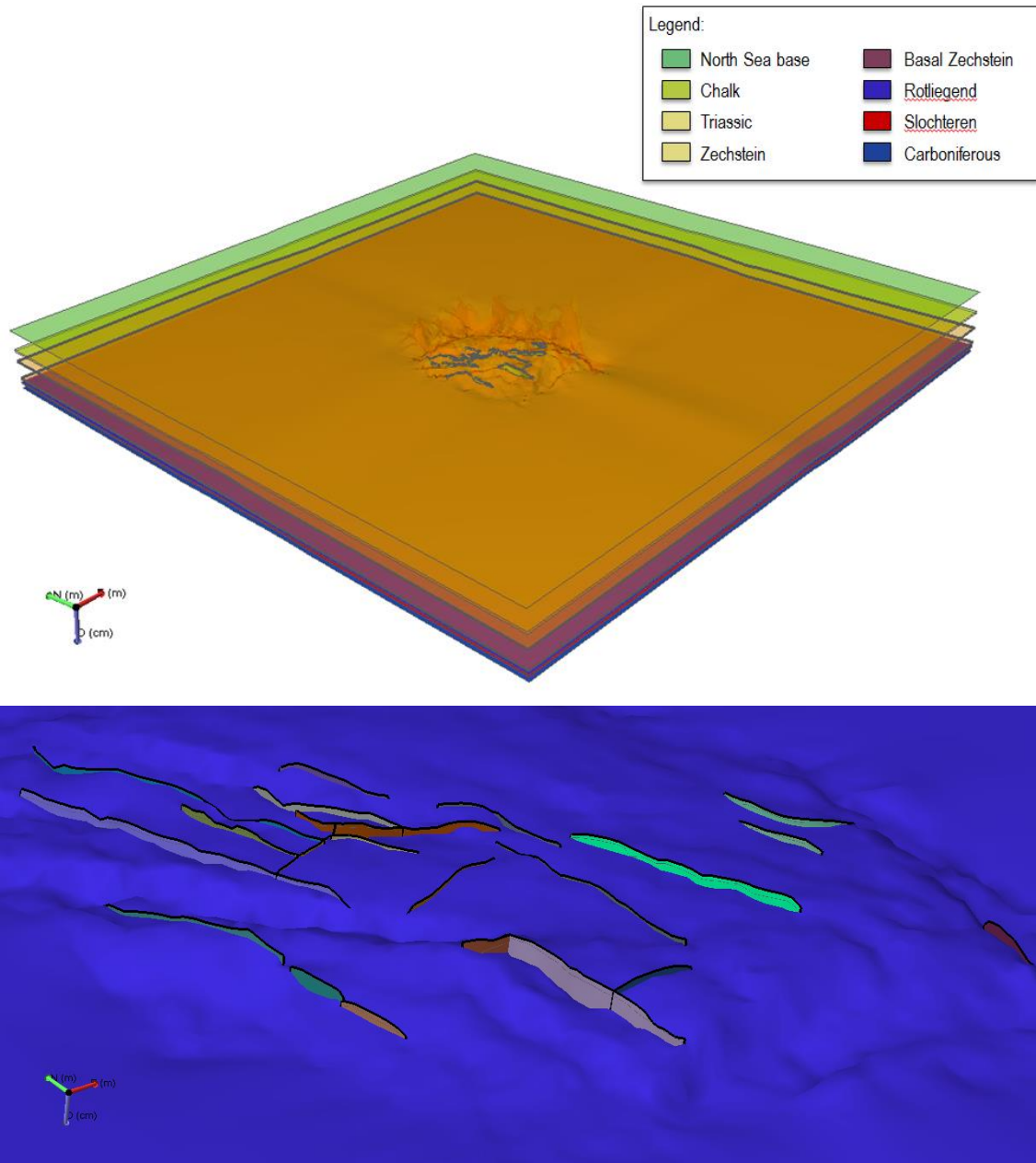


Figure 4. (Top) Available horizons and faults used for the 3-D dynamic geomechanical modelling. (Bottom) Selected faults used for the 3-D dynamic modelling at the top Ten Boer formation.

Selected Horizons	Selected Faults	
<ol style="list-style-type: none"> 1. Surface (mean sea level) 2. North Sea Base 3. Chalk 4. Triassic 5. Zechstein 6. Basal Zechstein 7. Ten Boer 8. Slochteren 9. Carboniferous 	<ol style="list-style-type: none"> 1. B24 2. B40 3. B40a 4. B44 5. B58 6. INT_8 7. INT_12 8. INT_14 9. M2 10. M6 11. M39 	<ol style="list-style-type: none"> 12. Merged M40/M41 13. M69 14. Merge msF7 15. mFS7_Fault38 16. mFS7_Fault50 17. mFS10_Fault_27 18. mFS10_Fault_38 19. mFS11_Fault_14 20. mFS14_Fault_19 21. MFS15_Fault_22

Table 2. Selected faults and horizons for the 3-D structural model

The 2D point sets of the horizons provided by NAM had a horizontal resolution of 25 meters. Each point set was first converted into a tri-mesh, i.e. triangulated surface, of the same resolution as the 2D point set. However to avoid generating a 3-D structure with a very high level of detail, which would eventually lead to very large computational requirement for the finite element simulations, each horizon was coarsened to limit the size of the model. The resulting resolution of the horizons, i.e. the typical separation distance between two nodes, is around 700 meters (see Figure 5) with the density of nodes homogeneously distributed across the field.

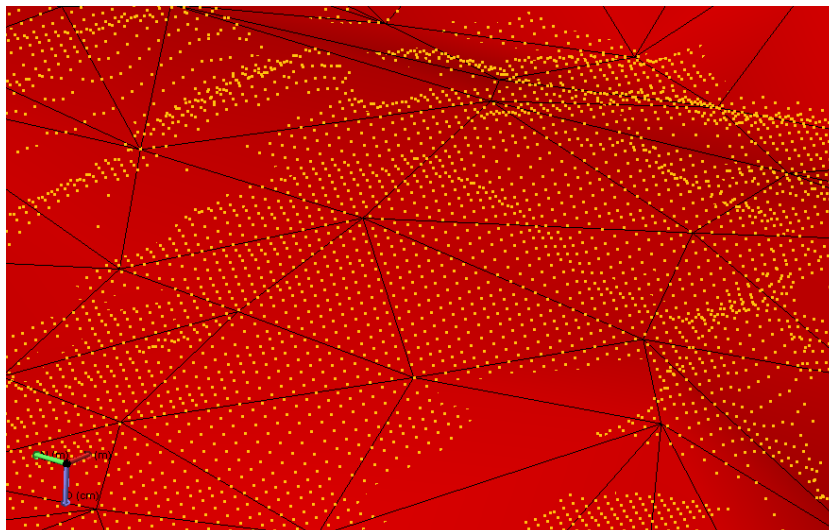


Figure 5. Original 2D points set (Orange dots) of the Slochteren horizon and resulting coarsened tri-meshed horizon (red triangulated surface)

During the process of coarsening, particular care is taken to ensure that the tri-meshed surfaces reproduce the original surface as exactly as possible (see **Figure 6**). This approach, consisting of coarsening fine structural details far away from the zone of interest, is essential in order to limit modelling time. On the outer part of the model where the structure is extrapolated (no seismic coverage), the model resolution was coarsened to 5 kilometres.

The polylines, defining the geometry of the faults, are converted into tri-meshes with a resolution comparable to the horizons prior to being incorporated within the structure of the model.

The horizons intersected by faults were cut through within a short distance of the fault and projected onto the fault in order to obtain a realistic structure. As a result the integration of faults within the model was done by performing some structural interpretation. This approach also limits the risk of obtaining intersecting horizons and poorly shaped finite elements in faulted areas.

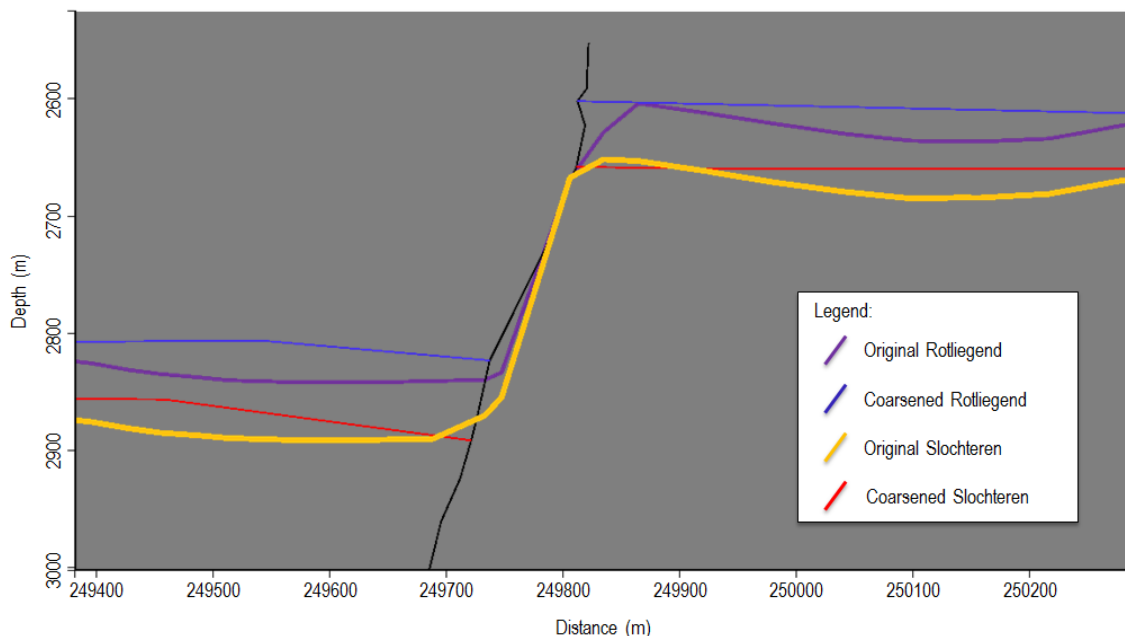


Figure 6. Detail of a cross section of the interpreted geological structure. The original horizons, obtained from 2D grids – Purple and orange coloured lines - were coarsened and adapted in order to reduce the size of the computational domain. The interpreted horizons – Blue and red coloured lines – were modified such that offsets and throws are observed along the M6 fault instead of strongly steepening the formation. Fine scale structural features located away from the geomechanical area were smoothed to diminish the size of the model

2.3 Construction of the 3-D Finite Element mesh

2.3.1 Generation of the mesh based on the structural model

The structure of the geomechanical volume is made entirely “watertight” by connecting all horizons and faults to each other so that no gap exists within the full volume (**Figure 7**). The structural modelling also

involves editing and adapting the geometry of the horizons and faults in various locations to remove inconsistent structures caused by the coarsening of the horizons, for instance where consecutive horizons intersect each other.

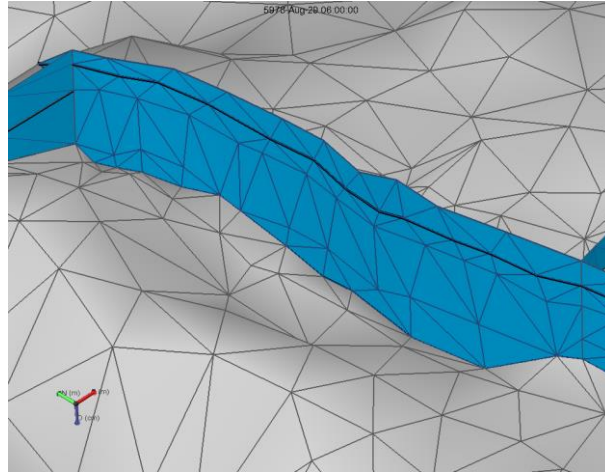


Figure 7. View of a watertight structural model (Slochteren horizon is grey, intersecting faults in blue).

Once this step is realised, a 3-D Finite Element mesh is constructed using ABAQUS/CAE, the pre-processor of the finite element software ABAQUS™ (see **Figure 8**). A total of 351,812 elements (2nd order tetrahedrons containing 10 nodes) were necessary to honour the interpreted structure of the Groningen Field (see **Table 3** for a detailed count of elements per layer). The size and the number of finite elements are constrained by the size of the tri-meshes, the number of horizons and faults. The mesh resolution was designed to achieve an optimal resolution to perform the numerical simulations while following precisely the geometry imposed by the tri-meshes.

All faults are explicitly integrated in the structural model; therefore their geometries constrain the construction of the FE mesh by generating a discontinuity at these locations. For the present simulation slipping surfaces were not considered for the model. This assumption is reasonable since the study consists of assessing the risks of stability of the faults, therefore all faults included in the model should be in a stable state during the entire production period. During the post simulation analysis, the stability of the faults will be assessed by calculating the shear to normal stress ratio on the fault plane. The stress reorganization caused by fault slippage is not considered in the present study.

The boundary conditions applied to the nodes located on the side edges of the computational volume restrict their displacement along the vertical directions. The nodes located at the base of the model are not allowed any displacement in the horizontal or vertical direction. Finally, all the remaining nodes in the model are allowed to move freely in all directions.

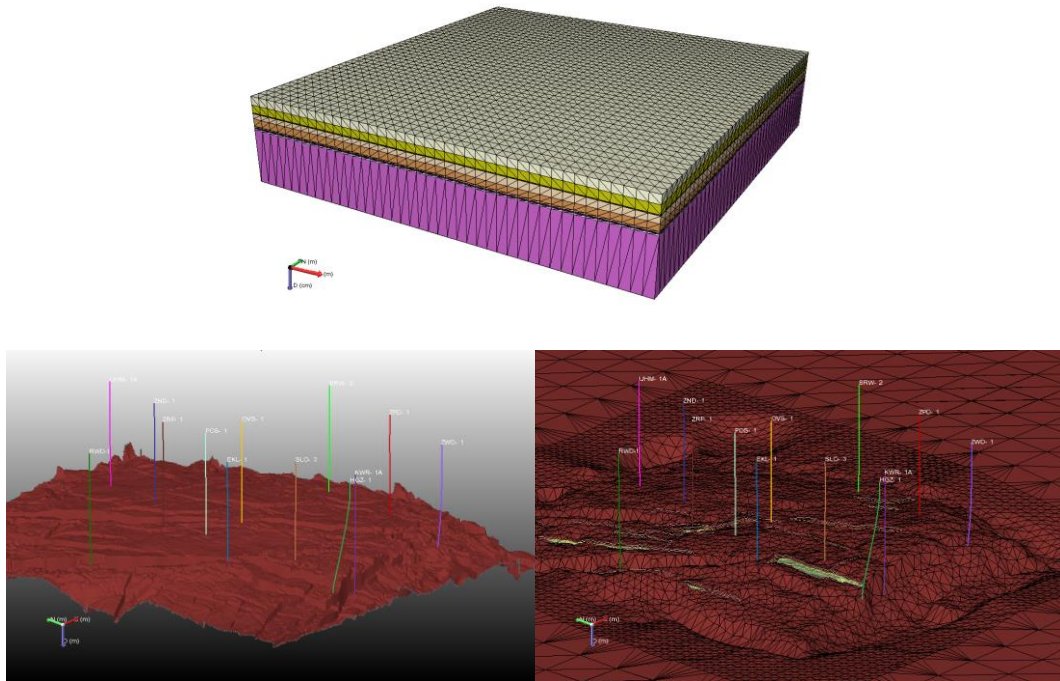


Figure 8. Top) Overview of the 3-D meshed structure used for the finite element modelling. Bottom) Overview from the Ten Boer layer used for the finite element modelling before (left) and after (right) discretization and lateral extension.

Layer Name	Number of elements
Overburden	20,327
North Sea base	42.320
Chalk	35,134
Triassic	37,797
Zechstein	45,708
Basal Zechstein	36,976
Ten Boer	36,999
Slochteren	37,988
Carboniferous	58,563

Table 3. Number of elements per layer utilised to mesh the Groningen Field

2.3.2 Material properties

The “water tight” structural model allows the assignment of different material properties to every formation in the model. All layers have poro-elastic properties except the Zechstein salt layer for which visco-elastic properties are allocated and the Carboniferous layers which behaves elastically (i.e this formation will not endure any pore pressure variation (see **Figure 9**)).

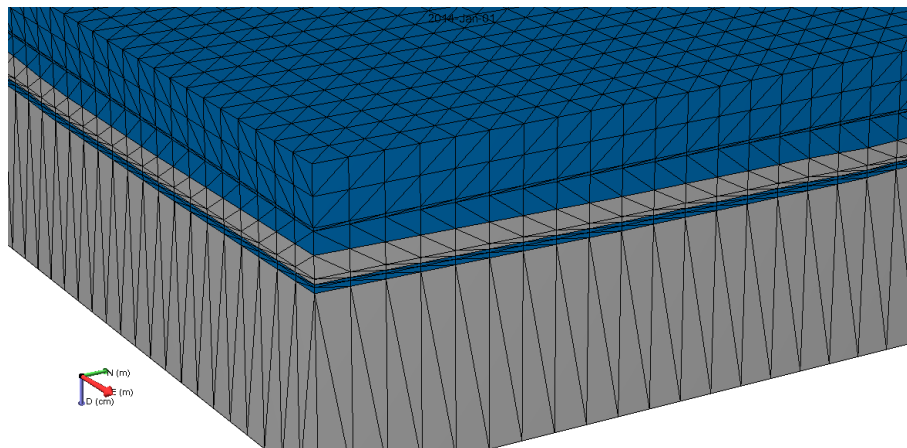


Figure 9. New FE-Mesh using poro-elastic elements (in blue) in the Ten Boer formation, the Slochteren formation and the shallow layers and visco-elastic elements (in grey) in the salt layer and the base carboniferous layer.

Carboniferous layer

Using C3D10M elements in the Carboniferous layers permits removal of one degree of freedom at each calculation point, and allows consideration of sharp pore pressure variations below the reservoir.

The decision to use those elements for mapping material properties in the Carboniferous layer was based on the calibration of subsidence with in-situ measurements. **Appendix 1 displacement element in the Carboniferous layers below the reservoir**” describes the reason for this approach.

Salt creep behaviour in the Zechstein Layers

The choice between an elastic-power-law creep material model and an elastic-only material model for salt layers is based on the trade-off between calculation time and increased model accuracy.

The calculation time significantly increases if the salt creep is calculated during the analyses. Since the key objective of the analyses is to use the results to rank the different scenarios relative to the risk of fault slip, accuracy is certainly an important factor. The authors agree that calculation time should never be the only factor in the choice of the approach, but if the accuracy does not significantly increase by introducing creep then it may not warrant the additional calculation time required. A complete discussion on the influence of salt creep during the field production is available in section 3.2.1 (page 48).

2.4 Property Modelling and Mapping

The following step consists of allocating properties to each node forming the finite element mesh in order to finalize the input for the ABAQUS™ simulations.

2.4.1 Rock properties

The rock mechanical properties required for the finite element modelling, i.e., Density, Young’s modulus and Poisson ratio, are calculated from the 1-D geomechanical models using calibrated log based

relationships (see paragraph **2.3.2. Log-Based Mechanical Properties in the 1-D Geomechanical Model – Final Report²**). Because the difference between the vertical resolution of the wireline log data used to obtain well centric rock mechanical properties and the resolution of the finite element mesh, material properties need to be carefully upscaled in order to assign the nodal properties to the FE mesh. The geomechanical properties required for the finite element simulations, i.e. Young's modulus, Poisson's ratio and material density were upscaled at each well location to a vertical resolution comparable to the FE mesh. Based on these considerations, the rock mechanical properties are averaged arithmetically to an upscaled log resolution varying between 150 m in the coarsely meshed over- and under-burden and 20 m in the more finely discretized reservoir layers. The arithmetic averaging is found to provide the most consistent responses for the numerical modelling (internal investigation). More detail on the log upscaling is provided in the **Appendix 3 Upscaling data**. The result of the upscaling process for the density log can be seen in **Figure 10**.

² Dynamic Geomechanical Modelling to Assess and Minimize the Risk for Fault Slip during Reservoir Depletion of the Groningen Field – 1-D Geomechanical Model – Final Report, **NAM0001** – January 2014

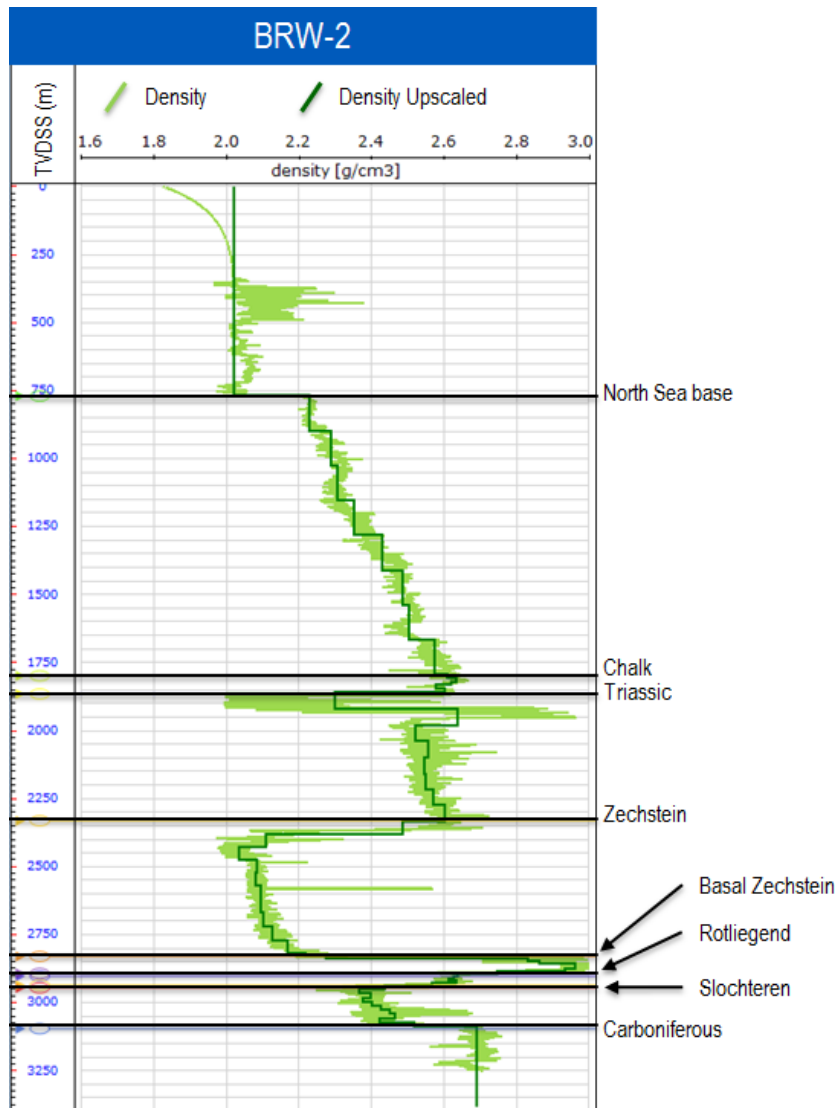


Figure 10. Comparison between the original properties (composite density log) and the resulting upscaled density log for the well BRW-2

After upscaling the rock mechanical properties, the rock densities, Young's modulus and Poisson ratios are mapped onto a Jewel grid³. The jewel grid is a grid that comprises all the structural detail of the model, including all the relevant faults and horizons. We use this intermediate structure to interpolate the well based properties to the field wide structure prior to mapping it onto the finite element mesh. Because the relatively small number of offset wells available in the Groningen Field area, the population

³ A Jewel grid is a particular 3-D grid using grid cells that can share I and J coordinates to produce the most uniform grid structure available, including your complex geological features.

of the well properties onto the 3-D volume is based on an inverse distance weighting⁴ (IDW) algorithm (see **Figure 10**). Several other geo-statistical methods are available for populating properties through the area. However, in addition to its simplicity, the IDW algorithm provides a reasonable distribution of properties considering the well distribution over the field. The Jewel Grid is then used to allocate the nodal properties of the finite elements using mapping algorithms available from JewelSuite.

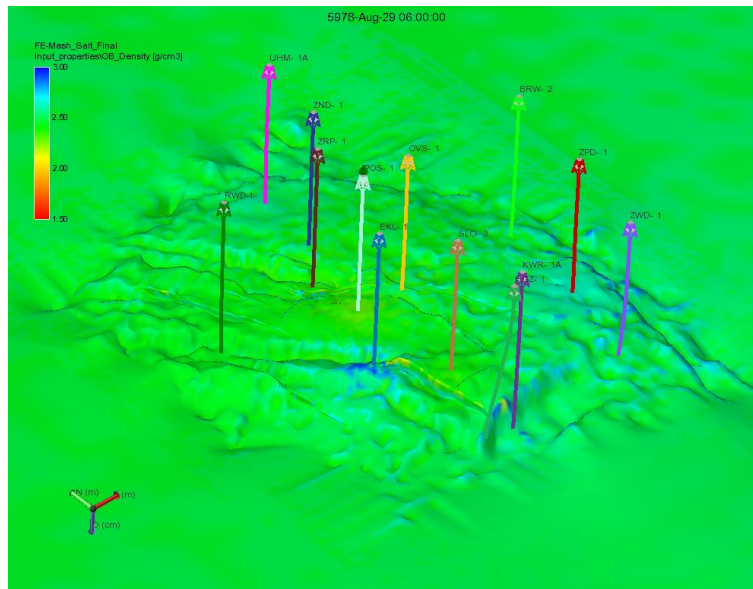


Figure 11. Distribution of the density populated onto the mesh for the Slochteren Formation. The density mapping was performed by interpolation of well log data using an inverse distance weighting algorithm.

Young's modulus

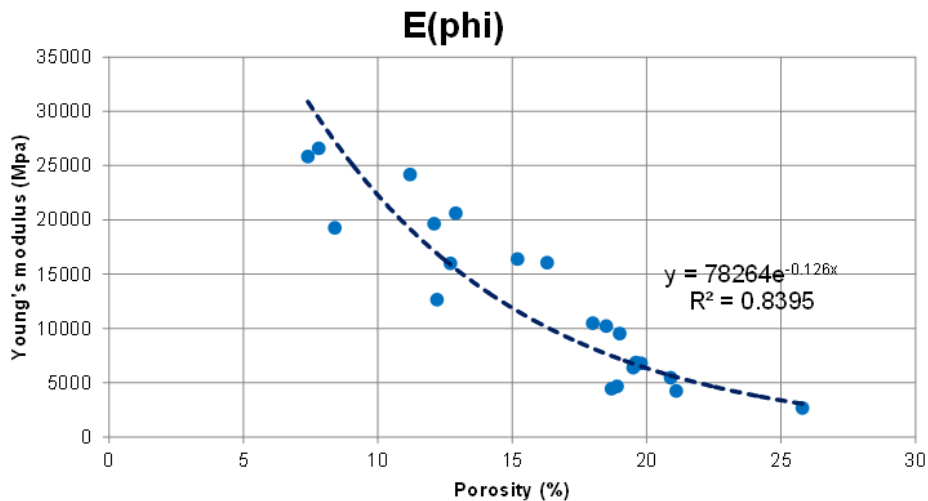
The mapping of the Young's modulus parameter in the 3-D Model can be described as follow:

- In the overburden and the under-burden, the Young's modulus from the 1-D geomechanical model was mapped in the 3-D model using a similar approach described previously for the other rock parameters, namely, an interpolation algorithm based on inverse distance weighting.
- In the far field zone (i.e. outside the zone of interest representing the entire Groningen Field), the Young's modulus is also mapped from the 1D geomechanical model. In the reservoir, an empirical formula from the porosity data mapped onto the reservoir grid was used to assign to every element a porosity value correlated with the Young's modulus (see **Figure 12**). The

⁴ The Inverse Distance Weighting is a type of deterministic method for multivariate interpolation with a known scattered set of points. A parameter p called the power parameter defines the influence to values closest to the interpolated point.

formula has been estimated using the relationship derived from laboratory tests of Young's modulus and porosity carried out in the wells Eemskanaal-12 and Zuiderpolder-12.

Figure 13 shows a view of the resulting Young's modulus on the Zeichstein Formation.



NB: Formula defined for porosity comprised between 7% and 26%

Figure 12. Porosity-Young's modulus relationship based on data from the NAM internal report "Groningen Fault Stability Analysis" (Van Den Bogert et al., 2013)

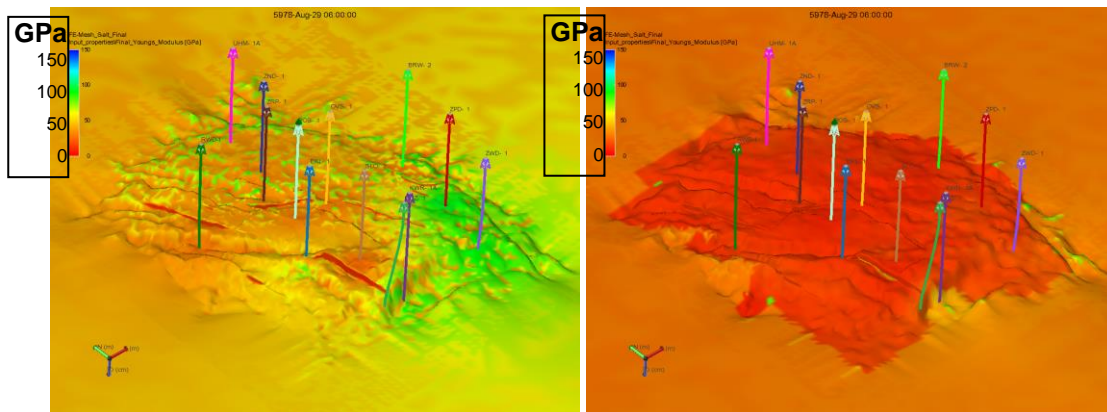


Figure 13. Distribution of the Young's Modulus on the finite element mesh for the Ten Boer formation (left) and the Slochteren formation (right). The Young's modulus in the Slochteren reservoir is significantly lower ($E_{\text{slochteren}} \sim 10$ GPa) compared with the overlying non reservoir units ($E_{\text{slochteren}} \sim 40 - 90$ GPa). While the Young's modulus was obtained from porosity values mapped in the reservoir grid, the Young's modulus was obtained from interpolated log data on the side of the structure.

Poisson's Ratio

The Poisson's ratio is upscaled for each well from the 1-D Poisson's ratio log to the vertical resolution of the structural grid. Similarly to the Young's modulus, the Poisson's ratio is based on the upscaled log

derived responses and mapped within the entire 3-D volume using an Inverse Distance Weighting (IDW) mapping algorithm.

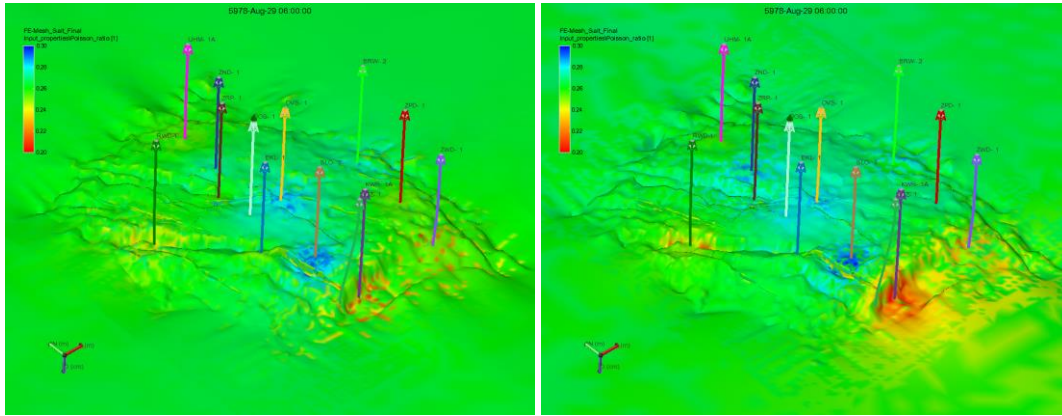


Figure 14. Distribution of the Poisson's ratio at the top of the Ten Boer formation (left) and the Slochteren formation (right). The colour bar varies between 0.20 (red) to 0.30 (blue).

Viscous properties of the Zechstein salt:

One aspect of the study consists of determining the 3-D stress field at a pre-production stage. Because the reservoir unit is topped by a large salt layer (Zechstein and basal Zechstein), it is important that the finite element simulations capture the changes in stress magnitude and orientation caused by the viscous relation, i.e. creep, of the salt. The general formula that describes the creep properties of the salt were based on a study performed by Breunese et al. (2003). The total creep strain can be divided into two terms, a dislocation creep strain (negligible for this study) and a pressure solution creep can be expressed as follows:

$$\dot{\epsilon}_{tot} = \dot{\epsilon}_{dc} + \dot{\epsilon}_{ps} \approx B \cdot \frac{\sigma}{T \cdot d^3} e^{-\left(\frac{Q}{RT}\right)} = A_2 \cdot \sigma \cdot e^{-\left(\frac{Q}{RT}\right)}$$

- Where: $\dot{\epsilon}_{tot}$ Total creep strain
- $\dot{\epsilon}_{dc}$ Dislocation creep strain (neglected in the calculation)
- $\dot{\epsilon}_{ps}$ Pressure solution strain
- σ Differential stress ($\sigma_1 - \sigma_3$)
- $A_2 = 14.6 \text{ E-3 MPa}^{-1} \cdot \text{day}^{-1}$
- $\frac{Q}{RT} = 8.13$

Using the above equation, the viscosity of the Zechstein salt is $2 \cdot 10^{16}$ Pa.s, which was considered uniform for the finite element model. Note that the viscous relaxation is considered only in the salt and considered negligible for other lithologies.

2.4.2 Pore Pressure

Overburden Pore pressure

Pore pressure in the overburden, the under-burden and the formations surrounding the reservoir was mapped based on the 1-D pore pressure analysis performed during the 1-D geomechanics phase. Similarly to the rock mechanical properties, the pore pressure was upscaled vertically for each well from a vertical resolution of around 700m in the shallowest section down to around 10m in the reservoir layers (**Figure 15**) and then populated onto the structural grid using IDW (Inverse Distance Weighting) algorithm to interpolate the property to the entire field. The structural grid, also known as Jewel Grid, was used as an intermediate grid for mapping the pore pressure to each node of the finite element mesh.

Reservoir model

For the reservoir formations, five reservoir scenarios were provided by NAM covering a period from 1964 to 2080. The reservoir model provides at each simulation time step a value for the reservoir pressure in the entire Groningen Field (see **Figure 17** and **Figure 18**). For the dynamic modelling of the reservoir depletion, a total of ten (10) time steps were used in the simulations to cover the entire time range from 1964 to 2080. The following reservoir simulation models were utilized within the scope of this study and identified as such:

1. BestMatch_v31_Prod2011_S0F1EN6_TBKH_SubCorrection_SodM → RM1
2. BestMatch_v31_Prod2013_SubCorrection_SodM_Rescue → RM2
3. Basedeck_OptBaseKHM1_Jan2014_Rev_G1_SL_KHM__GFR2012_G1_Prod2013 → RM3
4. Basedeck_OptBaseKHM1_Jan2014_Rev_G1_SQ_KHM__GFR2012_G1_Prod2013 → RM4
5. Basedeck_OptBaseKHM1_Jan2014_Rev_G1_WP2013__GFR2012_G1_Prod2013 → RM5

The reservoir models provided by NAM each contained a total number of 43 horizontal (k) layers covering the entire reservoir thickness. By comparing the structural tops incorporated in the structural model (top Ten Boer, top Slochteren and top Carboniferous) with the reservoir model provided it was determined that the k layers 1 to 3 are within the Ten Boer and layers 4 to 43 are for the Slochteren unit. To obtain a meaningful representation of the 43 sub-layers of the reservoir model within the two main formations that it covers, it is necessary to upscale the reservoir grid to a resolution similar to the finite element mesh (the vertical resolution of the mesh is one quadratic finite element per reservoir layer). The upscaling procedure that was undertaken is represented schematically in **Figure 16**. The idea consists of calculating for each stack of the reservoir between two layers the average pore pressure weighted by the volume of each cell. Using this approach it is possible to accurately allocate pore pressure conditions for the reservoir.

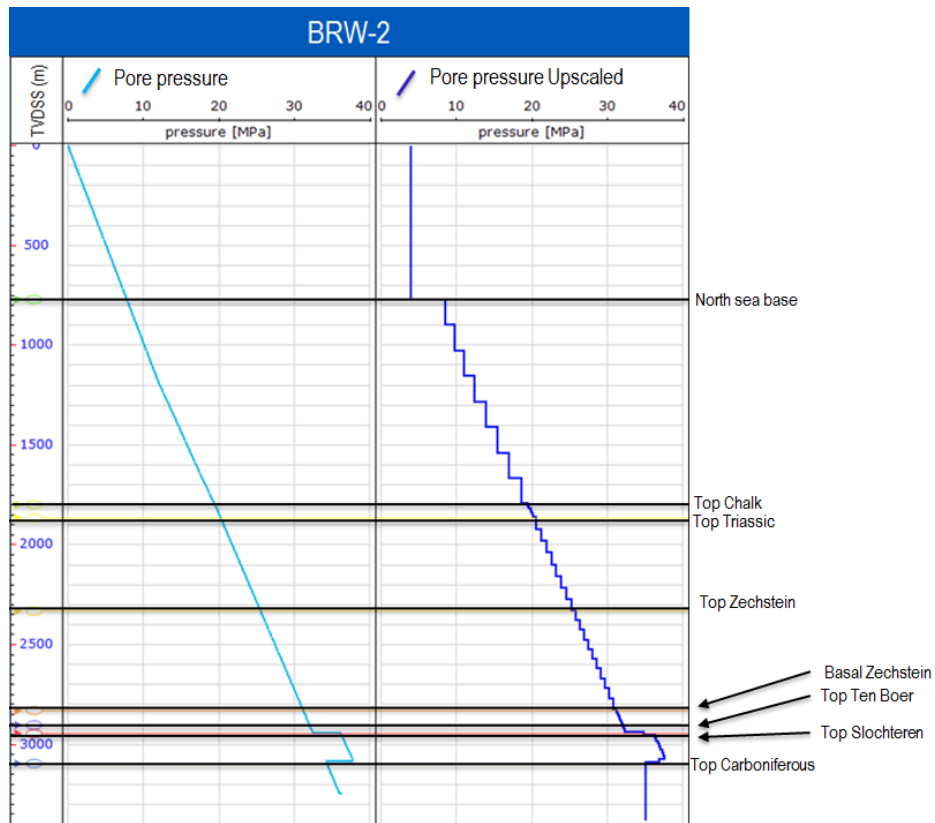


Figure 15. Comparison between the original properties (pore pressure in the figure) in the left and the results of the upscaling in the right for the well BRW-2. The higher pore pressure trend below 3000 meters TVDSS corresponds to the reservoir section.

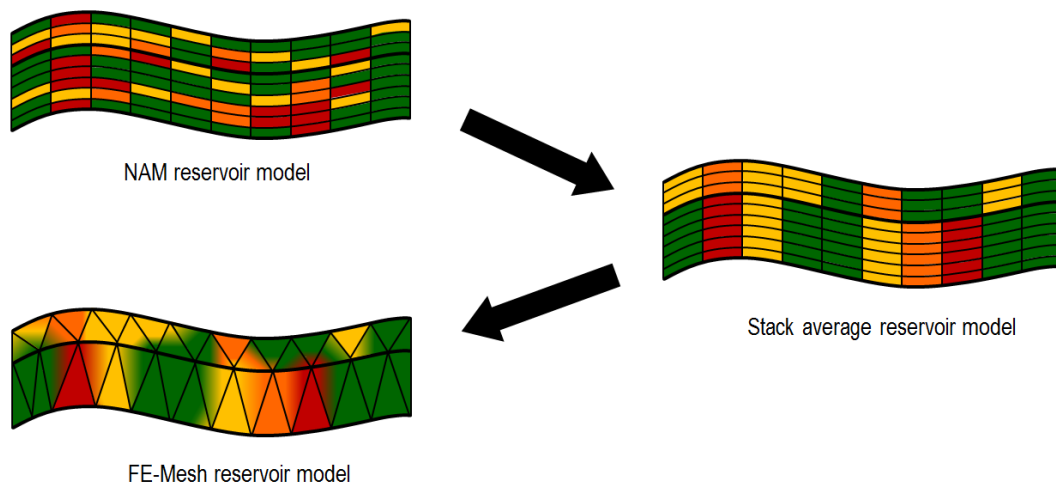


Figure 16. Schematic of method used to map the reservoir pressure into the FE-Mesh

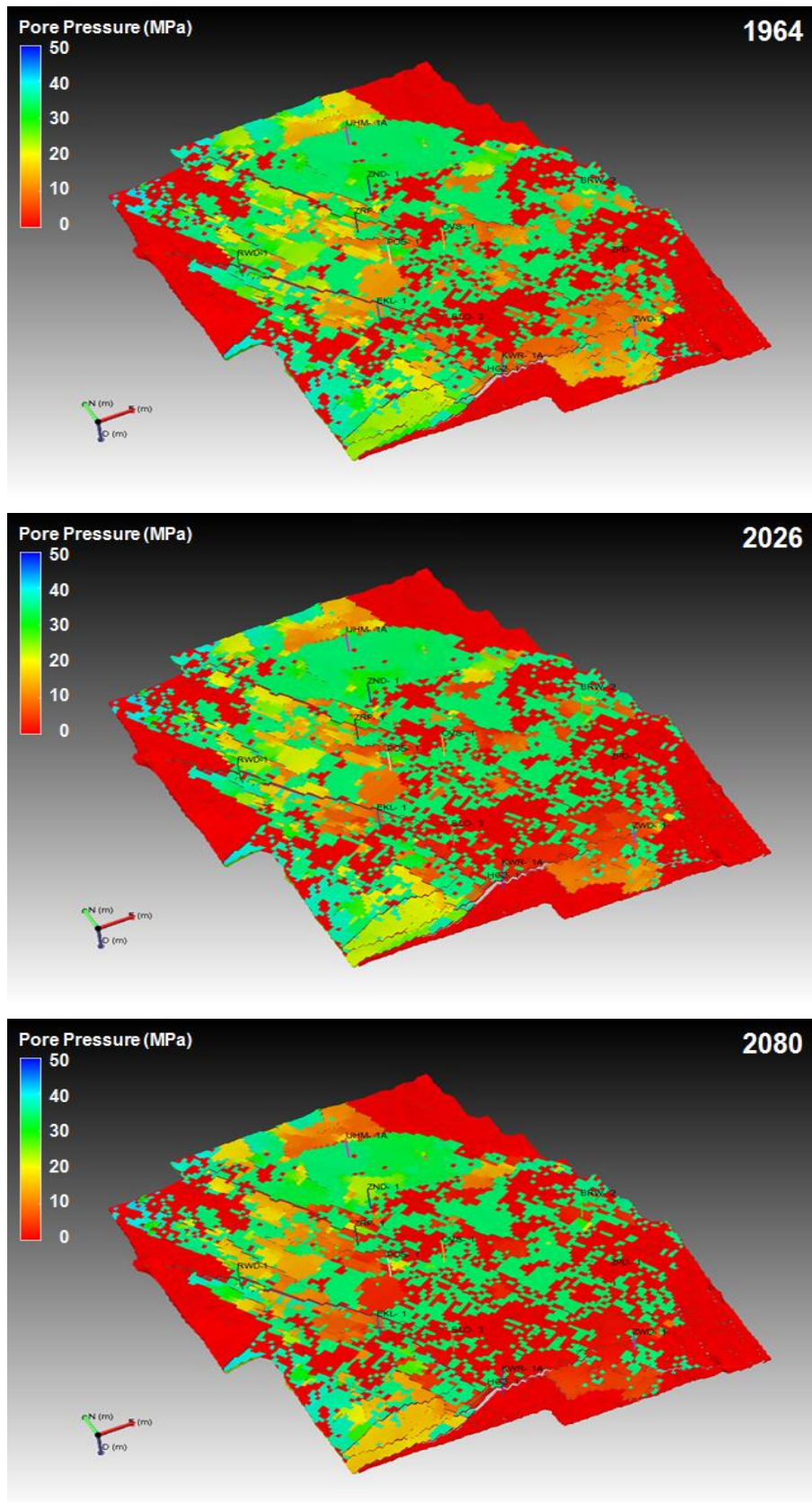


Figure 17. Example of the reservoir pore pressure history and forecast at the top of the Ten Boer reservoir for the years 1964, 2026 and 2080 after upscaling (snapshots from RM3). The blue-green

patches visible correspond to shaley rock types with low permeability that are not undergoing any depletion.

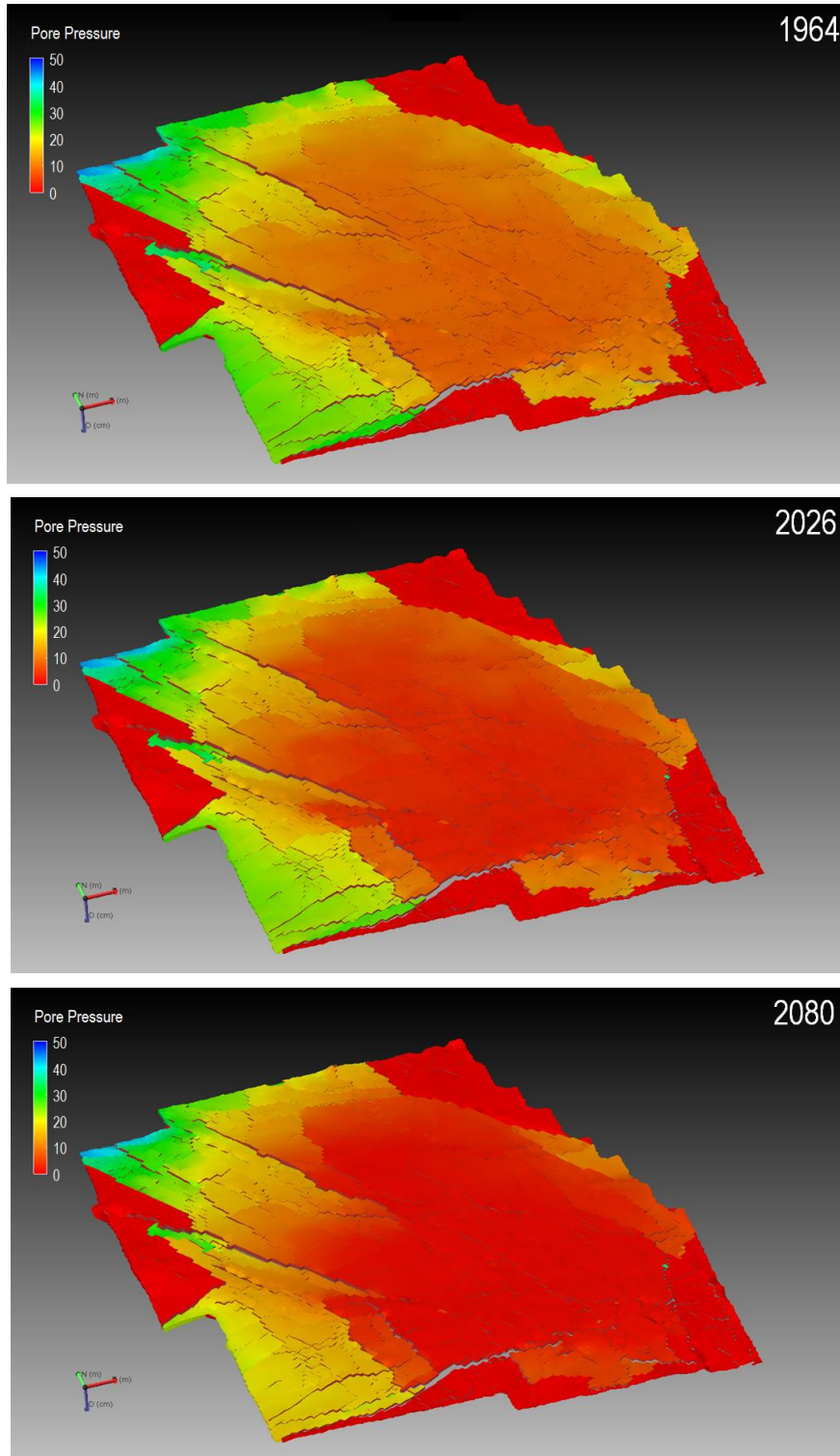


Figure 18. Example of the reservoir pore pressure history and forecast at the top of the Slochteren reservoir for the years 1964, 2026 and 2080 after upscaling (snapshots from RM3). The red areas on the

side of the reservoir are indicating cells with no pore pressures. For the simulations, the pore pressure allocated to these cells is obtained from interpolated pressures from the 1D model interpretation.

3 3-D Dynamic Geomechanical Modelling

3.1 Set up of the dynamic model

3.1.1 Initial in-situ stress state from the offset well analysis

The final step for setting up the initial finite element model consists of finding the correct starting in-situ stress state which matches the stress magnitudes and directions found in the 1-D model.

The combination of the material properties, the pore pressure and the initial stress state may not be in equilibrium when the finite element model is first run. The initial run would result in deformations as the finite element model always seeks an equilibrium state. These deformations must be minimal to avoid large changes in the geometry, and to avoid generation of unrealistic (near surface) stresses. To overcome this issue, a two tier approach was used, which is a modification of the method described by Ellis (2006).

- In the first tier, we applied a rough initial stress and pore pressure field to the FE model. This model was run for a geostatic step which only calculates the elastic equilibrium. During this single step, gravity is applied instantaneously to the whole model and the vertical stress is calculated. For every finite element in the FE model, the full stress tensor is calculated using the vertical stress combined with the knowledge of the horizontal stress orientation, AZI_{SHmax} and the effective stress ratios for S_{hmin} and S_{Hmax} . These stresses are used as the initial stress condition for the second tier.
- In the second tier, the original boundary conditions and the un-deformed mesh shape are used together with the initial stresses calculated in the first tier. The calculation of the stress perturbations is done in two steps:
 - Geostatic analysis to calculate the elastic equilibrium of the model,
 - Creep step to model the salt creep.

In the second step, the differential stresses in the salt body cause salt creep which, in turn, reduces these differential stresses. This step is chosen over a long enough period (over 10,000 years in this particular case) to reduce the differential stresses within the salt structure to a level approximately equal to the magnitude of measured/expected values (2-3 MPa, Diggs & Urai, 1997) (see **Figure 19**). **Figure 20** shows the Von Mises stress⁵ in the salt layer is very low at the end of the creep period. During the creep step, the model stays in elastic equilibrium. Outside of the influence of the salt layer, the maximum horizontal stress (S_{Hmax}) should be similar to the values used to calculate and calibrate the initial stress state and have the same stress direction as described in the 1-D geomechanical models. The stress direction at the level of the reservoir equals the expected stress direction.

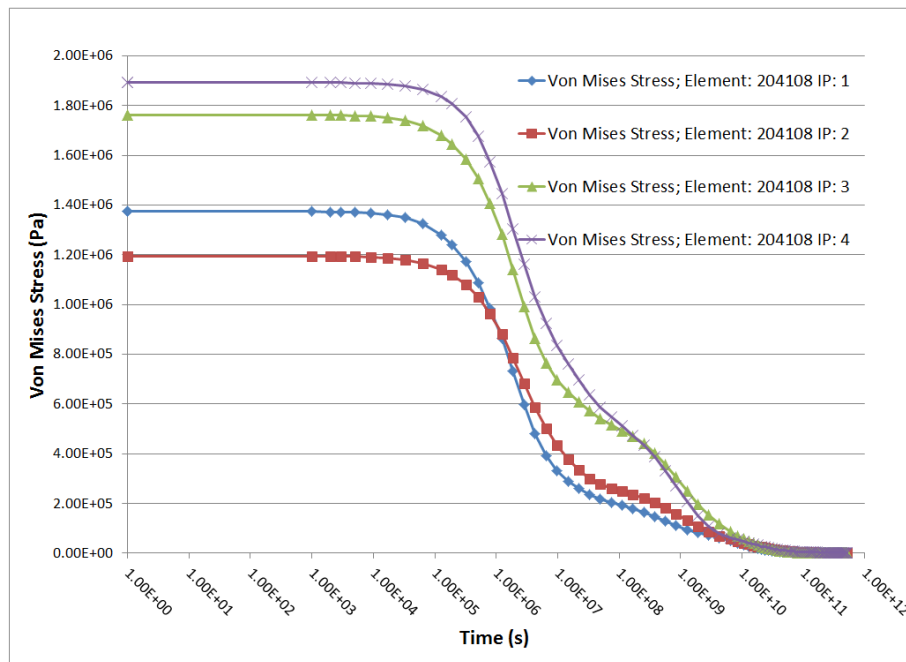


Figure 19. Decrease of the Von Mises stress during the relaxation of the salt through pressure solution creep. At the end of the salt creep modelling, which correspond to the date prior to the beginning of the field production, the salt exhibits very small differential stress (less than 10 kPa to compare with an overburden pressure close to 60 MPa in the Slochteren. Subsequently the stress state in the Zechstein

⁵ Differential stresses can be defined by the Von Mises stress formula as per:

$$S_{Mises} = \sqrt{(S_1 - S_2)^2 + (S_1 - S_3)^2 + (S_2 - S_3)^2}$$

- With
- S_{Mises} Von Mises stress
 - S_1 Maximum principal stress
 - S_2 Intermediate principal stress
 - S_3 Minimum principal stress

formation, immediately above the reservoir unit is nearly isotropic. Note that the salt creep is largely influenced by the complex structure of the salt body.

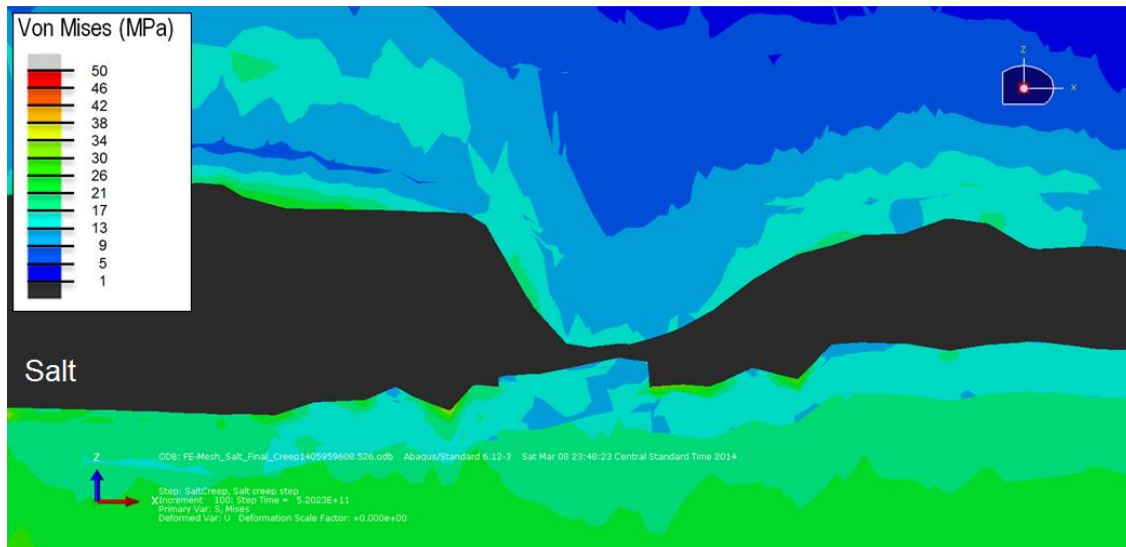


Figure 20. Display of Von Mises stresses in the Zechstein salt layer after the 2nd tier set up of the initial in situ stress state. Most of the salt has less than 1 MPa differential stress (dark grey colour), which is in agreement with sub-grain size piezometer measurements on natural salt samples (Diggs & Urai, 1997).

At the end of this initialization period the model is in equilibrium with the boundary conditions and with the mechanical properties of the salt layer and the surrounding formations. The initialisation is used to relax the system to an equilibrium state (using some convergence criterion).

Once the initialisation is achieved, the vertical stress from the finite element model is compared to the 1-D model to validate the numerical response. Following that step, both horizontal stresses are calculated using the effective ratios applied in the 1-D model. At this stage, the stress state should be consistent with the calibrated 1-D geomechanical models built for the undepleted field conditions.

Note that the displacements that occur during the initialisation phase are not accounted for. The deformation values are calculated after completion of this step.

3.1.2 Finite Element Simulations – Simulation Steps

Five (5) different pore pressure scenarios were provided by NAM to be simulated. The two first scenario models (RM1 and RM2) consisted of two history matched reservoir models which provide reservoir pressures (43 k layers within the Slochteren and Ten Boer formations between 1964 and 2013). The following three (3) reservoir models describe three different plausible scenarios of depletion from 1964 to 2080.

The numerical simulation was performed by coupling Abaqus with the reservoir models for the following years:

- History match models (RM1 and RM2): 1964 – 1974 – 1985 – 1990 – 1995 – 2000 – 2006 – 2008 – 2010 – 2013

- Forecast scenarios (RM3, RM4 and RM5). 1964 – 2014 – 2016 – 2018 – 2020 – 2022 – 2026 – 2030 – 2050 – 2080

The following pages show some illustrations (time steps) of the reservoir depletion over time for the reservoir model 1 (RM1) and the reservoir model 3 (RM3).

Reservoir model 1 (RM1)

The reservoir model RM1 was used for the calibration of the geomechanical response with existing surface measurements and the validation of the numerical approach undertaken to assess fault stability. It contains the reservoir pressure evolution for the Groningen Field area and indicates that the pore pressure within the depleted Ten Boer and Slochteren formation in 2013 decreased from a virgin pressure state close to 35 MPa to a minimum of 6MPa.

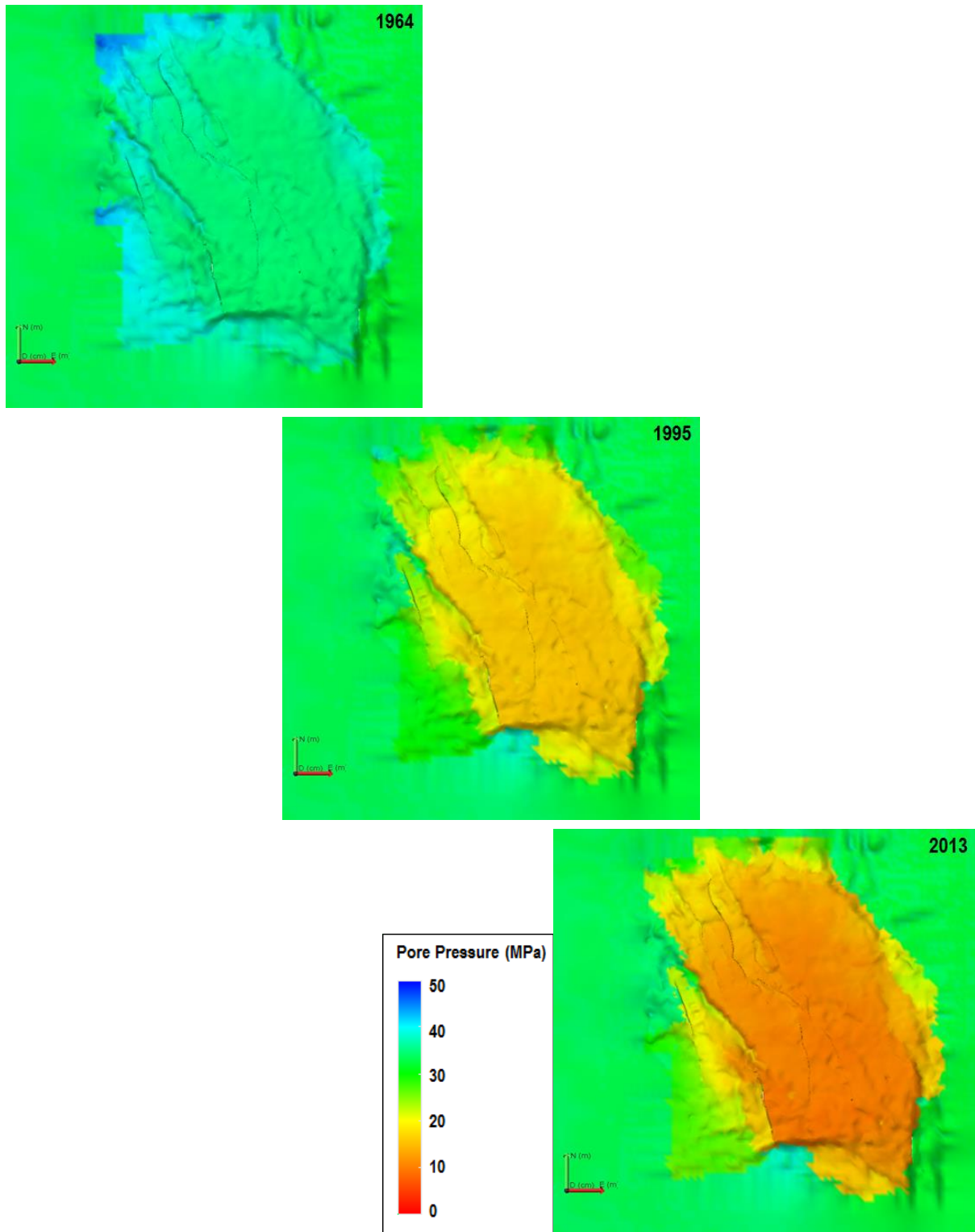


Figure 21. Evolution of the pore pressure for the reservoir model RM1

Reservoir model 3 (RM3) – Production forecast

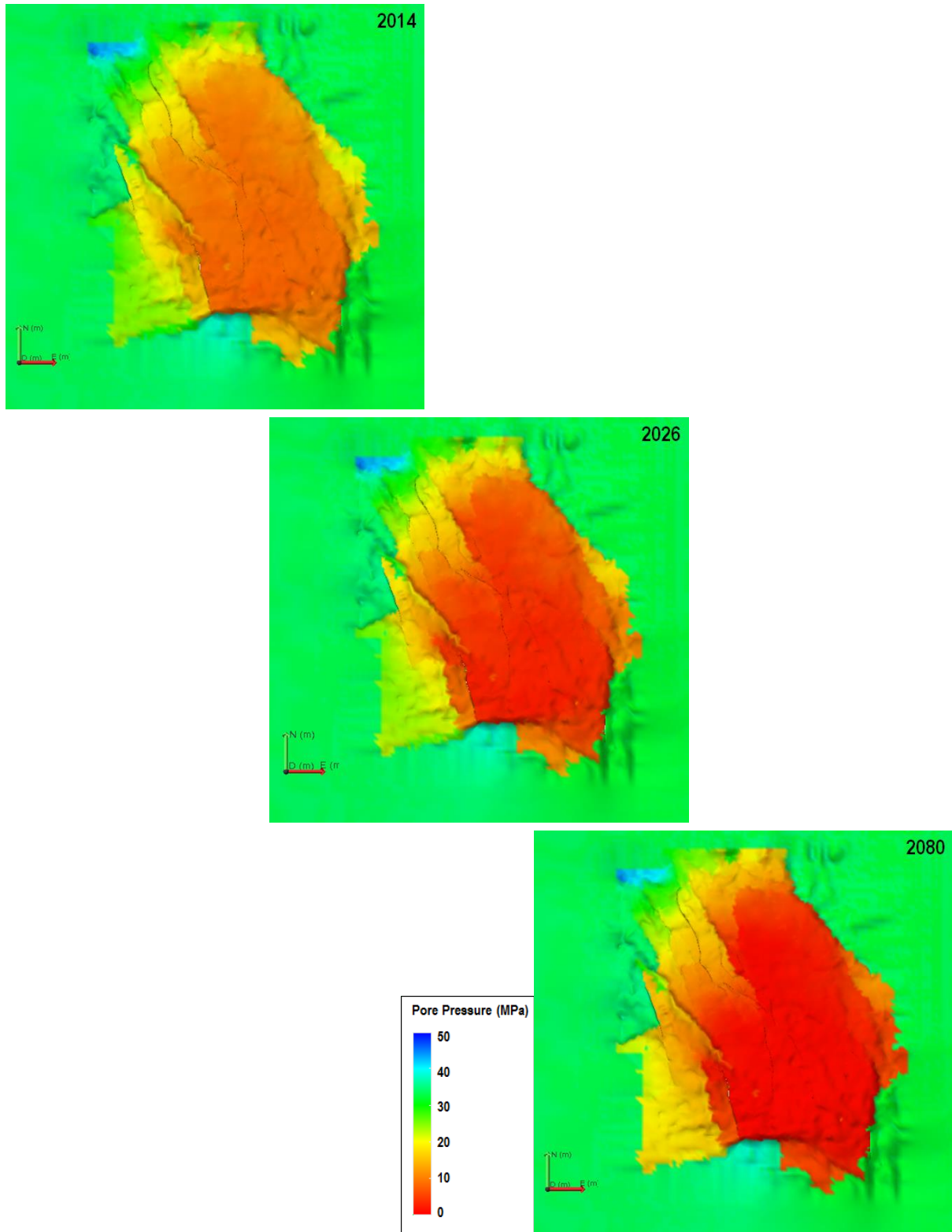


Figure 22. Evolution of the pore pressure for the reservoir model RM3

3.2 3-D dynamic simulation results

3.2.1 Calibration of the geomechanical response based on the strain response

An extensive amount of subsidence data was utilised to calibrate and verify the accuracy of the geomechanical model results. The dataset used consisted of surface elevation measurements for 433 locations across the Groningen Field available between 1964 and 2012. The reservoir models RM1 and RM2 are both used to assess the subsidence response of the Groningen Field. While both reservoir models appear to exhibit similar pressure distribution over the produced period, the North West part of the field of the reservoir model RM2 shows less depletion.

The initial step in the validation process consists of comparing the virgin stress field obtained from the finite element simulations with the well-based geomechanical model. In **Figure 23**, the data exported along the BRW-2 trajectory indicates a match between the vertical stresses (less than one MPa of difference).. The variations between the 1-D and 3-D horizontal stress magnitudes are essentially caused by the difference in vertical resolution of the 1-D models and the FE simulations (typically one quadratic element per layer).

Secondly, the vertical component of the strain response modelled through FE analysis can be compared to the subsidence measurements performed during the production of the Ten Boer and Slochteren formations. A good agreement between the response of the numerical model and the field measurements is essential to validate the numerical model and the subsequent fault stability analysis.

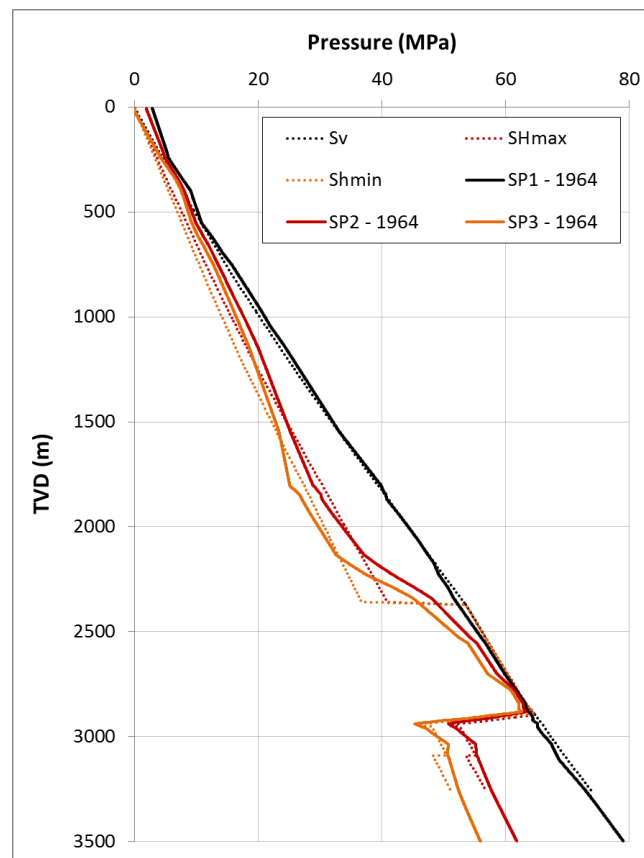


Figure 23. Comparison between the initial principal stress magnitudes obtained from the 1D model (dotted lines) and the stress field exported along the trajectory based on the Finite Element calculations (solid lines). The data are based on the BRW-2 well location.

In **Figure 24**, the comparison between the surface deformations obtained from the finite element modelling using the reservoir model RM1 and the field data indicates a reasonable match except for the most northern part of the field. After discussion with the NAM team, it was highlighted that the depletion in this part of the field had likely been overestimated in order to obtain a satisfying history match of the reservoir pressure. In the Central and Southern area of the field, the agreement between the calculated and measured subsidence is good; most of the surface data showing less than 5 cm of difference. A map of the subsidence predicted by the finite element analysis coupled with the reservoir model RM1 is available in **Figure 26**: it shows that the simulations indicate a maximum subsidence at the surface of the Groningen Field ranging between 35 and 40 cm in 2012.

In comparison, the geomechanical response based on the reservoir model RM2 (**Figure 25**), where the North-West area of the field is less depleted, appears to match more accurately in the North part of the field while maintaining good agreement in other part of the field. The computed subsidence using finite element modelling matches the recorded subsidence data with less than 10cm difference in most of the cases (for 98.5% of the subsidence data points). Similarly to the RM1 simulation model, the maximum subsidence calculated using the RM2 model is between 35 and 40 cm near the centre of the model in 2012.

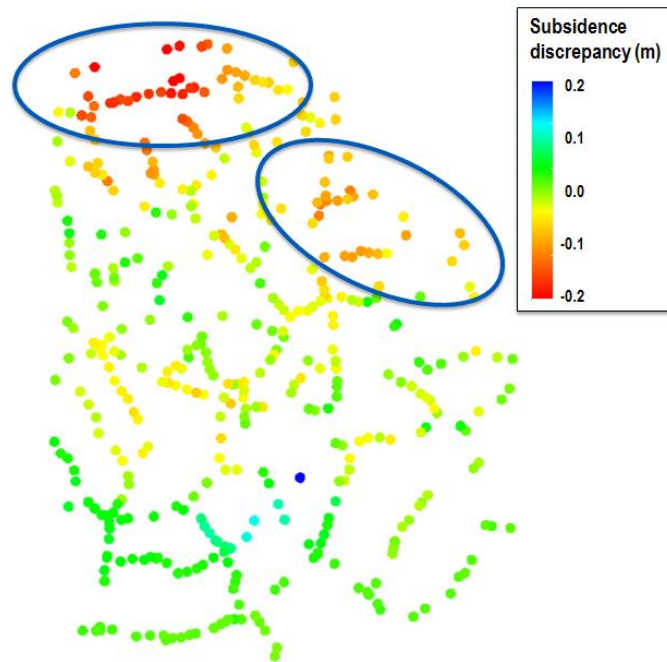


Figure 24. Difference between the subsidence measured in the Groningen Field location vs. the calculated subsidence based on the 2012 reservoir model RM1. The mismatch reaches a value of about 20 cm in the North West part of the field which is essentially due to the original reservoir model used to estimate the geomechanical response.

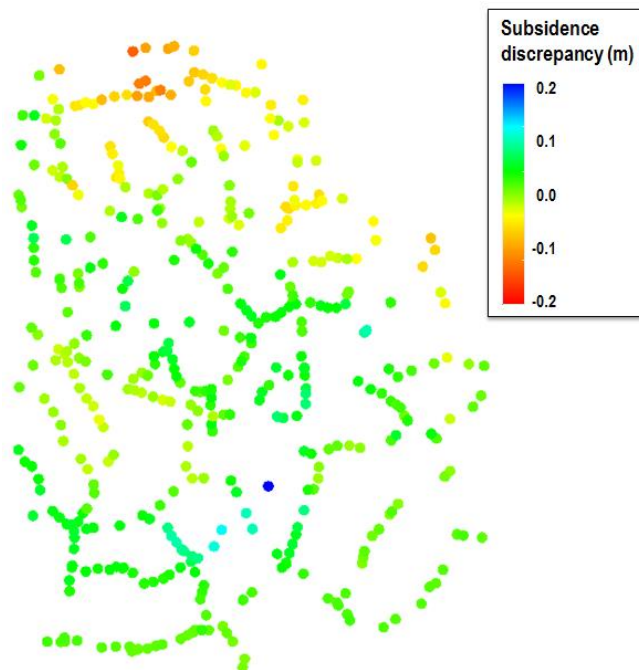


Figure 25. Difference between the subsidence measured in the Groningen Field location vs. the calculated subsidence based on the 2012 reservoir model RM2 in 2012. 98.5% of the modelled subsidence points have less than 10 cm difference with the measured data.

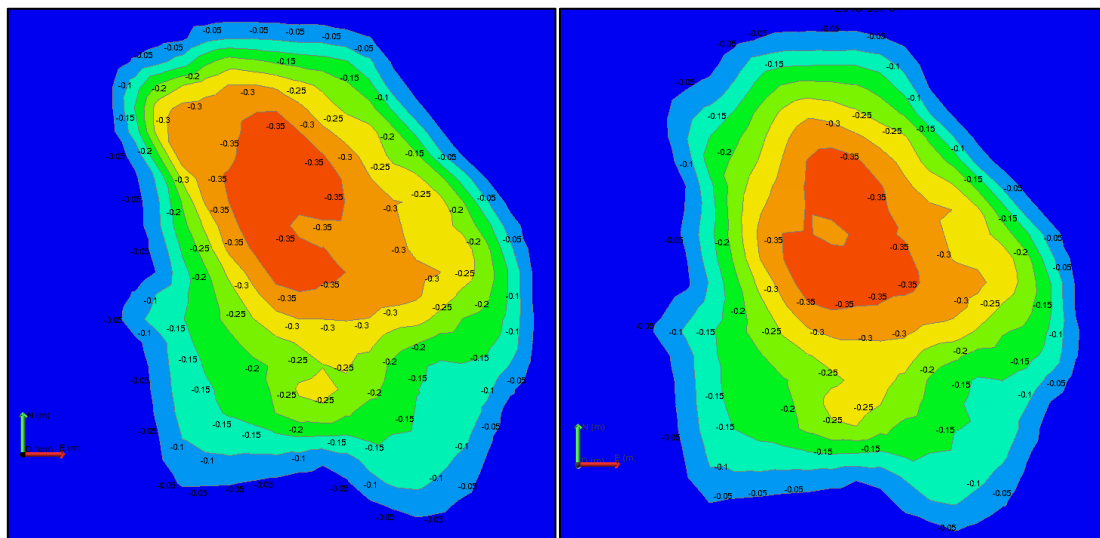


Figure 26. Contour map of the surface subsidence estimate in 2012 using the finite element analysis based on: (left) the reservoir model RM1 and (right) RM2. The scale reported on the contour lines is in meters, therefore the maximum amount of subsidence obtained by both reservoir models is between 35 and 40 cm.

Influence of Salt Creep during production

Comparison between the model with a creeping salt through the depletion stage and the model with an elastic salt layer in the depletion stage shows that the effect of the creeping salt on the stress in the most critical part of the fault is minimal. **Appendix 2 Assessment of the Effect of Salt Creep on the 3-D geomechanical model** describes the additional analyses performed on this subject. These analyses concluded that the creeping behaviour of the salt is used to determine the in-situ stress state before the production of the field. During the production simulations, no creep behaviour is used in the calculations because the effects were assessed to be minimal and, at the same time, were increasing significantly the calculation time.

The calibration results discussed above did not include the effects of salt creep during the depletion stage. Because of the depletion encountered in the reservoir formations located just underneath the salt, higher differential stresses should be expected near in the base of the salt layer. This excess of differential stress will cause some salt creep during the production phase. To determine the accurate response of the salt relaxation and its influence on the stress field during the production, the most rigorous approach consists of coupling the visco-elastic response of the salt with the poro-elastic response of the reservoir. Unfortunately, modelling this non-linear material response requires significant computational power beyond the scope of this study.

The impact of salt creep during the production period spanning from 1964 to 2012 is investigated by comparing the simulation results of a model accounting for salt creep during the production period with a model without salt creep. The approach consists of first modelling the field under virgin reservoir conditions and letting the relaxation act within the salt until the differential stress drops below very small values (< 1 MPa). As discussed in section **3.1.1 Initial in-situ stress state from the offset well**

analysis, this stress condition establishes our initial conditions for all the production scenarios considered for this study. Depletion is then simulated using two distinct cases:

1. The reservoir pressure decrease during the 1964-2012 period without considering the effects of the Zechstein salt relaxation.
2. The reservoir pressure decrease from 1964 to 2012 similarly to the previous case. Following the production period, the Zechstein and basal Zechstein salts are allowed to relax viscously during a 48 years time-span following reservoir production.

Because of the modelling limitations, the Zechstein salt relaxation is not performed simultaneously with the reservoir depletion, but successively. Using this approach tends to over-estimate the amount of differential stress observed at the base of the Zechstein, which in return could provide an excessive amount of creep during the production.

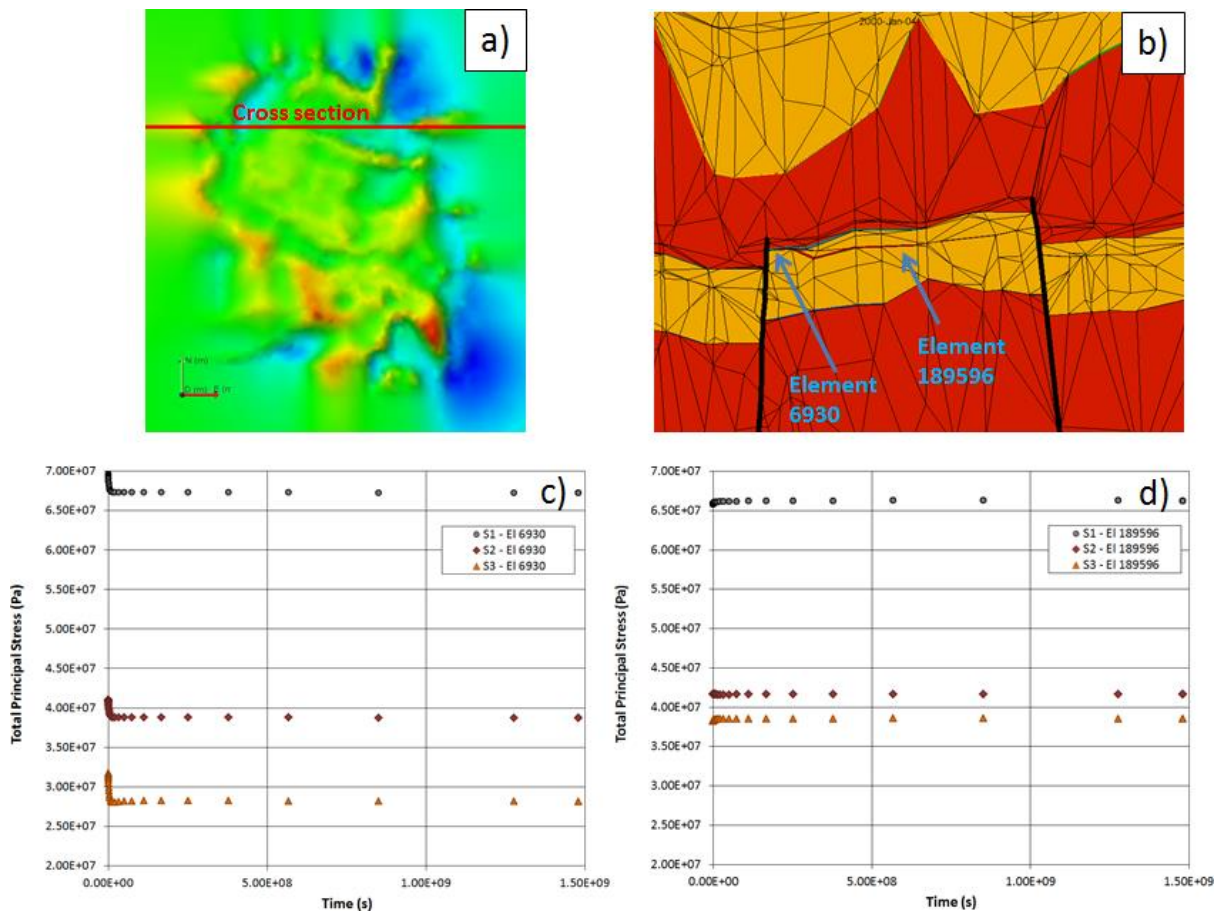


Figure 27. a) Localisation of the cross-section where the salt creep effects are investigated. b) Cross section view of the viscous layer (yellow) and the poro-elastic formations (red). The stress response during the visco-elastic response occurring subsequent to the first 48 years of reservoir production is investigated at two locations; Element 6930, located in the depleted reservoir along large offset faults so that the element is adjacent to the salt. Element 189,596 is located in the Slochteren reservoir, at some distance to faults. Figures c) and d) show the stress response of the three principal stress components during the viscous response.

The two simulation cases were compared in order to estimate the influence of production induced salt creep. **Figure 27** and **Figure 28** show that the viscous response is not distributed homogeneously throughout the field. The viscous response is maximal when the viscous material is located close to a produced unit, a condition encountered near large offset faults. In addition, the stress and strain response is also significant (variation of S_{hmin} larger than 3 MPa) in areas with large structural variations or near the limit of the reservoir, where a virgin formation is adjacent to a depleted, therefore altered, stress field (**Figure 28**). Although the differential stress within the Zechstein is minimal for the pre-production in-situ conditions, the stress field disturbance caused by the production of the underlying Ten Boer reservoir will cause some time dependent response within the Zechstein.

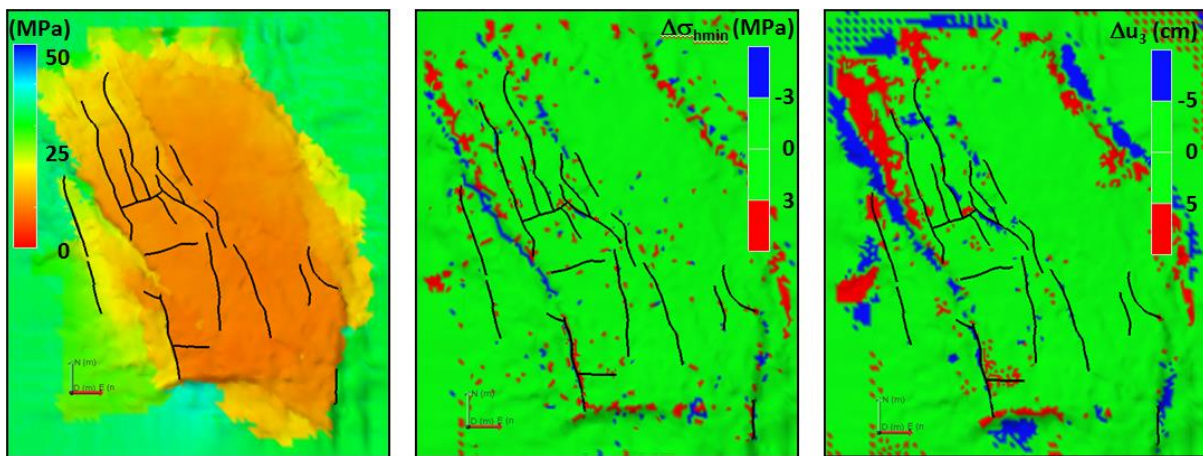


Figure 28. left) pore pressure distribution in the Slochteren reservoir in 2012 based on the RM1 model. Middle) difference between the stress response (S_{hmin}) in 2012 with and without salt relaxation. Right) vertical displacement comparison. The faults incorporated in the model are marked in black colour.

During the 48 years of production, we observe that the viscous response of the salt can account for up to 5 additional centimetres of vertical displacement compared to a purely elastic model in the Ten Boer and Slochteren formations. At surface the influence of the salt creep on the calculated subsidence is attenuated by the overlying formations. When located away from faults with large vertical offset, the impact of the viscous relaxation is moderate, with the horizontal stress magnitudes varying by less than 3 MPa (**Figure 27** and **Figure 28**). For instance, the stress response observed at BRW-2 location indicates that the salt creep would cause an increase of the principal stress magnitudes lower than 1 MPa (**Figure 29**) compared to absolute stress magnitude in the range of 40 MPa (S_{hmin}) to 65 MPa (S_v). For the case of large offset faults, where the salt is next to the depleting reservoir, larger amount of viscous relaxation takes place due to the larger stress differential imposed to the structure. This results in some stress rebalancing near the limit of the reservoir and some of the faults (**Figure 28**). The horizontal stress magnitudes change by about 3 MPa due to the salt creep caused by the field production and the subsidence locally varies by up to 5 cm compared to a case where viscous effects are neglected.

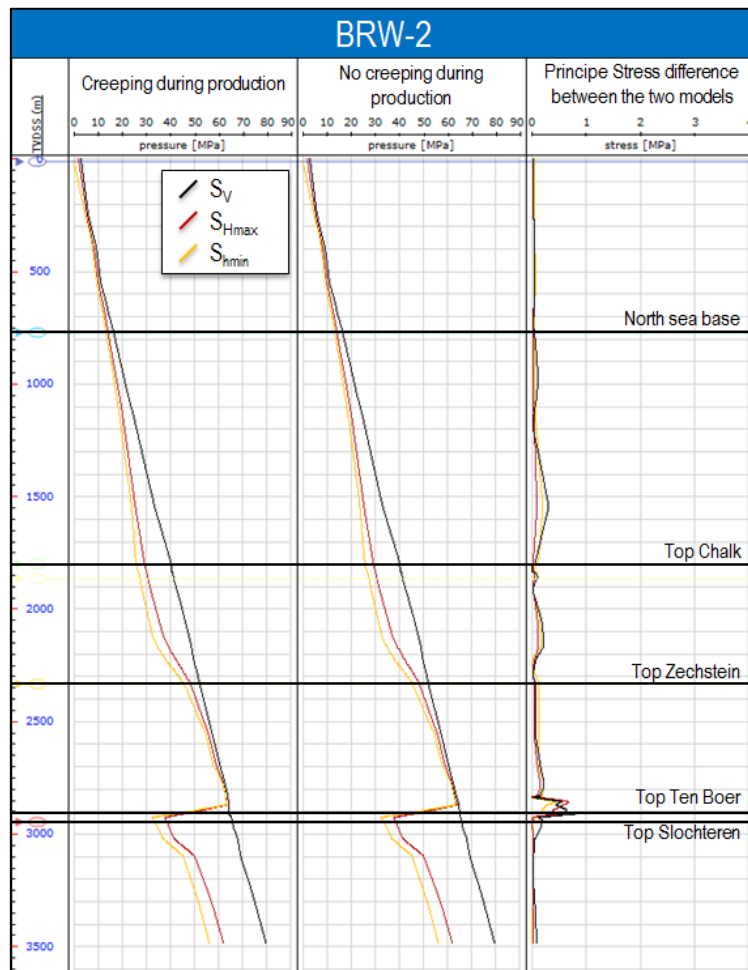


Figure 29. Comparison of the stress response between the model without salt creep during production (case 1) and one with salt creep during production (case 2)

As discussed later in this report (section 3.3), the poro-elastic response of the reservoir impacts the horizontal stress magnitude by nearly 20 MPa over the life of the field. While the time dependent effects alter the stress field, particularly close to faults, these effects are nearly an order of magnitude lower than the depletion induced changes. Because of the additional computational cost of including the salt creep during the production phase is high, and its impact on the stress magnitude is limited in comparison to the poro-elastic response induced by the field depletion, the following results do not consider this parameter unless explicitly stated.

3.2.2 Results of the stress response of the Groningen Field

After careful calibration of the stress and strain response, a number of reservoir models were coupled to the finite element simulator (one way coupling) in order to verify and predict the field response for

several production scenarios. **Figure 31** and **Figure 32** illustrate the stress evolution from 2014 to 2080 for the reservoir model 3 (RM3) as an example of the output provided by the simulations.

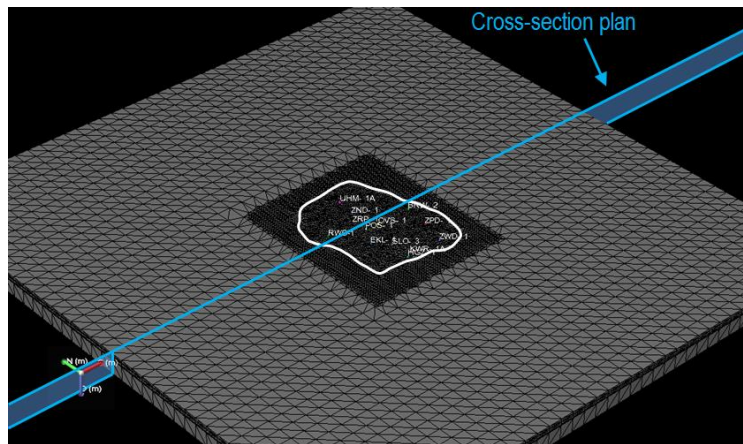


Figure 30. Position of the cross-section plan used for the two following figures on the Groningen Field

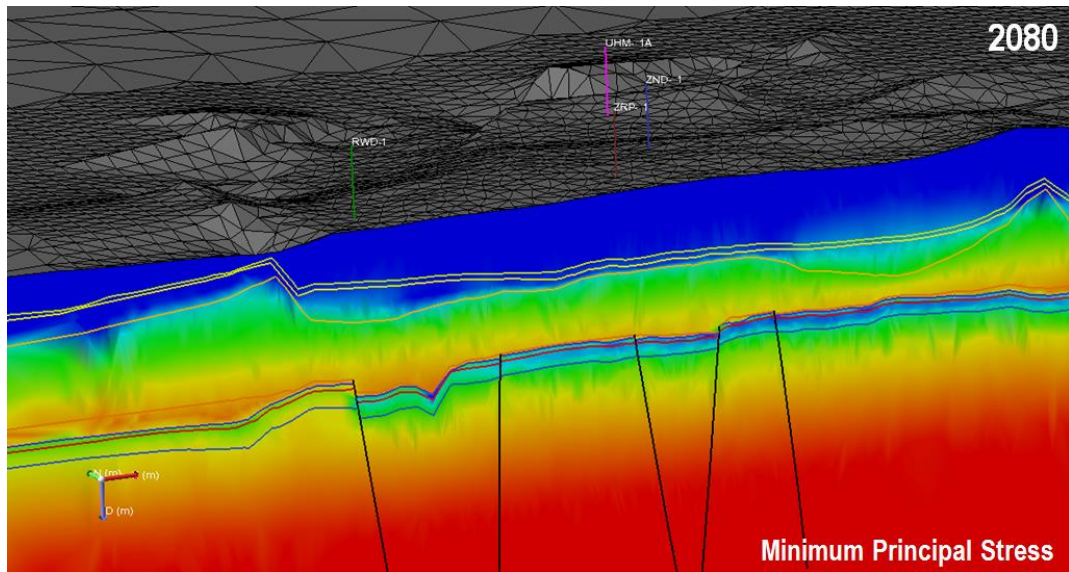
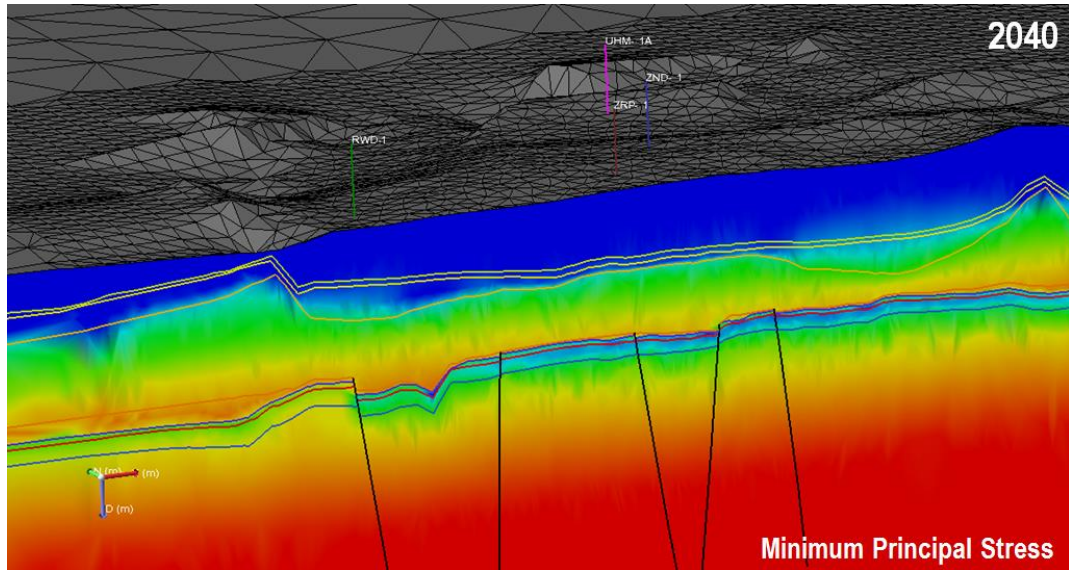
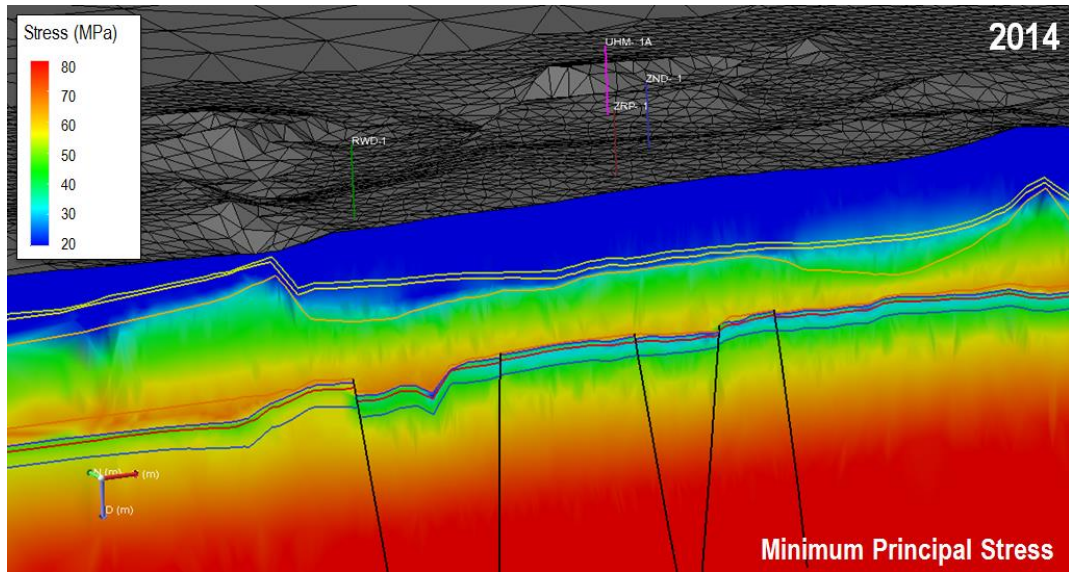


Figure 31. Cross Evolution of the minimum principal stress from 2014 to 2080 for the Reservoir Model 3 (RM3)

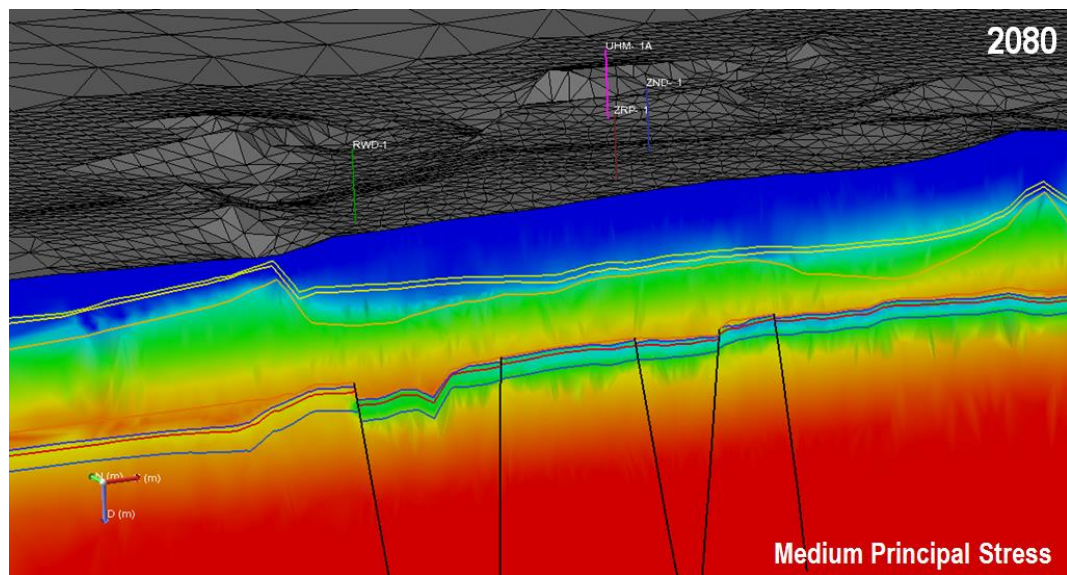
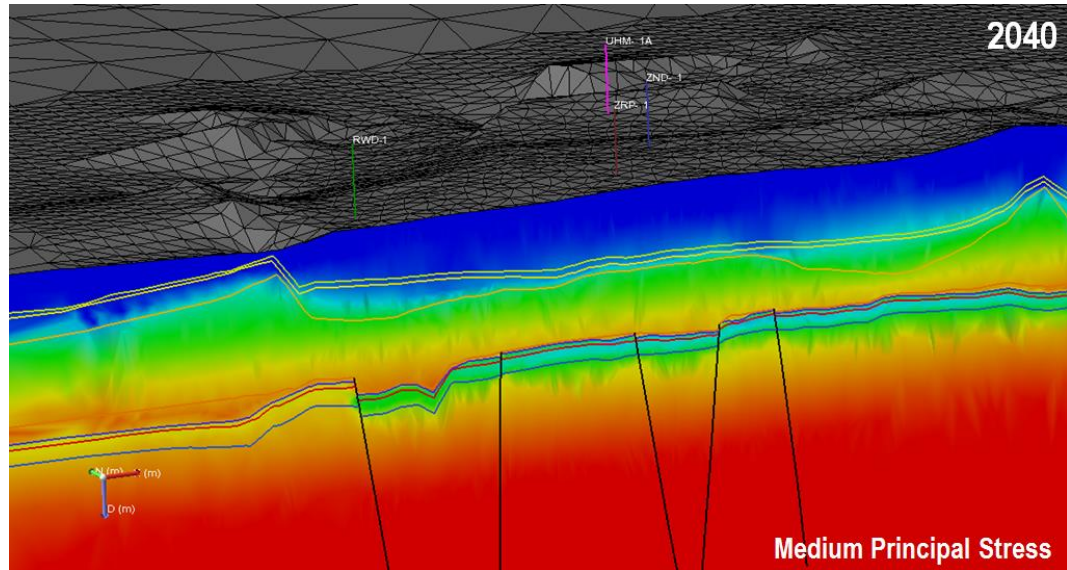
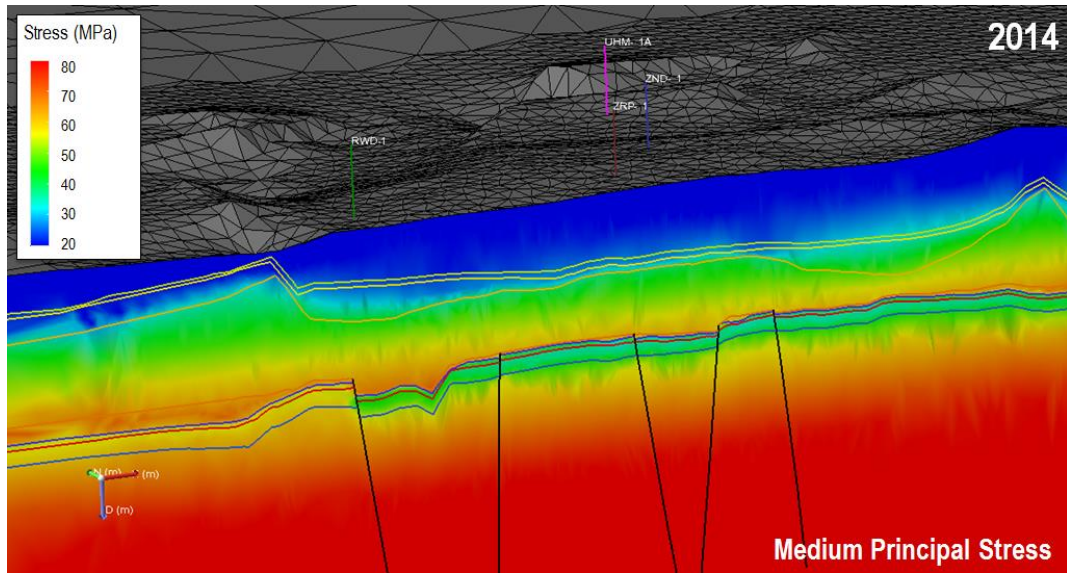


Figure 32. Cross Evolution of the medium principal stress from 2012 to 2080 for the Reservoir Model 3 (RM3)

3.3 Evolution of the principal stress magnitudes with depletion (stress paths)

One of the objectives covered by this project consists of understanding the evolution of the horizontal total stress magnitudes (S_{hmin} and S_{Hmax}) during the production of the Groningen Field. That is, to constrain the so called stress path which reflects the changes of all principal in situ stresses; in particular the least principal stress, S_{hmin} , during field life (i.e. during production and injection). Using the available minifrac and step rate tests, we attempt to establish the stress path parameter for the reservoirs. The stress path parameter is defined as follows for S_{hmin} (similar definition applies to S_{Hmax}):

$$A_{Shmin} = \frac{\Delta S_{hmin}}{\Delta P_p} \quad (16)$$

Where	A_{Shmin}	Stress path parameter for S_{hmin}
	ΔP_p	Pore pressure depletion
	ΔS_{hmin}	S_{hmin} change due to the depletion

The determination of the stress path parameter for the least principal stress (A_{Shmin}) would usually require minifrac or extended leak-off tests performed at various intervals during the field production to be validated. However, no assessment of the minimum horizontal stress was available in the depleted reservoir that could be used to calibrate the dynamic response of the reservoir.

In the absence of numerical models, the stress path parameters are often calculated analytically based on hypothesis regarding the geometry of the reservoir (bilateral constraints) and its mechanical properties (Biot Coefficient and Poisson's ratio), in which case the variation of horizontal stress magnitudes, ΔS_h is expressed as follow:

$$\Delta S_{hmin} = \alpha \frac{(1-2\nu)}{(1-\nu)} \Delta P_p \quad (17)$$

Where α is the Biot coefficient and ν is the Poisson's ratio.

The Equation 17 provides reasonable estimates of the stress path in the environment where the aforementioned assumptions are justified. In faulted or compartmentalized structures, where the reservoir thickness is not negligible and not uniform compared to the lateral extensions of the formation, this approach has limitation. The best alternatives consist of calibrating the response with field observations, if available, or undertaking numerical simulation to account for the structural effects.

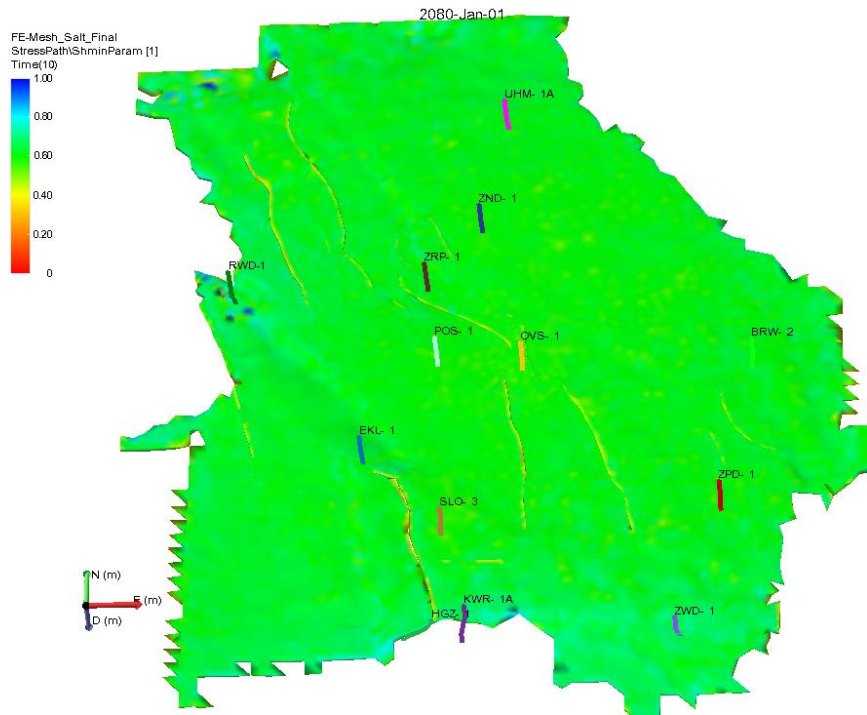


Figure 33. Top view from the Slochteren of the S_{hmin} stress path parameter in the Groningen Field (Reservoir model scenarios 3). The stress path parameter shows little variation across the field, with a typical value close to 0.6.

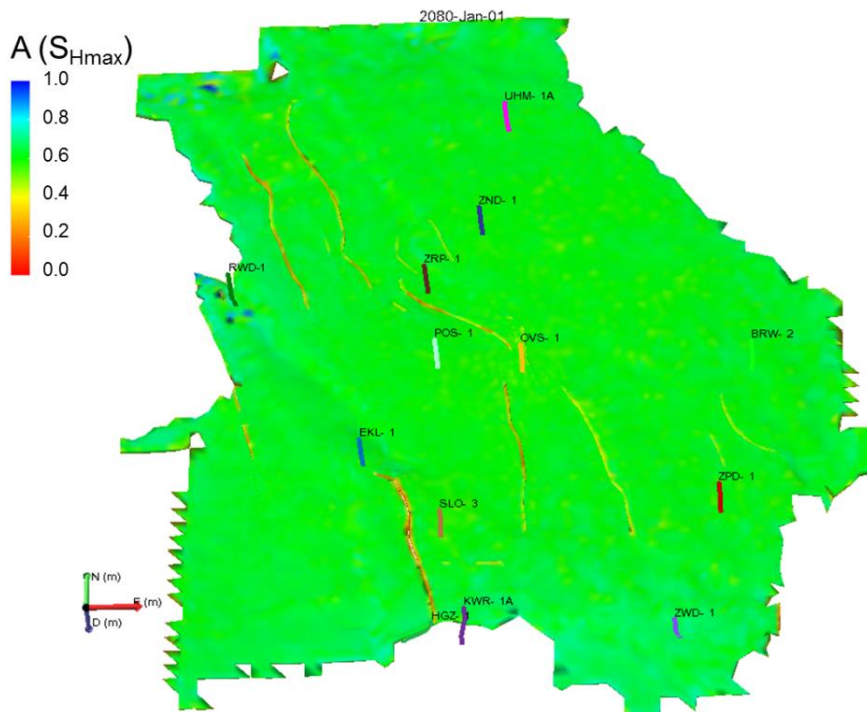


Figure 34. Top view from the Slochteren of the S_{hmin} stress path parameter in the Groningen Field (Reservoir model scenarios 3). The stress path parameter shows little variation across the field, with a typical value close to 0.6, very similar to the minimum horizontal stress.

An intrinsic advantage of finite element simulations is that the variations of the stress field, caused by reservoir production, are calculated regardless of the complexity of the structural geology. As a consequence, the variations of the horizontal stress magnitudes are primarily constrained by the amount of depletion, the rock mechanical properties (Young’s modulus and Poisson’s ratio) and the geometry/structure of the depleted unit. The reservoir stress paths for the principal horizontal stresses can therefore be estimated directly from the resulting numerical simulations, rather than assuming a value (typically $A_{S_{Hmin}} = A_{S_{Hmax}} = 2/3$ for poroelastic behaviour) as is commonly done with a well centric approach. Another important note is that the stress path parameter is not necessarily constant everywhere the field (formation thickness and rock properties vary across the field, discontinuities near faults) and is in principle different for both horizontal stresses.

Figure 33 and **Figure 34** show maps of the stress path parameters for S_{Hmin} and S_{Hmax} respectively for the Groningen Field (Reservoir model 3). Note that only values within the reservoir are represented, as the reservoir is the only location where depletion occurred. In other bounding formations, the stress response is essentially limited to arching effects and visco-elastic relaxation (Zechstein salts).

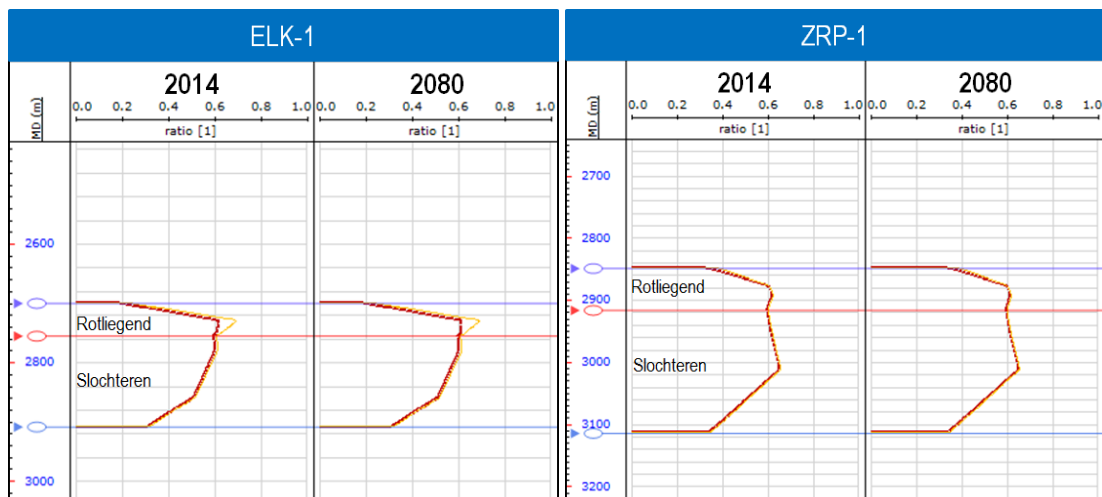


Figure 35. Export of the Stress Path Parameters of both S_{Hmin} (yellow) and S_{Hmax} (red) for the timesteps 2014 and 2080 (Reservoir Model 3) in well ELK-1 (left) and ZRP-1 (right)

Figure 35 illustrates that the S_{Hmin} stress path for the reservoir layers is $A_{S_{Hmin}} \sim 0.6$ and does not exhibit major variations throughout the field. Similarly, the stress path for S_{Hmax} ($A_{S_{Hmax}}$) is similar to $A_{S_{Hmin}} \sim 0.6$. To validate the stress path parameters, it is possible to back calculate the theoretical Poisson’s ratio needed to obtain a stress path of 0.6 using the relationship presented in **Equation 17**. Combined with this equation, a Poisson’s ratio of approximately 0.28 would be expected for a stress path parameter of 0.6, which is consistent with the Poisson’s ratio values mapped onto the simulation mesh (**Figure 14**). It is expected that variations in Poisson’s ratio will affect the horizontal stress response from the finite element calculations. For instance, smaller Poisson’s ratio, such as 0.18 close to values obtained from laboratory samples collected in the Slochteren would lead to larger stress path values around 0.80.

However the depletion of the reservoir units has no significant effects on the magnitude of the vertical stress, S_v (see **Figure 36**). The stress path for S_v is A_{S_v} close to 0.0, indicating that arching effects is not significant. As illustrated in Figure 36, the magnitude of the vertical stress remains practically unchanged above the reservoir units (stress arching is minimal), meaning that most of the changes in reservoir conditions are balanced by an adjustment of the horizontal stress components.

Stress path parameters were similarly interpreted for the other reservoir models and were similar to the values discussed above.

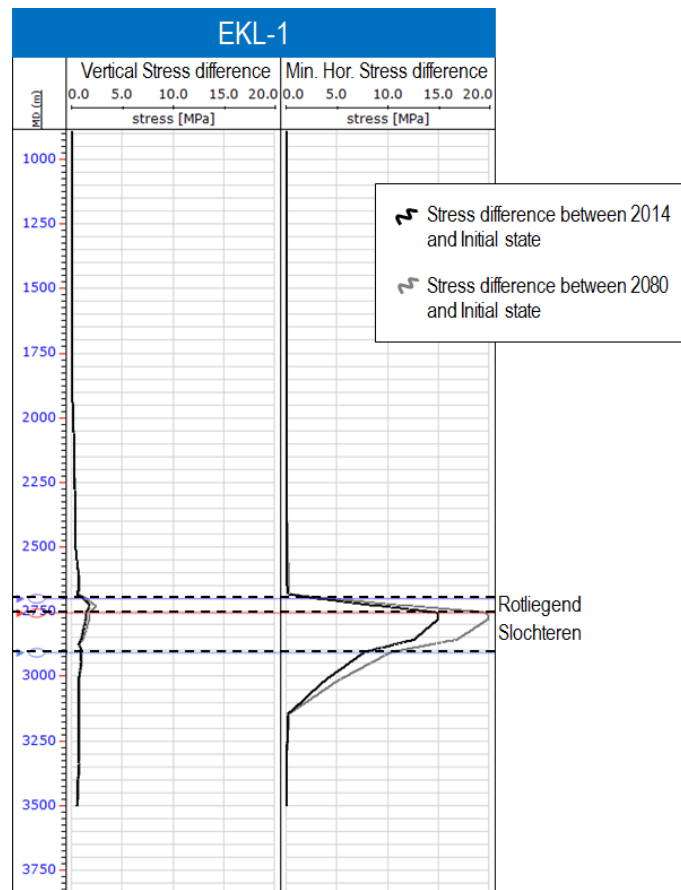


Figure 36. Export of the stress differences between the 2014 and the initial time-steps (black) and between the 2080 and the initial time-steps (grey) for the vertical stress and the minimum horizontal stress.

4 Fault stability analysis

The numerical simulations are used to capture the stress and strain fields throughout the depletion history of the entire field, for both reservoir and non-reservoir formations. The approach assumes that geological discontinuities are static, i.e. no displacement is permitted along fault planes. Therefore it considers only the static effective stress condition on the fault planes.

Since poro-elasticity and visco-elasticity are acting during the field production, the principal stress magnitudes are constantly evolving. This stress response implies that the mechanical stimulation applied on a fault surface varies with time. Within this context it is possible to assess the potential risk of slip for each fault patch during reservoir production. To perform this action, the concept of critically stressed faults was applied. The approach is based on the hypothesis that a fault patch can sustain an amount of shear stress that is proportional to the normal stress applied on this surface (Mohr-Coulomb theory) while the material surrounding the faults remains intact.

If the ratio of shear to effective normal stress exceeds the frictional strength of the fault, the fault is considered to be critically stressed. Due to the evolution of the pore pressure throughout time and the related change in horizontal stresses, some fault patches can become critically stressed or, on the conversely, reach a more stable configuration. When in a critical state, a fault has a larger likelihood for slip, which can cause induced seismicity and potential fault leakage.

4.1 Principles

Since the numerical simulation provides an arbitrarily oriented stress tensor, it is possible to project each principal component onto any surface and to extract a normal and tangential component of the tensor along an oriented fault. Each node describing the surface of the fault is therefore characterised by a normal and tangential stress, a pore pressure as well as the mechanical characteristics of the fault (sliding friction and cohesion). For every fault plane orientation, where geometry is defined by a trimmed area constructed from the polylines sets, the fault stability can be characterised using the Mohr-Coulomb representation (**Figure 37**).

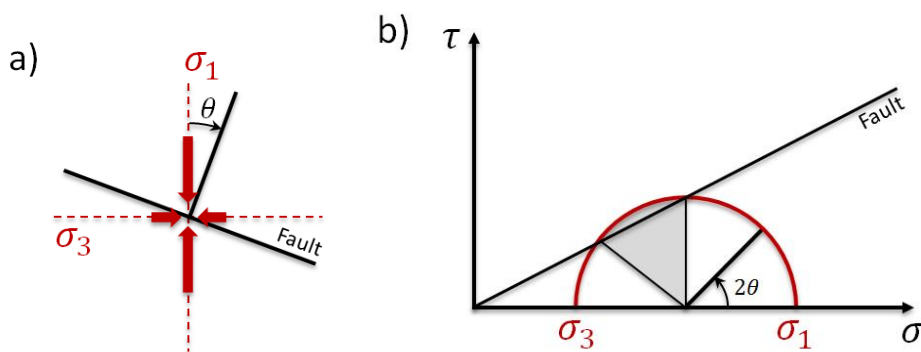


Figure 37. a) Figure showing the stress conditions on a patch of a fault in a normal 2-D coordinate system. b) Mohr diagram corresponding to the fault presented in a). (The grey zone shows the range of fault orientation that would be critically stressed under the presented state of stresses)

The increased seismic activity occurring during the last decades in the Loppersum area is used as a baseline to constrain the frictional properties of the faults. Initially, the cohesion was set to 0 while the friction coefficient was set to 0.6 for this analysis. The initial decision to set the friction coefficient at 0.6 (Byerlee’s law) was driven by the study performed by Zoback and Townend (2001) which states that in situ stress measurements in relatively deep wells in crystalline rock indicate that stress magnitudes seem to be controlled by the frictional strength of faults with coefficients of friction between 0.6 and 1.0 (**Figure 38**). The case of cohesionless fault with a coefficient of sliding friction of 0.6 is identified as case 1.

The properties that describe the slip behaviour of fault planes can however not be easily constrained. Van den Bogert et al (2013) presented an alternative set of parameters based on the assumption that fault properties should be weaker than the surrounding formation. In other words a fault has a lower capacity to support shear stress compared to an intact host rock. This case is identified as case 2.

Therefore, two sets of faults failure properties are compared in this study:

1. Case 1: $C_0 = 0$ MPa and $\mu_s = 0.6$ (30.6 degrees)
2. Case 2: $C_0 = 7$ MPa and $\mu_s = 0.23$ (13 degrees)

Both fault stability analysis cases are presented and discussed in section 4.2.1 **Comparison between the fault properties cases.**

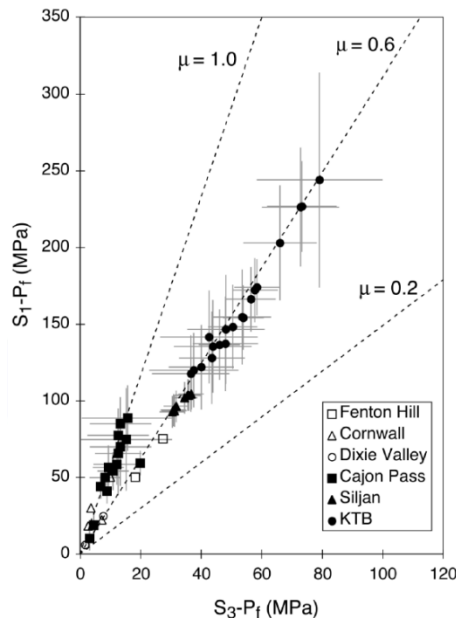


Figure 38. In situ stress measurements in relatively deep wells in crystalline rock (Zoback and Townend (2001))

4.1.1 Tau ratio

Tau ratio is a relative property related to the shear stresses acting on a fault plan and provides a measure of the fault slip potential. To calculate Tau ratio (τ_{ratio}), the observed shear stress, τ , is divided by the critical shear stress τ_{max} :

$$\tau_{ratio} = \frac{\tau}{\tau_{max}}$$

The values τ_{ratio} can be interpreted as follows:

- If $\tau_{ratio} < 1$, the fault is considered stable.
- If $\tau_{ratio} \geq 1$, the fault is critically stressed.

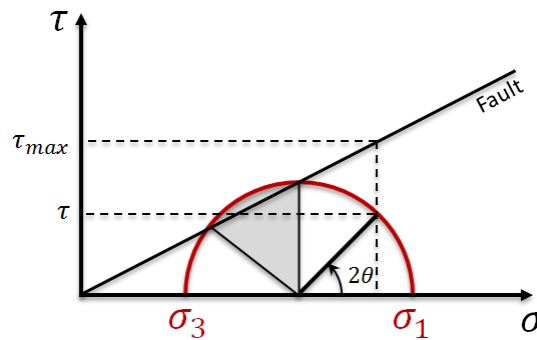


Figure 39. Tau ratio describes the fault slip potential by taking the ratio between the observed or calculated shear stress τ and the critical shear stress τ_{max} .

The angle between the maximum principal stress direction and the fault, represented by the angle θ in **Figure 39**, controls fault slip. Only the optimal range of values of θ where Tau ratio is equal or greater to 1 will allow fault slip (grey zones in Figure 39). Fractures in this range are critically stressed. For values of the angle θ that are not within this optimal range slip is unlikely since the shear stress will not exceed the frictional strength of the fault.

4.1.2 Mohr representation of fault stability

The ratio of shear to normal stress varies along the fault planes because of local stress variations (due to salt creep, faults, depletion, etc...) or changes in fault dip and azimuth. Both normal and tangential stress can be calculated in different locations of the fault (nodes). Knowing the frictional strength and the cohesion of the fault it is therefore possible to represent graphically if a fault, or at least the most critically stressed area of a fault, is evolving towards an unstable or stable state. As seen on **Figure 40**, the Mohr representation is an ideal way of representing this evolution. In this figure position 1 represents the initial stress state of a critically stressed fracture, point 2 the fracture becomes stable as a result of depletion, and in position 3, re-injection has again changed the proximity of fracture to frictional failure.

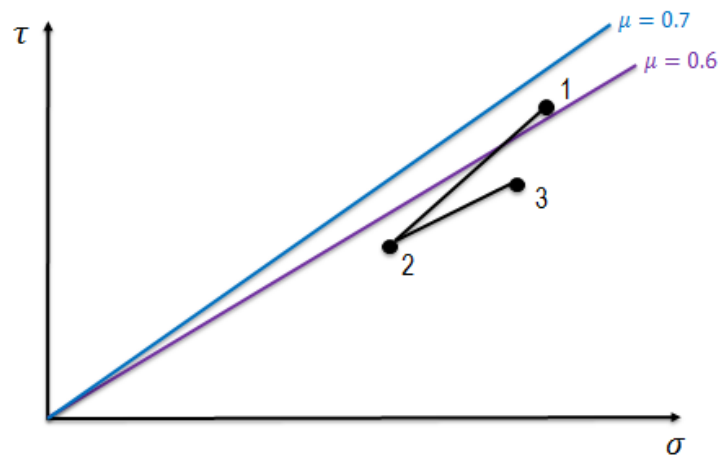


Figure 40. Mohr representation of the normal and tangential stress applied on a fault patch caused by the variations in reservoir pressures (not from the analysis)

4.2 Results

The results of the fault stability analysis performed for the different reservoir models are presented below. In order to visualize the field wide risk of fault reactivation in connection to the seismicity recorded in the Loppersum area, the faults were allocated colour codes bracket by values of Tau ratio observed on a given fault.

The colour mapping rule adopted in this report (**Figure 43** and following) is defined as follow:

- Red colour: the tau ratio exceeds the critical value of 1 anywhere along the fault surface
- Orange colour: the maximum value of the tau ratio calculated on the fault surface is between 0.9 and 1, i.e. the fault is close to its critical limit.
- Green colour: the maximum value of the tau ratio calculated one the fault surface is lower than 0.9, therefore the fault is expected to support further stress variation before reaching a critical state.

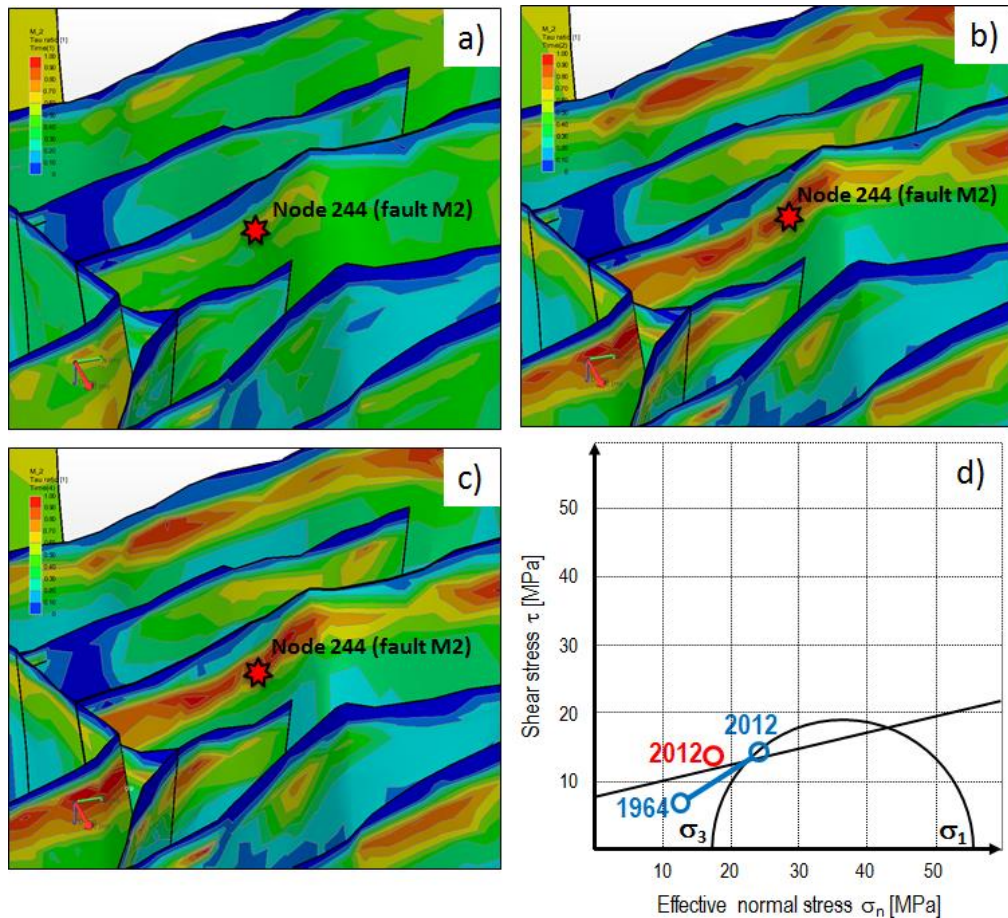


Figure 41. a) Tau ratio on the M_2 fault in 1964. b) Tau ratio in 2012 following 48 years of production without consideration of the viscous relaxation. c) Tau ratio in 2012 after 48 years of production and associated creep effects. d) The plots illustrate the variation of the shear to normal stress on the node 244 (indicated by a red star in a) b) and c)). The red symbol is utilized for the case inclusive of the salt creep effects during the production. The analysis shows that under the expected sliding friction and cohesion, the M_2 fault initially stable, moves towards an unstable state with increasing depletion. The critical state for this node is reached during the first 48 years of production using the reservoir model RM2.

It is important to mention that the colour mapping convention applied for the result visualization is based on the maximum value of the tau ratio calculated on a fault surface. Since the tau ratio is a function of the fault geometry (dip and strike) and the pressure applied on the fault, the value of the tau ratio changes along the fault surface (**Figure 41**). Therefore, it is possible for most of the fault surface to be in a stable configuration despite being identified to be at or near a critical state.

As discussed in the section **Influence of Salt Creep during production**, some viscous relaxation occurs during production, especially close to large offset faults. Figure 41 illustrates that the magnitude of the stress change induced by the time-dependent visco-elastic effects is significantly smaller than the variation in pore pressure during this time period. The impact of the salt creep tends to demobilize faults since it reduces both the effective normal stress and the shear stress resolved on the faults. As a result, the overall effect of viscous relaxation is minimal and is not considered in the remaining discussion.

4.2.1 Comparison between the fault properties cases

The fault slip analysis was performed using two separate sets of failure properties for the faults. For case 1, we assumed zero cohesion and a coefficient of sliding friction of 0.6 and for the case 2 we used a much lower sliding friction ($\mu=0.23$) and a cohesion of 7 MPa. The fault properties used for the case two were provided by NAM based on their internal analysis.

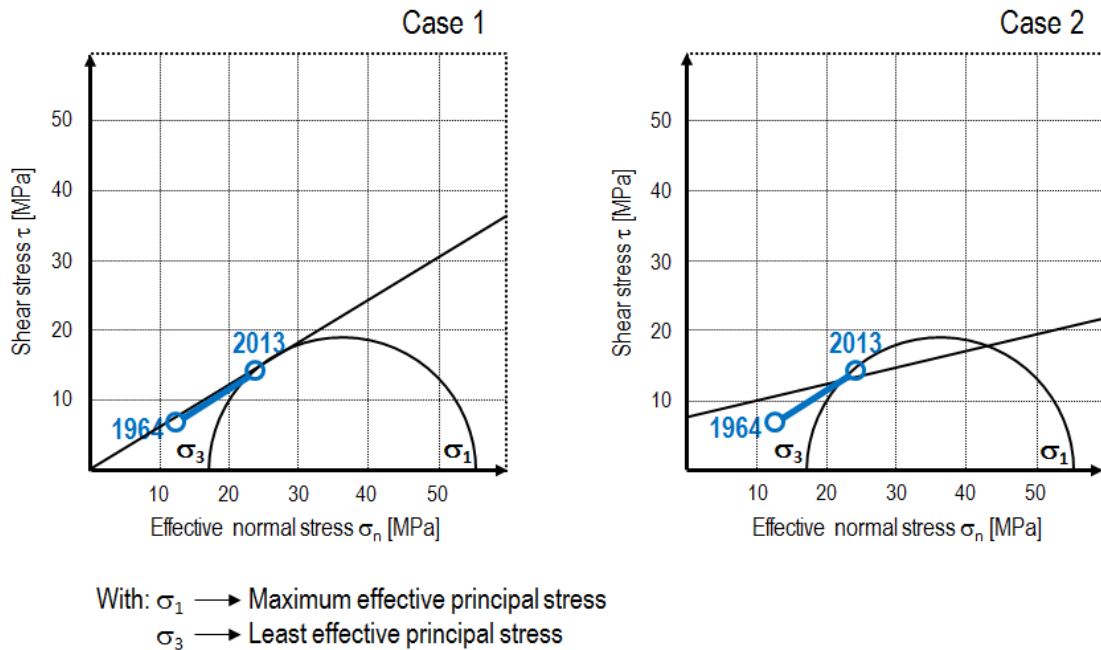


Figure 42. Comparison between the stability of the fault M2 - node 244 – (Figure 42) for the case 1 and case 2 during the production history of the reservoir. The fault properties assumed for case 2 (sliding friction=0.23; cohesion=7 MPa) to assess the fault stability suggests that the faults become critically stressed during the production (sometimes between 1990 and 1995), which is not the case when assuming the case 1 properties.

Figure 42 illustrates the importance of the fault mechanical characteristics for estimating the potential risk of reactivation. For case 1, the fault M_2 does not evolve towards an unstable state despite the larger differential stress applied on each fault patch exposed to the reduced reservoir pressure. In fact, the reservoir production causes an increase in effective normal stress applied to the fault which moves the Mohr circle to the right, which in turn tends to stabilize the fault. If the Coulomb failure line is less steep (i.e., a small coefficient of sliding friction as in case 2), the stability of the fault is Mohr sensitive to the larger differential stress (Mohr circle becomes larger with depletion) than it is to the variation in effective stress. Therefore in case 2, the fault M_2 is initially stable but becomes critically stressed between 1990 and 1995.

A comparison between the failure properties of case 1 (**Figure 44** to **Figure 48**) and those of case 2 (**Figure 49** to Error! Reference source not found.) indicates that several faults located near recorded seismicity are in a critical state when using the case 1 properties but stable using case 2 properties. In addition, the superposition of the critically stressed faults and the location of the recorded seismicity

between 1991 and 2010 (**Figure 53**) shows a good agreement when using the case 2 parameters. Consequently it was concluded that the fault properties used for case 2 describes more accurately the fault activity linked to the field production. These parameters are also aligned with NAM internal analysis of fault stability.

4.2.2 Analysis (Case 2: $C_0 = 7 \text{ MPa}$, $\mu_s = 13^\circ$ ($\mu = 0.23$))

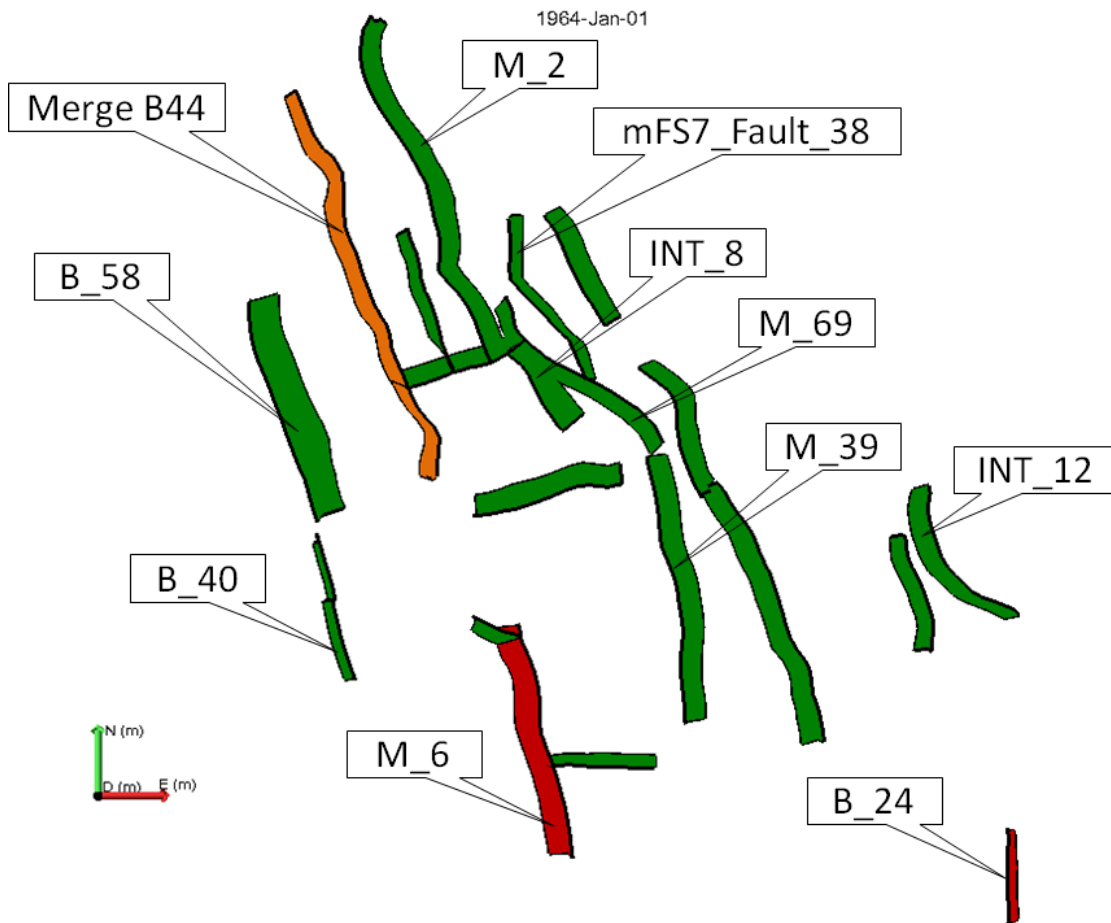


Figure 43. Location of the principal faults considered for the fault slip analysis. The colours indicates the stability conditions of the faults at the least stable point of the fault (critically stressed (red), in near critical condition (orange) or stable (green) in 1964 considering the fault stability parameters of case 2)

The fault slip analysis was performed for several time-steps using the five reservoir models. For this assessment, the faults were given the mechanical properties discussed in the case 2 of section 4.2.1. For each time step of each reservoir models, the stability of the faults was described using the risk coding defined in section 4.2. A discussion of the results is available in section 4.2.4 (page 74).

Discussion

Reservoir model 1

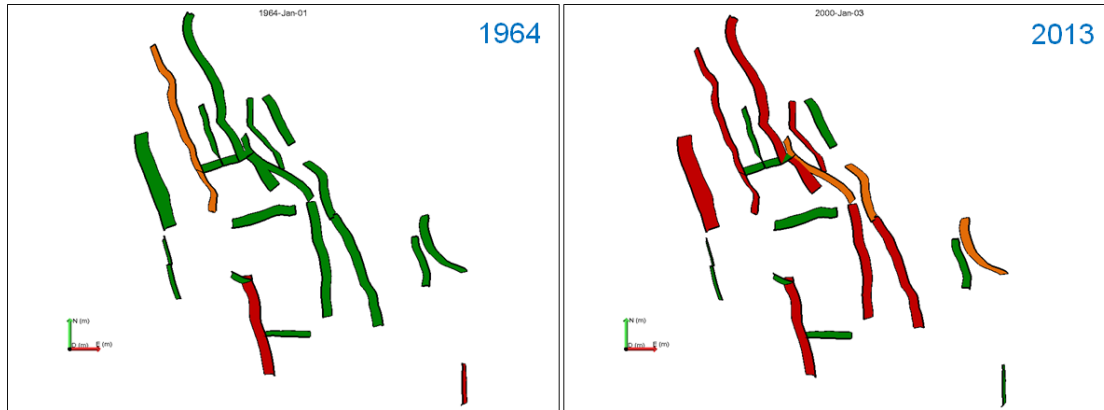


Figure 44. Comparison between the fault stability prior to field production and as of 2013.

Reservoir model 2

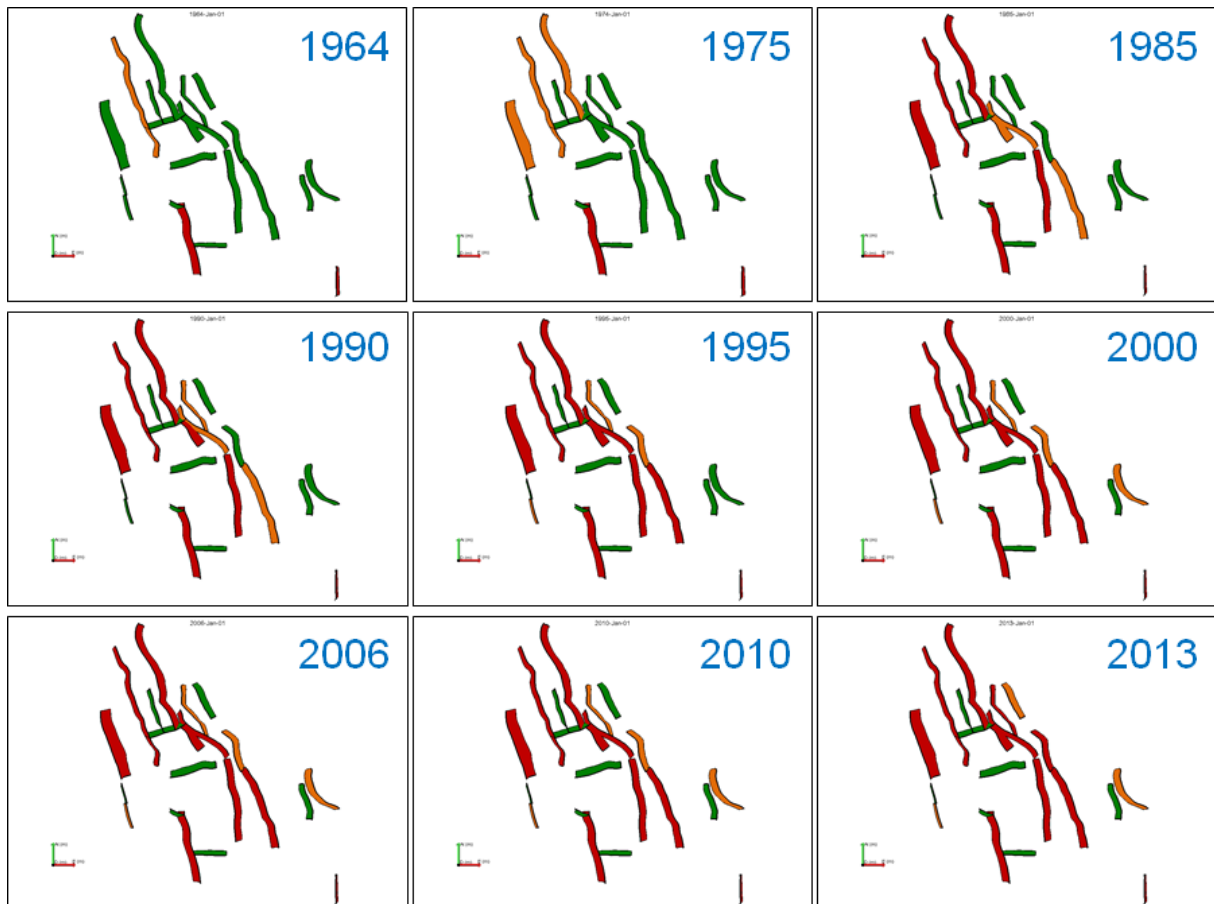


Figure 45. Representative time-steps presenting the reactivation risk of the different modelled faults in the Groningen Field (from 1964 to 2013). Most of the faults striking east west have lower risk of reaching an unstable state compared to faults striking NNE-SSW.

Forecast reservoir model 3

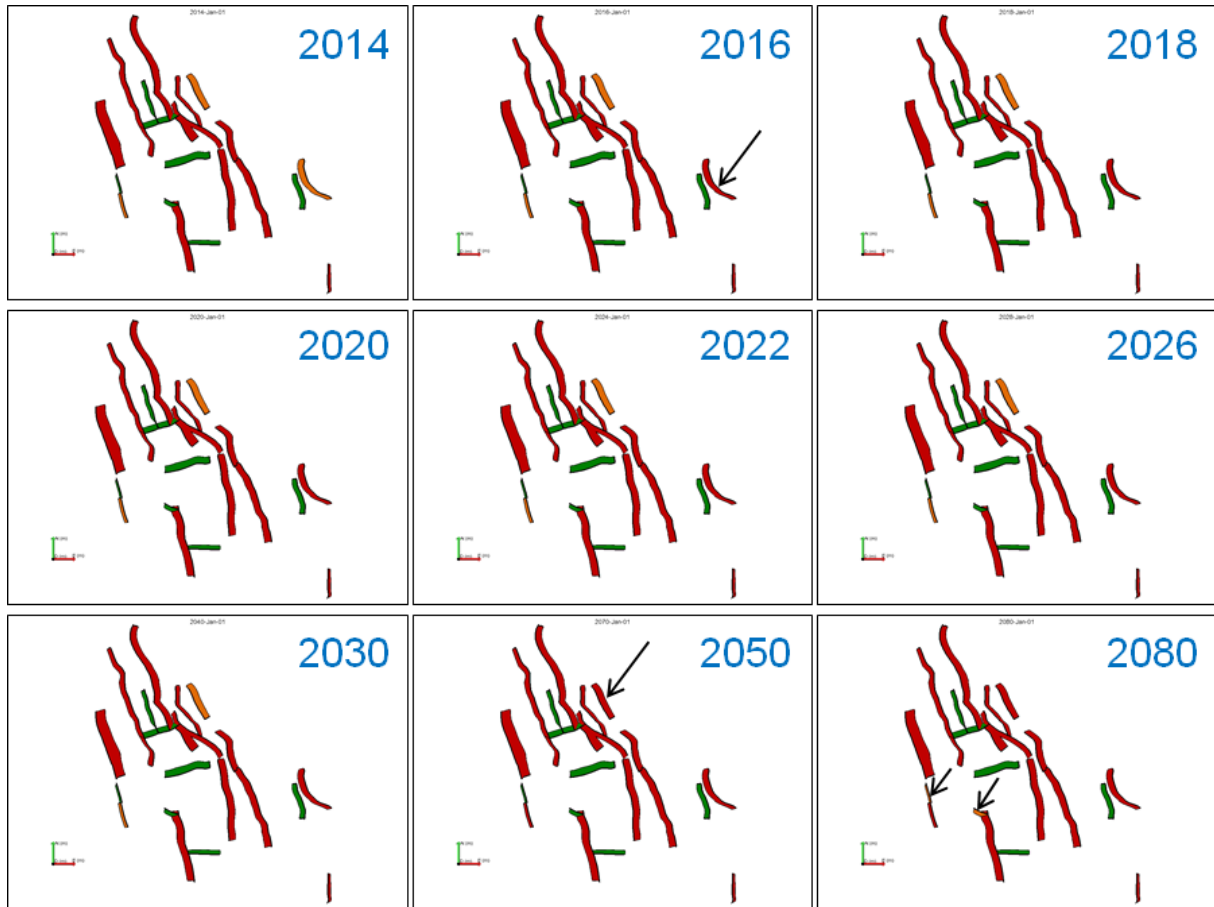


Figure 46. Time evolution of the fault stability assessment (forecast model RM3). The black arrows indicates locations where a fault passes into a less stable state

Reservoir model 4

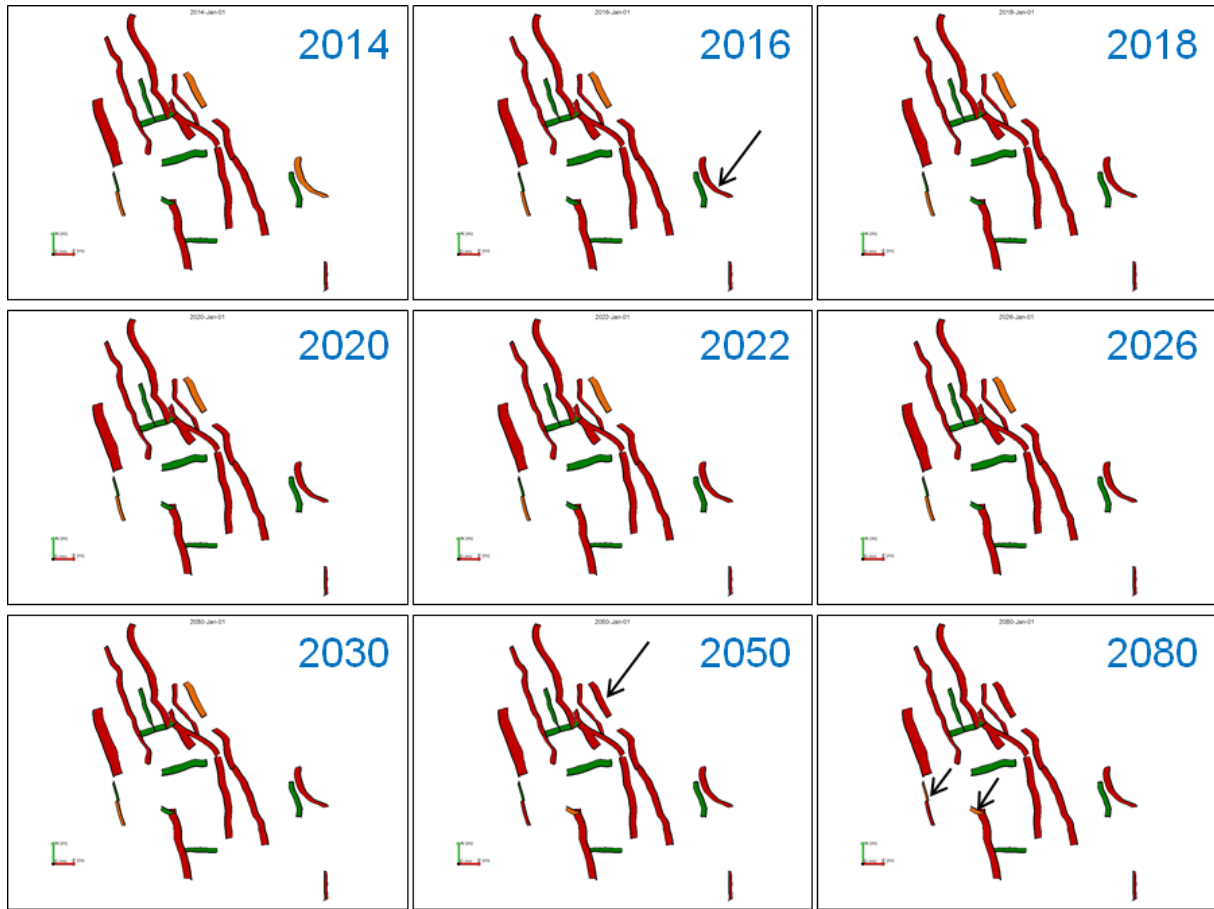


Figure 47. Time evolution of the fault stability assessment (forecast model RM4). The black arrows indicates locations where a fault passes into a less stable state

Reservoir model 5

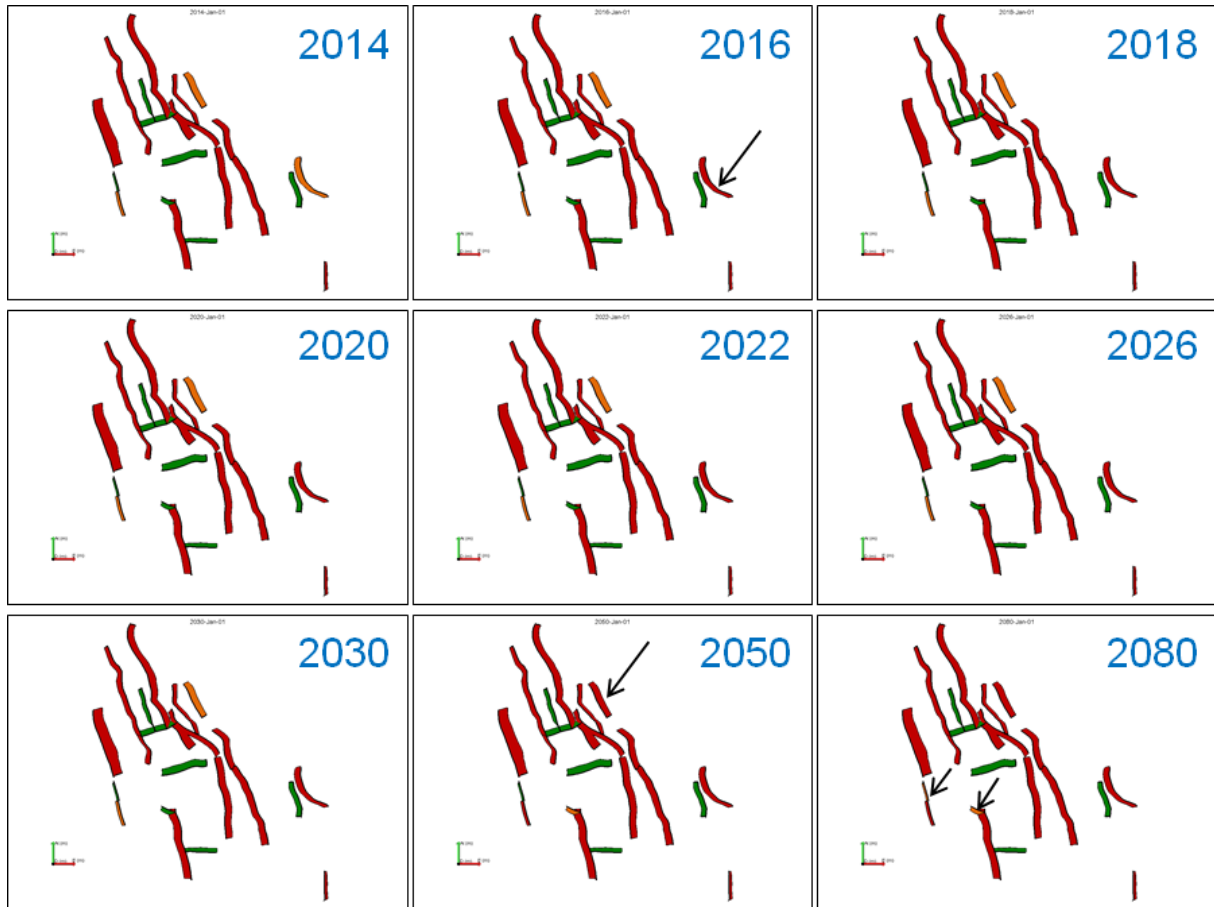


Figure 48. Time evolution of the fault stability assessment (forecast model RM5). The black arrows indicates locations where a fault passes into a less stable state

4.2.3 Analysis (Case 1: $C_0 = 0$ MPa, $\mu_s = 31^\circ$ ($\mu=0.6$))

This section summarises the fault stability assessment based on the Case 1. As described previously, this case was first established based on the study performed by Zoback and Townend (2001).

As discussed in a previous section, the results obtained using the fault mechanical parameters of this case (zero cohesion and sliding friction of 0.6) did not provide a satisfying match of the evolution of the fault stability through time with observations. Case 2 was preferred to represent the faults' activity over time.

The fault slip analysis was performed for similar time-steps as in section 4.2.2. For each time step of each reservoir models, the stability of the faults was described using the risk coding explained in section 4.2.

Reservoir model 2

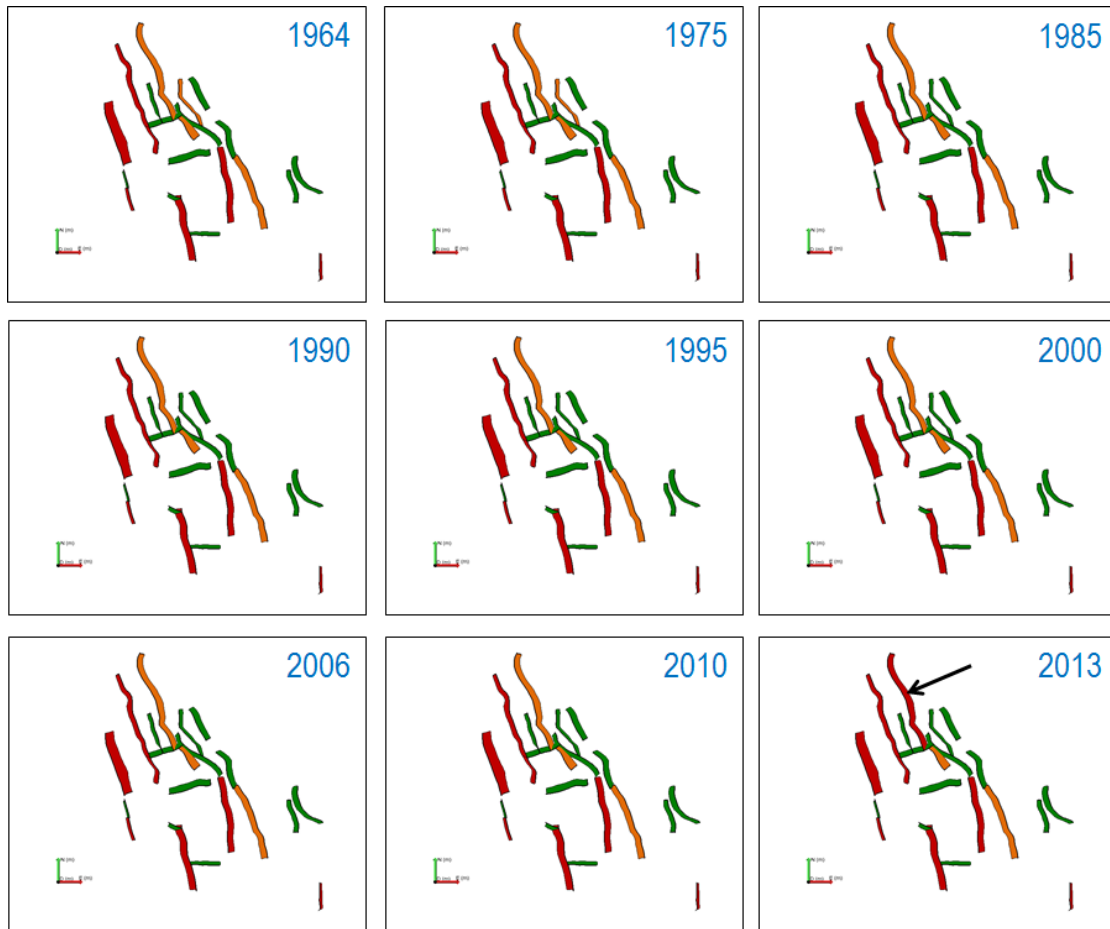


Figure 49. Representative time-steps presenting the reactivation risk of the different modelled faults in the Groningen Field (from 1964 to 2013) using case 1's parameters. The black arrow indicates location where a fault passes into a less stable state.

Reservoir model 3

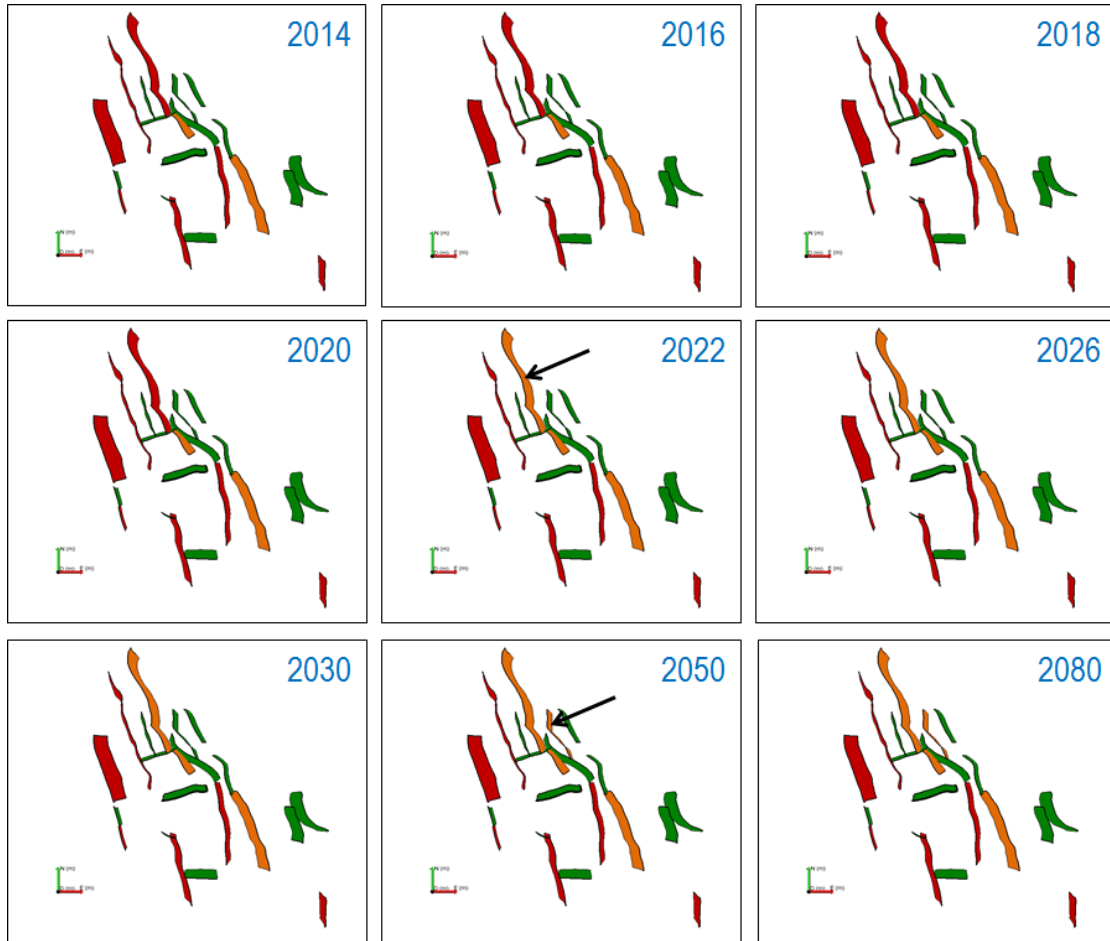


Figure 50. Time evolution of the fault stability assessment (forecast model RM3) using case 1's parameters. The black arrows indicate locations where a fault passes into a less stable state.

Reservoir model 4

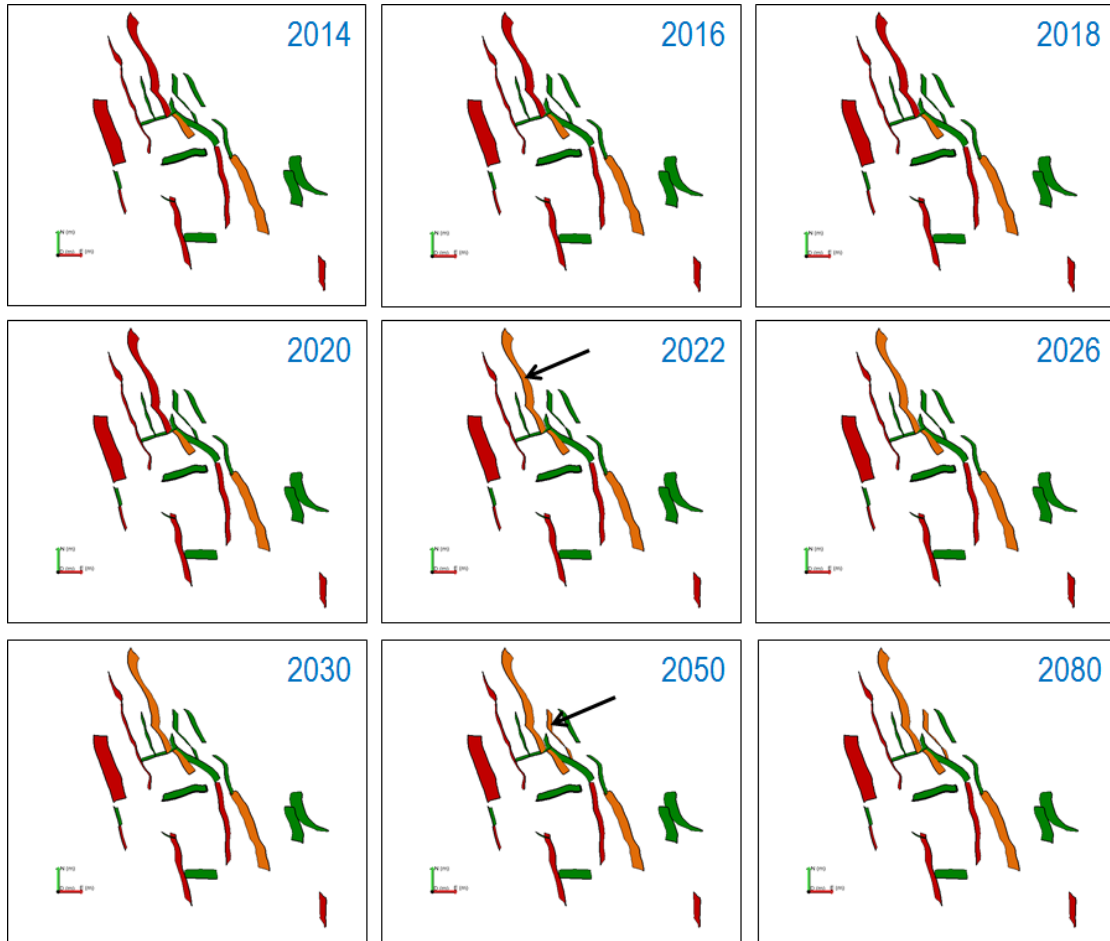


Figure 51. Time evolution of the fault stability assessment (forecast model RM4) using case 1's parameters. The black arrows indicate locations where a fault passes into a less stable state.

Reservoir model 5

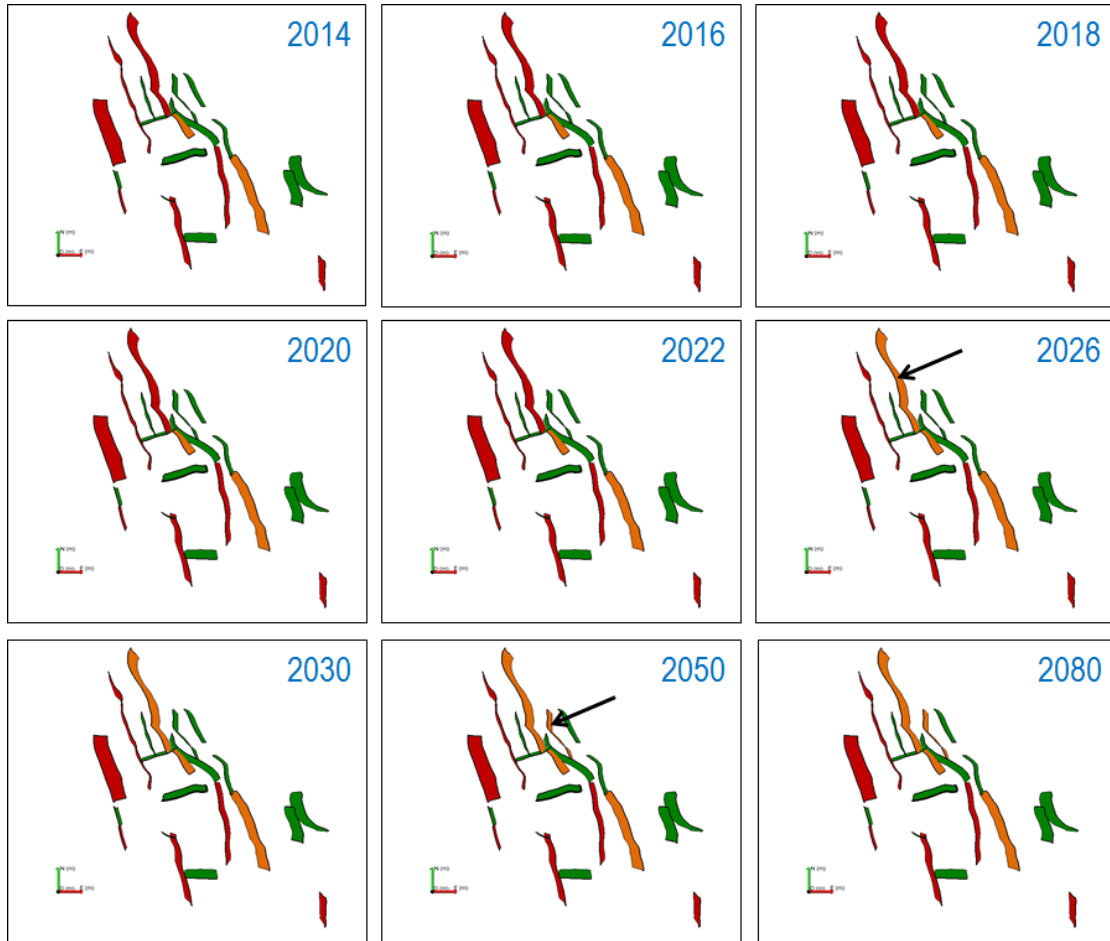


Figure 52. Time evolution of the fault stability assessment (forecast model RM5) using case 1's parameters. The black arrows indicate locations where a fault passes into a less stable state.

4.2.4 Discussion

The numerical modelling applied for the present study does not take into account fault movement (slip). Although the models provide the onset of fault slip, the stress redistribution (the drop in tangential stress) caused by fault motion and its impact on surrounding faults, is therefore not considered.

The finite element simulations provide a description of the 3-D stress field for different times throughout the history of production of the Groningen Field using a realistic description of the field structural geology. The stress and strain response was calibrated by comparing the surface subsidence with the vertical displacement calculated from the simulations. The field depletion causes significant stress readjustments to occur, which impact the stability of the faults. While depletion induces a reduction of the total horizontal stresses, the effective stresses applied on each fault sub-patches increases (**Figure 55**), which causes some faults to become critically stressed (**Figure 54**). In the following discussion, we made the assumption that the seismicity observed in the Groningen Field is caused by shear movement along fault planes.

In 1964, under virgin pressure conditions, most of the faults are in a stable state (**Figure 43**) which is consistent with the absence of seismicity during the early stage of the field production (NAM internal report). M6 and B24 appear to have a Tau ratio larger than one for at least one of the fault sub-patches. The two faults, although possibly critically stressed, could be in reality both more cohesive frictional than modelled in the analysis. If field evidence confirms this hypothesis, this would explain the later occurrence of seismicity along this two faults. This however cannot be verified since these fault properties are not directly measurable. This initial condition seems consistent with the absence of seismicity during the earliest stages of production.

With increasing reservoir depletion, several faults rapidly reach critical conditions (**Figure 45**), particularly in the Loppersum area where the largest seismic events have been recorded. The modelling indicates that slip on faults can be expected as early as 1985. This risk of seismicity increases with time as a larger portion of the fault becomes critically stressed (**Figure 41**). Overall the location of the observed seismicity is reasonably close to faults where Tau ratio is larger than one (**Figure 53**) providing a confident history match between the seismic experience and the numerical model.

The fault stability calculations have been carried out at each node locations within each fault plane. A precise analysis of the stress distribution along a fault patch can provide a more robust assessment of the sections of the fault that are in critical state for slip. It is noted that the faults located in areas where differential depletion (i.e. the reservoir depletes faster on one side of the fault than another) are more likely to have higher Tau ratio values than faults located within uniformly depleted regions.

Shallower or deeper intervals such as the Carboniferous where no pore pressure changes are observed are unlikely to face increasing risks of fault slippage according to the model since post failure softening behaviour is not considered (**Figure 41**).

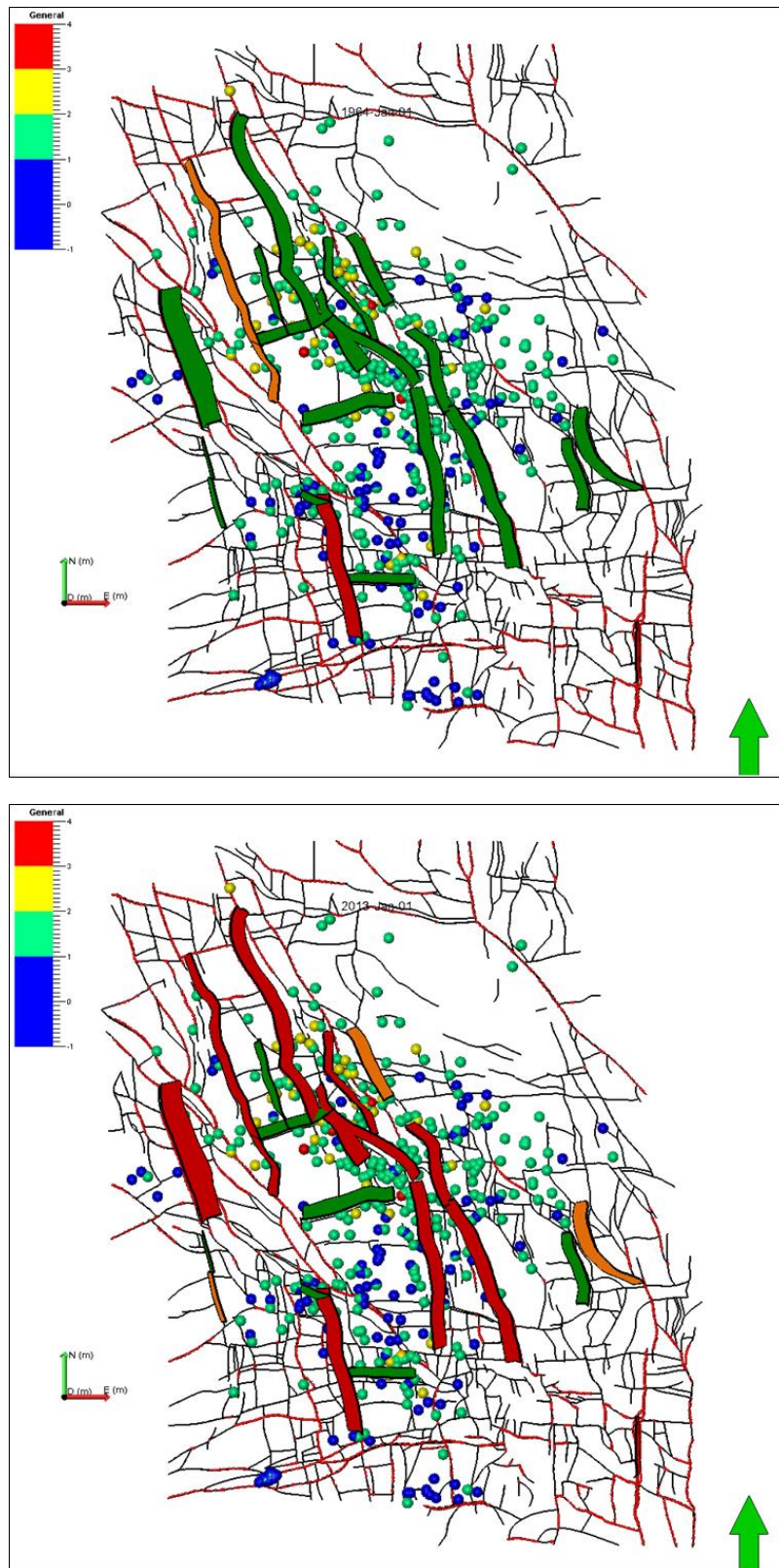


Figure 53. Superposition of the faults included in the model, ranged by critical state using the case 2 failure properties, with the map of the recorded seismic events (1991 – 2010 period) sorted by magnitude. Initial (1964) fault stability state (top) vs. 2012 fault stability assessment (bottom).

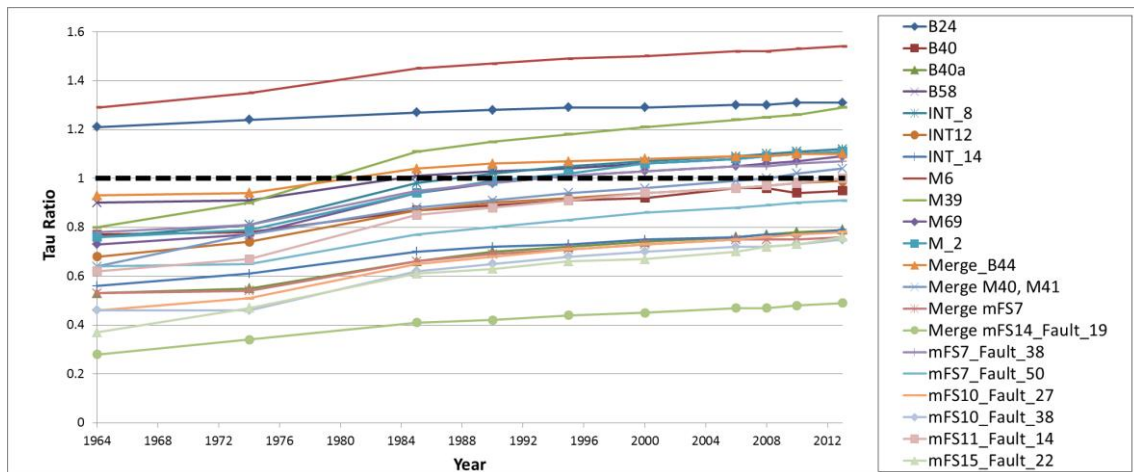


Figure 54. Evolution of the tau ratio on each fault during the production of the Groningen Field. The analysis was performed using the fault characteristics from case 2 ($\mu=0.23$ and cohesion = 7 MPa). The results show that most faults are initially in a stable configuration (tau ratio <1) but become critically stressed after years of production. Critically stressed faults starts to appear around 1985, and their numbers increase with time. In 2012, about half of the faults are unstable.

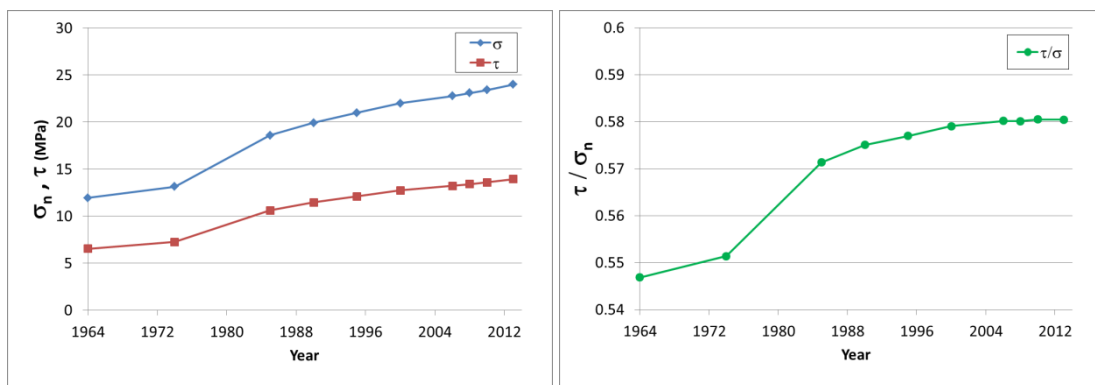


Figure 55. Evolution of the normal stress and the shear stress on the node 244 of the fault M_2 (location visible on the Figure 42) (left). Evolution of the shear to normal stress at this location of the M_2 fault.

The comparison between the critically stressed faults identified when using the case 1 of the fault mechanical properties did not provide a good correlation with observed seismicity whereas a good correlation was achieved using the case 2 fault mechanical properties. . Therefore, case 2 properties, sliding friction 0.23 (friction angle $\approx 13^\circ$) with a cohesion of 7 MPa were used in the field-wide fault study. A comparison between the two cases is provided in section **4.2.1 Comparison between the fault properties cases**.

The comparison of the field response imposed by the coupling of the two history matched production models (RM1 and RM2) suggests some small differences. For instance the fault M69 and mFS11_Fault_14 are not in a critical state using the reservoir pressure from the RM1 model while their Tau ratio is found slightly above 1 when using the reservoir pressure of the RM2 model in 2012. This difference is likely due to slight differences in reservoir pressures in the part of the field where these two faults are located. Otherwise, the overall trend indicates that faults oriented NNE-SSW will be

critically stressed in 2013, while most faults striking E-W remain stable despite field evidence of nearby seismic tremors in some locations (Merge mFS14_Fault_19, mFS10_Fault_27 and mFS10_Fault_38). The forecasted production models were analysed by coupling the reservoir models RM3, RM4 and RM5. For each production scenario the reduction of the pore pressure will continue to alter the stress field and increase the risk of seismicity on the faults included in the model based on the increasing calculated values of Tau ratio (**Figure 46** to Error! Reference source not found.). The differences in reservoir pressure anticipated for each of the depletion scenarios are small (a maximum of a few MPa) compared to the overall changes in pore pressure expected throughout the entire life of the field (more than 30 MPa of depletion). Therefore, the field response does not change significantly among the depletion models provided, and the distribution of the critically stressed faults is similar for each case.

Because most faults included in the models would have already experienced seismicity or a high risk of slippage during the first 50 years of production, few additional faults will exceed a critical Tau ratio from 2014 to 2080. During the later stage of field production, the fault planes showing new risk of seismicity during the later stage of production tend to be located on the outer part of the field (**Figure 46** to **Figure 48**). Although few currently stable faults will reach a critical state by 2080, it is important to note that additional fault patches on faults already identified as critically stressed are likely to reach that state between 2014 and 2080. Therefore, the risk of fault slip still exists in areas that are approaching the re-activation threshold. **Figure 41** shows that different areas of the faults can reach critical conditions at separate times, which suggests that a single fault can slip at different locations and generate multiple seismic events with limited magnitude.

Because the present modeling does not allow any displacement along the fault plane, the stress field perturbation caused by a seismic event is not accounted for in the modelled stress field. The stress redistribution caused by fault slippage can, however, impact the stability of nearby faults. While the modeling suggests that the faults with an East-West strike are not critically stressed, local adjustments in stress field caused by seismic activity along neighbouring faults could explain the occurrence of seismicity close to these structures.

5 Model Uncertainties

The geomechanical analysis performed for the Groningen Field has several source of uncertainty that could impact the interpretation of the results presented in this report. These uncertainties include:

5.1 1D Geomechanical Model

- No XLOT or mini frac data at virgin conditions were available for determination of the fracture closure pressure (FCP) in order to provide an accurate estimation the least principal stress (S_{hmin}). As a result, the magnitude of S_{hmin} has been constrained to the lower limit of the LOT dataset and hence its estimation is conservative. An estimated error bar of $\pm 15\%$ should be assumed for the resulting S_{hmin} to assess the uncertainties surrounding the model. The provided error bar has been estimated from the scattered LOT points used in this study.
- The variation of rock strength (UCS) across the Slochteren formation is large (15-26 MPa) which would increase the uncertainties in the estimation of the magnitude of S_{Hmax} . There is also poor knowledge of the rock properties in the overburden formations.
- The range of possible S_{Hmax} magnitude is related to the UCS uncertainties as a large variation in the rock strength has a direct impact on the estimation of S_{Hmax} .
- The 1-D geomechanical model is a non-unique solution. Therefore, it is possible to model the occurrence of breakouts using different stress models particularly at intervals where some of the input parameters provide relatively poor constraints. The impact of the uncertainties in the 1-D models has not been investigated in this study.

5.2 3-D Geomechanical Model

- The 3-D geomechanical response assumes that the rock materials have a poro-elastic response and therefore variations in formation pressures impact the magnitude of the horizontal stresses, S_{hmin} and S_{Hmax} . Although the dynamic response of the field is well calibrated by the subsidence measurements, no direct measurements, such as xLOT or minifrac tests, are available to confirm the changes in stress magnitude in the current depleted field conditions.
- The fault dynamics are assumed to be controlled by the cohesion, the sliding friction and fault orientation. These parameters are constrained empirically by comparing the Tau ratio acting on a fault plane with the level of seismicity recorded in the fault vicinity. It was assumption that the faults included in the model have identical mechanical properties.
- Finally, the finite-element simulations performed during this analysis do not consider any fault movement. Hence, the stress reorganisation subsequent to any fault slip events is not taken into account in this study.

6 Summary & Conclusions

Finite element simulations of the geomechanical response of the Groningen Field were performed by considering five different reservoir models (2 history matched, and 3 forecast scenarios). The aim of the analysis was to estimate the stability of the faults during the production of the Groningen Field by including a realistic geological structure and geomechanical properties constrained by 13 offset wells disseminated throughout the field (see part 1 of the study delivered on a separate report).

The main investigation addressed in this study consisted of:

1. Building a structural model and constructing a 3-D finite element mesh representative of the structure (including 9 horizons and 21 faults)
2. Determining rock mechanical properties, pore pressure and virgin in situ pressures at the field scales
3. Simulating the geomechanical response (stress and strain field) by coupling the finite element solver with five different reservoir simulation models.
4. Assessing the stability of the faults and its evolution during the depletion of the Groningen Field.

Firstly, it is important to emphasise that the present model does not consider a sensitivity analysis of the input parameters (rock mechanical properties, stress field, pore pressure). In addition, the stress reorganisation subsequent to a fault slip event (the decrease in tangential stress) is not considered in this study. Therefore, the finite element simulations permit the determination of the stress applied on a fault before any slip occurs.

3-D geomechanical modelling

- Geomechanical simulations of the response of the Groningen Field were performed by coupling five different reservoir models (2 history matched, and 3 forecast scenarios) with a finite element solver. The computed 3-D stress and strain fields were calibrated by comparing the vertical displacement calculated from the finite element analysis with the surface measurements of subsidence. The two history matched models (RM1 and RM2) showed reasonable agreement throughout the field (98.5% of the points have less than 10 cm of difference).
- The influence of salt creep during depletion was assessed prior to performing the fault slip analysis. It was shown that these effects were small in comparison to the poro-elastic effects characterising the depleted formations (3 MPa vs 20 MPa).
- The reservoir stress paths, indicative of the sensitivity of the horizontal stresses to variation in pore pressure, were determined based on the first 45 years of production. Although the stress path parameters could not be calibrated using field measurements, it is observed that $A_{SHmin} = A_{SHmax} \sim 0.6$ throughout the field based on the Poisson's ratio distribution.

Fault slip analysis

-
- The calibrated 3-D stress and strain field was used to assess the stability of the faults during the production of the field. The comparison between two different cases of fault failure properties indicate that the analysis show a better consistency with the recorded seismic events when using a cohesion of 7 MPa and a sliding friction angle of 13° (sliding friction coefficient = 0.23).
 - The first two reservoir models indicate that several faults (essentially those oriented NNE-SSW) became critically stressed during production and that the risk of fault slip increased. The Loppersum area, where the most intense seismicity has been recorded, concentrated a large number of critically stressed faults.
 - The three other reservoir models (RM3, RM4 and RM5) allowed an evaluation of the Tau ratio on each fault from 2014 to 2080. The results indicate that few additional faults would move towards an unstable state using the three forecast models. This does not preclude the possible occurrence of seismic tremors in areas where faults have already been critically stressed for a number of years.
 - Based on the geomechanical simulations and the fault slip analysis performed for this study, there is a likelihood to reactivate slip along existing fault planes. Each of the three (3) projections of the reservoir model of the Groningen Field suggests that some faults could further destabilize between 2016 and 2050.

7 References

- Breunese J.N., van Eijs R.M.H.E., de Meer S., Kroon I.C. (2003) Observation and Prediction of the relaxation between salt creep and land subsidence in solution mining. The Barradel Case. Solution mining research institute, Fall 2003 Conference, Chester UK
- Byerlee J. (1978). Friction of Rocks. *Pageoph* 116(4-5), 615-626
- Chang A., Zoback, M.D. (2000) Deformation analysis in reservoir space (DARS): A simple formalism for prediction of reservoir deformation with depletion, SPE78174. SPE/ISRM Rock Mechanics Conference, Irving, Tx, SPE
- Diggs T. N., Urai, J. L., Carter N. L. (1997) Rate of flow in Salt sheets, Gulf of Mexico: Quantifying the risk of casing damage in subsalt plays, EUG 9, Strasbourg. *Terra Nova*, 9, Abstract Supplement No 1: 172.
- Ellis S. (2006) Attaining geostatic equilibrium and initial stress states: crustal faulting experiments using Abaqus. Presented at Geoqus Workshop, Bochum.
- Zoback M.D. (2008) *Reservoir Geomechanics*, Cambridge University Press, New York
- Van den Bogert P.A.J., van Eijs R.M.H.E., van der Wal, O. Groningen Fault Stability Assessment (2013), Shell Global Solution, internal report

8 Nomenclature

Abbreviation	Meaning
DDR	Daily Drilling Report
FWR	Final Well Report
LOT	Leak Of Test
MDRT	Measured Depth from Rig Table
MDT	Modular formation Dynamic Tester
RFT	Formation Test
S_{Hmax}	Maximum Horizontal Stress
S_{Hmin}	Minimum Horizontal Stress
TVDRT	True Vertical Depth from Rig Table
TVDSS	True Vertical Depth from Sea Surface
UCS	Unconfined Compressive Stress
ESR	Effective Stress Ratio
BO	Breakout
IF	Internal Friction
FEM	Finite Element Method
μ_s	Coefficient of Sliding Friction
C_o	Cohesion

Appendix 1 displacement element in the Carboniferous layers below the reservoir

Figure 56 shows artefacts which could be interpreted as drainage of the pore pressure out of the reservoir zones within the under-burden (black arrow in the figure). This typical phenomenon could there be interpreted as an over-estimation of the reservoir thickness.

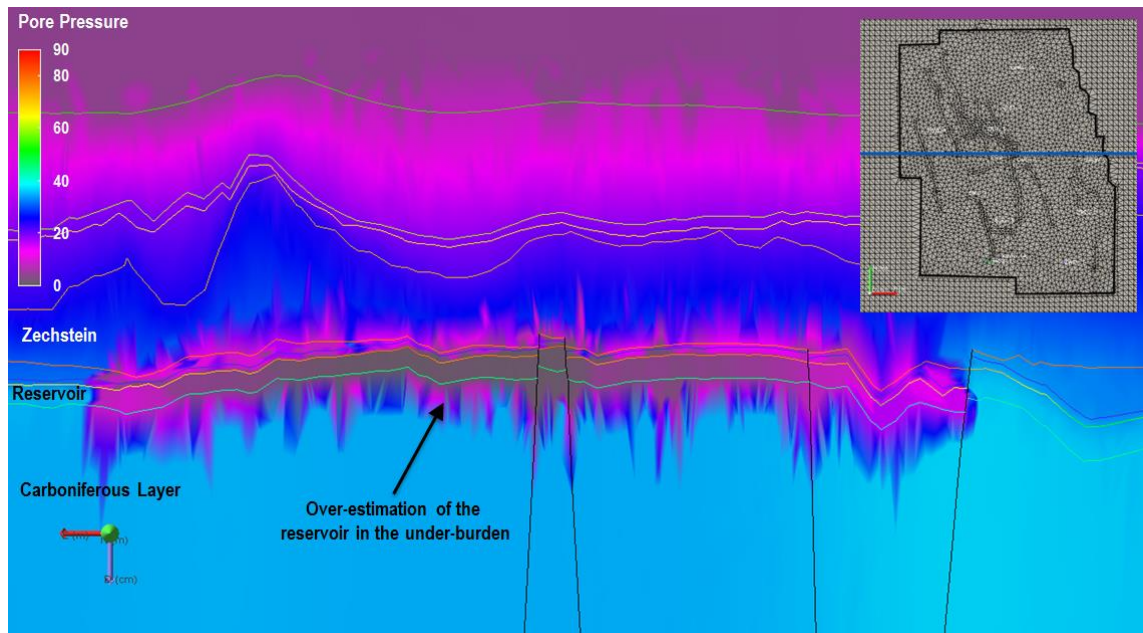


Figure 56. Cross section of the pore pressure in a modelled FE-Mesh using porous elements

In principle, all the calculations are performed on nodes that are defined by the mesh and the type of elements used in this mesh. In our typical case, each element contains ten (10) nodes with 9 of them shared to other elements (the last node being in the center of the tetrahedral element).

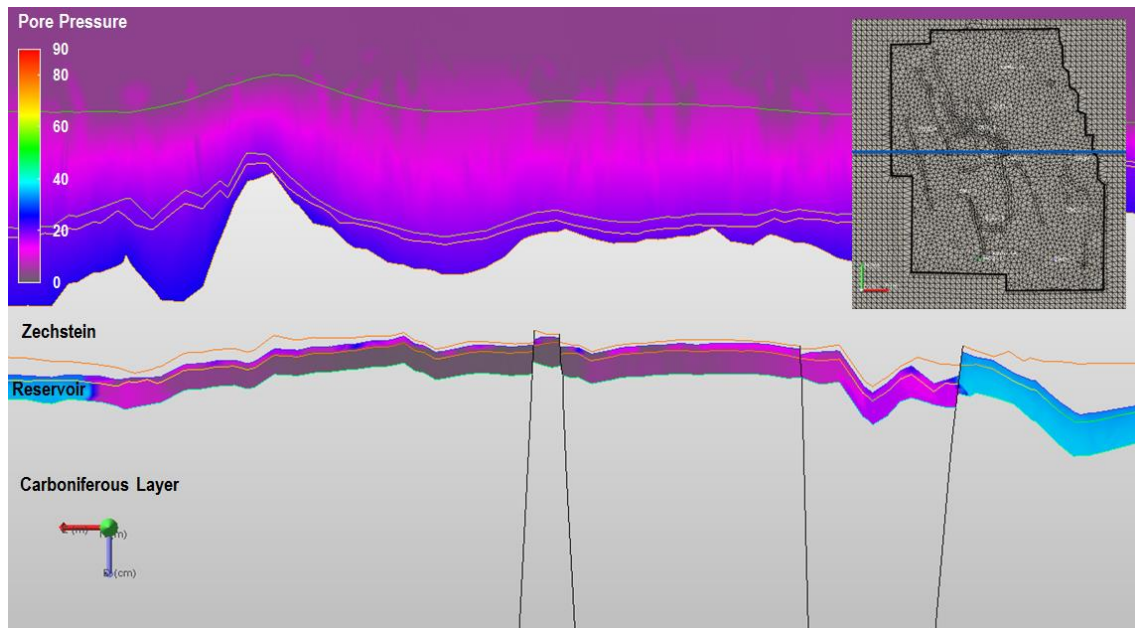


Figure 57. Cross section of the pore pressure in the modelled FE-Mesh using non-porous elements in the Zechstein and the carboniferous layers

The problem comes from the mapping of the data into the 3-D-Mesh as only the mapped values are assigned on the nodes located on the edges of the elements. The software then interpolates linearly the values of the other nodes. Depending on the location and the density of the nodes, some erroneous nodes values can occur despite all the precautions taken to avoid them.

In order to avoid these undesired artefacts, it was decided to use non poro-elastic elements (known as C3D10M elements in Abaqus) in the under-burden (Carboniferous layer) (see **Figure 9**). By adopting the approach, the reservoir thickness is then not over-estimated as no pore pressure can be propagated within the Carboniferous layers (see **Figure 57**).

Appendix 2 Assessment of the Effect of Salt Creep on the 3-D geomechanical model

A model of the salt creeping over the 45 years of production was performed to investigate its effect on the results of the 3-D dynamic geomechanical model.

We simulated salt creep that occurred as an effect of pore pressure depletion from 45 years of production. The results of this simulation were then compared to a simulation without the salt creep during production.

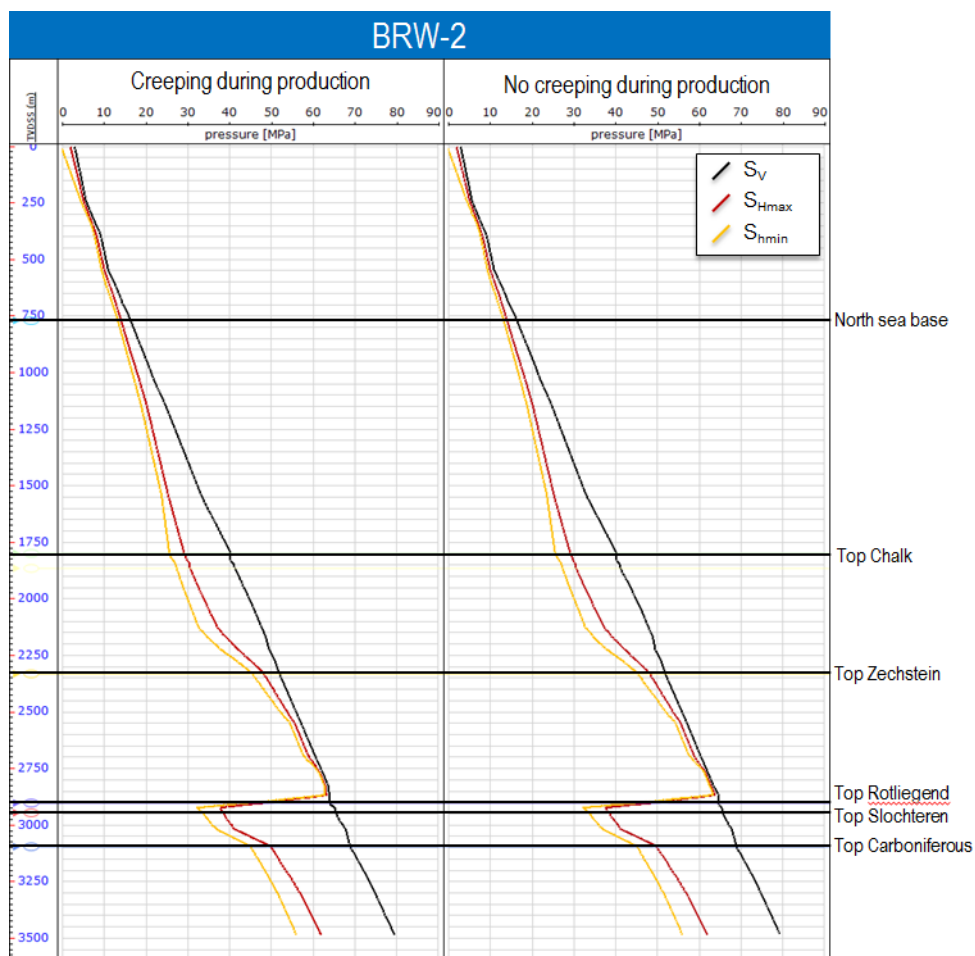


Figure 58. Overview of the principal stresses for the two models (with salt creep and without salt creep).

Comparison of the models reveals that no major variations of the stress tensor could be identified within the zone of interest represented by the Groningen Field. **Figure 58** summarises this comparison for the well BRW-2 with a difference in the principal stresses between the models of less than 1MPa.

The effect of the salt creep is also minimal on the subsidence as visible on **Figure 59**.

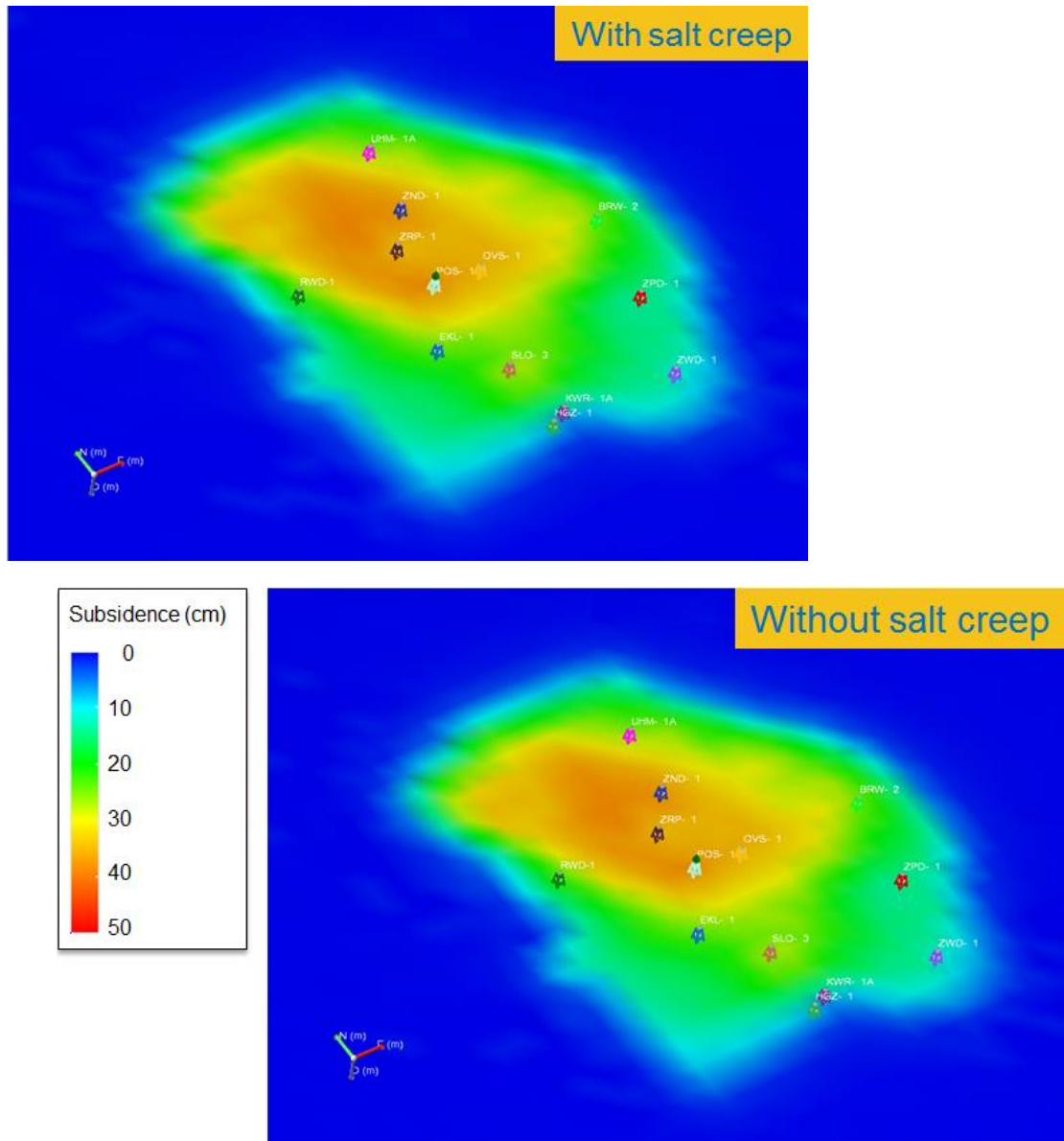


Figure 59. Overview of subsidence for the two models (with salt creep and without salt creep).

Appendix 3 Upscaling data

The process of upscaling consists of adapting data from a well (usually a high resolution log such as density log for example) that is to be mapped to a 3-D grid. In the absence of upscaling, the mapping of data into a 3-D grid would not reflect the distribution of the log.

The population of a well datum into a 3-D grid consists of mapping the nearest value from the well data at each of the centers of the elements constituting the 3-D grid as shown in **Figure 60**. The mapped values in the grid tend to over predict (as for the element n+1) or under predict (as for the element n+5) the distribution of the data for each element.

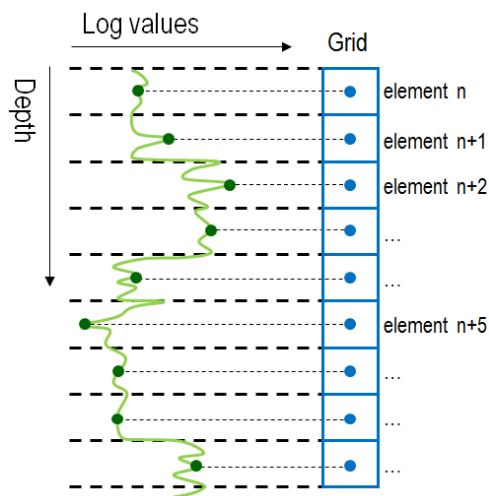


Figure 60. Mapping log data into a 3-D grid without upscaling

The upscaling process helps to determine a coherent value for each element. In this particular case, the arithmetic average was considered and applied to each interval of element thickness. The well datum is then customised for the grid prior to mapping the datum (see **Figure 61**).

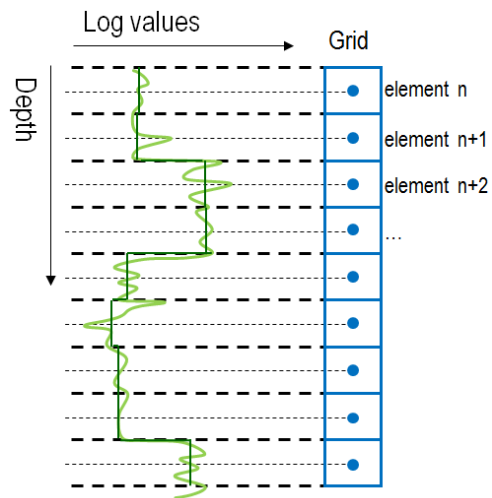


Figure 61. Mapping log data into a 3-D grid with upscale processing